Fluorescence Emission Enhancement in Molecular Solids: Insight into the Critical role of Oriented Assembly and Entry into Functional Molecular Phase Change Materials

A Thesis Submitted for the Degree of
DOCTOR OF PHILOSOPHY

by

P. Srujana

School of Chemistry
University of Hyderabad
Hyderabad 500 046
INDIA

November 2018

Dedicated

To

My Family Members

CONTENTS

DECLARATION

I hereby declare that the matter embodied in this thesis is the result of the investigations carried out by me in the School of Chemistry, University of Hyderabad, Hyderabad under the supervision of Prof. T. P. Radhakrishnan.

In keeping with the general practice of reporting scientific observations, due acknowledgements have been made wherever the work described is based on the findings of other investigators.

P. Srujana

CERTIFICATE

This is to certify that the thesis entitled "**Fluorescence Emission Enhancement in Molecular Solids: Insight into the Critical role of Oriented Assembly and Entry into Functional Molecular Phase Change Materials**" submitted by **P. Srujana** bearing registration number **12CHPH14** in partial fulfillment of the requirements for award of Doctor of Philosophy in the School of Chemistry is a bonafide work carried out by her under my supervision and guidance.

This thesis is free from plagiarism and has not been submitted previously in part or in full to this or any other University or Institution for award of any degree or diploma.

Parts of this thesis have been:

A. Published in the following publications:

1. P. Srujana, T. Gera and T. P. Radhakrishnan, *J. Mater. Chem. C*, 2016, **4**, 6510-6515. **(Chapter 2)**
2. P. Srujana and T. P. Radhakrishnan, *Chem. Eur. J*., 2018, **24**, 1784-1788. **(Chapter 3)**
3. P. Srujana and T. P. Radhakrishnan, *Mater. Chem. Front.*, 2018, **2**, 632-634. **(Chapter 4)**
4. P. Srujana and T. P. Radhakrishnan, *Angew. Chem. Int. Ed.*, 2015, **54**, 7270-7274. **(Chapter 5)**
5. P. Srujana, P. Sudhakar and T. P. Radhakrishnan, *J. Mater. Chem. C*, 2018, **6**, 9314-9329.

B. Presented in the following Conferences:

1. Materials for the Millennium (MATCON-2016), Cochin University of Science and Technology, Kochi, India, January 14-16, **2016** (International).
2. International Collaborative and Cooperative Chemistry Symposium (ICCCS-8, 2017), University of Hyderabad, Hyderabad, India, December 18-19, **2017** (International).

Further the student has passed the following courses towards fulfillment of course work requirement for Ph.D:

Course code	Name	Credits	Pass/Fail
1. CY-801	Research Proposal	3	Pass
2. CY-805	Instrumental Methods A	3	Pass
3. CY-806	Instrumental Methods B	3	Pass
4. CY-882	Organometallic Chemistry	2	Pass
5. CY-892	Stereoselective Organic Synthesis	2	Pass

Prof. T. P. Radhakrishnan
(Thesis Supervisor)

Dean
School of Chemistry

ACKNOWLEDGEMENTS

I would like to acknowledge and extend my heartfelt gratitude to Prof. T. P. Radhakrishnan, my research supervisor for his constant guidance, encouragement and for the freedom he gave me in carrying out my research. His innovative thoughts, commitment to the work with a great sense of discipline and patience are highly admirable and motivating which I always have aspired to imbibe. My association with him is a memorable one.

I thank present and former Deans, and faculty members of the School of Chemistry for their support and help on various occasions. I thank Prof. K. C. Kumara Swamy and Prof. Akhila Kumar Sahoo for their support as doctorial committee members. I thank all the faculty members for their cooperation whenever required. I thank all the non-teaching staff, School of Chemistry for their cooperation. I would also like to thank Prof. M. Durga Prasad (School of Chemistry), Prof. D. Narayana Rao, Prof. Nirmal K. Viswanathan and Dr. N. Sri Ram Gopal (School of Physics), and Dr. Jayanti Subbalakshmi (BITS-Pilani, Hyderabad campus) for their support and help in some of my doctoral research. I thank Prof. Chitoshi Kitamura (University of Shiga Prefecture, Japan) for providing the spectral data required for some of my studies. My sincere thanks to all the teachers from my schooling to master′s course for their excellent teaching.

I would like to express my sincere gratitude to Mr. Durga Prasad (FLIM, School of Chemistry), Mr. Sunil (FESEM, School of chemistry), Mr. Shyam and Mrs. Gomati (FT-IR), Mr. Bhaskar Rao (CHN analysis), Mr. Raghavaiah, Mrs. Sree Lakshmi and Mr. Venkata Ramana (SC-XRD), Mr. Kumar (PXRD), Mrs. Asia and Mr. Subramanyam (HRMS) and Mr. Anand (N_2 gas), Mr. Pavan (SEM, CIL), Rajesh (DSC, CIL), Ms. Nalini (LSCM, CFN), for their assistance in various instruments. I thank School of Chemistry and Central Instruments Laboratory (CIL), University of Hyderabad for instrumentation facility, and Center for Modelling, Simulation and

Design, University of Hyderabad for computational facility. I thank CSIR for providing the fellowship.

It is a great pleasure to thank my seniors Dr. Gupta and Dr. Hari for their help and cooperation. I am extremely thankful to Kesav for his help, support and encouragement during my Ph.D. I thank Lasya, Divya, Senthil, Sasi, Dr. Jony, Dr. Sudhakar and Durga Prasad for their support in lab. I also acknowledge all the project students worked in our lab. I would like to thank Dr. Ashok Keerthi, Dr. Ashok Pabbati, Dr. Sudheer, Dr. Chandrasehkar and Dr. SivaRamakrishna for their help, support, suggestions and guidance during my Ph.D. ***I thank all the research scholars of School of chemistry and friends*** for the cheerful and enlivening atmosphere they maintained and for making my stay in the campus unforgettable. I also thank all the friends from School of Life Sciences and School of Physics for making my stay pleasant and for their support.

My special thanks to Chakradhar Sahoo, Nabil and Rashmi Ranjan from School of Physics for their help in laser related work. I am also thankful to Dr. Krishna Reddy, Dr. Leela Siva Kumari, Dr. Krishna Rao, Dr. Siva Reddy, Satyanarayana, Arun and Prachi for their help in aspects like synthesis and computational studies during my research.

I am at a loss of words to express gratitude to my parents. The way I grew up, the values I imbibed, the education I received and the person I am now is all due to them. I am grateful to my caring and loving sister and brothers who have always been an ardent listeners and a strong support to me. I would like to acknowledge all my relatives for their love and encouragement.

P. Srujana

COMMON ABBREVIATIONS

A↔C	reversible amorphous-crystalline transformation
ACT	amorphous-to-crystalline transformation
AIE	aggregation-induced emission
d	doublet
DADQ	diaminodicyanoquinodimethane
dec.	decomposition
DSC	differential scanning calorimetry
FEE	fluorescence efficiency enhancement
m	multiplet
ml	millilitre
mmol	millimole
nm	nanometer
PMMA	poly(methyl methacrylate)
PVAc	poly(vinyl acetate)
PXRD	powder X-ray diffraction
rpm	revolutions per minute
s	singlet
t	triplet
T_c	crystallization temperature
T_m	melting temperature
TCNQ	7,7,8,8-tetracyanoquinodimethane
W	Watt
x	dye to polymer weight ratio

CHAPTER 1

Introduction

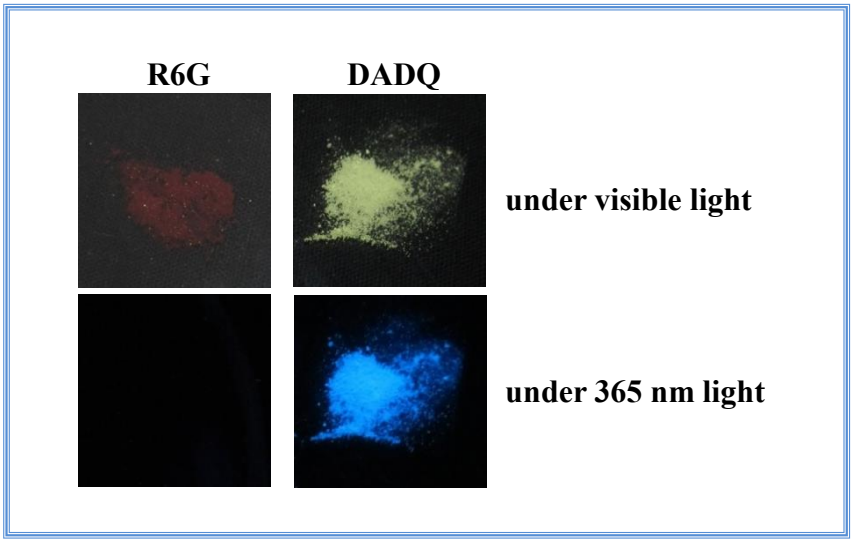

Photographs of rhodamine 6g (R6G) and a diaminodicyanoquinodimethane derivative (DADQ) under visible light and the corresponding emission observed under UV light (365 nm) irradiation.

Scope

Molecular materials that are highly emissive in the aggregate/solid state are of great interest in diverse fields ranging from sensors and devices to biology and medicine. Most of the conventional fluorophores are prone to self-quenching or aggregation caused quenching of fluorescence, limiting their use in various technological and biological applications. Enhanced emission of aggregates/solids has been realized in select classes of molecules and is often referred to as "aggregation induced emission". Basis of the enhanced emission of aggregates/solids has largely been attributed to the restriction of intramolecular motions that would otherwise cause non-radiative excited state decay. As such a scenario (restriction of intramolecular motions upon aggregation) should in principle be applicable to most solids, emission enhancement observed only in a few classes of molecules is a matter of fundamental interest. Role of other factors that could potentially quench the fluorescence in the aggregates, primarily through intermolecular effects, and how they are surmounted to effect enhanced fluorescence in aggregates/solids, have not been explored in great detail. A systematic exploration of the correlation between molecular assembly and fluorescence efficiency enhancement is essential for designing new optical materials. One of the major goals of this thesis is to gain insight into the critical factors that lead to fluorescence efficiency enhancement in the aggregated systems and solids; this is done primarily by exploring a class of diaminodicyanoquinodimethanes (DADQs) followed by a few other systems. We have developed a methodology to analyze the factors governing the fluorescence efficiency enhancement from isolated molecule to the solid state. We have also investigated the basic issue of fluorescence efficiency enhancement from an amorphous to crystalline state of molecular materials based on the DADQ framework. This culminated in the realization of thermally induced reversible amorphous↔crystalline phase transformation accompanied by a distinct change in the fluorescence emission response between the two phases.

This chapter provides an introduction to molecular materials (Section 1.1), highlighting the tuning of materials property by harnessing structure, assembly and size control. This is followed by an overview of the relevance of amorphous phase and amorphous molecular materials and the emergence of the extent of crystallinity as a design tool for molecular materials. The phenomenon of fluorescence, factors responsible for fluorescence quenching in aggregates, and the importance of solid state fluorescent materials are discussed in Section 1.2. A brief discussion of the well-known classes of molecules exhibiting enhanced emission in aggregates/solids, followed by the models proposed for the phenomenon of aggregation-induced emission and applications of such materials are also provided. Section 1.3 provides a brief introduction to phase change materials and their application in different fields. Layout of the thesis is outlined in Section 1.4.

1.1. Molecular Materials

Molecular materials are constituted of building blocks based on molecules or molecular ions, unlike the other solids such as ionic, covalent, and metallic solids built up of atoms and ions connected through extended bonding. In molecular materials, the building blocks are assembled through a variety of relatively weak, non-covalent interactions like hydrogen bonding, electrostatic, π-π stacking and van der Waals.[1] Polymeric materials made up of covalently bonded macromolecular building units can be visualized as sharing characteristics of traditional solids and small molecule based materials. The unique characteristic of molecular materials is that when disassembled, the individual constituents retain to a large extent the essential properties of the parent material. The uniqueness of molecular materials arises from the method of fabrication involving the two steps of synthesis and assembly (Fig. 1.1). In the first step, the desired molecules/building blocks are synthesized from appropriate precursors (formation of covalent interactions); they are assembled to form the desired material

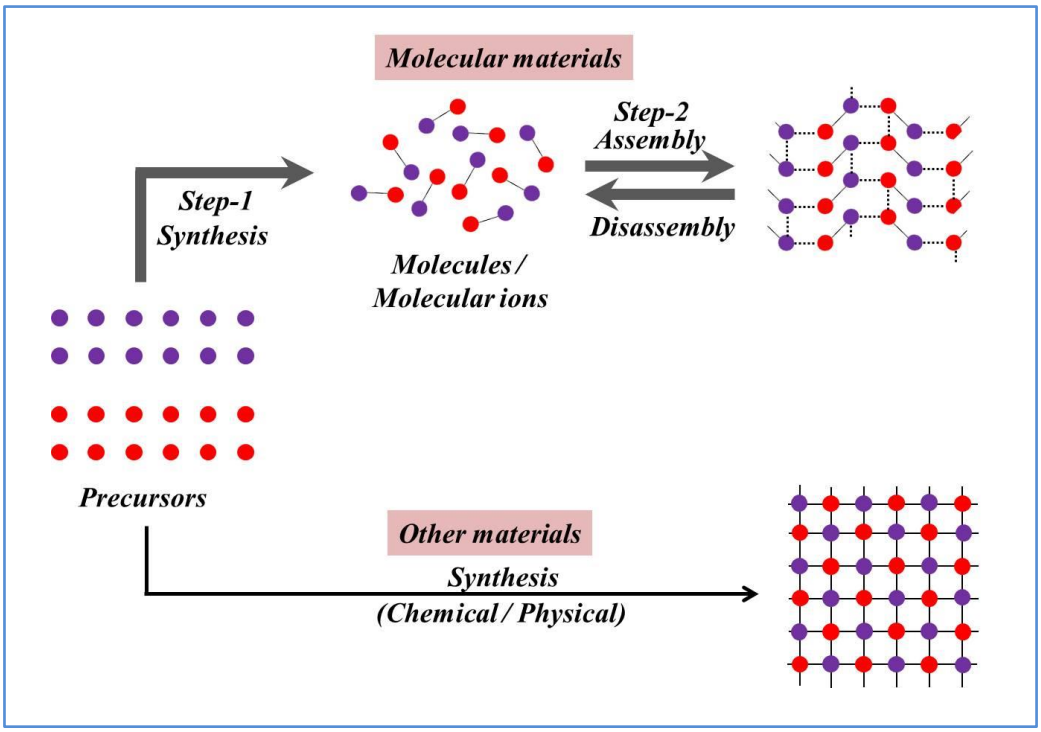

Figure 1.1. *Schematic representation of the fabrication of molecular materials and other materials.*

in the second step (non-covalent interactions employed). The building blocks can be simple organic molecules, organometallic compounds or coordination complexes. Assembly of molecules into materials can be achieved *via* a variety of methods like simple crystallization, host-guest complexation, self-assembly techniques, steered assembly by Langmuir-Blodgett (LB) technique, and sol-gel methods. The fabrication of molecular materials thus provides two-step control for fine-tuning of materials properties; one is through chemical structure modification of the building block and the other by manipulating the assembly pattern. Different classes of molecular materials have been designed and developed for a wide variety of applications. Liquid crystals are perhaps the earliest examples; various conducting, magnetic, and optical materials have been developed over the last several decades, following the discovery of semiconduction in organic molecular material in 1954.[2,3] A brief discussion of magnetic, conducting, and optical materials is provided below.

Molecular magnetic materials

Several of the traditional magnetic materials are element based, containing transition (Fe, Co, Ni) or lanthanide (Gd) metals, with unpaired spin in d or f orbitals. Oxides and alloys like CrO_2, Fe_3O_4, Co_5Sm and $Nd_2Fe_{14}B$ are also well known magnetic materials. They are generally fabricated by metallurgical processes involving high temperatures. Synthesis of purely organic ferromagnetic materials (with spin moment arising from electrons in s and p orbitals) posed a major challenge in this field. Several organometallic and metal coordination complexes were developed that formed a transition from traditional magnets towards organic molecule based magnetic materials. The first molecular ferromagnetic material to be reported was a complex of tetracyanoethylene (TCNE) with decamethylferrocene $[Fe(C_5Me_5)_2]$, with a ferromagnetic ordering (Curie temperature) at 4.8 K.[3] The first purely organic ferromagnet reported was the *β*-polymorph of *p*-4-nitrophenylnitronyl nitroxide (*p*-NPNN) with an ordering temperature of 0.6 K.[4] Several magnetic materials based on organic radicals such as nitroxides/nitronylnitroxides and thia/selena-azolyls, and TCNE containing materials have been developed.[5] Single-molecule magnets (SMM) and spin-crossover systems are attractive classes of magnetic materials with potential technological applications in areas like information storage and display devices.[6]

Molecular conducting materials

Materials with high electrical conductivity are metals and semiconductors, primarily inorganic in composition. Most organic materials are electrical insulators. Semiconductivity was first realized in π-conjugated molecules; perylene-bromine complex with a resistivity as low as 1 Ω cm is the first molecular material in which semiconducting behavior was reported.[7] Synthesis of strong π-electron donors and acceptors such as tetracyanoquinodimethane (TCNQ) and tetrathiafulvalene (TTF) led to the development of electrically conducting organic charge transfer complexes. TTF-TCNQ exhibits an electrical conductivity of 10^3 S cm^{-1} at ambient temperature while metallic behavior below 70 K. Several organic metals based on charge transfer complexes have been synthesized and studied subsequently.[8] Examples of π-electron donor molecules include *N*,*N*,*N*′,*N*′-tetramethyl-*p*-phenylenediamine (TMPD), tetramethyltetraselenafulvalene (TMTSF), TTF, tetrakis(dimethylamino)ethylene (TDAE) and bis(ethylenedithio)tetrathiafulvalene (BEDT-TTF). π-electron acceptors include TCNQ, TCNE, chloranil and dicyanoquinodiimine (DCNQI).[9] Organic molecular materials possess the advantage of facile tailorability of chemical structure and assembly. Conjugated polymers form an important class of semiconductors; polypyrrole, polyacetylene, polythiophene and polyaniline are some of the well-known conducting polymers.[10] The first superconducting molecular material reported is bis(tetramethyltetraselenafulvalene)hexafluorophosphate [$(TMTSF)_2PF_6$]; $(BEDT\text{-}TTF)_2X$, (X = PF_6, TaF_6, ReO_4 and ClO_4), κ-$(BEDT\text{-}TTF)_2Cu[N(CN)_2]Br$ and salts of fullerene are examples that followed.[11]

Molecular optical materials

Materials capable of strong light emission upon suitable electronic excitation have attracted great attention in several fields ranging from sensors and devices to biology and medicine. Based on the source of excitation, the emission may be termed as photoluminescence, electroluminescence, chemiluminescence and mechanoluminescence, the excitation source being light, electric field, chemical reaction and mechanical stimulation respectively. Photoluminescence can be either fluorescence, if the emission is from a singlet excited state or phosphorescence if it is from a triplet state. Organic semiconducting π-conjugated systems and light emitting materials based on small organic molecules and polymers have found applications in

field-effect transistors,[12] light emitting devices[13] and optical waveguides;[14] photochromic materials, photoconductors, and photovoltaics are also important optical and optoelectronic materials.

Nonlinear optical (NLO) materials exhibit nonlinear variation of electric polarization due to the strong electric field associated with the incident light. NLO response is observed only with high intensity light; the advent of lasers was crucial for the full realization of these effects. NLO processes include frequency-mixing (second- and third-harmonic generation, sum- and difference-frequency generation, optical parametric amplification etc.), multi-photon absorption, optical Kerr effect and four-wave mixing.[15] Single crystal quartz, potassium dihydrogen phosphate (KDP) and lithium niobate ($LiNbO_3$) are the classic examples of inorganic NLO materials, and methyl-(2,4-dinitrophenyl)-aminopropanoate (MAP) and *N*-(4-nitrophenyl)-(L)-prolinol (NPP) are some of the examples of molecular NLO materials.[16] Efficient second harmonic generation response in a class of zwitterionic molecules based on diaminodicyanoquinodimethanes (DADQs) has been reported from our laboratory.[2]

1.1.1 Tuning of materials properties

As mentioned in the previous section, molecular materials offer two stage control over tuning of the materials properties. The obvious option is the chemical modification of the molecular structure; a more subtle handle is provided by the assembly of the molecules. In addition to structure and assembly, size of the molecular assemblies or aggregates can play a crucial role in tuning the materials property, specifically in the nanometric size regime. Fabrication of organic nanoparticles by techniques such as reprecipitation provides a novel approach to tuning the materials characteristics and attributes.[17] The role of molecular structure, assembly and particle size in determining the materials properties is discussed below. The extent of crystallinity of a material can influence some of the specific properties and functions. Relevance of the amorphous phase and application of amorphous molecular materials is also discussed. The specific problem of tuning of solid state fluorescence emission of small molecule based materials using molecular structure and assembly is discussed in Sec. 1.2.3.

Structure

Understanding of the basic structure-property relationship is of fundamental interest and also crucial for designing new materials. Molecular structure modification affecting the materials properties have been explored in several fields and also exploited for improving the materials performance in technological applications. Organic photovoltaics is one such case where the continuous research efforts at structural modifications has led to steady increase of power conversion efficiencies (PCE) of organic solar cell up to ~ 13%.[18] Chemical modifications involving electroactive and functional group modulation for tuning the frontier orbital energy levels and electronic absorption, as well as side chain engineering for improving solution processability and charge carrier mobility have led to better photovoltaic materials.[19] Li et al., studied the effect of increasing methyl substitution on the end groups of the electron acceptor, and fluorination of electron donor and acceptor on the performance of solar cells.[18,20] Consequence of the structure modification was that the open-circuit voltage increased when dimethylated electron acceptor was used instead of the unmethylated derivative. Further, fluorination of both electron donor and acceptor increased the PCE to 13% compared to the 12% of non-fluorinated derivatives. A simple structural modification imparted to the molecule, the ability of forming supramolecular fused ring structure by conformational locking, and increased the PCE of the solar cell from 2.3% to 9.6%.[21] The effects of molecular structure and hence packing on the optoelectronic properties of several materials have been reviewed.[22] Simple structural modification based on the alkyl substitution position was shown to tune the property of acceptor-donor-acceptor type molecules from electron donating to electron accepting.[23] Position of the alkyl substituent affected the molecular packing; the one with low steric hindrance formed ordered lamellar structure with good π-stacking and acted as donors, whereas the other with higher steric hindrance had weak π-stacking interactions and acted as acceptors. Noncentrosymmetric crystal lattice, an essential criterion for second order NLO properties is often achieved by introducing stereogenic centers on the relevant molecules.[24]

Assembly

Assembly of molecules play a crucial role in determining the material properties such as ferroelectric behavior, second harmonic generation (SHG), and solid state

photochemical reactions.[25] Electronic structure of a molecule is greatly affected by the intermolecular distances and relative orientation of the neighboring molecules in the solid state. Dramatic differences observed in some polymorphic structures clearly demonstrate the critical role of molecular assembly. Efficient second harmonic generation (SHG) is achieved by inducing preferred assemblies through processes such as electric field poling, fabrication of X and Z type LB films, host-guest complexation and co-crystallization.[2] Control of supramolecular organization using ionic and π-interactions, and polyelectrolyte templating, leading to noncentrosymmetric lattices/assemblies for efficient SHG, have been studied in several molecules.[26] Supramolecular organic ferroelectric systems and LB films of molecular conducting and magnetic materials have also been reported.[27] Control of molecular assembly in monolayer films using mechanical compression in Langmuir films has been shown to lead to significant changes in fluorescence emission of LB films of 7,7-bis(4-octadecyloxyethylpiperazino)-8,8-dicyanoquinodimethane.[28] In bulk heterojunction solar cells, self-assembly of electron donors and acceptors in the active layer has significant effect on the device performance. The size of the domains should match the exciton diffusion length for exciton splitting and charge carrier transport to be efficient. Stupp et al., have reported the role of self-assembly of hairpin-shaped donor molecules forming grooved nanowires, on the solar cell performance. Fullerene based acceptors efficiently interact with the grooved architectures of the donor assemblies facilitating efficient charge transport, enhancing the device performance by 50%.[29]

Size

Nanomaterials based on metals and semiconductors are quite well-known; in many respects they show superior performance compared to the bulk materials. Molecular nanomaterials are attracting increasing attention because of the versatility and flexibility in the fabrication of the molecular building blocks followed by the nanostructures; they also show wide ranging application potential.[30] Interesting optical and optoelectronic properties have been realized in several functional organic materials when fabricated as low-dimensional nanostructures.[31] Enhanced performance of photovoltaic cell and polymer based light emitting diode are achieved by employing the active materials in the form of nanostructures.[32] Field-effect transistors fabricated using nanowires of organic semiconductors like perylenetetracarboxyldiimide and hexathiapentacene exhibit good carrier mobility and current on/off ratio.[33] Enhanced

conductivities have been achieved from the ordered nanostructures of several conducting polymers like polyacetylenes, polypyrroles, polythiophenes, and polyanilines synthesized using template methods.[34] Voltage dependent electroluminescence of the co-oligomer, thiophene/*p*-pehenylene is attributed to the carrier confinement in the nanocrystals of the co-oligomer.[35] Nanosized hierarchical structures of polypyrrole and polyvinylcarbazole obtained by confined polymerization in the nanospaces present in the mesocrystals of biominerals exhibit different conducting, optical and thermal properties, from that of the polymers synthesized by conventional methods.[36] Enhanced second-order NLO property is achieved by confining centrosymmetric molecules inside the carbon nanotube in head-to-tail fashion.[37] Size dependent optical properties have been realized in the nanoparticles of bis(4-chloroanilino)-8,8-dicyanoquinodimethane,[38] pyrazoline,[39] dibenzoylmethane[40] and azulene based conjugated polymer.[41] Nanowires of hexaphenylsilole show gradual red-shift of fluorescence emission with decrease in the diameter of the nanowires.[42] Nanostructures of 9-*tert*-butylanthroate exhibit anisotropic expansion and bending of nanorod upon UV irradiation, whereas the bulk crystal disintegrates.[43]

Crystallinity: Amorphous molecular materials

Fabrication of molecular materials involves the transition from the molecular to the material state. Tuning of materials property is mostly achieved either by chemical structure modification at the molecular level or by the assembly process as discussed above. Hierarchical assembly of molecules from the isolated state (in solution) to the well-organized assembly/crystalline state with fine-tuning of the characteristics and properties at each level is of fundamental interest. Amorphous form can be considered as one such intermediate state between the isolated and the final periodically organized crystalline state.

The coexistence of amorphous and crystalline regions, and the effect of degree of crystallinity on the materials properties is well recognized in the case of polymers.[44] The amorphous state and the level of crystallinity of small molecule based materials are important in many fields like pharmaceuticals, optoelectronics, and memory devices. In pharmaceutics, amorphous materials are often preferred over the crystalline forms, owing to their better solubility and dissolution, and hence bioavailability.[45] Bioavailability of sulfathiazole drug having poor aqueous stability, is enhanced by

preparing co-amorphous forms of the drug with water soluble additives.[46] Techniques like cryogrinding, melt quenching, and ball milling are used at small scale, and lyophilization, precipitation and spray drying are used for large scale production of amorphous active pharmaceutical ingredients.[47] Optoelectronic devices like organic light emitting diodes, organic field-effect transistors, and organic photovoltaics use organic materials as the active layers for charge carrier generation, transport, and light emission. Though some devices using organic single crystals exhibit better performance, growing defect free, single crystals for large area application is difficult; polycrystalline materials suffer from grain size effects and grain boundaries. Amorphous molecular materials are promising candidates in several such applications, due to their isotropic and homogenous properties and efficient contact with the adjoining layers in the device.[48] Triphenylamine and 1,3,5-triphenylbenzene cored molecules, thiophene and oligothiophene end-capped triarylamines, tris(oligoarylenyl)amines, and triarylboranes, are examples of charge carrier transporters based on amorphous materials.[48,49] Photochromic amorphous molecular materials for technological applications like surface relief gratings and optical switching have been reported.[50] Phase change materials, form an important class of materials for information storage, and involve reversible amorphous-crystalline (A↔C) transformations. We discuss this in detail in Sec. 1.3.

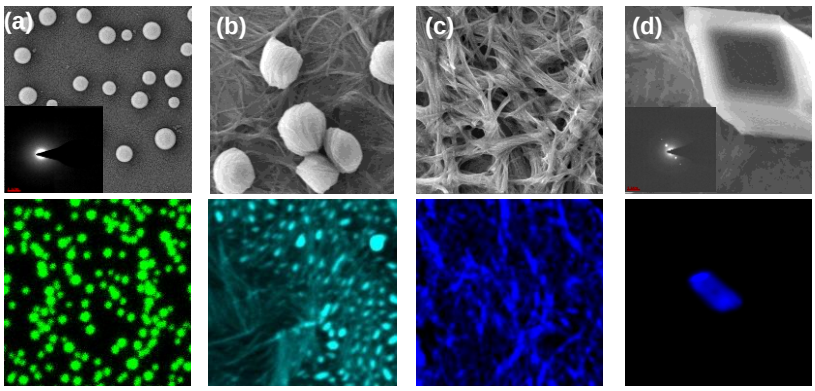

Figure 1.2. *Evolution of crystallinity of the particles in thin films formed by drop-casting PBEDQ in acetonitrile-toluene mixtures with increasing toluene fraction:* ***(a)*** *100:0,* ***(b)*** *80:20,* ***(c)*** *40:60 and* ***(d)*** *10:90; the parallel changes in the fluorescence emission is shown by the corresponding confocal fluorescence images (false-colored based on the emission spectrum recorded in the microscope). Insets of* ***a*** *and* ***b*** *shows the SAED pattern recorded with the TEM images of nano/microstructures. Adapted with permission from ref. 53.*

Solvent vapor and thermally induced amorphous-to-crystalline transformation (ACT) has been observed in dye aggregates.[51] Potential role of ACT in monolayer Langmuir film subjected to mechanical compression has been reported from our laboratory.[28] A more well defined ACT accompanied by fluorescence emission enhancement in DADQ based microparticles has also been reported.[52] ACT was achieved by confining the amorphous microparticles (formed by drop-casting) of the dye in a polymer thin film and fuming with solvent vapor. This study provides some insight into the well-known two step nucleation problem. More interestingly thin films of another DADQ derivative, 7-pyrrolidino-7-benzylamino-8,8-dicyanoquinodimethane (PBEDQ) fabricated by drop casting acetonitrile-toluene solvent mixtures of increasing toluene fraction, exhibited a gradual variation in the fluorescence emission wavelength and efficiency.[53] Microscopy investigations revealed a smooth progression of morphology from amorphous spherical particles to microcrystals with their fluorescence emission matching with that of solution and the crystalline states at the two extremes (Fig. 1.2). This experiment clearly demonstrated the possibility of using crystallinity as a tool for the hierarchical assembly of molecular materials.

1.2. Fluorescent Molecular Materials

Fluorescence: Basic concepts

Photoexcitation of molecules results in electronically excited state species that can relax to the ground state via several de-excitation pathways that are broadly classified as radiative and non-radiative. Apart from the photochemical events, considering only the photophysical processes, the excited state molecule can decay non-radiatively by vibrational relaxation, internal conversion, and inter-system crossing, and radiatively by emitting photons (fluorescence and phosphorescence) (Fig. 1.3a). Fluorescent molecules have found applications in several fields like imaging, optoelectronics, and as sensing probes to investigate various chemical and biological processes/systems. Current technologies allow fluorescence signals even from a single molecule (single molecule fluorescence spectroscopy) to be detected. The high selectivity and sensitivity of fluorescence based detection and the sensitivity of the fluorescent molecule to the surrounding medium make the technique as well as the fluorophores very popular.[54]

Fluorescence quenching

Emission efficiency of a fluorophore is described in terms of the fluorescence quantum yield, Φ, defined as the ratio of number of photons emitted to the number of photons absorbed. Φ will be 1 if all the absorbed photons are emitted; in practice, this happens rarely and the decrease in Φ arises due to quenching effects. Fluorescence emission of molecules in dilute solutions can be quenched by various non-radiative de-excitation processes including vibrational relaxation, intramolecular rotations of conformationally flexible groups, and collisional quenching by solvent molecules. Non-radiative energy transfer to other species (quencher) also leads to fluorescence quenching. When molecules aggregate or assemble into crystalline lattices to form materials, the effects of quenching by intramolecular motions as well as molecular collisions are considerably reduced or eliminated. Such a scenario should in principle, lead to fluorescence emission enhancement in molecular aggregates and solids. However, other factors that arise upon aggregation not only lessen the enhancement,

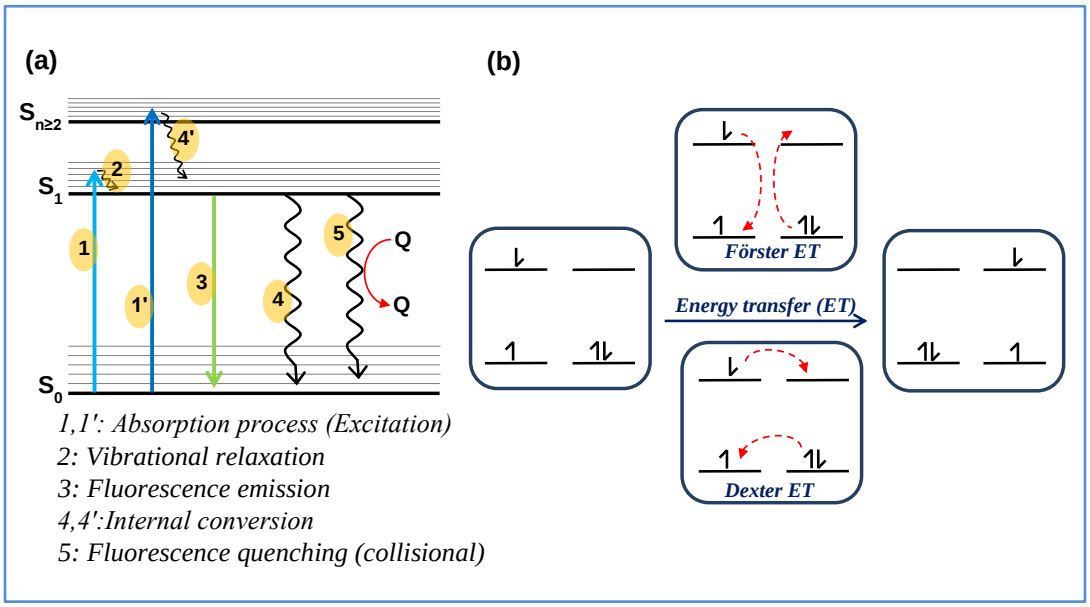

Figure 1.3. ***(a)*** *Modified Jablonski diagram showing the radiative and non-radiative decay processes along with collisional quenching and* ***(b)*** *Schematic representation of energy transfer through the Förster and Dexter mechanisms. Figure adapted from ref. 54.*

but often lead to significant reduction of the fluorescence. This fluorescence quenching can be due to the formation of excimers/exciplexes, complexation in the ground state, and intermolecular energy transfer via the Förster and Dexter modes (Fig. 1.3b). In most of the molecules, impact of the various intermolecular pathways leading to non-radiative excited state energy loss overwhelms the effect of molecular rigidification and loss of collisional effects. Hence the net effect of molecular aggregation is often fluorescence quenching; this has been termed in different contexts as, self-quenching or concentration quenching (in solutions), and also aggregation-caused quenching (ACQ).

In many technological applications like displays, light emitting devices, lasers and sensors, fluorophores are used in the form of thin films, aggregates or crystals. As noted above, many of the conventional fluorescent dyes are prone to self-quenching in concentrated solutions or upon aggregation. The same is the situation with biological studies, where the conventional dye molecules, mostly being hydrophobic, tend to aggregate in the biological media. If the quantum efficiency of the dye molecule is very low, there will be no detectable emission from dilute solutions; if high intensity laser beams are used, photobleaching of the dye could arise as a major problem. In order to overcome these issues, high concentrations of dyes should be used. All these issues point to the need to develop fluorophores that exhibit bright emission in the materials (aggregates/solids) state.

1.2.1 Enhanced fluorescence in aggregates/crystals

In view of the adverse impact of aggregation on fluorescence emission discussed above, the relatively less common occurrence of enhanced emission efficiency in supramolecular assemblies and crystals of select classes of molecules has attracted wide attention. The phenomenon gives rise to enormous possibilities of applications of luminescent materials in the form of nanostructures, thin films and bulk solids. It is popularly known as 'aggregation-induced emission' (AIE).[55] AIE can be quantified by the fluorescence efficiency enhancement (FEE), the ratio of the quantum yields of emission of a given molecule in its aggregated/solid (material) state over that in the isolated (molecular) state (FEE = $\Phi_{solid}/\Phi_{solution}$). Early examples of solid state fluorescent materials include diketopyrrolopyrroles,[56] poly(*p*-phenylene),[57] platinum complex [Pt(bph)$(CO)_2$][58] and cyclophane tethered poly(*p*-phenylene ethylene).[59] Later, several classes of molecules emerged exhibiting strong solid state fluorescence

emission. These include cyclic siloles,[60] substituted ethenes like tetraphenylethenes (TPEs),[61] triarylethenes,[62] cyano(bisphenyl)ethenes,[63] butadienes,[64] diaminodicyanoquinodimethanes (DADQs),[65] and substituted benzenes and anthracenes.[66] Selected classes of molecules such as siloles, tetraphenylethenes, triphenylamines, DADQs and butadienes are discussed in detail below.

Cyclic siloles

Cyclic siloles form one of the most extensively studied classes of molecules that exhibit enhanced emission in the solid state because of the attractive electronic properties and the possibility of facile modifications of the chemical structure. Tang et al., reported for the first time, the enhanced emission of aggregates of 1-methyl-1,2,3,4,5-pentaphenyl silole (Fig. 1.4a) in water-ethanol mixture compared to the molecularly dissolved solution.[67] They coined the term 'aggregation-induced emission' (AIE) to describe the observed phenomenon. Fig. 1.5 shows the enhanced emission upon aggregation of 1,1,2,3,4,5-hexaphenylsilole in THF-water mixtures with increasing water fraction.[68] Several control experiments and computational studies

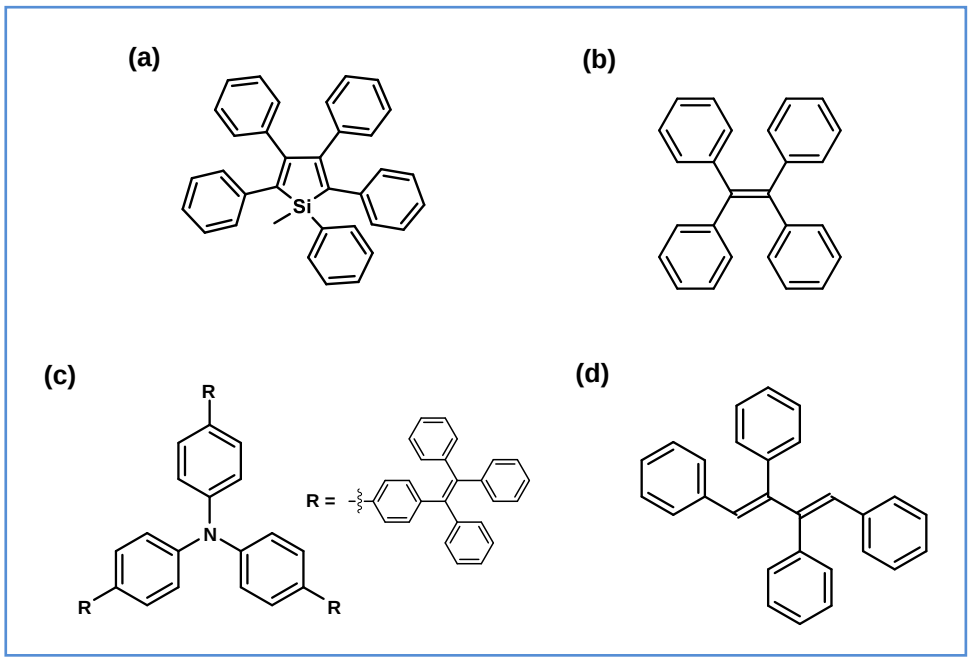

Figure 1.4. *Molecular structure of **(a)** 1-methyl-1,2,3,4,5-pentaphenylsilole, **(b)** tetraphenylethene (TPE), **(c)** triphenylamine adduct with TPE and **(d)** 1,2,3,4-tetraphenylbutadiene (TPBD) exhibiting enhanced solid state fluorescence emission.*

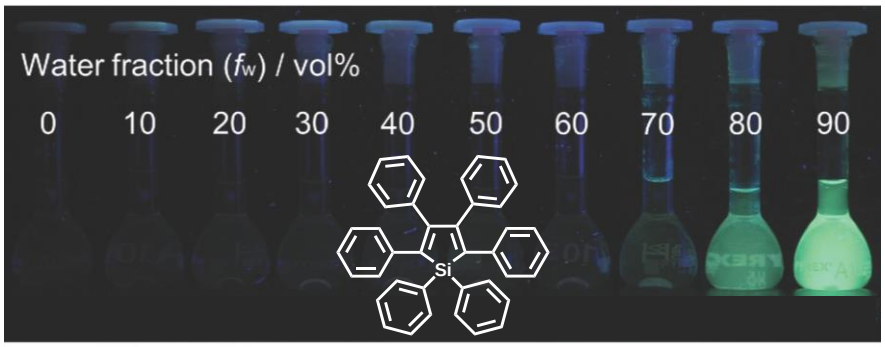

Figure 1.5. *Photograph showing emission of 1,1,2,3,4,5-hexaphenylsilole (molecular structure shown as an inset) in THF-water solvent mixture with varying fraction of water. Adapted with permission from ref. 68.*

have shown that the restriction of intramolecular motions upon aggregation or in the solid state is responsible for the enhanced emission. The propeller like geometry adopted because of steric repulsion between the peripheral phenyl rings prevents face-to-face packing of molecules. Inhibition of π-stacking and intramolecular rotational motions of the flexible substituents resulted in enhanced emission upon aggregation. Mechanisms reported for the enhanced emission is discussed in detail in Sec. 1.2.2. Structurally modified siloles having triphenylsilyl, tetraphenylethene, (trialkylsilyl)ethynyl substituents have been synthesized and their properties and potential applications based on enhanced emission explored.[60] A wide variety of macromolecules containing silole moieties as pendants on the non-emissive backbone, as well as homo- and co-polymerization of emissive siloles alone and with other molecules have been developed as solid state emitting materials.[69]

Tetraphenylethenes

Early reports of tetraphenylethenes (TPEs) include enhanced emission from aggregates of *n*-bromoalkoxy substituted derivatives and complexes of cationic TPEs (having triethylammonium bromide substituents) with deoxyribonucleic acid and bovine serum albumin (BSA); the latter is used as fluorescent turn-on probes for bio-macromolecules.[70] Later, aggregate formation with concomitant emission enhancement from bare TPE (Fig. 1.4b) and its diphenylated derivative were reported; they have found use in chemical vapor sensing and organic light emitting diodes (OLEDs) application.[71] Structural modification of TPE by incorporating electron donor-acceptor

groups and alkyl linkages[72] leads to enhanced properties; the former showed emission color that can be tuned using the electron donating groups, and the latter, enhanced solid state emission efficiency. TPE linked with planar aromatic molecules like pyrene, naphthalene, anthracene and phenanthrene, exhibiting solid state fluorescence quantum yield of unity, have been shown to be useful in OLEDs; pyrene decorated with multiple TPE units showed good device performance with an external quantum efficiency of 4.95%.[73] Adducts of TPE with triphenylamine, dimesityl boron and carbazole are efficient emitters with good hole-transporting, electron-transporting capability and bipolar charge mobility respectively, because of synergistic effect between TPE and its counterpart.[74] Several functionalized TPE derivatives have been synthesized as ligands and incorporated in rigid frameworks through coordination-driven self-assembly. Depending on the structural modification and immobilization in such frameworks, complexes emitting in solution as well as in the aggregated form have been developed.[75]

Triphenylamines

Triphenylamine (TPA) is well known for its electron donating and charge carrier transport properties in optoelectronic applications. Owing to the propeller geometry, TPA is a potential candidate for strong solid state emissive materials. Donor-acceptor-donor (D-A-D) triad composed of iodo-triphenylamine donor and anthracene or diphenyloxadiazole acceptor shows enhanced emission upon aggregation.[76] TPA linked to 1,3,5-triazine core, symmetrically functionalized TPA with acceptors *via* conjugation bridges, and starburst molecules containing TPA (Fig. 1.4c) units exhibit enhanced emission and large two-photon absorption cross section.[77] Several D-π-A type conjugated molecules bearing TPA units as donor and *N*-methylbarbituric acid, indanedione, and cyanostyrene as acceptors, exhibit strong solid state emission and are stimuli responsive in some cases.[78] TPA adducts with benzothiadiazole, benzoselenadiazole, and quinoxaline exhibit efficient red emission upon aggregation in THF/water mixture.[79]

Butadienes

1,1,4,4-Tetraphenyl-1,3-butadienes have attracted attention as blue light emitters for OLEDs,[80] gain medium for lasing application,[81] and fluorescent film in noble element scintillators,[82] and electron donor-acceptor substituted butadienes as mechanochromic luminescent materials.[83] 1,4-Diphenylbutadienes containing electron

donating alkoxy group and various electron accepting moieties,[64,84] and 1,2,3,4-tetraphenylbutadienes (TPBD, Fig. 1.4d) also exhibit enhanced emission in aggregate state and fluorescence on-off switching useful in sensing vapors of organic amines.[85] Enhanced emission upon aggregation,[86] effect of *E*/*Z*-isomerization on the solid state emission and mechanochromic response,[87] and turn-on fluorescence sensors for explosives, volatile amines and γ-globulins have been realized with hexaphenyl butadienes.[88]

Diaminodicyanoquinodimethanes

7,7-Diamino-8,8-dicyanoquinodimethanes (DADQs, Fig. 1.6) are zwitterionic push-pull molecules, formed by the reaction of primary and secondary amines with TCNQ.[89] Steric hindrance between the substituents in the diaminomethylene group and

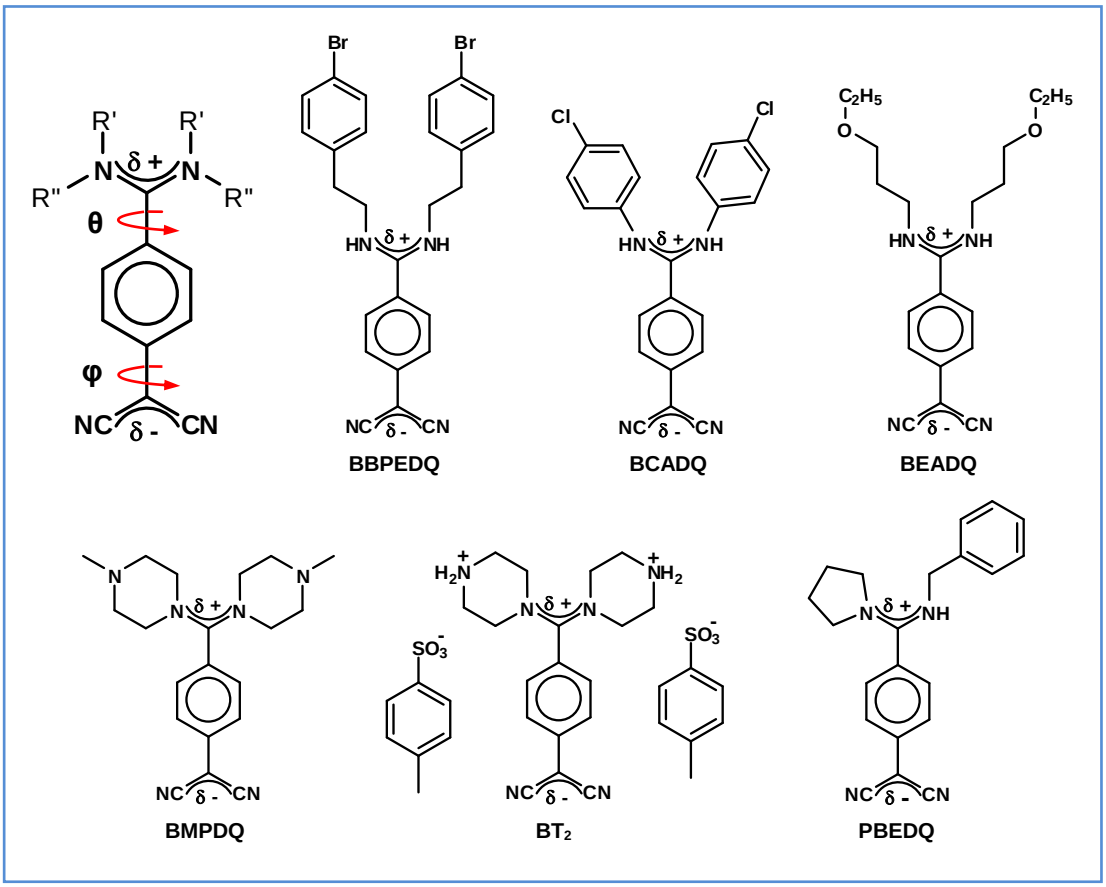

Figure 1.6. *The generic DADQ structure showing the relevant torsional angles, and the molecular structure of the various derivatives discussed in the text.*

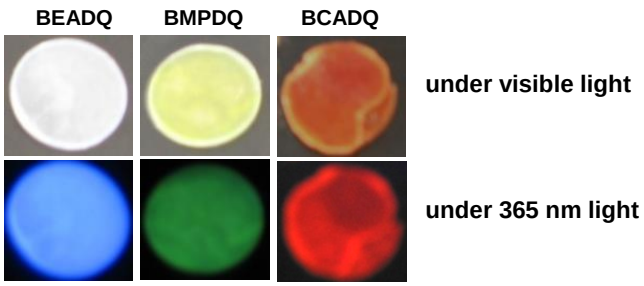

Figure 1.7. *Photographs of KBr pellets of selected DADQ derivatives under visible light and the corresponding blue, green and red emission under UV (365 nm) light irradiation. [7,7-bis(ethoxypropylamino)-8,8-dicyanoquinodimethane, BEADQ; 7,7-bis(methylpiperazino)-8,8-dicyanoquinodimethane, BMPDQ; 7,7-bis(4-chloro-anilino)-8,8-dicyanoquinodimethane, BCADQ. Structures are provided in Fig. 1.6]*

the *ortho* H atom on the benzenoid ring leads to substantially twisted structure. The charge localization leads to large ground state dipole moment as well.[90] DADQs generally possess high melting/decomposition temperatures, possibly due to strong electrostatic intermolecular forces in the crystal lattice. The ease of synthesis, the wide range of substitutions that can be easily incorporated, and the thermal stability, makes the class of DADQs, versatile candidates to explore for various materials applications.

DADQs have been explored in connection with several applications such as SHG (due to the large hyperpolarizabilities), electroluminescence and displays.[2,91] They have been proposed as good candidates for singlet fission application.[92] Enhanced fluorescence has been realized in crystals, nanocrystals, ultra-thin films and amorphous particles of DADQs.[65] Blue, green and red emitting DADQs (Figs. 1.6 and 1.7) have been reported from our laboratory.[65] Enhancement of fluorescence efficiency in solution and colloids by polyelectrolyte templating was explored with 7,7-bis(piperazinium)-8,8-dicyanoquinodimethane bis(*p*-toluenesulfonate) (BT_2, Fig. 1.6).[93] Fluorescence switching accompanying amorphous-to-crystalline transformation of microparticles confined in polymer thin film and fluorescence wavelength tuning by variation of the crystallinity of the nanoparticles were demonstrated with 7,7-bis(2-(4-bromophenyl)ethylamino)-8,8-dicyanoquinodimethane (BBPEDQ, Fig. 1.6) and PBEDQ (Fig. 1.6) respectively.[52,53] DADQs for selective and efficient imaging of epidermal and stomatal cells have also been reported from our laboratory.[94] This thesis is largely based on novel DADQ systems and their fluorescence related attributes.

Other systems

Highly efficient and tunable emission in the solid state is reported from 1,4-bis(alkenyl)-2,5-dipiperidinobenzenes and 1,4-terephthalates with electron donating groups at 2,5-positions.[66b,95] (2-hydroxyphenyl)Propanone and 2,5-bis(alkylamino)-terephthalate derivatives exhibited enhanced solid state emission and lasing behavior from single crystals.[96] Diphenylquinoxaline and anthracene/pyrene based D-A-D triad exhibited stimuli responsive enhanced solid state emission.[78a,97] Other solid state emissive systems include diphenyldibenzofulvenes,[98] distyrylanthracenes and benzenes,[66c,99] triarylethenes,[62,100] tetraphenyldistyrylbenzenes,[66a] tetrathienylethene derivatives,[101] bispiperidylanthracenes[102] and diaminomaleonitrile-based Schiff bases.[103]

1.2.2 Models for the enhanced emission in aggregates/solids

Unraveling the underlying mechanism of enhanced emission in aggregates and solids is not only useful for understanding this interesting phenomenon, but also for designing and developing new materials in this domain. The mechanism proposed often in this context involves, the restriction of intramolecular motions like rotation and vibration in the electronically excited state, when molecules aggregate.[55] Alternate views and models developed include the presence or absence of energetically accessible conical intersections, emission from higher excited states and the impact of local environment on the fluorescent molecule. J-aggregate formation, restriction of twisted intramolecular charge transfer and excited state intramolecular proton transfer have also been considered as reasons for the enhanced emission in specific molecules.[68]

Restricted intramolecular motions

Restriction of intramolecular motions (RIM) is proposed as one of the major reasons for the enhanced emission observed in aggregates/solids of propeller kind of molecules including siloles, tetraphenylethenes and triarylamines with rotatable/flexible peripheral substituents.[55] Decrease of temperature, increase of solvent viscosity, introduction of sterically bulky groups on the peripheral substituents and covalent modification to lock the flexible phenyl rings, can potentially affect intramolecular motions. Control experiments involving such effects have been carried out to demonstrate the relevance of RIM in realizing enhanced emission.[104] Several computational studies have shown that low-frequency molecular motions like

vibrations, rotations and twists contribute to the non-radiative decay in solution/isolated state, whereas they are hindered in aggregates leading to emission enhancement.[105] Beyond the role of rotational and vibrational motions, possible impact of photo-cyclization and photo-isomerization (*cis-trans* or *E-Z*) processes on the radiative decay of the archetype molecule, TPE and its derivatives have been examined.[106] Relevance of the restriction of intramolecular rotations in enhancing the emission, upon aggregation of TPE and 9,10-distyrylanthracene has been proposed based on temperature-resolved terahertz spectroscopy and ultrafast spectroscopy studies respectively.[107] Structurally constraining fluorescent molecules by immobilizing them in rigid frameworks such as metal organic frameworks, metallacycles, and coordination complexes, has been shown to be a route to enhance the emission of otherwise weakly emitting fluorophores.[108]

Inaccessibility of a conical intersection

Restricted access to conical intersection has been proposed as an alternate approach to understand the enhanced emission in the aggregated state. Computational studies on several molecules (Fig. 1.8) have shown the presence of an energetically accessible conical intersection (CI) below the Franck-Condon (FC) state for an isolated

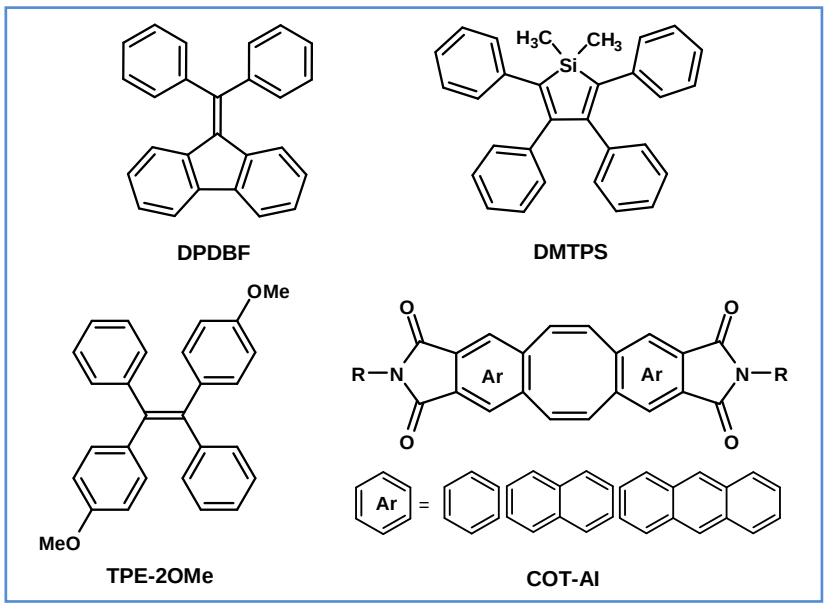

Figure 1.8. *Molecular structure of some fluorophores studied in the context of the availability of minimum energy conical intersections.*

molecule in the solution state, the reaction coordinate being a rotation about exocyclic double bond (DPDBF),[98a] π-twist (TPE-2OMe),[109] or a combination of the silole ring twist with the flapping motion of phenyl rings (DMTPS).[110] In the solid state, the CI is either unavailable because of the hindered intramolecular motions, or energetically higher than the FC geometry and hence inaccessible. Thus upon photo-excitation, the molecule in isolated state decays non-radiatively via the S_1-S_0 CI whereas in the aggregates/solids, the excited fluorophore decays radiatively (Fig. 1.9).[111] Fluorescence quenching in solution of several TPE derivatives has been attributed to the non-radiative decay of the excited state through S_1-S_0 CI via photo-cyclization or photo-isomerization.[105d,109] Simple aromatic hydrocarbons like anthracene and naphthalene have been turned into efficient solid state emitters by introducing *N*,*N*-dialkylamine at *para*-positions. The excited state relaxation in these systems involving the planarization and rotation of the amine groups leads to a minimum energy CI in the solution state.[102,111] In the solid state with closely packed molecules, the large structural change is hindered, preventing the excited state from reaching the CI, resulting in enhanced emission. Introduction of dialkylamine group on pyrene has also led to similar fluorescence response.[112] Variation in a wide range of fluorescence emission behaviors in the solution and solid states of cyclooctatetraenes-aceneimides (COT-AI) (Fig. 1.8) has been explained based on the accessibility or inaccessibility of a CI.[113]

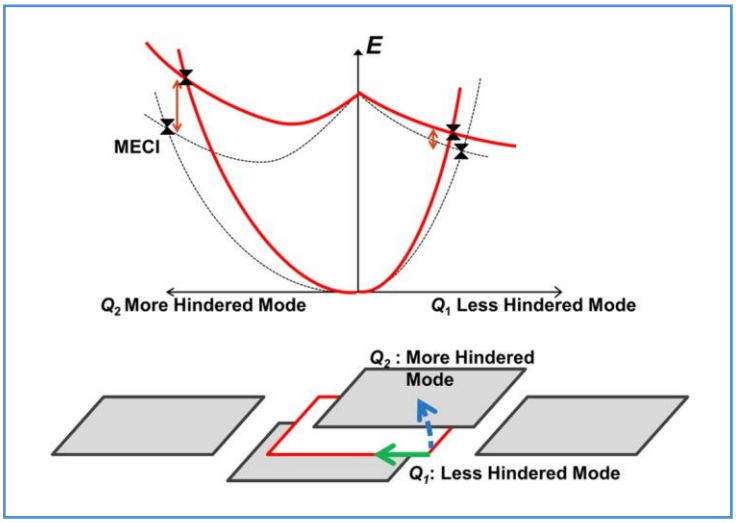

Figure 1.9. *Schematic of the potential energy surfaces in solid (red solid lines) and gas phase (black broken lines) along two reaction coordinates involving less and more hindered intramolecular motions. The different intramolecular motions are shown schematically. Adapted with permission from ref. 111.*

Non-Kasha processes

Photophysical and photochemical processes occurring from higher excited states, outside the ambit of Kasha's rule, have been reported in several classes of molecules.[114] Such non-Kasha processes have been proposed as the probable mechanism for the enhanced emission of BF_2-hydrazone (Fig. 1.10a) based molecular rotors in viscous solutions and solid state.[115] TD-DFT calculations showed that the S_1 state is dark, and the emissive state is a higher one. In solution, mainly in low viscosity solvents, structural relaxation from the higher excited states via rotation about the rotor axis leads to decreased energy gap between the emissive and dark states, and the dark S_1 state is populated via internal conversion; decay to the ground state is non-radiative. In highly viscous solutions and solids, suppression of the structural changes in the excited state prevents the internal conversion, and efficient fluorescence occurs from the higher excited state (Fig. 1.10b). Similarly, fluorescence observed in the H-aggregates of a naphthalenediimide based peptide has been attributed to the emission from the S_2 state.[116] Clark et al., reported emission from H-aggregates formed in the thin films of a regioregular poly(3-hexylthiophene).[117]

Impact of solid environment

Enhanced emission and bathochromic shift observed in the aggregates of 2,7-diphenylfluorenone have been explained by considering a single molecule process within the solid state environment.[118] Different computational models were explored to explain the fluorescence emission spectrum of concentrated THF solution of the

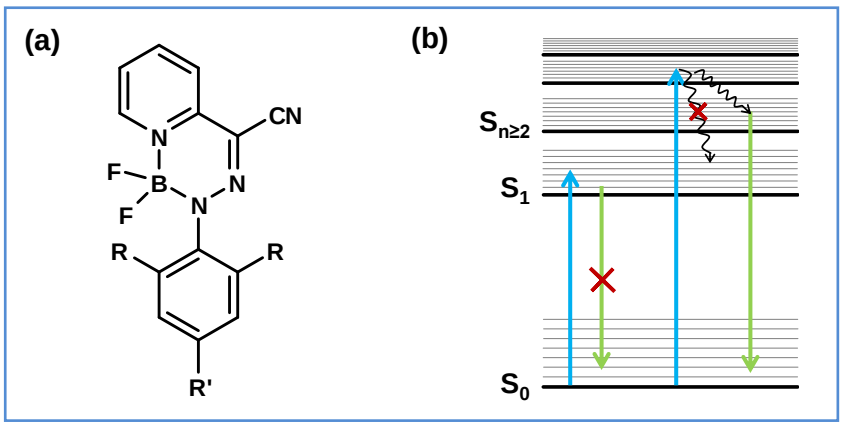

Figure 1.10. ***(a)*** *Structure of BF_2-hydrazone molecular rotor, and* ***(b)*** *schematic representation of emission from higher excited states (non-Kasha process).*

molecule containing two peaks, due to the isolated molecule and the aggregate. Computations were performed on a system consisting of three regions: the cluster of interest treated quantum mechanically, a spherical zone with its partial charges fixed, and a zone with point charges allowed to vary during the fitting process. Excited state electrostatic embedding model (self-consistent Ewald approach) is found to be the most successful in understanding the fluorescence response from isolated and aggregated species.[118,119]

Impact of supramolecular organization and interactions

The mechanisms and models described above are focused on intramolecular effects (within a specific environment) that influence excited state energy decay channels. Fluorescence emission is also critically affected by intermolecular energy transfer pathways, which in turn are controlled by the molecular organization in the aggregates or crystals. Despite the increasing number of publications with the term "aggregation induced emission" (AIE), the critical role of intermolecular energy transfer has not been explored in any great detail. Even though the relevance of this issue is noted in many instances, only a few have attempted a systematic analysis. Yamaguchi et al., have explored the crucial role of molecular structure of boron pyridinoiminate complexes and their mode of aggregation, on the fluorescence emission.[120] The complex with a fused structure having favorable π-stacking interactions showed typical ACQ, whereas the open structure complex with twisted phenyl ring exhibited enhanced emission in aggregated and crystalline states. Pyrene is well known for self-quenching in concentrated solutions or aggregates. Decorating pyrene with bulky substituents prevented π-stacking, leading to the enhancement of solid state fluorescence quantum yield over that of the solution.[121] A gradual variation of fluorescence quantum efficiency of the three crystal forms obtained from the same molecule, azaacene based fluorophore (1,4,9,12-tetrakis((triisopropylsilyl)ethynyl)benzo[1,8]-*as*-indaceno[2,3-*b*:6,7-*b′*]diquinoxaline), is attributed to the variation of π-π stacking in the crystals.[122] The impact of inhibiting π-π stacking of chromophores on solid state fluorescence emission has been reported in other fluorophores,[123] and reviewed recently.[124] Our current investigations of the impact of molecular structure and hence assembly, and intermolecular effects on the fluorescence efficiency enhancement of DADQ derivatives and other systems are presented in detail in chapters 2 and 3.

1.2.3 Tuning of fluorescence emission

Covalent modification

Molecular structure modification is the most common approach for tuning the fluorescence emission of materials as it affects the electronic energy levels of the molecules. TPE a well-known luminogen, emits at 445 nm in the solid state, whereas the emission of its dimer, BTPE (Fig. 1.11), peaks at 488 nm.[71,125] Introduction of benzo-2,1,3-thiadiazole (TD) and thiophene (T) moieties into BTPE further red shifted the emission wavelength into green and red regions. Thin films of BTPE containing only TD core (BTPETD, Fig. 1.11) and additional one (BTPETTD, Fig. 1.11) or two thiophene rings (BTPEBTTD, Fig. 1.11) emit at 539, 600 and 661 nm respectively with high emission efficiencies.[126] Thus the emission wavelength is tuned from blue to red region by increasing the conjugation length. Electroluminescence spectra of these derivatives matches their fluorescence emission spectra and are promising candidates for white OLEDs. Tunable emission covering the visible region is observed by varying the electron donors in *p*-bis(2,2-dicyanovinyl)benzene,[127] both electron donating and withdrawing groups in tetrasubstituted benzene,[95] and alkenyl substituent in 1,4-bis(alkenyl)-2,5-dipiperidinobenzenes.[66b] 3-Dimesityl-2,2′-bithiophene derivatives exhibit high fluorescence quantum efficiency and tunable emission from 486 nm to 657 nm by modifying the end aryl groups.[128] *N*-Methylpyrazoline fused flavanones,[129] tetra(alkyl)anthracenes,[130] and 9,10-bis((4-*N*,*N*-dialkylamino)styryl)anthracenes[66c] with

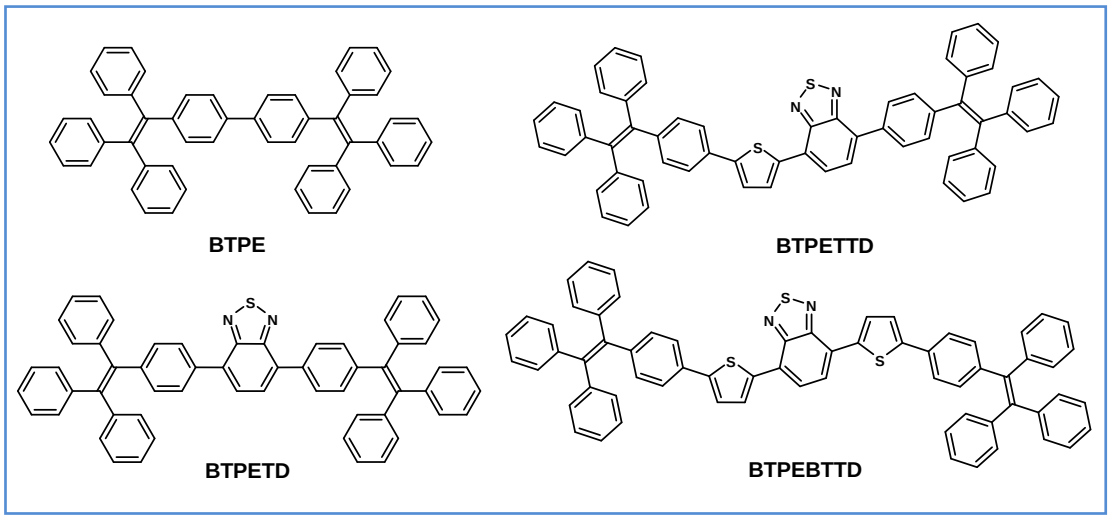

Figure 1.11. *Molecular structure of TPE derivatives exhibiting tunable, enhanced fluorescence emission by covalent modification of the parent structure.*

varying emission efficiency have been developed by simple structural modifications which further affect the molecular packing in the crystals. Thiazolo[5,4-*b*]thieno[3,2-*e*]pyridines also exhibit tunable fluorescence emission color and efficiency by chemical modification.[131] Li et al., observed the effect of styryl position on the emission wavelength and quantum yield in (9-anthryl)vinylstyrylbenzene.[99] The effect of alkyl chain length on the solid state optical properties of alkoxy substituted phenylene ethynylenes[132] and donor-acceptor substituted butadienes[84b] have been investigated.

Non-covalent modification

As discussed earlier, formation of excimers and exciplexes greatly contribute to fluorescence quenching in aggregates or solids. Pyrene is one of the well-known fluorophore which exhibit excimer emission.[133] In addition to excimers and exciplexes, molecular aggregation (J- and H-aggregates) also affect the fluorescence emission response of the molecular assemblies. H-aggregates have sandwich-type intermolecular association (parallel or plane-to-plane stacking) and J-aggregates are composed of molecular assemblies with a head-to-tail intermolecular association (end-to-end formation).[134] H-aggregates generally exhibit low fluorescence quantum yield due to more channels available for non-radiative dissipation of the excitation energy, whereas J-aggregates show strong emission.[135] Fluorescence spectral shift and intensity variation upon aggregate formation have studied in rhodamine and cyanine dyes.[135,136]

As the solid state emission of the materials is strongly affected by the relative orientation and interaction of neighboring molecules, molecular assembly also plays a crucial role in tuning solid state emission. Compared to covalent modification which often involves laborious synthesis, tuning of fluorescence by non-covalent routes is more attractive; polymorphism is one such strategy. He et al., observed blue, green and red emission from two polymorphs and an amorphous form of ditolylmethylene substituted 9,10-dihydroanthracene.[137] Molecular packing and conformation dependent emission were observed in different crystal forms of thiazolothiazole and *N*,*N*-diphenylamine based π-conjugated fluorophore,[138] and 1,4,7,10-tetra(*n*-butyl)tetracene.[139] Organic salts of anthracene-1,5-disulfonic acid (ADS) with various linear and branched amines exhibit tunable emission depending on the packing arrangement of the anthracene fluorophore. *n*-Pentylamine salt of ADS emits at 415 nm whereas *t*-butylamine salt has a broad peak at ~ 570 nm; the former with large

interplanar distances show monomer like emission while the latter with relatively closely spaced anthracene rings exhibit excited oligomer emission.[140] Intermolecular π-stacking interactions have significant effect on the photophysical properties of organic solid state luminescent materials. Red shifted fluorescence emission with increasing π-overlap of the aromatic chromophores is observed in the polymorphs of *N*,*N*-di(*n*-butyl)quinacridone,[141] and 9-anthrylpyrazole derivatives.[142] Thermoresponsive reversible fluorescence switching and the role of molecular packing have been investigated in alkoxy-cyano[64] and alkoxy-pyridine[84a] substituted butadienes. The effect of molecular packing and polymorphism on solid state fluorescence and phosphorescence have been explored with several fluorophores, for realizing enhanced responses and to obtain a better understanding of the structure-property relationships.[123b,143]

Stimuli-responsive materials

Emission of light by a material when subjected to mechanical stimuli like pressure, fracture/deformation and sound is called piezoluminescence, triboluminescence (mechanoluminescence) and sonoluminescence respectively. Such materials have found application in mechanical sensors, displays and storage devices. 2-([1,1′:3′,1″-terphenyl]-5′-yl)-4,4,5,5-Tetramethyl-1,3,2-dioxaborolane (DPP-BO, Fig. 1.12) exhibits fluorescence-phosphorescence dual emission under mechanical deformation.[144] Investigation of 5-(4-(1,2,2-triphenylvinyl)phenyl)thiophene-2-carbaldehyde (P_4TA, Fig. 1.12), and 4-(1,2,2-triphenylvinyl)benzaldehyde (*p*-P_4A, Fig. 1.12) and their structural variants revealed the importance of molecular packing that lead to piezoelectric effects required for mechanoluminescence.[145] The phenomenon of triboluminescence, relevant materials and their application potential are reviewed recently by Xie and Li.[146] Phenothiazine derivative exhibited repeatable and reversible fluorescence switching upon mechanical grinding and fuming with dichloromethane. Powder X-ray diffraction and differential scanning calorimetry studies showed that a crystalline-to-amorphous phase transformation was responsible for the fluorescence switching.[147] Roy et al., studied multi-stimuli responsive behavior of isoindolinone based D-A molecules and their application in cell imaging, rewritable devices and fluorescence thermometers.[148] Tunable mechanofluorochromism and white light emission were observed from the halo substituted *N*-(4-trifluoromethylphenyl)-phthalimide,[149] and phenothiazine/carbazole containing sulfonyl compounds.[150] In

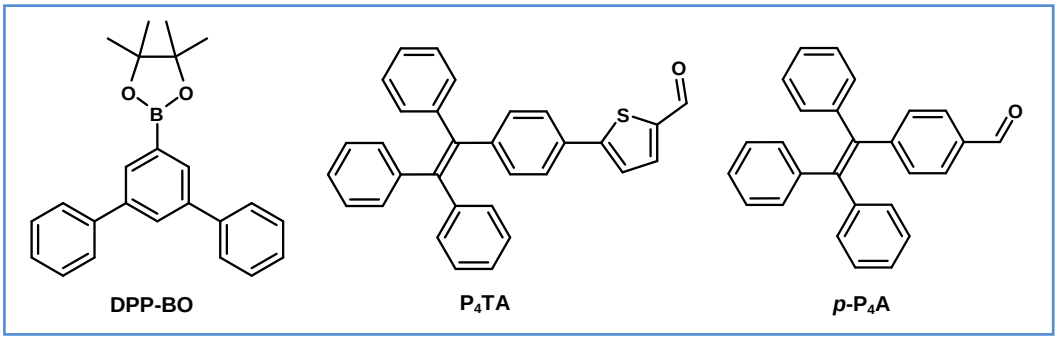

Figure 1.12. *Molecular structure of selected mechanoluminescent molecules studied in the context of stimuli-responsive materials.*

addition to fluorescence, room temperature phosphorescence is responsible for the white light emission in the former, whereas thermally activated delayed fluorescence occurs in the latter. Mechanoresponsive fluorescence emission wavelength/efficiency switching of a large number of TPEs and other solid state emissive systems have been reviewed.[151] Besides mechanical grinding, fluorescent materials responsive to other stimuli like acids, bases, and temperature have also been studied.[152]

1.2.4 Applications

Enhanced emission of molecular aggregates and solids finds application in a wide range of scenarios. Some of the prominent ones are discussed below.

Technological applications

The electronic structure and properties of siloles made them suitable candidates for optoelectronic applications like light emitting devices, photovoltaics, and field-effect transistors. Small molecules like spiro siloles, siloles fused with hetero-aromatic systems like phenylthiophene, biselenophene, benzofuran and polymers based on siloles along with hetero-aromatic systems have found use in some technological applications related to light emitting devices, sensors and photovoltaics.[153] A series of TPE dimers with different linkage modes are reported as blue and deep blue emitters for electroluminescent (EL) devices.[125,154] Several blue emitting luminogens based on TPE and its adducts with TPA and carbazole, TPE decorated with TPA on the peripheral phenyl rings and *vice-versa*, TPE units linked via an acceptor core, and pyrene decorated with peripheral TPE units exhibit good current efficiencies and external quantum efficiencies (η_{ext}) in EL devices.[155] Non-doped OLEDs fabricated using green

emitting 1,2-diphenyl-1,2-dipyrenylethene showed current efficiency and η_{ext} of 10.2 Cd A^{-1} and 3.3% respectively at a low turn-on voltage of 3.2 V.[156] Fluorene derivatives with *cis*-stilbene fused at C-9 position exhibited good OLED performance with η_{ext} as high as 7.8% at a low turn-on voltage of 2.8 V.[157] Owing to the electron donating and hole transporting properties and enhanced emission, TPA and its adducts have found efficient use in photovoltaics[158] and non-doped OLEDs.[159] Single crystals of 1,4-bis(2-cyano-2-phenylethenyl)benzene employed in organic field effect transistors exhibit very high carrier mobilities of 2.5 and 2.1 cm^2 V^{-1} s^{-1} for electron and hole respectively.[160] Thin film of a polyamide consisting of diphenylamine-TPE conjugate exhibits electrofluorochromic response during electrochemical switching between emissive neutral and non-emissive cationic forms; solid state fluorescence of the polyamide is imparted by the TPE unit.[161]

Biological applications

Biocompatible fluorescent organic nanoparticles of several red emitting luminogens with low cytotoxicity have found application in cell imaging. Examples include cyano-substituted diarylethene,[162] a FRET donor-acceptor pair consisting of fluorenyldivinylene based conjugated polymer and far-red/NIR emitting TPE adducts,[163] diaminomaleonitrile functionalized Schiff bases, TPE based oligourethane,[164] and phenothiazine derivatives[165] encapsulated in polymer matrices (Pluronic F127, BSA, polyethylene glycol, and a glycopolymer).[103] Nanodots of (dimesitylboranyl)thiophen-2-yl substituted silole functionalized with cell penetration peptide, and a red fluorescent alkyl-triphenylamine end-capped triazines with large two-photon absorption cross sections have been used for one- and two-photon fluorescence based imaging.[166] Tetrathienylethene based solid state emissive probes exhibit high photostability and cell membrane specific staining property.[101] Fluorescent silica nanoparticles made up of TPE and silole decorated siloxanes,[167] polydopamine,[168] and several other solid state emissive fluorophores have been used as potential probes for imaging and monitoring processes in biological systems.[169] As noted earlier bio-imaging capability of DADQ derivatives have been demonstrated using leaf stomatal cells recently.[94]

Sensors

High sensitivity of the fluorescence response to the surrounding environment, makes the fluorescence based sensing/detection highly attractive. Luminogens

containing acidic and basic functional groups are prone to protonation and deprotonation depending on the pH of the medium which in turn can potentially alter the emissive properties of the fluorophore making them useful as pH sensors. Diethylamino-functionalized distrylanthracene and hexaphenylsilole are non-emissive at low pH as they have good solubility in the salt form and the emission is turned-on at high pH where the amine functionality is reverted and the fluorophores tend to aggregate.[170] Detection of biomolecules like BSA protein in trace amounts and their folding/un-folding state by disulfonated anionic TPE derivative has been reported;[171] recognition of several nucleotides have been achieved either by fluorescence emission enhancement or quenching of anthracene functionalized with imidaolium, quarternary ammonium groups, and boronic acid groups.[172] Selective and sensitive detection of explosives like trinitrotoluene (TNT) by TPE linked pillararenes,[173] picric acid by nanoaggregates of quinoxaline derivatives,[174] and enantioselective recognition of chiral acids and α-aminoacids by TPE macrocycle bearing chiral diphenylethylenediamine have been reported.[175]

1.3 Phase Change Materials

Materials exhibiting reversible transformation between phases, accompanied by large latent heats or specific change in a relevant property or response between the phases involved are called phase change materials (PCMs). The phase change commonly induced by thermal effects, can be of solid-solid, solid-liquid or liquid-gas type. Transitions involving the gaseous phase are not generally preferred for applications because of the large volume changes involved. Phase transformations involving large transition enthalpies find extensive use in thermal energy storage applications, whereas those with a significant change in materials characteristics are used in information storage.

1.3.1 PCMs for thermal energy storage

Thermal energy storage (TES) involves temporary storage of available excess heat energy and its use in the off-peak hours. TES can be of sensible or latent heat storage type; thermal energy is stored by raising the temperature of the solid or liquid in the former, whereas the material undergoes a phase transformation by absorbing/releasing heat in the latter. Latent heat storage is the commonly used method

due to high storage densities and narrow temperature range for the operation. Typically the heat of fusion is stored in a solid-liquid transition, which is retrieved during the reverse phase change. A good PCM for TES requires easily accessible phase-transition temperature with large latent heat of transition, good thermal conductivity for better heat transfer, low volume change ratio, no phase separation, no/low supercooling, high chemical stability, limited corrosivity and compatibility with the container. Numerous reviews have been published on PCMs useful for TES, and in other applications.[176] A large number of materials, inorganic, organic and eutectics are employed as PCMs for TES applications.[177]

Materials

Most of the inorganic PCMs are salts, salt hydrates, and metallic alloys.[178] The advantage with inorganic PCMs is high phase transition latent heats per unit volume and relatively high thermal conductivity compared to organic PCMs. The melting behavior can be congruent, incongruent or semi-congruent in nature. Phase segregation and supercooling can be major drawbacks for these PCMs; the performance can be enhanced by adding gelling/thickening and nucleating agents to prevent phase segregation and supercooling respectively. Among the large number of salt hydrates, $Na_2SO_4.10H_2O$ and $CaCl_2.6H_2O$ have found extensive use in heat storage devices.[179] Inorganic salts and salt hydrates are promising candidates for high-temperature PCMs for TES in the range of 120-1000°C.[180] Low melting metals and metallic alloys with their high thermal conductivity are potential candidates for TES applications.[181]

Organic PCMs include paraffins, and non-paraffinic compounds; non-paraffins are fatty acids, esters, alcohols, and glycols.[182] Advantages with paraffins are the wide temperature range of melting depending on the carbon chain length, high heats of fusion, non-corrosivity, and chemical inertness. Despite these advantages, they suffer from poor thermal conductivity. Thermal properties such as melting temperature and heats of fusion for a large number of paraffin and non-paraffinic PCMs are reported.[183] Non-paraffin PCMs possess relatively higher thermal conductivity compared to paraffins. Both paraffins and non-paraffins have been well studied for TES applications.

Eutectics are composite materials that melt and solidify at a single temperature lower than that of the constituents. They offer the great advantage of no phase

segregation during reversible phase transformations, as the mixture exhibits congruent melting behavior. Many organic and inorganic eutectics, and composite PCMs have been reported with wide melting temperature range depending on the composition.[184] The use of molecular alloys of *p*-dihalobenzenes for TES has been reported by Mondieig et al.[185] Thermal conductivity of the eutectic mixture, capric acid-myristic acid is enhanced by 85% by doping with 2 wt% of expanded graphene.[186] Several organic polymers like polyurethanes, polyethylene glycol/poly(glycidyl methacrylate) crosslinked copolymers, and methoxy polyethylene glycol grafted cellulose diacetate are used as solid-solid PCMs for TES.[187] Microencapsulation of PCMs by other materials offer advantages like large heat transfer area, reduced exposure to outside environment, prevention of corrosion etc.[188] Microencapsulated PCMs found application in heat storage, textile industry, buildings, and medical applications.[189]

Applications

Paraffins, $CaCl_2.6H_2O$, and $Na_2SO_4.10H_2O$ are widely used in solar heating systems (solar based water heaters and cookers), and are more beneficial than sensible heat storage materials.[177b] A large number of PCMs employed in solar heat storage and related applications, and methods for enhancing the heat transfer for active and passive solar heating systems have been reviewed.[190] PCMs are used for heating and cooling of interior space of the buildings by integrating them in the building walls.[191] In buildings, PCMs are used in Trombe wall, ceiling boards, wall shutters and under-floor heating systems by incorporating them in the concrete. PCM embedded Trombe wall showed improved thermal performance for passive solar heating compared to ordinary concrete Trombe wall. Microencapsulated PCMs have been utilized in textile industry for fabricating temperature regulated smart textiles.[192] In addition, PCM incorporated textiles find use in space suits, insulation and protective clothing for biomedical applications, and clothing for cold environments.[193] PCMs are also commonly employed in domestic refrigerator freezer compartments to reduce temperature fluctuations during power outage.

1.3.2 PCMs for information storage

Materials capable of undergoing reversible amorphous-crystalline (A↔C) phase transition with significant change in some distinguishable property are useful for

information storage. Change in the optical reflectivity of the phases is used to store information in compact and digital versatile disks (CDs and DVDs) and the difference in electrical resistivity in phase change random access memory (PCRAM) devices. The process of information storage involves localized heating of the amorphous phase (using relatively low power laser pulse for sufficiently long time) of the material above its crystallization temperature for enough time for crystallization to occur (Fig. 1.13). The reverse process of erasing is done by melt-quench of the crystalline material (using higher power laser pulse for relatively short time) so that it forms the amorphous phase. A↔C PCMs for technological applications require very fast crystallization times, of the order of nanoseconds, and stable amorphous forms that are stable for extended periods of time, typically ~10 years.[194]

Materials

Ovshinsky reported for the first time, fast and reversible switching of amorphous and crystalline forms by laser pulses in chalcogenide films[195] and reversible transformation between highly resistive and conductive states by electric pulses in amorphous semiconductors of groups III, IV and VI.[196] Commercially used PCMs for optical data storage are the inorganic materials based on alloys of germanium, antimony, and tellurium. Alloys of varying compositions have been extensively studied in the search for a material exhibiting fast switching with stable phases.[197] Organic

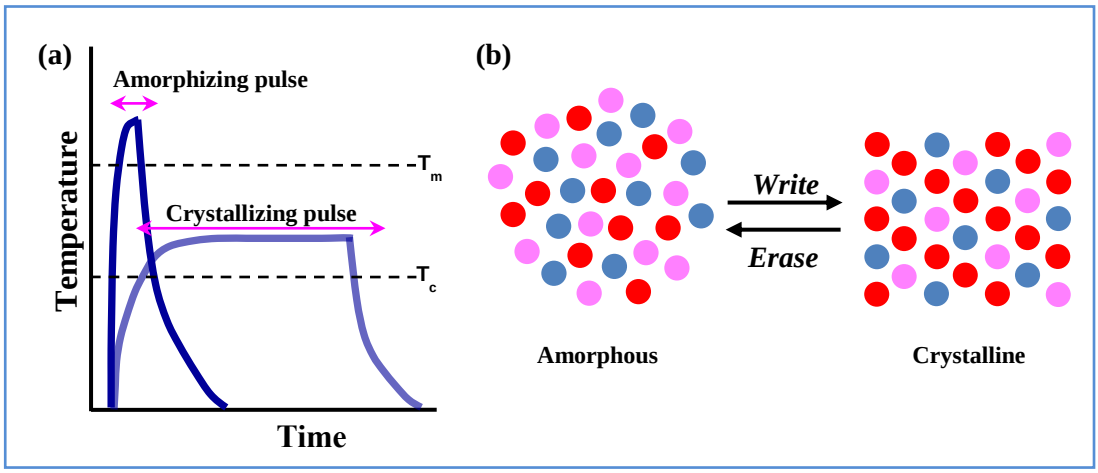

Figure 1.13. *Schematic of **(a)** amorphization and crystallization process induced by laser pulses in phase change material based memory devices, and **(b)** the lattice structure transformation, amorphous-crystalline, during write and erase process. (T_m and T_c are melting and crystallization temperatures respectively)*

molecules studied for optical data storage include cyanines and phthalocyanines, azo-derivatives, diarylethenes, and photoresponsive molecules.[198] Many of them are used for write once read many (WORM) type of storage by a permanent loss/change of the material in the irradiated region, and a few of them, for rewritable data storage utilizing the photoresponse of the molecule. Reversible transformation between disordered/ordered forms, monomer/aggregated forms in thin films of tetra-neopentoxy phthalocyanine zinc[199] and polymorphic forms of a squarylium dye film[200] using laser irradiation have been demonstrated as rewritable data storage media. Reversible amorphous to crystalline transformation over repeat cycles in anthraquinone films using laser pulses was first shown by Sporer; reversible phase transformation was monitored by the change in reflectivity of the phases.[201] We have also explored the phenomenon of thermally induced A↔C phase transformation followed by significant changes in fluorescence response as well as optical transmittance, in a class of DADQs; the details are presented in Chapter 5. Organic materials exhibiting reversible amorphous-crystalline phase transformation with a change in property are indeed, quite rare.

Applications

Optical data storage

CDs, DVDs and blue-ray disks (BDs) are the three generations of rewritable optical data storage media that employ A↔C PCMs. Laser pulses are used to carry out switching between the phases and the difference in reflectivity of the two phases is used to store and/or erase information. Storage capacity varies from 700 MB to 4.5 GB to 25/50 GB in commonly used CD, DVD and single/dual layer BD respectively, depending on the wavelength of the laser used (780 nm for CD, 650 nm for DVD, and 405 nm for BD). With decreasing wavelength, size of the written bits decreases and hence more number of bits can be written; this leads to increasing storage density. Commercially used PCMs are the alloy $Ge_2Sb_2Te_5$ for CDs and DVDs, and $Ge_8Sb_2Te_{11}$ for BDs; the former possess high optical contrast in near infrared and red spectral region, while the latter operates in the blue spectral region.[202]

Phase change random access memory

Reversible phase transformation in phase change random access memory (PCRAM) cell is brought about by current pulses, and the change in resistivity of the

amorphous and crystalline phase is used for information storage.[202a] PCRAM cell consists of top and bottom electrodes with the phase change material sandwiched in between.[203] Unlike the currently using dynamic RAM (a combination of transistor and capacitor, where the information is stored as the charge in the capacitor), PCRAM is of a nonvolatile memory device type, as the two phases are stable for longer periods. Design and fabrication of PCM cells as well as their potential application as static and dynamic RAM, flash and storage class memory devices have been investigated.[202]

1.3.3 Other applications of phase change materials

Drug delivery vehicles

Stimuli responsive drug delivery vehicles capable of controlled release of drug by an external stimulus have been developed based on PCMs, utilizing the phenomenon of phase change behavior. Multi-stimuli responsive, hybrid drug release vehicles based on magnetic Fe_3O_4 nanoparticles and doxorubicin loaded 1-tetradecanol, and gold nanocages encapsulating the dye loaded PCM offer great potential for the development of thermo-chemotherapy and theranostic systems.[204] The external stimulus for drug release is an alternating magnetic field and NIR irradiation or high-intensity focused ultra-sound, in addition to temperature. In addition to temperature triggered drug release from a PCM, the rate of release and thus the availability of the drug is controlled by careful selection of carriers with different solubilities.[205] Dye loaded polymeric particles exhibited temperature-controlled release of the loaded dye molecules upon the reversible solid-liquid transition of the PCM.[206] PCMs have found applications also in bio-medical field for storing and transporting of vaccines, pads for orthopedic applications, PCM embedded bandages, surgical dressing etc.[207]

Phase change hybrid materials

Hybrid materials show better performance and efficiencies compared to their individual counterparts, in several instances. PCMs combined with polymers either as composites or integrated into the polymer chain have been developed. Phase change hybrid materials with sensing and fluorescence switching properties have also been realized. Light to heat conversion and subsequent storage of the resulting thermal energy are exhibited by a polymer containing polyethylene polyamine back bone with azodyes and polyethylene glycol methyl ether as visible light absorbing and phase

change components respectively.[208] Multifunctional responses like thermomechanical actuation, sensing, and reversible fluorescence emission switching are observed from paraffin waxes infiltrated poly(diphenylacetylene) films.[209] InAs quantum dots exhibit reversible fluorescence shift due to the local strain provided by the volume change of $Ge_{10}Sb_2Te_{13}$ PCM.[210] Paraffin based miniaturized actuators and valves, and micropumps have been explored for technological applications.[211]

1.4 Layout of the thesis

The work presented in this thesis addresses some basic aspects of the importance of molecular assembly in materials exhibiting strong solid state fluorescence emission. One major focus is on the fluorescence efficiency enhancement (FEE) from the molecular to the material state useful for the design and development of efficient solid state fluorescent materials. We have attempted to understand the factors influencing FEE in terms of intramolecular effects discussed extensively in the earlier literature, and more importantly the critical role of intermolecular effects that has been paid very little attention so far. Our findings reveal interesting correlation between FEE and the molecular assembly that controls intermolecular energy transfer. Another investigation we have carried out relates to thermally induced reversible amorphous-crystalline phase transformation and the related fluorescence signatures sensitive to the mode of molecular assembly. The thesis is organized in five chapters. The basic concepts of molecular materials, solid state fluorescent materials and the mechanisms proposed for emission enhancement, followed by a brief overview of phase change materials and their applications have been presented in the previous sections of this chapter. A brief outline of the specific results presented in the following chapters is provided below.

Chapter 2

In this chapter, we present the structural tuning of fluorescence emission enhancement in a class of DADQs synthesized with ethylenediamine and its alkylated derivatives for the donor end. Subtle structural modifications affecting the intramolecular torsion angle resulted in a gradual and systematic variation in the FEE among the derivatives. A methodology based on molecular level *ab initio* computations and lattice energy calculations, together with an analysis of the organization of molecules and their transition dipoles in crystals is developed, to quantitatively assess

the inhibition of excited state relaxation and relative energy transfer rates in solids. This approach provides insight into the contribution of intra and intermolecular pathways to the structural tuning of the emission enhancement. An inverse correlation between the energy transfer rates and the enhancement factor reveals the critical importance of specific orientation of molecules in the crystals and hence the intermolecular energy transfer.

Chapter 3

An ideal case for studying the effect of aggregation/assembly on the emission enhancement would be a series of crystals of the same chromophore molecule having different molecular assembly patterns, exhibiting prominent variation in the emission enhancement. Three crystals (two enantiomorphic and one racemate) of *N*,*N*′-dimethyl-1,2-diaminocyclohexane substituted DADQs exhibiting varying FEEs facilitated such an analysis. Investigations following the methodology developed in Chapter 2, revealed once again a clear inverse correlation between the FEE values and the relative intermolecular energy transfer rates among the three crystals; intramolecular energy loss pathways is expected to be similar in all the cases. Analysis of the effect of molecular assembly/orientation on the emission enhancement in two other families of molecules is presented; they also highlight the importance of specifically oriented molecular aggregation, in realizing strong fluorescence enhancement in the crystalline state.

Chapter 4

The critical role of molecular orientations in hindering intermolecular energy transfer and the associated non-radiative excited state energy loss have been demonstrated in Chapters 2 and 3, based on examples from the DADQ family of molecules. In this chapter, examples based on other families of molecules from earlier reports are analyzed to test the general applicability of our model and analysis approach for understanding the concomitant role of intra and intermolecular effects in realizing enhanced fluorescence in molecular aggregates. The studies with 1,4,5,8-tetra(alkyl)anthracenes and bis(piperidyl)anthracenes, established unequivocally that the relative molecular orientations and the curtailment of intermolecular energy transfer are critical for the fluorescence efficiency enhancement in the molecular crystals, besides restricting excited state intramolecular relaxations. Inverse correlation between the FEE

and relative energy transfer rates was observed in these systems as well. The work presented in the previous two chapters and this chapter emphasizes that the evaluation of both the intra and intermolecular factors is crucial for the effective design and development of molecular assemblies that can exhibit strong light emission.

Chapter 5

In this chapter we present our detailed investigations of the thermally induced A↔C phase transformation in a class of DADQs containing alkoxypropylamino substituents. The reversible transformation is accompanied by a distinct change in the fluorescence emission wavelength and intensity. Formation and characterization of the amorphous and crystalline phases, the fluorescence switching response and the reversible transformation over repeat cycles are presented in this chapter. The A↔C phase transformation demonstrated in these new DADQs together with the characteristic fluorescence responses provides a new entry into the domain of functional molecular phase change materials. Preliminary explorations into the phase change and fluorescence switching induced by laser irradiation in doped polymer films is also discussed.

Chapter 6

The final chapter provides a brief summary of the investigations presented in the thesis and outlines the directions for future research. The highlights of the work include: (i) synthesis of novel fluorescent molecules based on DADQs suitable for studying structure-property correlation, (ii) development of a simple methodology to quantitatively assess the inhibition of excited state relaxation and relative energy transfer rates in solids, (iii) establishment of the critical role of molecular orientations on fluorescence efficiency enhancement, and (iv) development of novel functional molecular phase change materials exhibiting thermally induced reversible amorphous-crystalline phase transformation accompanied by fluorescence switching. New directions of further explorations of this research area are provided in the last section.

References:

1. (a) T. P. Radhakrishnan, *Resonance,* April 1998, 1989. (b) Simon, J.; Bassoul, P. Design of Molecular Materials: Supramolecular Engineering; Wiley: New York, 2000.
2. T. P. Radhakrishnan, *Acc. Chem. Res*., 2008, **41**, 367-376 and references 1-12 therein.
3. S. Chittipeddi, K. R. Cromack, J. S. Miller and A. J. Epstein, *Phys. Rev. Lett*., 1987, **58**, 2695-2698.
4. M. Takahashi, P. Turek, Y. Nakazawa, M. Tamura, K. Nozawa, D. Shiomi, M. Ishikawa and M. Kinoshita, *Phys. Rev. Lett*., 1991, **67**, 746-748.
5. J. S. Miller, *Chem. Soc. Rev*., 2011, **40**, 3266-3296. (b) J. S. Miller, *Mater. Today*, 2014, **17**, 224-235.
6. (a) D. N. Woodruff, R. E. P. Winpenny and R. A. Layfield, *Chem. Rev*., 2013, **113**, 5110-5148. (b) J. R. Friedman, M. P. Sarachik, *Annu. Rev. Condens. Matter Phys*., 2010, **1**, 109-128. (c) A. Bousseksou, G. Molnár, L. Salmon and W. Nicolazzi, *Chem. Soc. Rev*., 2011, **40**, 3313-3335. (d) O. Kahn, J. Kröber and C. Jay, *Adv. Mater*., 1992, **4**, 718-728.
7. H. Akamatu, H. Inokuchi and Y. Matsunaga, *Nature*, 1954, **173**, 168-169.
8. (a) J. Ferraris, D. O. Cowan, V. Walatka and Jr., J. H. Perlstein, *J. Am. Chem. Soc*., 1973, **95(3)**, 948-949. (b) A. F. Garito and A. J. Heeger, *Acc. Chem. Res*., 1974, **7**, 232-240.
9. J. Fraxedas, *Molecular Organic Materials: From Molecules to Crystalline Solids*, Cambridge University Press, Cambridge, 2006.
10. W. Jones, *Organic Molecular Solids: Properties and Applications*, CRC Press, Boca Raton, 1997.
11. (a) S. E. Brown, *Phys. C Supercond. its Appl.*, 2015, **514**, 279-289. (b) G. Saito and Y. Yoshida, *Chem. Rec*., 2011, **11**, 124-145.
12. C. Wang, H. Dong, W. Hu, Y. Liu and D. Zhu, *Chem. Rev*., 2012, **112**, 2208-2267.

13. Z, Li, *Organic Light-Emitting Materials and Devices*. CRC Press, Boca Raton, 2007.

14. C. Zhang, Y. S. Zhao and J. Yao, *Phys. Chem. Chem. Phys.*, 2011, **13**, 9060-9073.

15. R. W. Boyd, Nonlinear Optics. Academic Press, 2003.

16. (a) J. A. Giordmaine, *Phys. Rev. Lett.*, 1962, **8**, 19-20. (b) D. H. Jundt, M. M. Fejer, R. L. Byer, R. G. Norwood and P. F. Bordui, *Opt. Lett.*, 1991, **16**, 1856-1858. (c) J. L. Oudar and R. Hierle, *J. Appl. Phys.*, 1977, **48**, 2699-2704. (d) J. Zyss, J. F. Nicoud and M. Coquillay, *J. Chem. Phys.*, 1984, **81**, 4160-4167.

17. H. Kasai, H. S. Nalwa, H. Oikawa, S. Okada, H. Matsuda, N. Minami, A. Kakuta, K. Ono, A. Mukoh and H. Nakanishi, *Jpn. J. Appl. Phys.*, 1992, **31**, L1132-L1134.

18. W. Zhao, S. Li, H. Yao, S. Zhang, Y. Zhang, B. Yang and J. Hou, *J. Am. Chem. Soc.*, 2017, **139**, 7148-7151.

19. (a) Y. Lin, Y. Li and X. Zhan, *Chem. Soc. Rev.*, 2012, **41**, 4245-4272. (b) X. Liu, Y. J. Kim, Y. H. Ha, Q. Zhao, C. E. Park and Y.-H. Kim, *ACS Appl. Mater. Interfaces*, 2015, **7**, 8859-8867.

20. S. Li, L. Ye, W. Zhao, S. Zhang, S. Mukherjee, H. Ade and J. Hou, *Adv. Mater.*, 2016, **28**, 9423-9429.

21. Y. Liu, Z. Zhang, S. Feng, M. Li, L. Wu, R. Hou, X. Xu, X. Chen and Z. Bo, *J. Am. Chem. Soc.*, 2017, **139**, 3356-3359.

22. (a) P. M. Beaujuge and J. M. J. Fréchet, *J. Am. Chem. Soc.*, 2011, **133**, 20009-20029. (b) Z. F. Yao, J. Y. Wang and J. Pei, *Cryst. Growth Des.*, 2018, **18**, 7-15.

23. D. Liu, L. Yang, Y. Wu, X. Wang, Y. Zeng, G. Han, H. Yao, S. Li, S. Zhang, Y. Zhang, Y. Yi, C. He, W. Ma and J. Hou, *Chem. Mater.*, 2018, **30**, 619-628.

24. (a) P. Gangopadhyay, D. N. Rao, I. Agranat and T. P. Radhakrishnan, *Enantiomer* 2002, **7**, 119-127. (b) K. E. Rieckhoff and W. L. Peticolas, *Science* 1965, **147**, 610-611.

25. (a) S. Horiuchi and Y. Tokura, *Nat. Mater.*, 2008, **7**, 357-366. (b) V. Ramamurthy and K. Venkatesan, *Chem. Rev.*, 1987, **87**, 433-481.

26. (a) J. M. S. Becerra, S. H. Ortega, D. M. Morales and J. Valdés-Martínez, *CrystEngComm*, 2009, **11**, 226-228. (b) S. Jayanty, P. Gangopadhyay and T. P.

Radhakrishnan, *J. Mater. Chem.*, 2002, **12**, 2792-2797. (c) K. Rajesh, M. S. Chandra, S. Hirakawa, J. Kawamata and T. P. Radhakrishnan, *Langmuir*, 2007, **23**, 8560-8568.

27. (a) A. S. Tayi, A. Kaeser, M. Matsumoto, T. Aida and S. I. Stupp, *Nat. Chem.*, 2015, **7**, 281-294. (b) D. R. Talham, *Chem. Rev.*, 2004, **104**, 5479-5501. (c) D. R. Talham, T. Yamamoto and M. W. Meisel, *J. Phys.: Condens. Matter*, 2008, **20**, 184006.

28. B. Balaswamy, L. Maganti, S. Sharma, and T. P. Radhakrishnan, *Langmuir*, 2012, **28**, 17313-17321.

29. (a) I. D. Tevis, W. W. Tsai, L. C. Palmer, T. Aytun and S. I. Stupp, *ACS Nano*, 2012, **6**, 2032-2040. (b) A. Ruiz-Carretero, T. Aytun, C. J. Bruns, C. J. Newcomb, W. W. Tsai and S. I. Stupp, *J. Mater. Chem. A*, 2013, **1**, 11674-11681.

30. (a) D. Horn and Jens Rieger, *Angew. Chem. Int. Ed.*, 2001, **40**, 4330-4361. (b) A. M. Spokoyny, D. Kim, A. Sumrein and C. A. Mirkin, *Chem. Soc. Rev.*, 2009, **38**, 1218-1227. (c) J. Pecher and S. Mecking, *Chem. Rev.*, 2010, **110**, 6260-6279.

31. Y. S. Zhao, H. Fu, A. Peng, Y. Ma, D. Xiao and J. Yao, *Adv. Mater.*, 2008, **20**, 2859-2876.

32. (a) G. Yu, J. Gao, J. C. Hummelen, F. Wudl and A. J. Heeger, *Science*, 1995, **270**, 1789-1791. (b) Q. Niu, Y. Zhou, L. Wang, J. Peng, J. Wang, J. Pei and Y. Cao, *Adv. Mater.*, 2008, **20**, 964-969.

33. (a) A. L. Briseno, S. C. B. Mannsfeld, X. Lu, Y. Xiong, S. A. Jenekhe, Z. Bao and Y. Xia, *Nano Lett.*, 2007, **7**, 668-675. (b) A. L. Briseno, S. C. B. Mannsfeld, C. Reese, J. M. Hancock, Y. Xiong, S. A. Jenekhe, Z. Bao and Y. Xia, *Nano Lett.*, 2007, **7**, 2847-2853.

34. C. R. Martin, *Acc. Chem. Res.*, 1995, **28**, 61-68.

35. H. Yanagi, T. Morikawa and S. Hotta, *Appl. Phys. Lett.*, 2002, **81**, 1512-1514.

36. (a) Y. Oaki, M. Kijima and H. Imai, *J. Am. Chem. Soc.*, 2011, **133**, 8594-8599. (b) Y. Munekawa, Y. Oaki, K. Sato and H. Imai, *Nanoscale*, 2015, **7**, 3466-3473.

37. Y. Zhang and W. J. Blau, *Nat. Nanotechnol.*, 2015, **10**, 205-206.

38. A. Patra, N. Venkatram, D. Narayana Rao and T. P. Radhakrishnan, *J. Phys. Chem. C*, 2008, **112**, 16269-16274.

39. H. B. Fu and J. N. Yao, *J. Am. Chem. Soc.*, 2001, **123**, 1434-1439.

40. L. Zhao, W. Yang, Y. Luo, T. Zhai, G. Zhang and J. Yao, *Chem. -Eur. J.*, 2005, **11**, 3773-3778.

41. F. Wang, M. Y. Han, K. Y. Mya, Y. Wang and Y. H. Lai, *J. Am. Chem. Soc.*, 2005, **127**, 10350-10355.

42. L. Heng, J. Zhai, A. Qin, Y. Zhang, Y. Dong, B. Z. Tang and L. Jiang, *ChemPhysChem*, 2007, **8**, 1513-1518.

43. R. O. Al-Kaysi, A. M. Müller and C. J. Bardeen, *J. Am. Chem. Soc.*, 2006, **128**, 15938-15939.

44. (a) D. G. M. Wright, R. Dunk, D. Bouvart and M. Autran, *Polymer*, 1988, **29**, 793-796. (b) H. W. Starkweather, G. E. Moore, J. E. Hansen, T. M. Roder and R. E. Brooks, *J. Polym. Sci.*, 1956, **21**, 189-204.

45. B. C. Hancock and G. Zografi, *J. Pharm. Sci.*, 1997, **86**, 1-12.

46. A. P. Simonelli, S. C. Mehta and W. I. Higuchi, *J. Pharm. Sci.*, 1976, **65**, 355-361.

47. K. Nagapudi and J. Jona, *Curr. Bioact. Compd.*, 2008, **4**, 213-224.

48. Y. Shirota and H. Kageyama, *Chem. Rev.*, 2007, **107**, 953-1010.

49. Y. Shirota. *J. Mater. Chem.*, 2000, **10**, 1-25.

50. T. Tanino, S. Yoshikawa, T. Ujike, D. Nagahama, K. Moriwaki, T. Takahashi, Y. Kotani, H. Nakano and Y. Shirota, *J. Mater. Chem.*, 2007, **17**, 4953-4963

51. (a) S. W. Park, J. M. Choi, K. H. Lee, H. W. Yeom, S. Im and Y. K. Lee, *J. Phys. Chem. B*, 2010, **114**, 5661-5665. (b) X. Zhou, H. Y. Li, Z. G. Chi, B. J. Xu, X. Q. Zhang, Y. Zhang, S. W. Liu and J. R. Xu, *J. Fluoresc.*, 2012, **22**, 565-572.

52. (a) C. G. Chandaluri and T. P. Radhakrishnan, *Angew. Chem. Int. Ed.*, 2012, **51**, 11849-11852.

53. C. G. Chandaluri and T. P. Radhakrishnan, *J. Mater. Chem. C*, 2013, **1**, 4464-4471.

54. B. Valeur, *Molecular Fluorescence Principles and Applications*, Wiley-VCH Verlag GmbH, 69469, Weinheim (Federal Republic of Germany), 2002. (b) J. R. Lakowicz, *Principles of Fluorescence Spectroscopy*, Springer Science + Business Media, LLC, 233 Spring Street, New York, NY 10013, USA, 2006.

55. (a) A. Qin, B. Z. Tang, *Aggregation-Induced Emission: Fundamentals*, Vol. 1; John Wiley & Sons, Ltd., Chichester, UK, 2014. (b) M. Fujiki, B. Liu and B. Z. Tang, *Aggregation-Induced Emission: Materials and Applications*, Vol. 1 & 2, ACS Symposium Series 1226, 1227; American Chemical Society: Washington, DC, 2016.

56. (a) H. Langhals, T. Potrawa, H. Noth and G. Linti, *Angew. Chem. Int. Ed.*, 1989, **28**, 478-480. (b) H. Langhals, S. Demmig and T. Potrawa, *J. Prakt. Chem. (Leipzig)*, 1991, **333**, 733-748.

57. U. Lemmer, S. Heun, R. F. Mahrt, U. Scherf, M. Hopmeier, U. Siegner, E. O. Gobel, K. Mullen and H. Bassler, *Chem. Phys. Lett.*, 1995, **240**, 373-378.

58. G. Y. Zheng and D. P. Rillema, *Inorg. Chem.*, 1998, **37**, 1392-1397.

59. R. Deans, J. Kim, M. R. Machacek and T. M. Swager, *J. Am. Chem. Soc.*, 2000, **122**, 8565-8566.

60. Z. Zhao, B. He and B. Z. Tang, *Chem. Sci.*, 2015, **6**, 5347-5365.

61. Z. Zhao, J. W. Y. Lam and B. Z. Tang, *J. Mater. Chem.*, 2012, **22**, 23726-23740.

62. K. Itami, Y. Ohashi and J. Yoshida, *J. Org. Chem.* 2005, **70**, 2778-2792.

63. B. K. An, S. K. Kwon, S. D. Jung and S. Y. Park, *J. Am. Chem. Soc.*, 2002, **124**, 14410-14415.

64. R. Davis, N. S. S. Kumar, S. Abraham, C. H. Suresh, N. P. Rath, N. Tamaoki and S. Das, *J. Phys. Chem. C*, 2008, **112**, 2137-2146.

65. P. Srujana, P. Sudhakar and T. P. Radhakrishnan, *J. Mater. Chem. C*, 2018, **6**, 9314-9329.

66. (a) J. Freudenberg, F. Rominger and U. H. F. Bunz, *Chem. -Eur. J.*, 2015, **21**, 16749-16753. (b) M. Shimizu, Y. Takeda, M. Higashi and T. Hiyama, *Angew. Chem. Int. Ed.*, 2009, **48**, 3653-3656. (c) F. Li, N. Gao, H. Xu, W. Liu, H. Shang, W. Yang and M. Zhang, *Chem. -Eur. J.*, 2014, **20**, 9991-9997.

67. J. Luo, Z. Xie, J. W. Y. Lam, L. Cheng, H. Chen, C. Qiu, H. S. Kwok, X. Zhan, Y. Liu, D. Zhuc and B. Z. Tang, *Chem. Commun*., 2001, 1740-1741.

68. J. Mei, Y. Hong , J. W. Y. Lam, A. Qin, Y. Tang and B. Z. Tang, *Adv. Mater*., 2014, **26**, 5429-5479.

69. R. Hu, N. L. C. Leung and B. Z. Tang, *Chem. Soc. Rev*., 2014, **43**, 4494-4562.

70. H. Tong, Y. Hong, Y. Dong, M. Häußler, J. W. Y. Lam, Z. Li, Z. Guo, Z. Guoa and B. Z. Tang, *Chem. Commun*., 2006, 3705-3707.

71. Y. Dong, J. W. Y. Lam, A. Qin, J. Liu, Z. Li, B. Z. Tang, J. Sun and H. S. Kwok, *Appl. Phys. Lett*., 2007, **91**, 011111-1-3.

72. (a) X. Gu, J. Yao, G. Zhang, C. Zhang, Y. Yan, Y. Zhao and D. Zhang, *Chem. - Asian J*., 2013, **8**, 2362-2369. (b) D. Dang, Z. Qiu, T. Han, Y. Liu, M. Chen, R. T. K. Kwok, J. W. Y. Lam and B. Z. Tang, *Adv. Funct. Mater*., 2018, **28**, 1707210.

73. (a) Z. Zhao, P. Lu, J. W. Y. Lam, Z. Wang, C. Y. K. Chan, H. H. Y. Sung, I. D. Williams, Y. Mab and B. Z. Tang, *Chem. Sci*., 2011, **2**, 672-675. (b) Z. Zhao, S. Chen, C. Y. K. Chan, J. W. Y. Lam, C. K.W. Jim, P. Lu, Z. Chang, H. S. Kwok, H. Qiu and B. Z. Tang, *Chem. -Asian J*., 2012, **7**, 484-488. (c) Z. Zhao, S. Chen, J. W. Y. Lam, P. Lu, Y. Zhong, K. S. Wong, H. S. Kwoka and B. Z. Tang, *Chem. Commun*., 2010, **46**, 2221-2223.

74. (a) Z. Zhao, Z. Li, J. W. Y. Lam, J. L. Maldonado, G. R. Otiz, Y. Liu, W. Yuan, J. Xu, Q. Miao and B. Z. Tang, *Chem. Commun*., 2011, **47**, 6924-6926. (b) Z. Zhao, J. W. Y. Lam, C. Y. K. Chan, S. Chen, J. Liu, P. Lu, M. Rodriguez, J. L. Maldonado, G. R. Ortiz, H. H. Y. Sung, I. D. Williams, H. Su, K. S. Wong, Y. Ma, H. S. Kwok, H. Qiu and B. Z. Tang, *Adv. Mater*., 2011, **23**, 5430-5435. (c) W. Z. Yuan, S. Chen, J. W. Y. Lam, C. Deng, Pi. Lu, H. H. Y. Sung, I. D. Williams, H. S. Kwok, Y. Zhang and B. Z. Tang, *Chem. Commun*., 2011, **47**, 11216-11218.

75. (a) X. Yan, H. Wang, C. E. Hauke, T. R. Cook, M. Wang, M. L. Saha, Z. Zhou, M. Zhang, X. Li, F. Huang and P. J. Stang, *J. Am. Chem. Soc*., 2015, **137**, 15276-15286. (b) X. Yan, T. R. Cook, P. Wang, F. Huang and P. J. Stang, *Nat. Chem*., 2015, **7**, 342-348. (c) G. Q. Yin, H. Wang, X. Q. Wang, B. Song, L. J. Chen, L. Wang, X. Q. Hao, H. B. Yang and X. Li, *Nat. Commun*., 2018, **9**, 567-1-10. (d) Z. Wei, Z. Y. Gu, R. K. Arvapally, Y. P. Chen, R. N. McDougald, J. F. Ivy, A. A.

Yakovenko, D. Feng, M. A. Omary and H. C. Zhou, *J. Am. Chem. Soc.*, 2014, **136**, 8269-8276. (e) J. Zhao, D. Yang, Y. Zhao, X. J. Yang, Y. Y. Wang and B. Wu, *Angew. Chem. Int. Ed.*, 2014, **53**, 6632-6636.

76. B. Wang and Y. Qian, *New J. Chem.*, 2013, **37**, 1402-1407.

77. (a) Y. Jiang, Y. Wang, J. Hua, J. Tang, B. Li, S. Qianb and H. Tian, *Chem. Commun.*, 2010, **46**, 4689-4691. (b) L. Porrès, O. Mongin, C. Katan, M. Charlot, T. Pons, J. Mertz and M. Blanchard-Desce, *Org. Lett.*, 2004, **6**, 47-50. (c) B. Wang, Y. Wang, J. Hua, Y. Jiang, J. Huang, S. Qian and H.Tian, *Chem. -Eur. J.*, 2011, **17**, 2647-2655.

78. (a) P. S. Hariharan, P. Gayathri, A. Kundu, S. Karthikeyan, D. Moon and S. P. Anthony, *CrystEngComm*, 2018, **20**, 643-651. (b) X. Zhao, P. Xue, K. Wang, P. Chen, P. Zhanga and R. Lu, *New J. Chem.*, 2014, **38**, 1045-1051.

79. T. Ishi-i, K. Ikeda, Y. Kichise and M. Ogawa, *Chem. -Asian J.*, 2012, **7**, 1553-1557.

80. J. H. Kima, S. Noha, K. Kimb, S. T. Lima, D. M. Shin, *Synth. Met.*, 2001, **117**, 227-228.

81. (a) S. Tavazzi, L. Silvestri, L. Miozzo, A. Papagni, P. Spearman, S. Ianelli, A. Girlando, A. Camposeo, M. Polo and D. Pisignano, *ChemPhysChem*, 2010, **11**, 429-434. (b) A. Camposeo, Ma. Polo, P. D. Carro, Le. Silvestri, S. Tavazzi and D. Pisignano, *Laser Photonics Rev.*, 2014, **8**, 785-791.

82. V. M. Gehman, S. R. Seibert, K. Rielage, A. Hime, Y. Sun, D. M. Mei, J. Maasse and D. Moore, *Nucl. Instrum. Methods Phys. Res., Sect. A*, 2011, **654**, 116-121.

83. (a) Y. Zhang, T. Han, S. Gu, T. Zhou, C. Zhao, Y. Guo, X. Feng, Bin Tong, J. Bing, J. Shi, J. Zhi and Y. Don, *Chem. -Eur. J.*, 2014, **20**, 8856-8861. (b) T. Han, Y. Zhang, X. Feng, Z. Lin, B. Tong, J. Shi, J Zhib and Y. Dong, *Chem. Commun.*, 2013, **49**, 7049-7051.

84. (a) N. S. S. Kumar, S. Varghese, N. P. Rath and S. Das, *J. Phys. Chem. C*, 2008, **112**, 8429-8437. (b) N. S. S. Kumar, S. Varghese, C. H. Suresh, N. P. Rath and S. Das, *J. Phys. Chem. C*, 2009, **113**, 11927-11935.

85. (a) J. Chen, B. Xu, X. Ouyang, B. Z. Tang and Y. Cao, *J. Phys. Chem. A*, 2004, **108**, 7522-7526. (b) Y. Ezhumalai, T. H. Wang and H. F. Hsu, *Org. Lett.*, 2015, **17**, 536-539.

86. J. L. Banal, J. M. White, K. P. Ghiggino and W. W. H. Wong, *Sci. Rep.*, **4**: 4635-1-5.

87. Y. Zhanga, H. Maoa, L. Konga, Y. Tiana, Z. Tiana, X. Zenga, J. Zhib, J. Shia, B. Tonga and Y. Dong, *Dyes Pigm.*, 2016, **133**, 354-362.

88. Y. Zhang, H. Mao, W. Xu, J. Shi, Z. Cai, B. Tong, Y. Dong. *Chem. -Eur. J.*, 2018, **24**, 15965-15977.

89. W. R. Hertler, H. D. Hartzler, D. S. Acker and R. E. Benson, *J. Am. Chem. Soc.*, 1962, **84**, 3387-3393.

90. M. Ravi and T. P. Radhakrishnan. J. Phys. Chem. 1995, **99**, 17624-17627.

91. Y. Kagawaa, N. Takada, H. Matsuda, K. Yase, M. Halim, I. W. Samuel, G. H. Cross and D. Bloor, *Mol. Cryst. Liq. Cryst.*, 2000, **349**, 499-502. (b) L. O. Pålsson, H. L. Vaughan, A. Smitha, M. Szablewski, G. H. Cross, T. Roberts, A. Masutani, A. Yasuda, A. Beeby and D. Bloor, *J. Lumin.*, 2006, **117**, 113-122.

92. I. Paci, J. C. Johnson, X. Chen, G. Rana, D. Popovic, D. E. David, A. J. Nozik, M. A. Ratner and J. Michl, *J. Am. Chem. Soc.*, 2006, **128**, 16546-16553. (b) E. C. Greyson, B. R. Stepp, X. Chen, A. F. Schwerin, I. Paci, M. B. Smith, A. Akdag, J. C. Johnson, A. J. Nozik, J. Michl and M. A. Ratner, *J. Phys. Chem. B*, 2010, **114**, 14223-14232.

93. Ch. G. Chandaluri, A. Patra and T. P. Radhakrishnan, *Chem. -Eur. J.*, 2010, **16**, 8699-8706.

94. N. Senthilnathan, Ch. G. Chandaluri and T. P. Radhakrishnan, *Sci. Rep.*, 2017, **7**, 10583-1-11.

95. R. Huang, B. Liu, C. Wang, Y. Wang and H. Zhang, *J. Phys. Chem. C*, 2018, **122**, 10510-10518.

96. (a) B. Tang, H. Liu, F. Li, Yu. Wang and H. Zhang, *Chem. Commun.*, 2016, **52**, 6577-6580. (b) B. Tang, C. Wang, Y. Wang, and H. Zhang, *Angew. Chem. Int. Ed.*, 2017, **56**, 12543-12547.

97. (a) M. R. Rao, C. W. Liao, W. L. Su and S. S. Sun, *J. Mater. Chem. C*, 2013, **1**, 5491-5501.

98. (a) Q. Lia and L. Blancafort, *Chem. Commun.*, 2013, **49**, 5966-5968. (b) H. Tong, Y. Dong, Y. Hong, M. Ha1ussler, J. W. Y. Lam, H. H. Y. Sung, X. Yu, J. Sun, I. D. Williams, H. S. Kwok and B. Z. Tang, *J. Phys. Chem. C*, 2007, **111**, 2287-2294.

99. Y. X. Li, X. F. Yang, J. L. Miao, Z. W. Zhang and G. X. Sun, *CrystEngComm*, 2016, **18**, 2098-2104.

100. D. Ou, T. Yu, Z. Yang, T. Luan, Z. Mao, Y. Zhang, S. Liu, J. Xu, Z. Chi and M. R. Bryce. *Chem. Sci.*, 2016, **7**, 5302-5306.

101. J. J. Liu, J. Yang, J. L. Wang, Z. F. Chang, B. Li, W. T. Song, Z. Zhao, X. Lou, J. Dai and F. Xia, *Mater. Chem. Front.*, 2018, **2**, 1126-1136.

102. S. Sasaki, K. Igawa and G. Konishi, *J. Mater. Chem. C*, 2015, **3**, 5940-5950.

103. T. Han, X. Gu, J. W. Y. Lam, A. C. S. Leung, R. T. K. Kwok, T. Han, B. Tong, J. Shi, Y. Dong and B. Z. Tang, *J. Mater. Chem. C*, 2016, **4**, 10430-10434.

104. (a) N. L. C. Leung, N. Xie, W. Yuan, Y. Liu, Q. Wu, Q. Peng, Q. Miao, J. W. Y. Lam and B. Z. Tang, *Chem. -Eur. J.*, 2014, **20**, 15349-15353. (b) Y. Hong, J. W. Y. Lam and B. Z. Tang, *Chem. Commun*, 2009, 4332-4353.

105. (a) T. Zhang, Y. Jiang, Y. Niu, D. Wang, Q. Peng and Z. Shuai, *J. Phys. Chem. A*, 2014, **118**, 9094-9104. (b) Q. Peng, Y. Yi, Z. Shuai and J. Shao, *J. Am. Chem. Soc.*, 2007, **129**, 9333-9339. (c) T. Zhang, Q. Peng, C. Quan, H. Nie, Y. Niu, Y. Xie, Z. Zhao, B. Z. Tang and Z. Shuai, *Chem. Sci.*, 2016, **7**, 5573-5580. (d) Y. C. Duan, Y. Wu, J. L. Jin, D. M. Gu, Y. Geng, M. Zhang and Z. M. Su, *ChemPhysChem*, 2017, **18**, 755-762. (e) L. L. Bras, C. Adamo and A. Perrier, *J. Phys. Chem. C*, 2017, **121**, 25603-25616.

106. (a) Y. J. Gao, X. P. Chang, X. Y. Liu, Q. S. Li, G. Cui and W. Thiel, *J. Phys. Chem. A*, 2017, **121**, 2572-2579. (b) G. J. Zhao, K. L. Han, Y. B. Lei and Y. S. Dou, *J. Chem. Phys.*, 2007, **127**, 094307-1-6.

107. (a) E. P. J. Parrott, N. Y. Tan, R. Hu, J. A. Zeitler, B. Z. Tang and E. P. MacPherson, *Mater. Horiz.*, 2014, **1**, 251-258. (b) J. Zhang, S. Ma, H. Fang, B. Xu, H. Sun, I. Chan and W. Tian, *Mater. Chem. Front.*, 2017, **1**, 1422-1429.

108. N. B. Shustova, B. D. McCarthy and M. Dinca, *J. Am. Chem. Soc.*, 2011, **133**, 20126-20129.

109. K. Kokado, T. Machida, T. Iwasa, T. Taketsugu and K. Sada, *J. Phys. Chem. C*, 2018, **122**, 245-251.

110. X. L. Peng, S. R. Barragan, Z. S. Li, Q. S. Li and L. Blancafort, *J. Mater. Chem. C*, 2016, **4**, 2802-2810.

111. S. Sasaki, S. Suzuki, W. M. C. Sameera, K. Igawa, K. Morokuma and G. I. Konishi, *J. Am. Chem. Soc.*, 2016, **138**, 8194-8206.

112. S. Sasaki, S. Suzuki, K. Igawa, K. Morokuma and G. I. Konishi, *J. Org. Chem.*, 2017, **82**, 6865-6873.

113. S. Suzuki, S. Maeda and K. Morokuma, *J. Phys. Chem. A*, 2015, **119**, 11479-11487.

114. (a) A. P. Demchenko, V. I. Tomin and P. T. Chou, *Chem. Rev.*, 2017, **117**, 13353-13381. (b) T. Itoh, *Chem. Rev.*, 2012, **112**, 4541-4568.

115. H. Qian, M. E. Cousins, E. H. Horak, A. Wakefield, M. D. Liptak and I. Aprahamian, *Nat. Chem.*, 2017, **9**, 83-87.

116. S. Basak, N. Nandi, K. Bhattacharyya, A. Datta and A. Banerjee, *Phys. Chem. Chem. Phys.*, 2015, **17**, 30398-30403.

117. J. Clark, C. Silva, R. H. Friend and F. C. Spano, *Phys. Rev. Lett.*, 2007, **98**, 206406 (1-4).

118. D. Presti, L. Wilbraham, C. Targa, F. Labat, A. Pedone, M. C. Menziani, I. Ciofini and C. Adamo, *J. Phys. Chem. C*, 2017, **121**, 5747-5752.

119. L. Wilbraham, C. Adamo, F. Labat and I. Ciofini, *J. Chem. Theory Comput.*, 2016, **12**, 3316-3324.

120. M. Yamaguchi, S. Ito, A. Hirose, K. Tanaka and Y. Chujo, *Mater. Chem. Front.*, 2017, **1**, 1573-1579.

121. (a) J. N. Moorthy, P. Natarajan, P. Venkatakrishnan, D. F. Huang and T. Chow, *J. Org. Lett.*, 2007, **9**, 5215-5218. (b) Z. Q. Liang, Y. X. Li, J. X. Yang, Y. Ren and X. T. Tao, *Tetrahedron Lett.*, 2011, **52**, 1329-1333.

122. P.-Y. Gu, G. Liu, J. Zhao, N. Aratani, X. Ye, Y. Liu, H. Yamada, L. Nie, H. Zhang, J. Zhu, D. S. Li and Q. Zhang, *J. Mater. Chem. C*, 2017, **5**, 8869-8874.

123. (a) L. Zong, Y. Xie, C. Wang, J. R. Li, Q. Li and Z. Li, *Chem. Commun*., 2016, **52**, 11496-11499. (b) J. Yang, Z. Ren, B. Chen, M. Fang, Z. Zhao, B. Z. Tang, Q. Peng and Z. Li, *J. Mater. Chem. C*, 2017, **5**, 9242-9246. (c) M. Jiang, Z. He, Y. Zhang, H. H. Y. Sung, J. W. Y. Lam, Q. Peng, Y. Yan, K. S. Wong, I. D. Williams, Y. Zhao and B. Z. Tang, *J. Mater. Chem. C*, 2017, **5**, 7191-7199. (d) T. Ozdemir, S. Atilgan, I. Kutuk, L. T. Yildirim, A. Tulek, M. Bayindir and E. U. Akkaya, *Org. Lett*., 2009, **11**, 2105-2107.

124. Q. Li and Z. Li, *Adv. Sci*., 2017, **4**, 1600484-1-15.

125. Z. Zhao, S. Chen, X. Shen, F. Mahtab, Y. Yu, P. Lu, J. W. Y. Lam, H. S. Kwok and B. Z. Tang, *Chem. Commun*., 2010, **46**, 686-688.

126. Z. Zhao, C. Deng, S. Chen, J. W. Y. Lam, Wei Qin, P. Lu, Z. Wang, H. S. Kwok, Y. Ma, H. Qiub and B. Z. Tang. *Chem. Commun*., 2011, **47**, 8847-8849.

127. J. N. Zhang, H. Kang, N. Li, S. M. Zhou, H. M. Sun, S. W. Yin, N. Zhao and B. Z. Tang, *Chem. Sci*., 2017, **8**, 577-582.

128. A. Wakamiya, K. Mori and S. Yamaguchi, *Angew. Chem. Int. Ed*., 2007, **46**, 4273-4276.

129. B. Kupcewicz and M. Małecka, *Cryst. Growth Des*., 2015, **15**, 3893-3904.

130. 140C. Kitamura, Y. Abe, N. Kawatsuki, A. Yoneda, K. Asada, T. Kobayashi and H. Naito, *Mol. Cryst. Liq. Cryst*., 2007, **474**, 119-135.

131. M. Huang, S. Ye, K. Xu, J. Zhou, J. Liu, X. Zhua and Y. Wan, *J. Mater. Chem. C*, 2017, **5**, 3456-3460.

132. R. Thomas, S. Varghese and G. U. Kulkarni, *J. Mater. Chem*., 2009, **19**, 4401-4406.

133. J. B. Birks, *Photophysics of aromatic molecules*, John Wiley & Sons, New York, 1970.

134. A. Mishra, R. K. Behera, P. K. Behera, B. K. Mishra and G. B. Behera, *Chem. Rev*., 2000, **100**, 1973-2011.

135. J. Bujdák and N. Iyi, *Chem. Mater*. 2006, **18**, 2618-2624.

136. J. Bujdák, N. Iyi and R. Sasai, *J. Phys. Chem. B*, 2004, **108**, 4470-4477.

137. Z. He, L. Zhang, J. Mei, T. Zhang, J. W. Y. Lam, Zh. Shuai, Y. Qiang Dong, and B. Z. Tang, *Chem. Mater*., 2015, **27**, 6601-6607.

138. K. Wang, H. Zhang, S. Chen, G. Yang, J. Zhang, W. Tian , Z. Su and Y. Wang. *Adv. Mater*., 2014, **26**, 6168-6173.

139. C. Kitamura, T. Ohara, N. Kawatsuki, A. Yoneda, T. Kobayashi, H. Naito, T. Komatsuc and T. Kitamura, *CrystEngComm*, 2007, **9**, 644-647.

140. T. Hinoue, Y. Shigenoi, M. Sugino, Y. Mizobe, I. Hisaki, M. Miyata and N. Tohnai, *Chem. -Eur. J*., 2012, **18**, 4634-4643.

141. Y. Fan, Y. Zhao, L. Ye, B. Li, G. Yang and Y. Wang, *Cryst. Growth Des*., 2009, **9**, 1421-1430.

142. (a) H. Zhang, Z. Zhang, K. Ye, J. Zhang and Y. Wang, *Adv. Mater*., 2006, **18**, 2369-2372. (b) Z. Zhang, Y. Zhang, D. Yao, H. Bi, I. Javed, Y. Fan, H. Zhang and Y. Wang, *Cryst. Growth Des*., 2009, **9**, 5069-5076.

143. (a) C. Botta, S. Benedini, L. Carlucci, A. Forni, D. Marinotto, A. Nitti, D. Pasini, S. Righettoce and E. Cariati, *J. Mater. Chem. C*, 2016, **4**, 2979-2989. (b) X. He, A. C. Benniston, H. Saarenpä, H. Lemmetyinen, N. V. Tkachenko and U. Baischac, *Chem. Sci*., 2015, **6**, 3525-3532. (c) X. He, A. C. Benniston, H. Saarenpää, H. Lemmetyinen, N. V. Tkachenko and U. Baischac, *Chem. Sci*., 2014, **5**, 3922-3928.

144. J. Yang, Z. Ren, Z. Xie, Y. Liu, C. Wang, Y. Xie, Q. Peng, B. Xu, W. Tian, F. Zhang, Z. Chi, Q. Li and Z. Li, *Angew. Chem*., 2017, **129**, 898-902.

145. (a) Bi. Xu, J. He, Y. Mu, Q. Zhu, S. Wu, Y. Wang, Y. Zhang, C. Jin, C. Lo, Z. Chi, A. Lien, S. Liu and Ji. Xu, *Chem. Sci*., 2015, **6**, 3236-3241. (b) B. Xu, W. Li, J. He, S. Wu, Q. Zhu, Z. Yang, Y. C. Wu, Y. Zhang, C. Jin, P. Y. Lu, Z. Chi, S. Liu, J. Xua and M. R. Bryce, *Chem. Sci*., 2016, **7**, 5307-5312.

146. Y. Xie and Z. Li. *Chem*, 2018, **4**, 943-971.

147. J. Jia and H. Zhang, *J. Photochem. Photobiol. A*, 2018, **361**, 112-116.

148. B. Roy, M. C. Reddy and P. Hazra, *Chem. Sci*., 2018, **9**, 3592-3606.

149. J. Li, J. Zhou, Z. Mao, Z. Xie, Z. Yang, B. Xu, C. Liu, X. Chen, D. Ren, H. Pan, G. Shi, Y. Zhang and Z. Chi, *Angew*. *Chem*. *Int*. *Ed*., 2018, **57**, 6705-6705.

150. B. Xu, Y. Mu, Z. Mao, Z. Xie, H. Wu, Yi Zhang, C. Jin, Z. Chi, S. Liu, J. Xu Y. C. Wu, P. Y. Lu, A. Lienc and M. R. Bryce, *Chem*. *Sci*., 2016, **7**, 2201-2206.

151. (a) Z. Yang, Z. Chi, Z. Mao, Y. Zhang, S. Liu, J. Zhao, M. P. Aldred and Z. Chi, *Mater*. *Chem*. *Front*., 2018, **2**, 861-890. (b) Z. Chi, X. Zhang, B. Xu, X. Zhou, C. Ma, Yi. Zhang, S. Liua and J. Xu. *Chem*. *Soc*. *Rev*., 2012, **41**, 3878-3896.

152. (a) W. Fang, Y. Zhang, G. Zhang, L. Kong, L. Yanga and J. Yang, *CrystEngComm*, 2017, **19**, 1294-1303. (b) Y. Zhang, Y. Q. Feng, J. H. Wang, G. Han, M. Y. Li, Y. Xiaoa and Z. D. Feng, *RSC Adv*., 2017, **7**, 35672-35680. (c) Y. Zhou, L. Qian, M. Liu, X. Huang, Y. Wang, Y. Cheng, W. Gao, G. Wu and H. Wu, *J*. *Mater*. *Chem*. *C*, 2017, **5**, 9264-9272. (d) X. Wu, J. Guo, Y.Cao, J. Zhao, W. Jia, Y. Chen and D. Jia, *Chem*. *Sci*., 2018, **9**, 5270-5277.

153. Y. Cai, A. Qin and B. Z. Tang, *J*. *Mater*. *Chem*. *C*, 2017, **5**, 7375-7389.

154. J. Huang, N. Sun, Y. Dong, R. Tang, P. Lu, P. Cai, Q. Li, D. Ma, J. Qin and Z. Li, *Adv*. *Funct*. *Mater*., 2013, **23**, 2329-2337.

155. J. Yang, J. Huang, Q. Li and Z. Li, *J*. *Mater*. *Chem*. *C*, 2016, **4**, 2663-2684.

156. Z. Zhao, S. Chen, J. W. Y. Lam, Z. Wang, P. Lu, F. Mahtab, H. H. Y. Sung, I. D. Williams, Y. Ma, H. Si. Kwokc and B. Z. Tang, *J*. *Mater*. *Chem*., 2011, **21**, 7210-7216.

157. Y. Wei and C. T Chen, *J*. *Am*. *Chem*. *Soc*., 2007, **129**, 7478-7479.

158. Z. Ning and H. Tian, *Chem*. *Commun*., 2009, 5483-5495.

159. Z. Ning, Z. Chen, Q. Zhang, Y. Yan, S. Qian, Y. Cao and H. Tian, *Adv*. *Funct*. *Mater*., 2007, **17**, 3799-3807.

160. J. Deng, Y. Xu, L. Liu, C. Feng, J. Tang, Y. Gao, Y. Wang, B. Yang, P. Lu, W. Yanga and Y. Ma, *Chem*. *Commun*., 2016, **52**, 2370-2373.

161. N. Sun, K. Su, Z. Zhou, Y. Yu, X. Tian, D. Wang, X. Zhao, H. Zhou and C. Chen, *ACS Appl*. *Mater*. *Interfaces*, 2018, **10**, 16105-16112.

162. X. Zhang, X. Zhang, B. Yang, Y. Zhang and Y. Wei, *ACS Appl*. *Mater*. *Interfaces*, 2014, **6**, 3600-3606.

163. (a) D. Ding, K. Li, W. Qin, R. Zhan, Y. Hu, J. Liu, B. Z. Tang and B. Liu, *Adv*. *Healthcare Mater*., 2013, **2**, 500-507. (b) Z. Zhao, J. Geng, Z. Chang, S. Chen, C. Deng, T. Jiang, W. Qin, J. W. Y. Lam, H. Si. Kwok, H. Qiu, B. Liu and B. Z. Tang, *J*. *Mater*. *Chem*., 2012, **22**, 11018-11021.

164. T. Mondal, J. Sarkar and S. Ghosh, *Chem*. *-Eur*. *J*., 2016, **22**, 10930-10936.

165. M. Liu, K. Wang, X. Zhang, X. Zhang, Zh. Li, Q. Zhang, Z. Huang, and Y. Wei, *Tetrahedron*, 2015, 1-6.

166. (a) B. Chen, G. Feng, B. He, C. Goh, S. Xu, G. R. Ortiz, L. A. Ixta, J. Zhou, L. Ng, Z. Zhao, B. Liu and B. Z. Tang, *Small*, 2016, **12**, 782-792. (b) Y. Gao, Y. Qu, T. Jiang, Ha. Zhang, N. He, Bo. Li, J. Wu and J. Hua, *J*. *Mater*. *Chem*. *C*, 2014, **2**, 6353-6361.

167. M. Faisal, Y. Hong, J. Liu, Y. Yu, J. W. Y. Lam, A. Qin, P. Lu and B. Z. Tang, *Chem*. *-Eur*. *J*., 2010, **16**, 4266-4272.

168. X. Zhang, S. Wang, L. Xu, L. Feng, Y. Ji, L. Tao, S. Lia and Yen Wei, *Nanoscale*, 2012, **4**, 5581-5584.

169. (a) X. Zhang, X. Zhang, L. Tao, Z. Chi, J. Xu and Y. Wei, *J*. *Mater*. *Chem*. *B*, 2014, **2**, 4398-4414. (b) Q. Zhao and J. Z. Sun, *J*. *Mater*. *Chem*. *C*, 2016, **4**, 10588-10609. (c) D. Ding, K. Li, B. Liu and B. Z. Tang, *Acc*. *Chem*. *Res*., 2013, **46**, 2441-2453.

170. (a) H. Lu, B. Xu, Y. Dong, F. Chen, Y. Li, Z. Li, J. He, H. Li and W. Tian, *Langmuir*, 2010, **26**, 6838-6844. (b) Y. Dong, J. W.Y. Lam, A. Qin, Z. Li, J. Liu, J. Sun, Y. Dong, B. Z. Tang, *Chem*. *Phys*. *Lett*., 2007, **446**, 124-127.

171. H. Tong, Y. Hong, Y. Dong, M. Haussler, Z. Li, J. W. Y. Lam, Y. Dong, H. H. Y. Sung, Ian D. Williams and B. Z. Tang, *J*. *Phys*. *Chem*. *B*, 2007, **111**, 11817-11823.

172. H. N. Kim, J. H. Moon, S. K. Kim, J. Y. Kwon, Y. J. Jang, J. Y. Lee and J. Yoon, *J*. *Org*. *Chem*., 2011, **76**, 3805-3811.

173. J. H. Wang, H. T. Feng and Y. S. Zheng, *Chem*. *Commun*., 2014, **50**, 11407-11410.

174. L. Wang, M. Cui, H. Tang and D. Cao, *Dyes Pigm*., 2018, **155**, 107-113.

175. H. T. Feng, X. Zhang, Y. S. Zheng, *J*. *Org*. *Chem*., 2015, **80**, 8096-8101.

176. (a) K. Pielichowska and K. Pielichowski, *Prog. Mater. Sci.*, 2014, **65**, 67-123. (b) D. C. Hyun, N. S. Levinson, U. Jeong and Y. Xia, *Angew. Chem. Int. Ed.*, 2014, **53**, 3780-3795. (c) D. N. Nkwetta and F. Haghighat, *Sustain. Cities Soc.*, 2014, **10**, 87-100.

177. (a) M. M. Farid, A. M. Khudhair, S. A. K. Razack and S. Al-Hallaj, *Energy Convers. Manage.*, 2004, **45**, 1597-1615. (b) A. Sharma, V. V. Tyagi, C. R. Chen and D. Buddhi, *Renewable Sustainable Energy Rev.*, 2009, **13**, 318-345. (c) B. Zalba, J. M. Marín, L. F. Cabeza and H. Mehling, *Appl. Therm. Eng.*, 2003, **23**, 251-283.

178. (a) S. A. Mohamed, F. A. Al-Sulaiman, N. I. Ibrahim, M. H. Zahir, A. Al-Ahmed, R. Saidur, B. S. Yılbaş and A. Z. Sahin, *Renewable Sustainable Energy Rev.*, 2017, **70**, 1072-1089. (b) M. Kenisarin and K. Mahkamov, *Sol. Energy Mater. Sol. Cells*, 2016, **145**, 255-286.

179. H. Feilchenfeld and S. Sarig, *Ind. Eng. Chem. Prod. Res. Dev.*, 1985, **24**, 130-133.

180. M. M. Kenisarin, *Renew. Sustain. Energy Rev.*, 2010, **14**, 955-970.

181. J. N. Maestre, I. I. Torres, Z. A. Velasco, I. Kaltzakorta and M. M. Zubieta, in *AIP Conference Proceedings*, 2016, vol. 1734.

182. D. Feldman, M. M. Shapiro and D. Banu, *Sol. Energy Mater.*, 1986, **13**, 1-10.

183. (a) M. M. Kenisarin, *Sol. Energy*, 2014, **107**, 553-575. (b) A. Shukla, D. Buddhi and R. L. Sawhney, *Renewable Energy*, 2008, **33**, 2606-2614.

184. (a) P. Zhang, X. Xiao and Z. W. Ma, *Appl. Energy*, 2016, **165**, 472-510. (b) Q. He, S. Wang, M. Tong and Y. Liu, in *Energy Convers. Manage.*, 2012, **64**, 199-205. (c) X. Min, M. Fang, Z. Huang, Y. Liu, Y. Huang, R. Wen, T. Qian and X. Wu, *Sci. Rep.*, 2015, **5**, 12964-1-11.

185. D. Mondieig, Y. Haget, M. Labrador, M. A. Cuevas - Diarte, P. R. van der Linde and H. A. J. Oonk, *Mater. Res. Bull.*, 1991, **26**, 1091-1099.

186. A. Karaipekli and A. Sari, *Sol. Energy*, 2009, **83**, 323-332.

187. (a) C. Chen, W. Liu, H. Yang, Y. Zhao and S. Liu, *Sol. Energy*, 2011, **85**, 2679-2685. (b) Q. Cao and P. Liu, *Eur. Polym. J.*, 2006, **42** 2931-2939. (c) S. Cheng, Y. Chen, H. Yu and M. Zhu, *E-Polymers*, 2008, 136. (d) P. Xi, X. Gu, B. Cheng and Y. Wang, *Energy Convers. Manage.*, 2009, **50**, 1522-1528.

188. C. Y. Zhao and G. H. Zhang, *Renewable Sustainable Energy Rev*., 2011, **15**, 3813-3832.

189. M. Jurkowska and I. Szczygieł, *Appl. Therm. Eng*., 2016, **98**, 365-373.

190. M. Kenisarin and K. Mahkamov, *Renewable Sustainable Energy Rev*., 2007, **11**, 1913-1965.

191. F. Kuznik, D. David, K. Johannes and J. J. Roux, *Renewable Sustainable Energy Rev*., 2011, **15**, 379-391.

192. M. Ahrari, R. Khajavi, M. K. Dolatabadi, T.Toliyat and A. Rashidi, *International Scholarly and Scientific Research & Innovation*, 2017, **11,** 400-405.

193. S. Mondal, *Appl. Therm. Eng*., 2008, **28**, 1536-1550.

194. S. Raoux, W. Wełnic and D. Ielmini, *Chem. Rev*., 2010, **110**, 240-267.

195. J. Feinleib, J. Deneufville, S. C. Moss and S. R. Ovshinsky, *Appl. Phys. Lett*., 1971, **18**, 254-257.

196. S. R. Ovshinsky, *Phys. Rev. Lett*., 1968, **21**, 1450-1453.

197. T. Siegrist, P. Merkelbach and M. Wuttig, *Annu. Rev. Condens. Matter Phys*., 2012, **3**, 215-237.

198. (a) H. Mustroph, M. Stollenwerk and V. Bressau, *Angew. Chem. Int. Ed*., 2006, **45**, 2016-2035. (b) V. B. Jipson and C. R. Jones, *Journal of Vacuum Science & Technology*, 1981, **18**, 105-109. (c) P. Kivits, R. de Bont, and J. van der Veen, *Appl. Phys*., 1981, **A26**, 101-105. (d) F. Li, J. Zhuang, G. Jiang, H. Tang, A. Xia, L. Jiang, Y. Song, Y. Li and D. Zhu, *Chem. Mater*., 2008, **20**, 1194-1196. (e) B. Lohse, R. Vestberg, M. T. Ivanov, S. Hvilsted, R. H. Berg, C. J. Hawker and P. S. Ramanujam, *Chem. Mater*., 2008, **20**, 6715-6720.

199. (a) L. Tao and G. Fuxi, *Appl. Opt*., 1994, **33**, 3760-3763. (b) J. Yin and F. Gan, *Proc. SPIE*, 2001, **4085**, 146-149.

200. A. H. Sporer, *Appl. Opt*., 1984, **23**, 2738-2743.

201. A. H. Sporer, *Appl. Opt*., 1987, **26**, 1240-1245.

202. (a) S.Raoux and M. Wuttig, *Phase Change Materials: Science and Applications*, New York: Springer, 2009. (b) N. Yamada, R. Kojima, M. Uno, T. Akiyama, H. Kitaura, K. Narumi and K. Nishiuchi, *Proc. SPIE*, 2002, 4342, 55-63.

203. H.-S. P. Wong, S. Raoux, S. B. Kim, J. Liang, J. P. Reifenberg, B. Rajendran, H. Asheghi and K. E. Goodson, *Proc. IEEE*, 2010, **98**, 2201.

204. (a) Q. Zhang, J. Liu, K. Yuan, Z. Zhang, X. Zhang and X. Fang, *Nanotechnology*, 2017, **28**, 405101-1-11. (b) J. Li, Y. Hu, Y. Hou, X. Shen, G. Xu, L. Dai, J. Zhou, Y. Liu and K. Cai, *Nanoscale*, 2015, **7**, 9004-9012. (c) G. D. Moon, S. W. Choi, X. Cai, W. Li, E. C. Cho, U. Jeong, L. V. Wang and Y. Xia, *J. Am. Chem. Soc.*, 2011, **133**, 4762-4765.

205. S. W. Choi, Y. Zhang and Y. Xia, *Angew. Chem. Int. Ed.*, 2010, **49**, 7904-7908.

206. (a) D. C. Hyun, P. Lu, S. Il Choi, U. Jeong and Y. Xia, *Angew. Chem. Int. Ed.*, 2013, **52**, 10468-10471. (b) J. H. Park, H. Ahn, J. Kim and D. C. Hyun, *Macromol. Mater. Eng.*, 2016, **301**, 887-894.

207. A. Shukla, A. Sharma, M.Shukla and C. R. Chen, *J. Med. Eng. Technol.*, 2015, **39**, 363-368.

208. Y. Wang, B. Tang and S. Zhang, *J. Mater. Chem.*, 2012, **22**, 18145-18150.

209. Y. J. Jin, B. S. Il Kim, W. E. Lee, C. L. Lee, H. Kim, K. H. Song, S. Y. Jang and G. Kwak, *NPG Asia Mater.*, 2014, **6**, e137-1-6.

210. M. Takahashi, N. S. Humam, N. Tsumori, T. Saiki, P. Regreny and M. Gendry, *Appl. Phys. Lett.*, 2013, **102**, 093120-1-3.

211. S. Ogden, L. Klintberg, G. Thornell, K. Hjort and R. Bodén, *Microfluid. Nanofluid.*, 2014, **17**, 53-71.

CHAPTER 2

Fluorescence Enhancement in Crystals Tuned by a Molecular Torsion Angle: A Model to Analyze Structural Impact

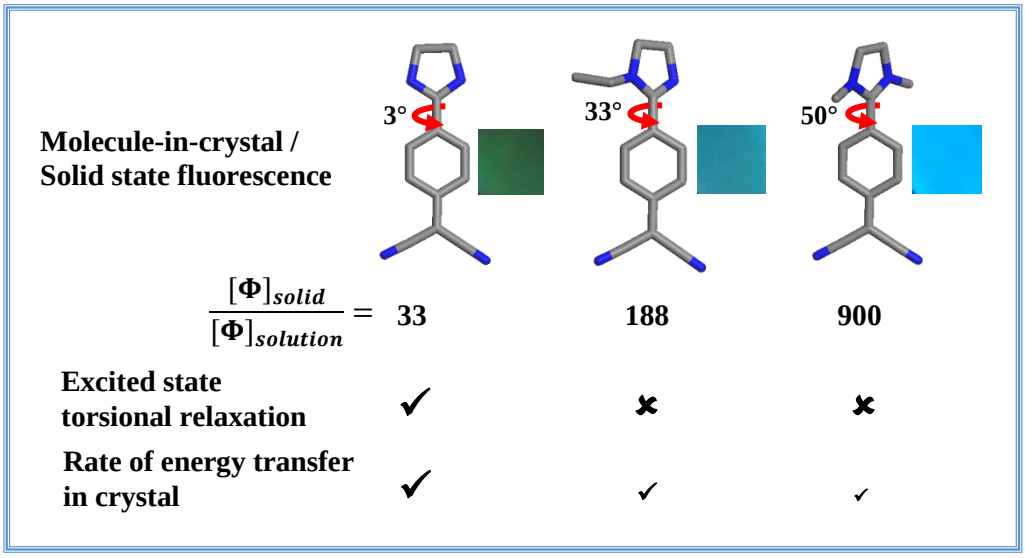

Subtle structural modifications facilitated the exploration of the critical impact of molecular structure and hence assembly on the fluorescence emission enhancement, through detailed analysis of the effects of intramolecular structural relaxation and intermolecular energy transfer.

Scope

Development of a coherent picture of enhanced fluorescence in the aggregated/solid state of molecular materials requires an exploration of the concomitant inhibition of intra and intermolecular non-radiative energy loss pathways. This requires a fluorophore that exhibits a systematic variation in the enhancement of emission from the molecular to the materials state, upon subtle structural tuning at the molecular and supramolecular levels. Diaminodicyanoquinodimethanes with an imidazolidine moiety, reported first in 1962 but never structurally characterized, is shown to be ideally suited for this. This chapter presents our investigations with the diaminodicyanoquinodimethanes synthesized using ethylenediamine and its N-ethyl and N,N'-dimethyl derivatives using a modified route; all the systems (the latter two being new molecules) are fully characterized, including their crystal structures. Systematic change in the molecular structure (a crucial torsion angle varying from ~3^o to 50^o) and hence assembly in crystals, increases the fluorescence enhancement factor (solution to solid) from ~30 to ~900 in unsubstituted to disubstituted derivative respectively. Computed ground and excited electronic state energy profiles and lattice energy, together with an analysis of the assembly of molecules and their transition dipoles in the crystals, reveal the impact of the alkyl groups on the torsion angle and intermolecular contacts that concomitantly control the excited state relaxation and the relative rate of intermolecular energy transfer in the solids. This approach provides insight into the contribution of intra and intermolecular pathways to the structural tuning of the emission enhancement, and a rational basis to tailor highly emissive molecular solids.

2.1. Introduction

Spectacular enhancement of the fluorescence efficiency of selected classes of molecules, from the solution (molecular) to the aggregated/solid state (materials) (often called aggregation-induced emission), is of great interest from both fundamental photophysics as well as materials application perspectives.[1-5] Examples of molecules exhibiting this phenomenon were discussed in detail in Sec. 1.2.1. The emission enhancement, also exhibited by colloids and nanoparticles of DADQs,[6] results from the blockade of intramolecular non-radiative decay channels such as internal rotations, and the suppression of intermolecular energy transfer (which otherwise causes concentration quenching). Extensive studies have focused on the development and application of molecules exhibiting very high enhancement factors; extension of a tetraphenylethene core by adding the same moiety is a typical example.[7]

Self-quenching or concentration-quenching of fluorescence accompanying aggregation is a common handicap for most of the conventional fluorophores. A dominant factor that contributes to concentration-quenching in solids is energy transfer;[8] the role of Förster transfer in phosphorescent complexes in a host matrix[9] and protein crystals,[10] as well as Dexter transfer in thermally activated delayed fluorescence systems[11] have been demonstrated. Since energy transfer contributes significantly to self-quenching, it is imperative to consider the role of specific molecular orientations that may hinder excited state energy loss *via* intermolecular pathways, an aspect that has been paid scant attention in the vast literature in the field of enhanced emission upon aggregation (often called AIE).[1] As highlighted in Sec. 1.2.2, even though some computational studies have probed the role of intramolecular excited state relaxation,[1,12] a coherent picture of the intra and intermolecular factors that together lead to the emission enhancement is yet to be established; the latter in particular has not been examined in any detail. A subtle and systematic structural tuning of the same fluorophore unit leading to a progressive and profound change in the fluorescence efficiency enhancement (FEE) factor (Sec. 1.2.1), not just the emission features, and an appraisal of the impact of the structural features at the molecular and supramolecular levels, are required to develop such a picture.

DADQs, have been shown to exhibit strong emission enhancement in different material forms (Sec. 1.2.1). The enhancement has been attributed to the inhibition of a torsional motion in the excited state using ultrafast dynamics of some derivatives explored recently.[13] The prototype molecule reported in 1962 having an imidazolidine group that can be viewed as a linked diaminomethylene moiety (**1**, Fig. 2.1),[14] has been the subject of several studies on nonlinear optics[15-18] and solar cell applications;[19,20] however, it has never been isolated in pure form or characterized structurally. DADQs that have been structurally characterized[13,21-24] have an unlinked diaminomethylene moiety (**2**, Fig. 2.1). We envisioned that **1** with a compact and conformationally rigid diaminomethylene (linked as imidazolidine) moiety would be ideally suited to systematic structural tuning through substitution on the nitrogen atoms, with potential impact on the FEE in the solid state, for which it could serve as a model system. In this chapter we describe the synthesis and structural characterization of **1** and two of its alkyl derivatives (the latter two are isomers), and the systematic variation of the emission enhancement across the three. We have also carried out structural and

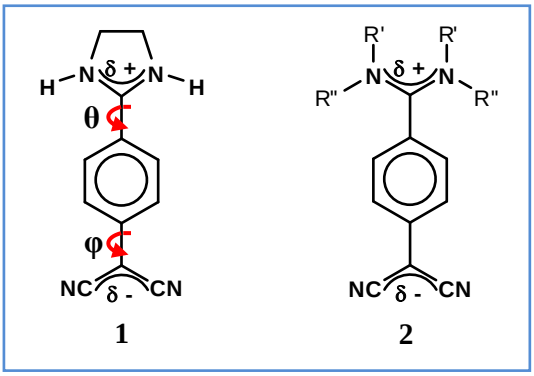

Figure 2.1. *Molecular structure of DADQs with linked (**1**) and unlinked (**2**) diaminomethylene group. Torsion angles θ and φ are indicated in **1**.*

computational analyses to explain the present observations, and attempted to provide a general framework to conceptualize the impact of intra and intermolecular interactions on the FEE of the new fluorophores in the solid state.

2.2. A New Class of DADQ Derivatives

2.2.1 *Synthesis and characterization*

Synthesis of **1a** reported earlier, used the direct reaction of 7,7,8,8-tetracyanoquinodimethane (TCNQ) with ethylenediamine.[14] Several prior and current explorations in our laboratory have indicated that the product from such a synthesis cannot be clearly isolated; polymeric contaminants appear to be present. We have now developed a two-step protocol involving monosubstituted TCNQ as the intermediate. Molecular structure of the new derivatives and the synthesis scheme are shown in Scheme 2.1; plausible mechanistic pathway is outlined in Scheme 2.2. The detailed synthesis procedure is as follows.

Step 1. *Synthesis of 7-pyrrolidino-7,8,8-tricyanoquinodimethane (PTCNQ)*:

Pyrrolidine (1.14 mmol) was added to a hot solution of 7,7,8,8-tetracyanoquinodimethane, TCNQ (1.4 mmol) in acetonitrile solvent (35 ml) at 65-70°C (caution: small amount of HCN gas is formed as the byproduct of the reaction). The solution turned dark purple immediately. The reaction mixture was stirred for 4 h and then cooled to 4°C. The microcrystalline solid precipitated over 2 days was filtered,

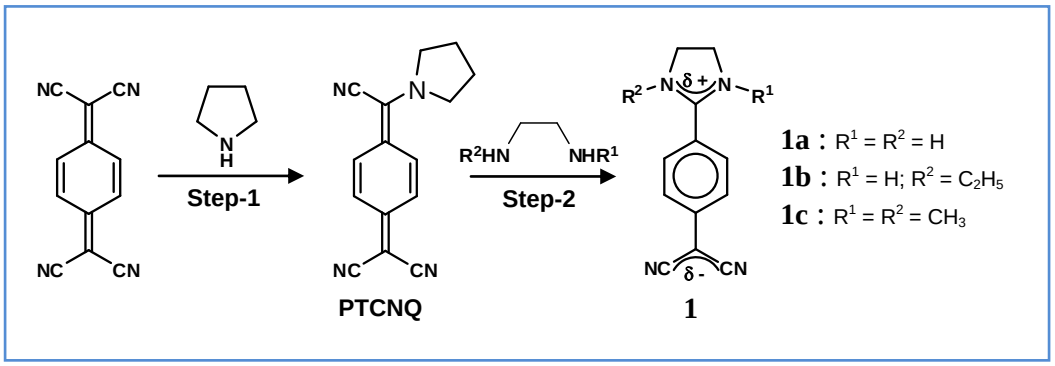

Scheme 2.1. *Formation of 2-(4-dicyanomethylenecyclohexa-2,5-dienylidene)imidazolidine and its alkyl derivatives (**1a-c**) by the two-step reaction of TCNQ with amines.*

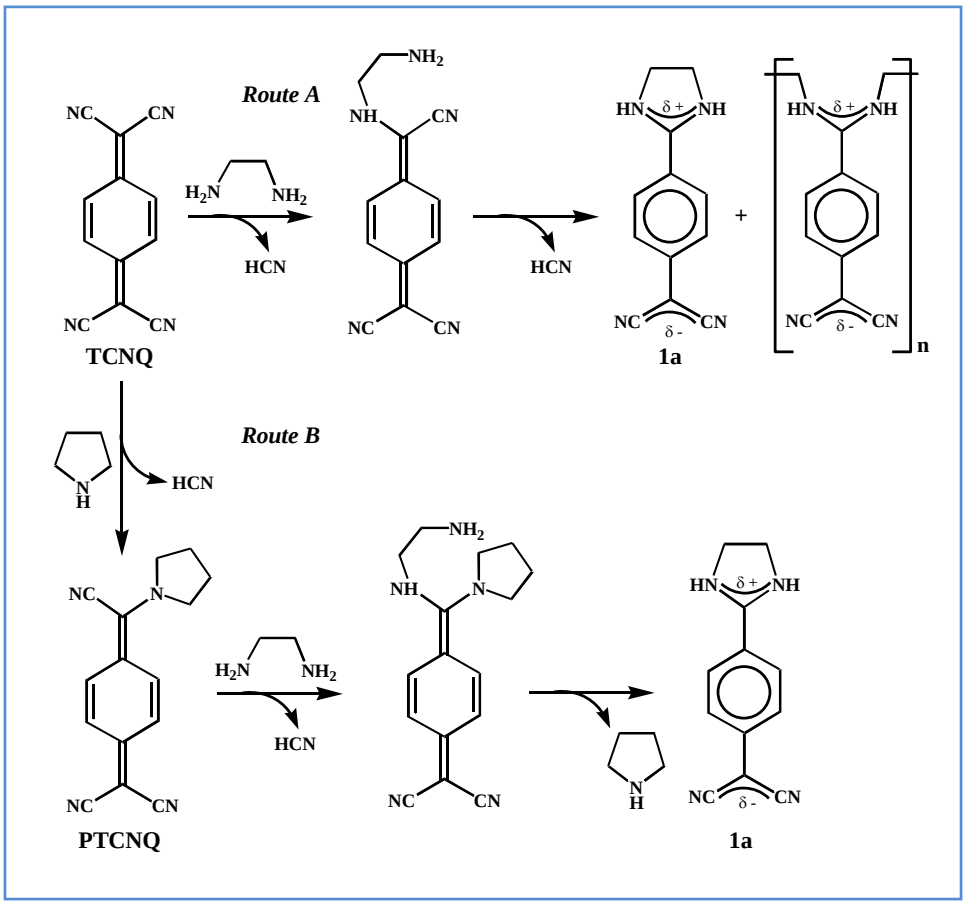

Scheme 2.2. *Plausible mechanism for the formation of **1a** from TCNQ following two routes; possible formation of polymeric products is indicated.*

washed with acetonitrile and dried to give 7-pyrrolidino-7,8,8-tricyanoquinodimethane, PTCNQ (0.23 g, 82% yield).

Step 2. *Synthesis of DADQs (**1a-c**)*:

Ethylenediamine or its appropriate derivative (0.806 mmol) was added to a hot solution of PTCNQ (0.806 mmol) in acetonitrile solvent (25 ml) at 65-70°C (caution: small amount of HCN gas is formed as the byproduct of the reaction). The solution turned dark green immediately and then to reddish orange in ~ 30 min; in the case of unsubstituted ethylenediamine, microcrystalline solid (**1a**) precipitated within 15 min of the addition of amine whereas for the other two the solution remained clear. The reaction mixture was stirred for 4 h and then cooled to 4°C. The microcrystalline solid precipitated over the time was filtered, washed with acetonitrile and dried to give the desired product **1a-c**. **1a** was purified by reprecipitation from DMF solution by adding acetonitrile. **1b** and **1c** were recrystallized several times from acetonitrile. All the compounds were characterized by NMR, IR and high resolution mass spectroscopies as well as single crystal structure analysis.

*2-(4-dicyanomethylenecyclohexa-2,5-dieny1idene)-imidazolidine (**1a**)*:
Yield: 79%; mp: 280°C (dec.); FTIR (KBr) - $\bar{\upsilon}$/cm^{-1}: 3199(broad, N−H stretch), 2191.7 and 2147.8 (asymmetric C≡N stretch), 1605.4 and 1506.8 (aromatic C=C stretch); NMR (400 MHz, DMSO-d_6) - δ/ppm ^{1}H: 9.77 (s, 2H, 2NH), 7.59-7.57 (d, 2H, 2 Ar-CH), 6.84-6.82 (d, 2H, 2 Ar-CH), 3.89 (s, 4H, 2CH_2); ^{13}C: 164.62, 150.43, 129.38, 123.31, 117.81, 108.6, 44.25, 35.34; HRMS (ESI) - *m*/*z*: 210.0905 (calculated for $C_{12}H_{10}N_4$ [M^+]: 210.0905).

*2-(4-dicyanomethylenecyclohexa-2,5-dieny1idene)-1-ethylimidazolidine (**1b**)*:
Yield: 82%; mp: 255-258°C (dec.); FTIR (KBr) - $\bar{\upsilon}$/cm^{-1}: 3545(broad, O−H stretch), 3150.2 (N−H stretch), 2186.2 and 2136.9 (asymmetric C≡N stretch), 1583.5 and 1512.3 (aromatic C=C stretch), 1331.5 (CH_3 deformation); NMR (400 MHz, DMSO-d_6) - δ/ppm ^{1}H: 9.71 (s, 1H, 1NH) 7.31-7.29 (d, 2H, 2 Ar-CH), 6.88-6.86 (d, 2H, 2 Ar-CH), 4.02-3.96 (t, 2H, CH_2), 3.85-3.83 (t, 2H, CH_2), 3.51-3.49 (q, 2H, CH_2), 1.25 (t, 3H, CH_3); ^{13}C: 166.18, 149.29, 129.67, 123.77, 117.97, 109.16, 49.70, 42.91, 42.20, 33.77, 13.19; HRMS (ESI) - *m*/*z*: 239.1294 (calculated for $C_{14}H_{15}N_4$ [M^++H]: 239.1297).

*2-(4-dicyanomethylenecyclohexa-2,5-dieny1idene)-1,3-dimethylimidazolidine (**1c**)*:
Yield: 63%; mp: 327-331°C; FTIR (KBr) - $\bar{\upsilon}$/cm^{-1}: 2936.9 (weak, alkyl C−H stretch),

2175.3 and 2131.4 (asymmetric C≡N stretch), 1594.5 and 1501.3 (aromatic C=C stretch), 1331.5 (CH_3 deformation); NMR (400 MHz, DMSO-d_6) - δ/ppm ^{1}H: 7.22-7.20 (d, 2H, 2 Ar-CH), 6.91-6.89 (d, 2H, 2 Ar-CH), 3.92 (s, 4H, $2CH_2$), 2.98 (s, 6H, $2CH_3$); ^{13}C: 166.32, 148.34, 130.02, 124.02, 118.01, 107.78, 50.20, 35.46, 32.96; HRMS (ESI) - *m*/*z*: 239.1296 (calculated for $C_{14}H_{15}N_4$ [M^++H]: 239.1297).

2.2.2 *Crystal structure of 1a-c*

Crystallization of **1a** was carried out by the diffusion of diethyl ether into the DMF solution, whereas for **1b** and **1c**, the crystals were grown by cooling the acetonitrile solution. The molecular structure and the packing of **1a-c** obtained by single crystal structure determination are shown in Figs. 2.2-2.4. The significant crystallographic details are collected in Table 2.1. The effect of alkyl substitution is clearly reflected in the extent of diaminomethylene twist (θ) with respect to the benzenoid ring plane. The dihedral angle, θ, (average of $\tau_{N9\text{-}C7\text{-}C1\text{-}C2}$ and $\tau_{N10\text{-}C7\text{-}C1\text{-}C6}$) is 3.4, 32.8 and 49.9° in **1a**, **1b** and **1c** respectively; **1b** has two similar molecules in the asymmetric unit (with very similar structural parameters) and hence only one is considered. **1a** with only H atoms on the imidazolidine N atoms, has the diaminometh-

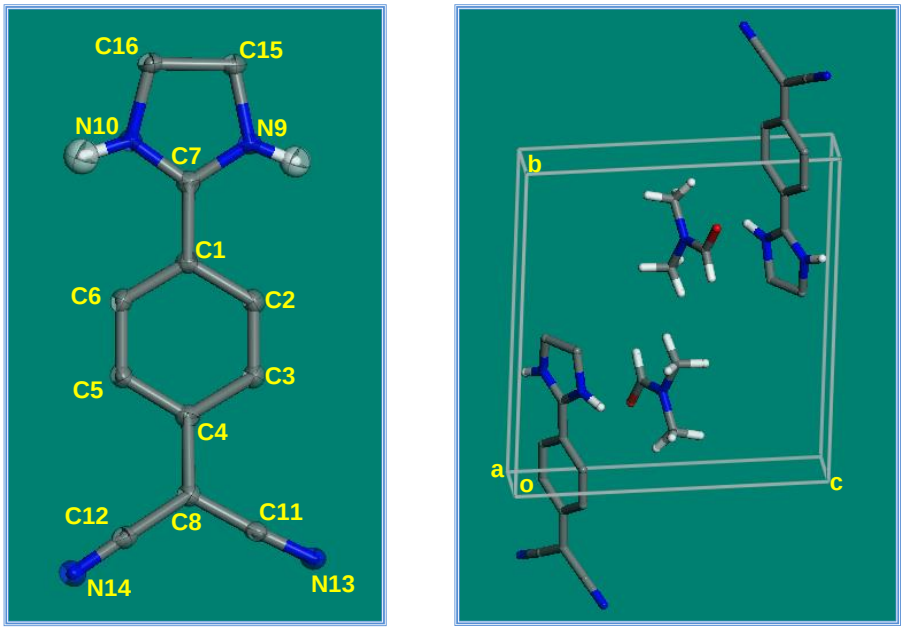

Figure 2.2. *Molecular structure showing 99% thermal ellipsoids and the unit cell of* ***1a****.*

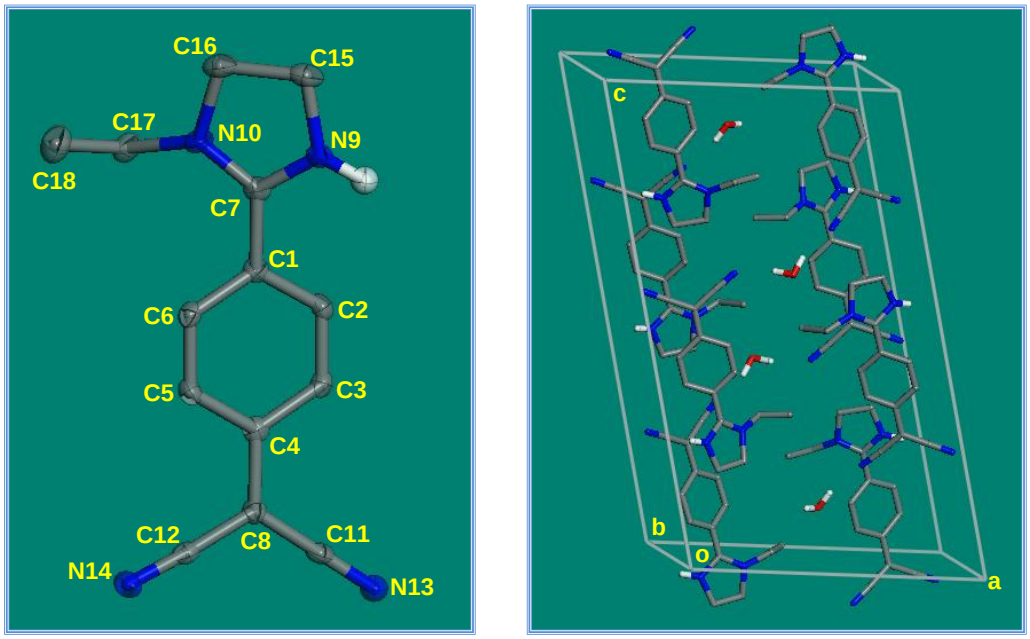

Figure 2.3. *Molecular structure showing 99% thermal ellipsoids and the unit cell of **1b**.*

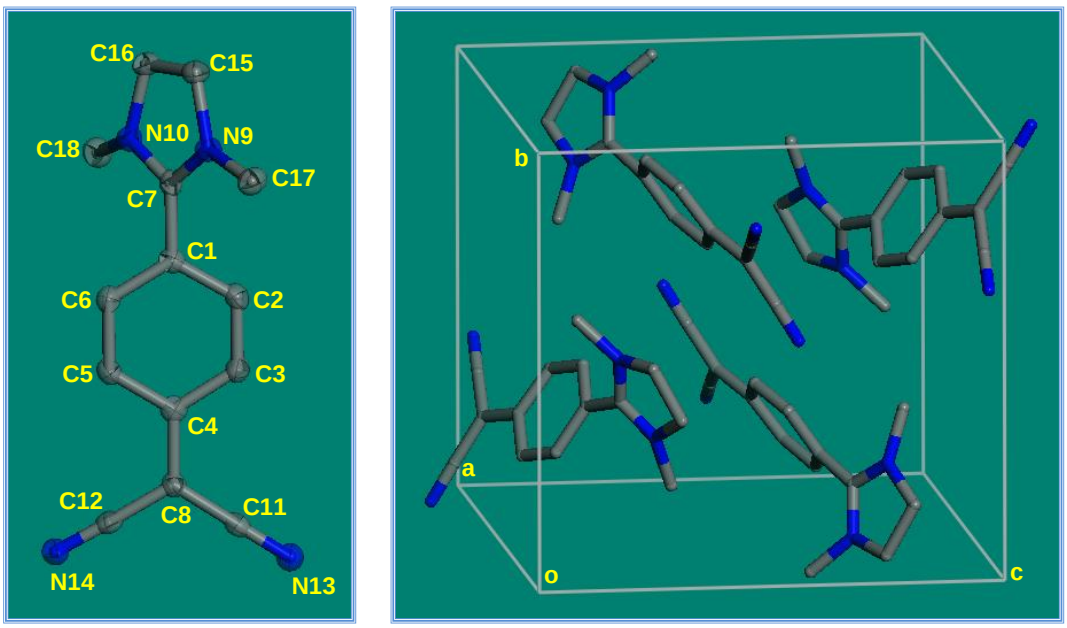

Figure 2.4. *Molecular structure showing 99% thermal ellipsoids and the unit cell of **1c**.*

Table 2.1. *Basic crystallographic details of **1a-c**.*

Molecule	**1a**	**1b**	**1c**
Empirical formula	$C_{15}H_{17}N_5O$	$C_{28}H_{30}N_8O$	$C_{14}H_{14}N_4$
Crystal system	Triclinic	Monoclinic	Monoclinic
Space group	*P-1*	$P2_1/c$	$P2_1/c$
a / Å	5.6328(5)	14.7692(12)	9.1349(6)
b / Å	11.2617(10)	7.3550(6)	11.5867(7)
c / Å	11.2686(10)	24.420(2)	11.7632(7)
α / deg.	86.4430(10)	90.00	90.00
β / deg.	77.4390(10)	105.3880(10)	98.4420(10)
γ /deg.	85.4860(10)	90.00	90.00
V / $Å^3$	694.81(11)	2557.6(4)	1231.57(13)
Z	2	4	4
$\rho_{calc.}$ / g cm^{-3}	1.354	1.285	1.285
μ / cm^{-1}	0.09	0.083	0.081
Temperature / K	100(2)	100(2)	100(2)
λ / Å	0.71073	0.71073	0.71073
No. of reflections	2813	4506	2165
No. of parameters	258	352	165
Max., Min. transmission	0.964, 0.991	0.990, 0.995	0.978, 0.992
GOF	1.047	1.127	1.05
R [for $I \geq 2\sigma_I$]	0.0360	0.0594	0.0353
wR^2	0.10	0.1210	0.0905
Largest difference peak and hole / e$Å^{-3}$	0.239, 0.048	0.239, 0.048	0.157, 0.041
CCDC deposition number	1444520	1444521	1444522

-ylene moiety nearly in plane with the benzenoid ring (i.e. $\theta = 3.4°$), and interacts with the neighboring molecules through H-bonding using both -NH groups (Fig. 2.5). **1b** and **1c** with one and two alkyl groups respectively has considerably twisted diaminomethylene moiety due to the steric repulsion between the alkyl substituent and the *ortho* H atom of benzenoid ring; the twist increases with increasing substitution, influencing the intermolecular separation and relative orientation of molecules (Fig. 2.5). **1b** utilizes the one -NH group for intermolecular H-bond formation, whereas **1c** has none. The critical role of molecular structure and assembly across the series in determining the solid state fluorescence efficiencies is discussed further below.

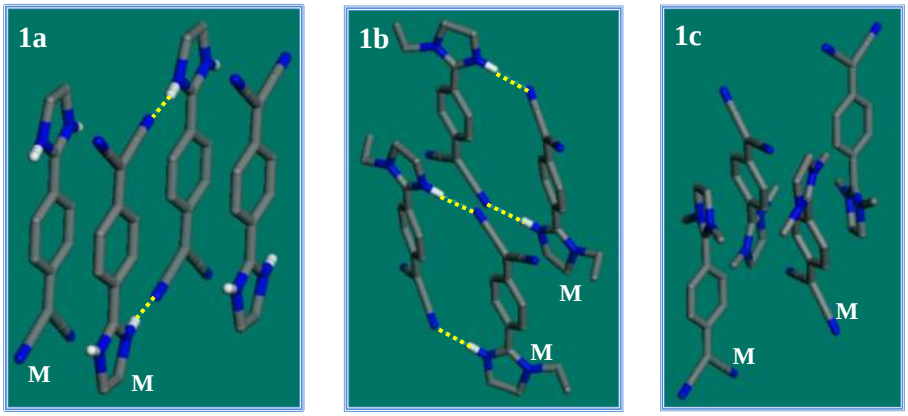

Figure 2.5. *Molecular assembly of **1a-c**; H atoms except the ones involved in H-bonding are omitted. (The molecules involved in H-bonding and the nearby molecules (M) considered to define intermolecular parameters in Table 2.3 are shown (H-bonds are indicated with yellow broken line); the H-bonds shown lead to extended supramolecular chains in **1a**.*

2.3. Spectroscopic Investigations

Electronic absorption and emission of **1a-c** in the solution state was examined using solvents of different polarity. Negative solvatochromism of the absorption, typical of DADQ molecules with strong intramolecular charge transfer in the ground state, is observed in all cases (Fig. 2.6).[25] No appreciable solvatochromism is observed in the fluorescence emission of **1a-c**. The electronic absorption and emission spectra of **1a-c** in acetonitrile solution and microcrystalline solid state are compared in Fig. 2.7; the salient features are listed in Table 2.2. Solid samples were prepared in the form of KBr pellets; weight ratio of DADQ to KBr was adjusted to match the optical density (OD) with that of the solutions at the excitation wavelength so that the fluorescence intensity comparison is meaningful; OD of the samples was maintained below 0.1 in all cases, to avoid any inner filter effect. The absorption spectra of solutions show λ_{max} ~ 400 nm with a small but steady blue shift from **1a** to **1c**, whereas the solids show peaks at similar wavelengths. The trend is consistent with the impact of the torsional angle on the electronic structure, the increasing twist leading to increasing absorption energy.[26]

Fluorescence quantum yield (Φ) of solutions (OD $\leq$ 0.1) was determined using quinine sulfate in 1N H_2SO_4 (Φ = 0.546) as the standard; absolute values of the quantum yield of solid samples were determined using an integrating sphere and the PLQY

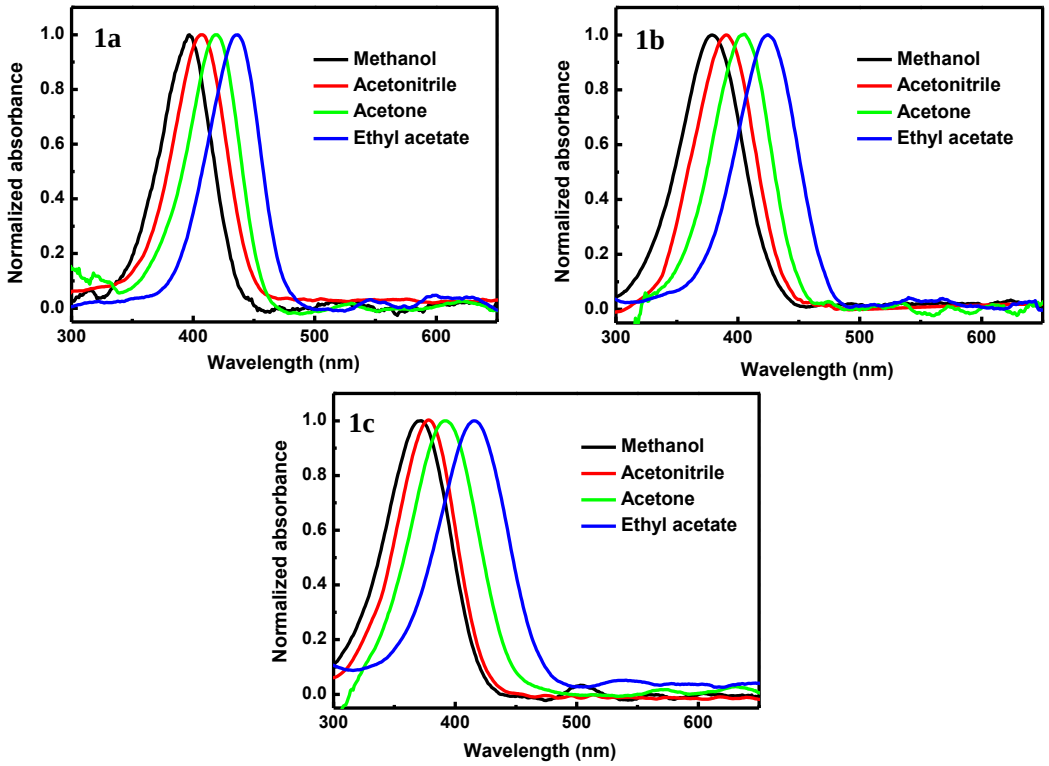

Figure 2.6. *Absorption spectra of **1a-c** in solvents of varying polarity; methanol (Reichardt parameter, E_T^N = 0.762), acetonitrile (E_T^N = 0.460), acetone (E_T^N = 0.355) and ethyl acetate (E_T^N = 0.228).*

Calculator v.3 software (Jobin Yvon). Quantum yield values of solution and solid samples are listed in Table 2.2. The increasing options for H-bond formation, from the disubstituted to the unsubstituted molecule, possibly leads to a parallel trend in the interactions with the polar solvent, reducing the extent of excited state relaxation and increasing the emission quantum yield (albeit low) from **1c** to **1a** in solution. As reported earlier with DADQs,[21] fluorescence emission from the solution of all the molecules is very weak, but enhanced significantly in the solid state (Fig. 2.7). The relatively small Stokes shifts in **1b** and **1c** crystals lead to bluish emission (Fig. 2.8) suggesting relatively small geometry relaxations in the excited state. Fluorescence excitation spectra of the solution and solid samples of **1a-c**, recorded at the respective emission wavelengths are provided in Fig. 2.9. Similarity of the spectra in both the solution and the solid suggests that the emitting state is the same in both forms. The prominent observation in Fig. 2.7 is the steady increase of FEE, the enhancement (from solution to solid) of emission intensity from **1a** to **1c**; the highest enhancement factor of

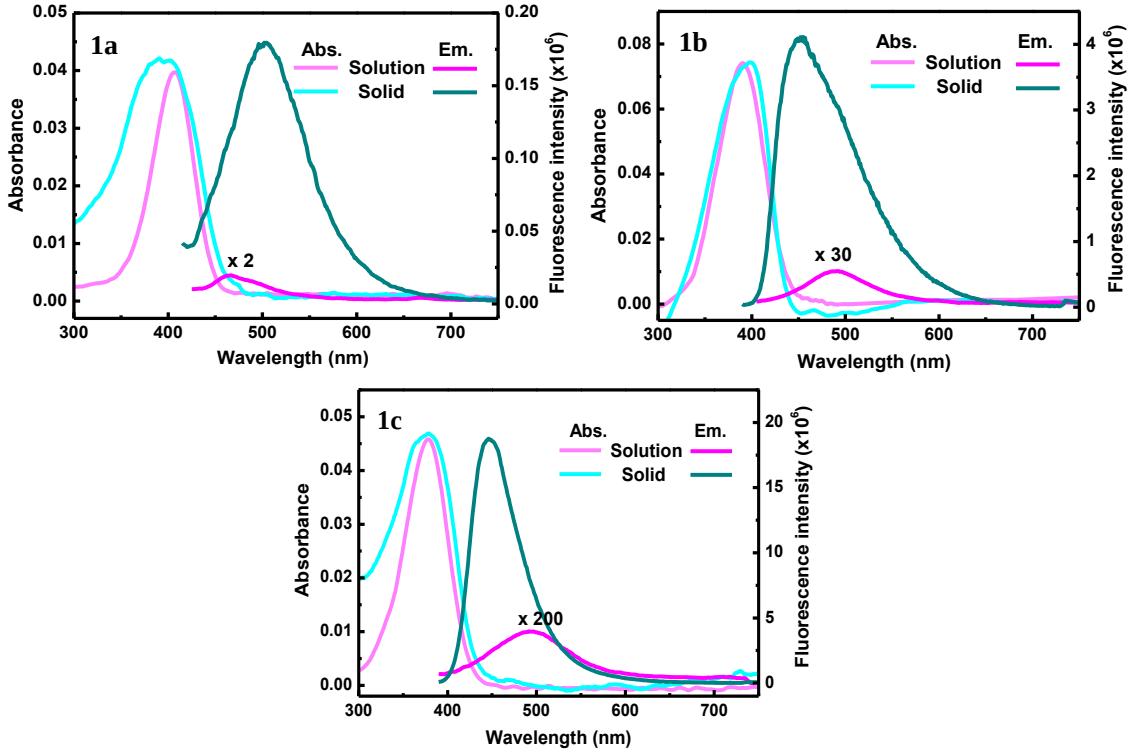

Figure 2.7. *Electronic absorption and emission spectra of **1a-c** in acetonitrile solution and microcrystalline solid state; the samples used for recording the emission have similar optical density and are excited at the absorption* λ_{max}.

Table 2.2. *Absorption and emission peak maxima in acetonitrile solution and solid state [computed values (Sec. 2.4.1) are shown in square brackets], the emission quantum yields [Φ (%)] and the fluorescence efficiency enhancement, FEE based on the ratio (solid/solution) of emission intensity (I) and quantum yields (Φ) for **1a-c**.*

Molecule	Solution			Solid			FEE based on	
	λ_{max}^{abs} (nm)	λ_{max}^{em} (nm)	Φ	λ_{max}^{abs} (nm)	λ_{max}^{em} (nm)	Φ	I	Φ
1a	408 [421]	466 [463]	0.27	400 [395]	502 [482]	9	18	33
1b	390 [416]	492 [474]	0.08	400 [395]	454 [475]	15	223	188
1c	380 [385]	494 [501]	0.05	375 [382]	447 [493]	45	945	900

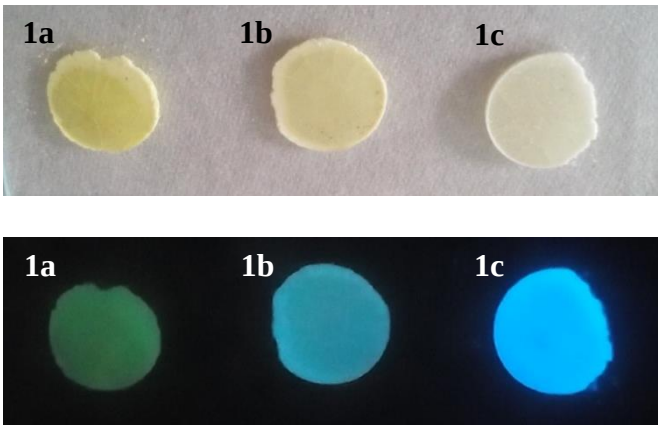

Figure 2.8. *Photographs of solid samples (KBr pellet) of **1a-c** under ambient (top row) and UV (365 nm) light (bottom row); solutions, even with OD ~ 0.1 show no visible fluorescence.*

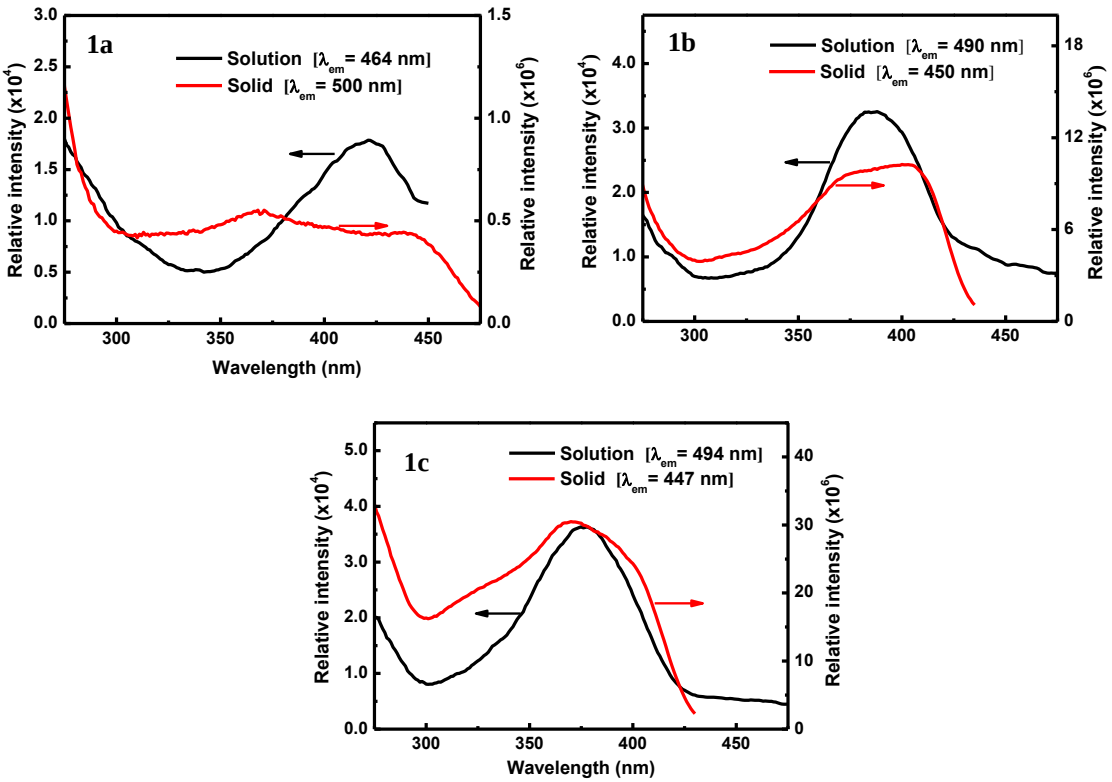

Figure 2.9. *Fluorescence excitation spectra of **1a-c** in acetonitrile solution and microcrystalline solid state; λ_{em} for each sample is indicated.*

~ 900 in **1c** (Table 2.2) is notably large. The large variation in the enhancement factor results from the combination of trends in the solution and solid state emissions. We analyze below, the various factors that lead to these interesting observations.

2.4. Computational Investigations

2.4.1 *Analysis of intramolecular excited state energy loss*

In order to probe the origin of the fluorescence emission enhancement (as opposed to the quenching in most dye molecules), we analyzed the molecular structures in the electronic ground and excited states in the solvent and crystal environments, as well as the intermolecular interactions in the latter. *Ab initio* computations were carried out using Gaussian 09 program at the B3LYP/6-31G* level; TD-DFT method was used for the excited states and SCRF to model the environment effect.[27]

The required input geometries for the computations were taken from the respective crystal structures. The structures in acetonitrile solution were explored by full optimization of the molecular structure; the optimized geometries were confirmed to be the energy minima by vibrational frequency calculations (Appendix C). In the electronic ground state calculation, the dihedral angle θ increases slightly with respect

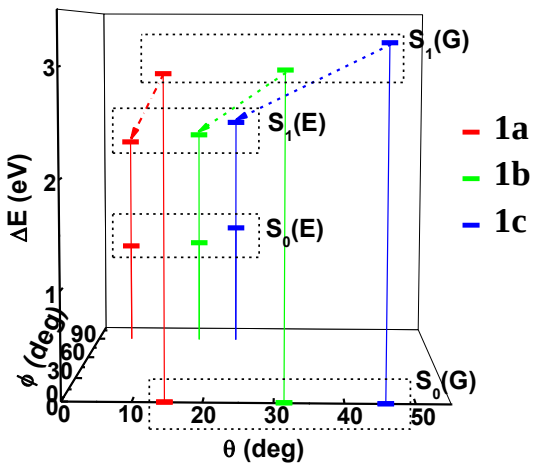

Figure 2.10 *Computed (DFT/TD-DFT) energies of the ground (S_0) and vertical excited (S_1) electronic states of* ***1a-c*** *in their fully optimized [B3LYP/6-31G*; SCRF (acetonitrile solvent)] ground (G) and excited (E) state geometries with reference to the torsion angles θ and φ in the optimized geometries; all energies are relative to that of S_0(G) for each molecule.*

Table 2.3. *Computed [B3LYP/6-31G*; SCRF (acetonitrile); TD-DFT for excited state] absorption and emission energy (wavelength maxima, λ_{max}^{abs} and λ_{max}^{em}) along with oscillator strength, f (shown in square brackets) for the first three excited states of the fully optimized excited state structures of **1a-c**.*

Molecule	Absorption λ_{max}^{abs} (nm) [*f*]			Emission λ_{max}^{em} (nm) [*f*]		
	$S_0 \rightarrow S_1$	$S_0 \rightarrow S_2$	$S_0 \rightarrow S_3$	$S_1 \rightarrow S_0$	$S_2 \rightarrow S_0$	$S_3 \rightarrow S_0$
1a	421 [1.092]	312 [0.004]	290 [0.0]	1107.0 [0.0]	386.2 [0.002]	304.4 [0.039]
1b	416 [0.986]	317 [0.006]	293 [0.0]	1065.3 [0.0]	388.9 [0.002]	314.2 [0.0]
1c	385 [0.702]	317 [0.003]	295 [0.0]	1093.1 [0.0]	385.9 [0.002]	324.0 [0.0]

to the initial geometry in **1a**, but remains nearly the same in **1b** and **1c** (Fig. 2.10); in this figure, S_0(G) and S_1(G) refer to the electronic ground state and first excited state of the optimized ground state geometry, and S_0(E) and S_1(E) to the corresponding states of the optimized excited state geometry. Computation of the excited state energies using these optimized geometries shows that the lowest excitation with appreciable oscillator strength is to S_1 (Table 2.3); they follow the trend seen in the experimental λ_{max}^{abs} across the series (Table 2.2). Full optimization of the geometry in the excited state reveals a decrease in θ in all the three molecules. More importantly, the dihedral angle (φ) between the dicyanomethylene group and the benzenoid ring plane increases from 0 to 90° in each case (Fig. 2.10); a similar observation has been reported earlier in a different DADQ molecule.[13] This major geometry change leads to significant energy relaxation in the excited state [S_1(G) to S_1(E)], so that the energy gap, [S_1(E) – S_0(E)] is reduced to the near infra-red region; the oscillator strength for this and higher energy transitions are negligible (Table 2.3). The fraction of excited state molecules undergoing this geometry relaxation do not contribute to any visible emission. The remaining molecules show the observed emission with Stokes shifts typically associated with simple vibrational relaxation. Computations of the partially relaxed excited state geometry without θ or φ rotation, gave emission wavelengths in good agreement with the observed values, and reasonable oscillator strengths (Tables 2.2 and 2.4). The weak fluorescence emission from the solution is consistent with the above discussion.

Table 2.4. *Computed [B3LYP/6-31G*; SCRF (acetonitrile)] emission energy (wavelength maximum, λ_{max}^{em}) and oscillator strength (f) for the first three excited states of the partially optimized (with θ and φ fixed at the values of fully optimized ground state geometry) excited state structures of* ***1a-c****.*

Molecule	$S_1 \rightarrow S_0$		$S_2 \rightarrow S_0$		$S_3 \rightarrow S_0$	
	λ_{max}^{em} (nm)	*f*	λ_{max}^{em} (nm)	*f*	λ_{max}^{em} (nm)	*f*
1a	463.2	0.999	320.3	0.002	293.1	0.000
1b	474.7	0.858	326.2	0.003	295.0	0.000
1c	500.9	0.634	329.1	0.004	296.3	0.000

The possibility of large structural change involving the φ twist in the solid state was investigated using force field based lattice energy computations (Materials Studio v 6.0.0, Accelrys Software Inc., GULP module and Dreiding force field).[28] Lattice energy was calculated for a cluster of molecules excised from the extended lattice; the molecule of interest (buried deeper in the cluster) is subjected to dicyanomethylene twist, with φ fixed at 10° interval, keeping the remaining molecules of the cluster frozen. These calculations clearly show that φ twist occurring in the solid state can be ruled out, as the energy increases significantly with the twist (Fig. 2.11a). The other potential factor left for excited state structural relaxation is the diaminomethylene twist, θ. Therefore exploration of the molecular structure in the solid state was focused on the torsion angle, θ, keeping φ fixed at the value in the crystal.

The angle θ, determined primarily by the π-electron conjugation and the steric interaction between the imidazolidine and benzenoid rings, is sensitive to the

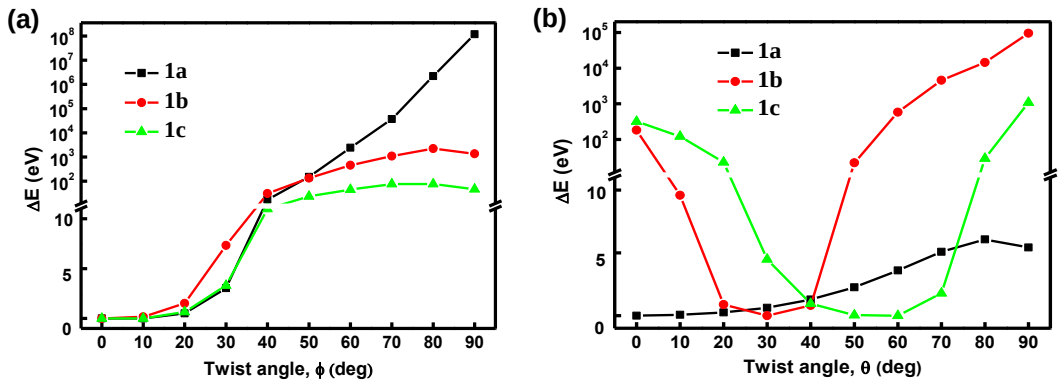

Figure 2.11. *Variation of the lattice energy as a function of the twist angle* ***(a)*** *φ and* ***(b)*** *θ for the crystals* ***1a-c****.*

substitution on the imidazolidine nitrogen atoms as well as the dielectric environment. Molecules-in-crystals have been modelled using standard solvation schemes in the earlier studies from our laboratory; θ of the optimized structure increases with the dielectric constant of the medium imposed in the computation.[29] Closest agreement between the values in the optimized structures and the molecules-in-crystals, is obtained for **1a** (θ_{calc} = 7°) in vacuum, **1b** (θ_{calc} = 30°) in propanonitrile environment (ε = 29.3), and **1c** (θ_{calc} = 45°) in acetonitrile environment (ε = 35.7). This is consistent with the enhancement of charge separation in the push-pull structures as well as the increasing steric hindrance due to the substituent alkyl groups. Further computations on the solid state structures were carried out in vacuum for **1a**, and the relevant environment for **1b** and **1c**. Partial geometry optimization calculations for the electronic ground state started with the molecular structure from the crystal structure analysis as the initial geometry with the torsion angle, φ frozen; in **1b**, the optimized geometry corresponded to the θ = 30° point, whereas in **1a** and **1c** these were at θ = 7° and 45° respectively. θ was fixed at 10° intervals (starting with 10°, 30° and 40° respectively in **1a**, **1b** and **1c**), each optimization is carried out using the previous point geometry as the initial one. These calculations, together with single point TD-DFT calculation at the partially optimized ground state geometry, generated the $S_0(G)$ and $S_1(G)$ profiles. The partially optimized geometry corresponding to the minimum of the $S_0(G)$ profile was used to optimize the excited state geometry (keyword ROOT=1), again freezing the angle φ. Following the protocol as in the case of the ground state geometry, the $S_0(E)$ and $S_1(E)$ profiles were computed. Energy profiles for the ground and vertical excited electronic states of the partially optimized ground state geometries [$S_0(G)$ and $S_1(G)$ respectively] with θ fixed at 10° intervals, are shown in Fig. 2.12 (in **1a** and **1c**, the point at the minimum of the $S_0(G)$ profile is also added; the minimum of **1b** happens to be at 30°). The λ_{max}^{abs} [$S_0(G) \rightarrow S_1(G)$] for the minimum energy point on the $S_0(G)$ profile in each case is in agreement with that observed in the solid (Table 2.2). The $S_1(G)$ profile of **1b** and **1c** shows a minimum at a θ smaller than that in the ground state, whereas the profile of **1a** shows energy steadily decreasing towards θ = 90°. Fig. 2.12 shows also the profiles of $S_0(E)$ and $S_1(E)$ corresponding to the partially optimized geometry of the first excited state; the excited state geometry relaxation involves opening of the angle θ to 90° in all cases. Lattice energy estimations indicate that this structural change (θ twist) is energetically prohibitive in **1b** and **1c**, but not in **1a**, due to the respective steric factors (Fig. 2.11b). Therefore the excited state structural relaxation can possibly occur

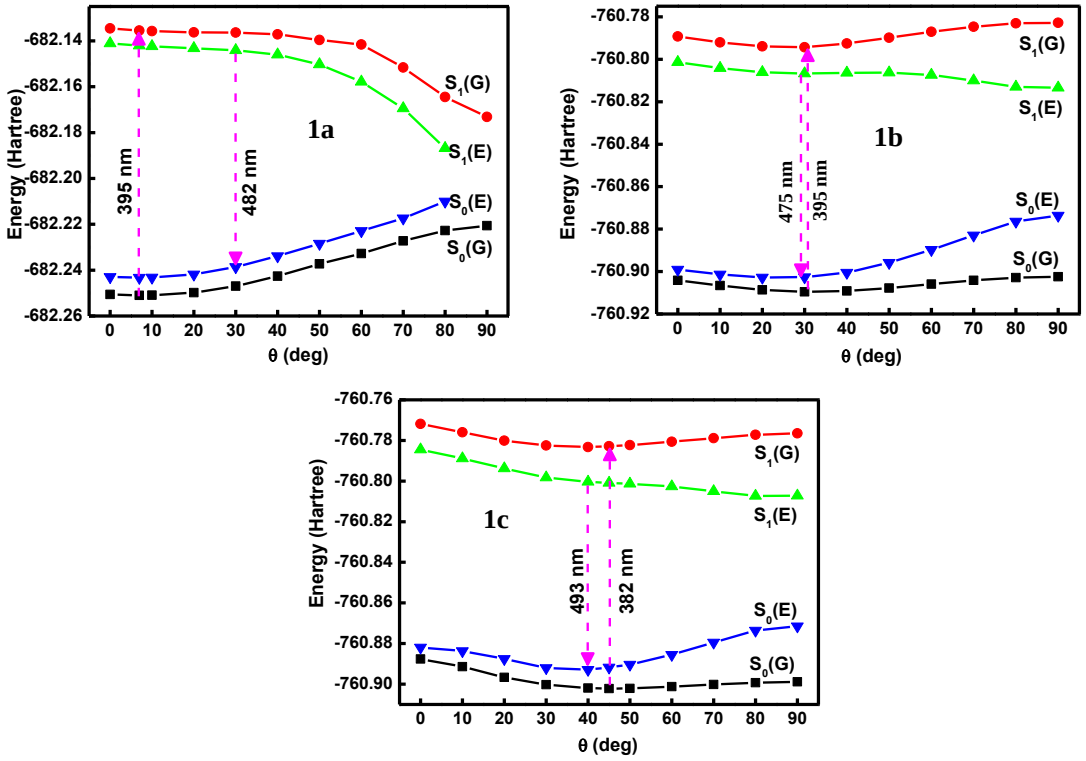

Figure 2.12. *Ground (S_0) and excited (S_1) state energy profiles for the partially optimized ground (G) and excited (E) state geometries of **1a-c** as a function of θ (φ fixed at the value in the crystal), computed using DFT/TD-DFT (B3LYP/6-31G*); **1a** in vacuum, **1b** in propanonitrile and **1c** in acetonitrile (the latter two using the SCRF model) [70 and 80° points of S_0(E) and S_1(E) of **1a** were obtained with lower thresholds for optimization; 90° point could not be optimized]. Estimated absorption/emission wavelengths are indicated using broken line with arrow.*

in solid **1a**, but not in the other two. Oscillator strength for the $S_1 \rightarrow S_0$ transition decreases monotonically with increasing θ (Fig. 2.13), suggesting that the excited state relaxation will lead to fluorescence quenching and hence a low fluorescence enhancement in solid **1a**, but not **1b** and **1c**. The relatively larger Stokes shift in solid **1a** compared to the other two is consistent with this picture. The computed λ_{max}^{em} [S_1(E) $\rightarrow$ S_0(E)] are shown in Fig. 2.12 and Table 2.2. Values for **1b** and **1c** are taken at the θ corresponding to the minimum on the S_1(G) profile (30 and 40° respectively), whereas the value for **1a** is for the point with the maximum θ (30°) for which the S_1(E) $\rightarrow$ S_0(E) transition still has good oscillator strength (Fig. 2.13). The calculated values are broadly in the range of the observed values.

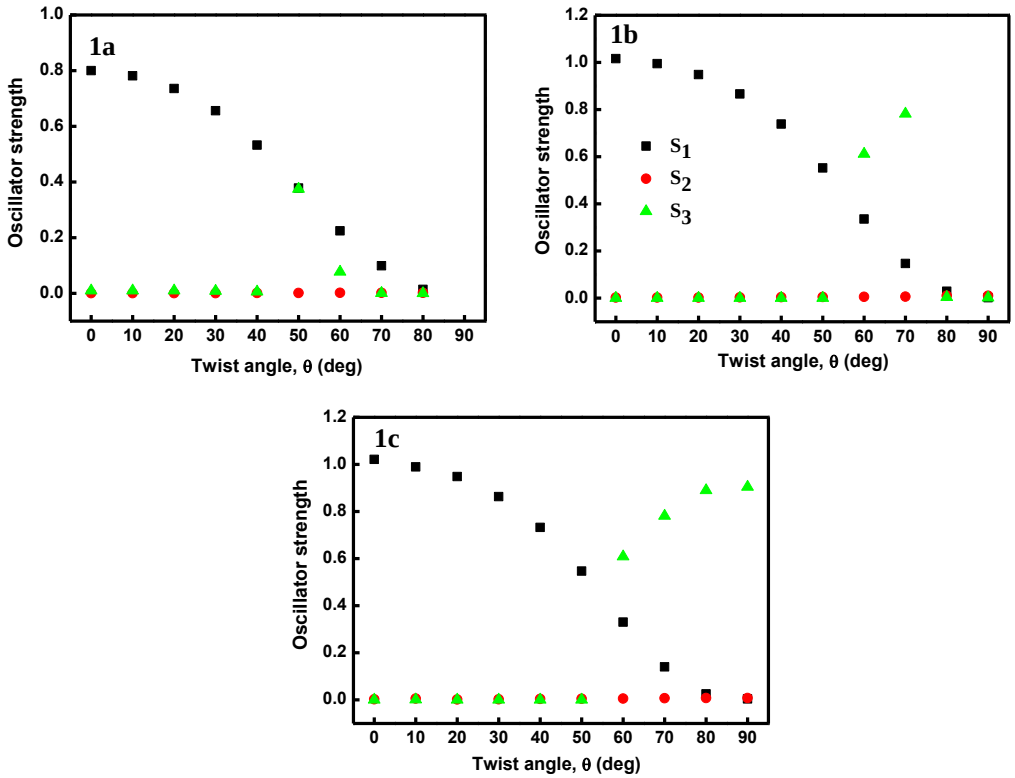

Figure 2.13. *Oscillator strength computed for the $S_1 \rightarrow S_0$, $S_2 \rightarrow S_0$, $S_3 \rightarrow S_0$ transitions of the excited state geometries (partially optimized, fixing the angle, φ at the value in the crystal structure and with different values of θ) of* ***1a-c****.*

2.4.2 *Model for estimating relative intermolecular energy transfer rates*

Intermolecular energy transfer is the other major contributor to the fluorescence efficiency change between the isolated (solvated) state of a molecule in solution and the assembled state in the crystal. In the current context, it is a case of homotransfer,[30] as it occurs between the excited and ground states of the same fluorophore unit. The rates of intermolecular energy transfer through the Förster and Dexter modes are given by the general equations:

$$k_F = \frac{9000(ln10)\kappa^2 \Phi}{128\pi^5 N_A n^4 r^6 \tau} J_F \quad ; \quad k_D = \frac{2\pi}{h} K J_D exp^{(-2r/L)}$$

where k_F and k_D are the energy transfer rate constants through Förster and Dexter

modes respectively, κ^2 is the orientation factor, N_A is the Avogadro constant, n is the refractive index of the medium, Φ and τ are the fluorescence quantum yield and lifetime of the donor, J_F and J_D are the spectral overlap integrals for Förster and Dexter modes of energy transfer respectively, r is the separation between acceptor and donor, h is the Planck's constant, K is a constant and L is the average Bohr radius.[30]

Even though the Dexter mode of energy transfer dominates at short intermolecular distances,[31] contributions from the Förster mode cannot be ruled out completely. In the present series **1a-c**, we are interested specifically in the relative energy transfer rates, not the absolute values; we have considered both modes of energy transfer. As the overlap between the absorption and emission spectrum is similar for each molecule in the series (Fig. 2.7), the main factor that determines the relative energy transfer rate in **1a-c** (having a common fluorophore moiety) will be the disposition of the near neighbor molecules in the crystal and their transition dipole moments. The transition dipole of each molecule was computed using its geometry from the crystal structure, with the appropriate environment as discussed earlier, to mimic the crystalline environment; in each case, it coincides closely with the long axis connecting the diaminomethylene and dicyanomethylene carbons (Fig. 2.14). The nearly planar geometry of **1a** allows close stacking of molecules in the crystal, whereas the increasing

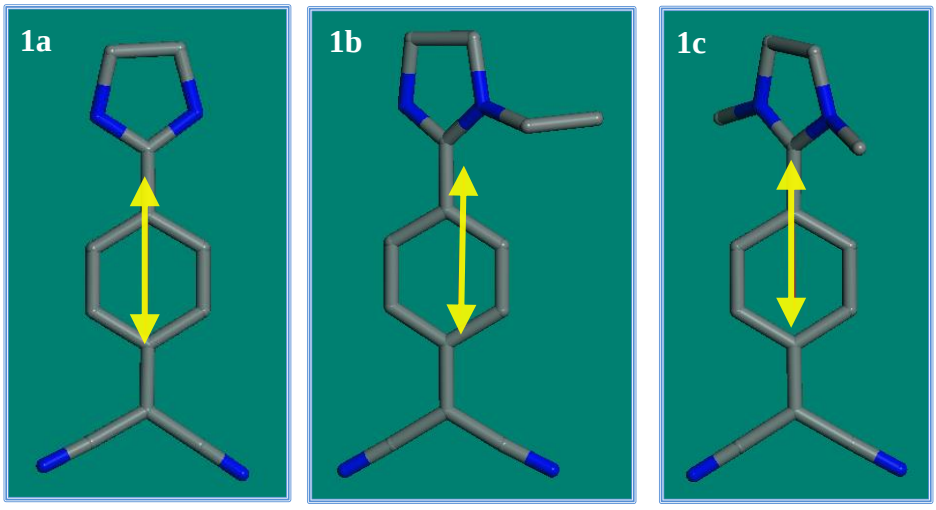

Figure 2.14. *Calculated [B3LYP/6-31G*, TD-DFT (ROOT=1)] transition dipole moments (yellow coloured double head arrow) of the molecules **1a-c** with the geometry taken from the crystal structure (**1a** in vacuum, **1b** in propanonitrile and **1c** in acetonitrile environments).*

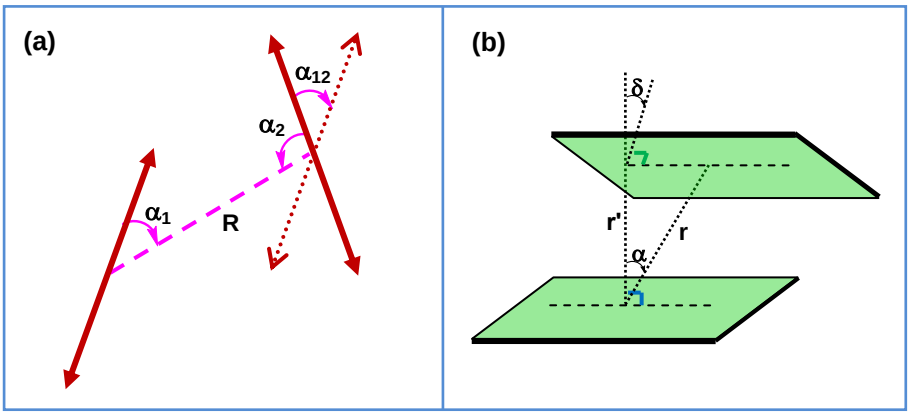

Figure 2.15. *Schematic diagrams showing the geometric parameters relevant for intermolecular energy transfer:* ***(a)*** *Förster: distance (R) and angles (α_1, α_2, α_{12}) between the transition dipoles (double arrows) and the vector connecting them;* ***(b)*** *Dexter: distance between the centroids (r), the perpendicular distance (r') and displacement (α) and interplanar (δ) angles between the mean molecular planes.*

θ and steric hindrance posed by the alkyl groups in **1b** and **1c** leads to greater separation of molecules and non-parallel orientation of the molecular planes (as discussed with Fig. 2.5 earlier). This suggests that the energy transfer rates (in crystals) are likely to decrease from **1a** to **1c**.

As a reasonable approximation for a uniform model to make quantitative estimates across the series, the moiety consisting of the benzenoid ring and the diaminomethylene and dicyanomethylene carbon atoms (C7 and C8 respectively in Figs. 2.2-2.4) was chosen to define the molecular plane. The critical parameters that control the Förster and Dexter modes of energy transfer (Fig. 2.15) are respectively, (i) the

Table 2.5. *Intramolecular torsion angle (θ); distance (R) and angle (α_{12}) between transition dipoles, intermolecular (r) and interplanar (r') distances, displacement (α) and interplanar (δ) angles of the closest neighbors with good overlap, in* ***1a-c****; angle θ is the average of the two closely similar values observed in the molecular structure in the crystal.*

Molecule	θ(°)	R (Å)	α_{12} (°)	r (Å)	r' (Å)	α (°)	δ (°)
1a	3.4	3.860	0.0	3.929	3.515	26.5	0.0
1b	32.8	6.061	3.1	6.132	3.263	57.9	14.0
1c	49.9	5.969	35.0	5.907	4.234	44.2	66.5

Box 2.1. Estimation of relative intermolecular energy transfer rates

When the overlap between the absorption and emission spectra are similar, the relative rates of energy transfer are controlled by mutual orientation of the transition dipoles and molecules.

Förster resonance energy transfer

The computed transition dipole is used in calculating the relative energy transfer rate through the Förster mode. Dependence of the rate of energy transfer on the relative orientation of the transition dipoles is estimated using the equation,

$$k_{ET}(Förster) \propto \frac{\kappa^2}{R^6} = \frac{(cos\alpha_{12} - 3 * cos\alpha_1 * cos\alpha_2)^2}{R^6}$$

where α_{12} is the angle between the transition dipoles of molecules 1 and 2, α_1 and α_2 are the angles between the transition dipoles and the vector connecting the two, and R is the distance between the transition dipoles (Fig. 2.15a). For each crystal, the neighboring molecules with transition dipoles within a certain cut-off distance (R), around that of a selected molecule in the crystal lattice can be considered, to estimate the values of $\frac{\kappa^2}{R^6}$.

Dexter energy transfer

Dependence of the rate of Dexter energy transfer on the relative molecular orientations is estimated by,

$$k_{ET}(Dexter) \propto Se^{-r'} = cos\delta.cos\alpha.\boldsymbol{e^{-r'}} = cos\delta.cos\alpha\boldsymbol{e^{-rcos\alpha}}$$

where r′ is the perpendicular distance between the mean planes of the molecules, r is the distance between the centroids, α is the angle between the normal to the mean plane of the reference molecule and the vector connecting the centroids of the two molecules, δ is the angle between the mean planes of molecules 1 and 2 (Fig. 2.15b). For each crystal, the neighboring molecules within certain cut-off distance (the length and width of the molecule) for r.sinα and r′ > 2.5 Å around a selected molecule in the crystal lattice can be considered to estimate the values of $e^{-r'}$.

In the case of **1a-c**, r.sinα < 10 Å [r.sinα = displacement of the centroid of one molecule with respect to the centroid of the other; 10 Å = the approximate length of the diaminodicyanoquinodimethane chromophore] and 2.5 Å < r' < 4.5 Å around a selected molecule in the crystal lattice are considered, to estimate the values of $e^{-r'}$. The sum of k_{ET} for each crystal and the relative values of energy transfer through both the modes for **1a-c** are listed in Tables 2.6 and 2.7.

Table 2.6. *The relevant geometric parameters [for molecules within a distance (R) of 10 Å from a reference molecule] and the relative rates of Förster energy transfer in the crystals of* ***1a-c****.*

Crystal	R (Å)	α_{12} (^{o})	α_1 (^{o})	α_2 (^{o})	$\lvert\kappa\rvert$	$\frac{\kappa^2}{R^6}$ (10^{-6})	Relative rate
1a	3.860	0.0	87.3	87.3	0.9934	298.356	**1.00**
	5.629	0.0	71. 7	71.7	0.7038	15.572	
	5.630	0.0	71. 7	71.7	0.7038	15.555	
	6.491	0.0	72.5	72.5	0.7293	7.111	
	7.145	0.0	77.2	77.2	0.8518	5.454	
	7.465	0.0	82.1	82.1	0.9426	5.134	
	8.019	0.0	84.7	84.7	0.9747	3.573	
					Total	**350.755**	
1b	6.061	3.1	36.9	34.2	0.9869	19.648	**0.202**
	6.507	2.4	34.7	37.4	0.9614	12.177	
	7.161	3.1	60.0	61.8	0.2896	0.623	
	7.198	0.0	75.7	75.7	0.8178	4.809	
	7.355	0.0	86.9	86.1	0.9860	6.142	
	7.355	0.0	86. 9	86.1	0.9860	6.142	
	7.626	0.0	80.4	80.4	0.9165	4.271	
	7.727	5.3	28.0	22.7	1.4487	9.860	
	8.465	5.3	30.1	34.6	1.1422	3.546	
	7.812	3.1	75.1	76.2	0.8137	2.913	
	9.665	3.0	71.4	70.5	0.6796	0.567	
					Total	**70.697**	
1c	5.911	0.00	86.4	86.4	0.9882	22.895	**0.130**
	5.969	35.03	54.3	61.3	0.0222	0.011	
	5.969	35.03	61.3	54.3	0.0222	0.011	
	6.272	35.04	86.5	60.3	0.7292	8.734	
	6.272	35.03	60.3	86.5	0.7293	8.737	
	9.135	0.00	31.0	31.0	1.2025	2.489	
	9.135	0.00	31.0	31.0	1.2025	2.489	
	7.647	0.00	59.7	59.7	0.2363	0.279	
	9.563	0.00	51.3	51.3	0.1730	0.039	
					Total	**45.683**	

Table 2.7. *The relevant geometric parameters (for molecules around a reference molecule, satisfying the conditions, 2.5 < r' < 4.5 Å and r.sinα < 10 Å, and the relative rates of Dexter energy transfer in crystals of **1a**-**c**.*

Crystal	r (Å)	r' (Å)	α (°)	δ (°)	r.sinα (Å)	S	$S.e^{-r'}$	Relative rate
1a	5.630	2.825	59.9	0.0	4.871	0.5017	0.0840	**1.000**
	5.630	2.825	59.9	0.0	4.871	0.5017	0.0840	
	3.929	3.515	26.5	0.0	1.756	0.8946	0.0934	
	8.052	4.206	58.5	0.0	6.866	0.5224	0.0328	
						Total	**0.2942**	
1b	7.737	2.645	70.0	38.4	7.271	0.2681	0.0190	**0.245**
	9.547	2.861	88.3	0.0	9.107	0.2997	0.0172	
	6.132	3.263	57.9	14.0	5.192	0.5163	0.0198	
	6.451	3.920	52.6	14.0	5.122	0.5895	0.0117	
	8.425	4.538	57.4	38.4	7.099	0.4224	0.0045	
						Total	**0.0722**	
1c	5.907	4.234	44.2	66.5	4.120	0.2858	0.0042	**0.014**
						Total	**0.0042**	

distance (R) and angle (α_{12}) between the transition dipoles of the molecules, and (ii) the distance between the centroids (r), the perpendicular distance (r′) and displacement (α) / interplanar (δ) angles between the mean molecular planes that define the relative position/orientation of the fluorophores and hence the overlap of their wave functions. The functional dependence of the molecular orientation factors relevant to the two modes of energy transfer and the estimation of the relative rates are presented in Box 2.1. Values of the geometric parameters for the nearest neighbour molecules (Fig. 2.5) with potential π-overlap in the crystals of **1a**-**c** are collected in Table 2.5. Data for all molecules within a cut-off distance of a reference molecule in the crystal, noted in Box 2.1 and the relative values of energy transfer rates estimated for each crystal are provided in Tables 2.6 and 2.7.

The shorter distances and favorable orientation of molecules lead to relatively high rates of energy transfer by both modes in **1a** (Fig. 2.16). Estimates for **1b** are significantly lower for both modes, and the highly unfavorable molecular orientations

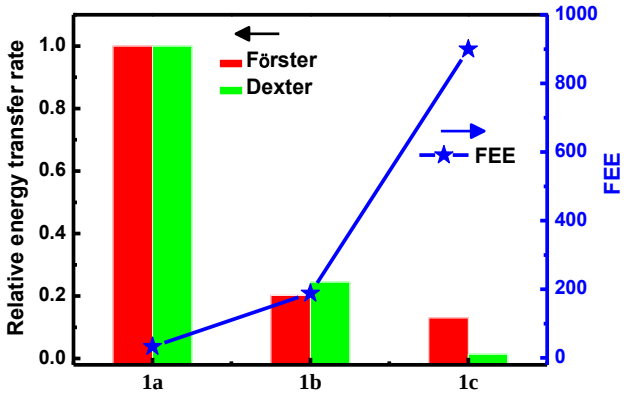

Figure 2.16. *Relative Förster and Dexter mode energy transfer rates in **1a-c** assessed based on the geometric parameters defined in Fig. 2.15.*

ensure still lower rates of energy transfer through the Dexter mode in **1c** (Fig. 2.16). Even though the intramolecular effects leading to emission enhancement are similar in **1b** and **1c** as shown earlier, the intermolecular effects lead to a clear difference in their response and a net effect of increasing fluorescence quenching from **1c** to **1a**. Concomitant impact of the excited state energy loss pathways and intermolecular energy transfer channels, thus lead to increasing FEE from **1a** to **1c**. Fig. 2.16 clearly reveals an inverse correlation between the relative intermolecular energy transfer rates and the FEE. It is important to note that, this ensues from the subtle role played by the alkyl groups on the imidazolidine framework and the consequent molecular structure and crystal packing of the fluorophore in the three solids.

2.5. Summary

1a-c provided an ideal model system wherein a simple and systematic molecular structure tuning induced significant intramolecular and intermolecular (in the crystal) effects leading to a smooth variation in the solution to solid state emission enhancement. The close correlation between the crystallographic and spectroscopic features discussed in this chapter, forms the basis of the structural tuning of the fluorescence enhancement across this family of molecules possessing the same fluorophore moiety. The role of intramolecular rotational relaxation addressed in earlier studies is shown to be important in this case as well. More significantly, it is demonstrated that the geometric effects of molecular packing that impacts upon intermolecular energy transfer are equally critical,

and need to be taken into account for a rigorous analysis of the fluorescence enhancement phenomenon. The fundamental insight gained from this study provides a deeper understanding of materials exhibiting strong light emission in the aggregated and solid states, and should aid in the design and development of new systems.

References

1. A. Qin and B. Z. Tang, *Aggregation-Induced Emission: Fundamentals and applications*, Vol. 1 and 2, (John Wiley and Sons Ltd, Chichester, 2013).
2. J. Mei, Y. Hong, J. W. Y. Lam, A. Qin, Y. Tang and B. Z. Tang, *Adv. Mater.*, 2014, **26**, 5429-5479.
3. J. Mei, N. L. C. Leung, R. T. K. Kwok, J. W. Y. Lam and B. Z. Tang, *Chem. Rev.*, 2015, **115**, 11718-11940.
4. J. W. Jia, Z. K. Wang, W. T. Lu, L. Yang, Q. W. Wu, W. Qin, Q. L. Hu and B. Z. Tang. *J. Mater. Chem. B*, 2014, **2**, 8406-8411.
5. Z. K. Wang, S. J. Chen, W. Y. Lam, W. Qin, T. K. Kwok, N. Xie, Q. L. Hu and B. Z. Tang, *J. Am. Chem. Soc.*, 2013, **135**, 8238-8245.
6. A. Patra, C. G. Gupta and T. P. Radhakrishnan, *Nanoscale*, 2012, **4**, 343-359.
7. Z. Zhao, S. Chen, X. Shen, F. Mahtab, Y. Yu, P. Lu, J. W. Y. Lam, H. S. Kwok and B. Z. Tang, *Chem. Commun.*, 2010, **46**, 686-688.
8. D. L. Dexter and J. H. Schulman, *J. Chem. Phys*., 1954, **22**, 1063-1070.
9. Y. Kawamura, J. Brooks, J. J. Brown, H. Sasabe and C. Adachi, *Phys. Rev. Lett*., 2006, **96**, 017404-1-4.
10. H. J. Oh, M. C. Gather, J. J. Song and S. H. Yun, *Opt. Express* 2014, **22**, 31411-31416.
11. a) J. Lee, N. Aizawa, M. Numata, C. Adachi and T. Yasuda, *Adv. Mater*., 2017, **29**, 1604856-1-6; b) H. S. Kim, S. R. Park and M. C. Suh, *J. Phys. Chem. C*, 2017, **121**, 13986-13997.
12. F. Bu, R. Duan, Y. Xie, Y. Yi, Q. Peng, R. Hu, A. Qin, Z. Zhao and B. Z. Tang, *Angew. Chem. Int. Ed.*, 2015, **54**, 14492-14497.

13. M. Szablewski, M. A. Fox, F. B. Dias, H. Namih, E. W. Snedden, S. M. King, D. Dai and L. Pålsson, *J. Phys. Chem. B*, 2014, **118**, 6815-6828.

14. W. R. Hertler, H. D. Hartzler, D. S. Acker and R. E. Benson, *J. Am. Chem. Soc.*, 1962, **84**, 3387-3393.

15. S. J. Lalama, K. D. Singer, A. F. Garito and K. N. Desai, *Appl. Phys. Lett.*, 1981, **39**, 940-942.

16. P. Gangopadhyay, S. Sharma, A. J. Rao, D. N. Rao, S. Cohen, I. Agranat and T. P. Radhakrishnan, *Chem. Mater.*, 1999, **11**, 466-472.

17. Y. M. Cai, S. Yamada, O. Zamani-Khamiri, A. F. Garito, K. Y. Wong, *Phys. Rev. B*, 1997, **55**, 12982-12988.

18. D. N. Rao, N. K. M. N. Srinivas, P. Gangopadhyay and T. P. Radhakrishnan, *J. Phys. Chem. A*, 2004, **108**, 5213-5219.

19. I. Paci, J. C. Johnson, X. Chen, G. Rana, D. Popovic, D. E. David, A. J. Nozik, M. A. Ratner and J. Michl, *J. Am. Chem. Soc.*, 2006, **128**, 16546-16553.

20. E. C. Greyson, B. R. Stepp, X. Chen, A. F. Schwerin, I. Paci, M. B. Smith, A. Akdag, J. C. Johnson, A. J. Nozik, J. Michl and M. A. Ratner, *J. Phys. Chem. B*, 2010, **114**, 14223-14232.

21. S. Jayanty and T. P. Radhakrishnan, *Chem. Eur. J.*, 2004, **10**, 791-797.

22. C. G. Chandaluri and T. P. Radhakrishnan, *Angew. Chem. Int. Ed.*, 2012, **51**, 11849-11852.

23. P. Srujana and T. P. Radhakrishnan, *Angew. Chem. Int. Ed.*, 2015, **54**, 7270-7274.

24. T. P. Radhakrishnan, *Acc. Chem. Res.*, 2008, **41**, 367-376.

25. M. Ravi, *Proc. Indian Acad. Sci.*, 1998, **110**, 133-141.

26. P. Gangopadhyay, M. Ravi and T. P. Radhakrishnan, *Ind. J. Chem.*, 2000, **39A**, 106-113.

27. M. J. Frisch, et.al., Gaussian 09, Revision C.01, Gaussian, Inc., Wallingford CT, 2010.

28. J. D. Gale and A. L. Rohl, The General Utility Lattice Program (GULP), *Molecular Simulation*, 2003, **29**, 291-341.

29. S. Jayanty and T. P. Radhakrishnan, *Chem. Mater.*, 2001, **13**, 2460-2462.

30. B. Valeur and M. N. Berberan-Santos, *Molecular Fluorescence: Principles and Applications*, Ed. 2 (Ch. 8), Wiley-VCH, Weinheim, Germany, 2012.

31. S. Zheng and P. Coppens, *Cryst. Growth Des.*, 2005, **5**, 2050-2059.

CHAPTER 3

Establishing the Critical Role of Specifically Oriented Aggregation in Molecular Solid State Emission Enhancement

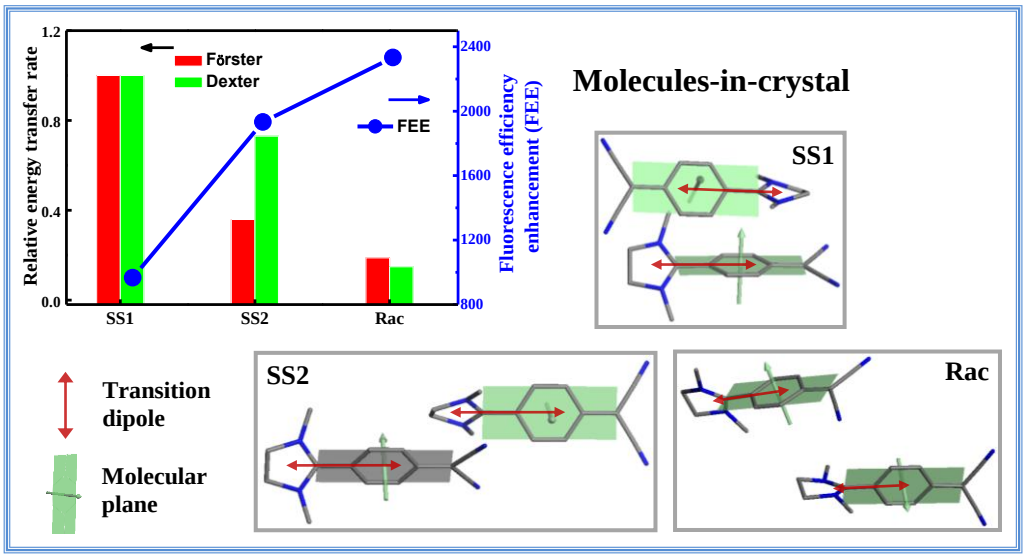

Three crystalline structures of a molecule showed varying fluorescence enhancement over the solution, depending on the molecular assembly. The critical role of specific molecular orientations and hence relative intermolecular energy transfer in affecting the fluorescence enhancement is established, demonstrating that intramolecular factors alone are insufficient to understand the phenomenon.

Scope

As has been highlighted in the earlier chapter, the enhanced fluorescence emission in molecular aggregates/solids of select classes of molecules has largely been attributed to the rigidification of the molecule and its environment that hinders non-radiative excited state energy loss through structural relaxation. In Chapter 2, it was demonstrated that subtle structural modification of a fluorophore led to systematically varying assemblies in the crystal lattice, and the fluorescence enhancement effect could be correlated to the assembly patterns. A more rigorous analysis would be possible if the same molecule formed crystals with different structures and hence molecular organizations, exhibiting significant variation in the fluorescence efficiency enhancement that could be correlated to the relative molecular orientations in the crystals. Discovery of three crystalline structures of a new push-pull molecule in its enantiomorphic and racemic forms, exhibiting not only very high, but distinctly different solid state fluorescence enhancements, allowed a systematic investigation of the role of intramolecular and intermolecular excited state energy loss pathways. Crystallographic, spectroscopic and computational investigations provide a detailed appraisal of the assembly patterns in the crystals, and led to the rigorous establishment of an inverse correlation between intermolecular energy transfer and solid state fluorescence enhancement. The study provides a clear visualization of the critical role of 'oriented molecular aggregation' in solid state fluorescence efficiency enhancement.

3.1. Introduction

The significance of enhanced fluorescence emission of molecules in aggregates or assemblies (nanoparticles, thin films, crystals), their application potential in diverse fields, and the classes of molecules exhibiting this phenomenon were discussed in detail in Sec. 1.2. Self-quenching or concentration-quenching of fluorescence accompanying aggregation and the role of Förster and Dexter energy transfer is discussed in Sec. 2.1. Several design strategies, focussing mainly on the chemical structure modification, have been proposed in the area of aggregation-induced emisssion for synthesizing efficient materials and understanding the structure-property relationship; the critical role of molecular assembly has not been explored in such detail.[1] Our study on the three closely related DADQ derivatives presented in Chapter 2 revealed the correlation between molecular assembly, energy transfer rates and fluorescence enhancement effects.[2] It would be highly instructive to identify a single molecule that forms different crystalline structures exhibiting distinctly different fluorescence efficiency enhancement

(FEE), with intramolecular relaxations hindered to a similar extent, but intermolecular energy transfer possibilities varying prominently; a quantitative appraisal of such systems would be a clinching test of the impact of molecular assembly on the fluorescence response.

We have explored three crystalline structures of a new DADQ derivative, 7,7-(*N*,*N*′-dimethylcyclohexane-1,2-diamino)-8,8-dicyanoquinodimethane (DCDADQ); two polymorphs of the (*S*,*S*) enantiomer (DCDADQ-**SS1**, DCDADQ-**SS2**) and the crystal of the racemate (DCDADQ-**Rac**). These crystals built up of the same molecule or its enantiomer show not only very large, but dramatically different fluorescence emission intensities and hence FEE, allowing the critical role of molecular organization to be probed. Following the methodology developed in our earlier study (Chapter 2), we have analyzed the influence of intramolecular excited state relaxation and intermolecular energy transfer in the three crystals. Computational optimization of the excited state geometry of DCDADQ, and lattice energy calculations show that the intramolecular effects are similar in all the three crystals. Analysis of the crystal structures and the relative intermolecular energy transfer (Förster and Dexter) rates controlled by the molecular assembly patterns, reveal that this is the dominant factor that determines the large fluorescence efficiency variation; the non-radiative excited state decay rate constants estimated from lifetime measurements show consistent trends. This study thus unequivocally establishes the critical role of oriented aggregation in inducing the solid state fluorescence enhancement.

3.2. Synthesis and Structural Analysis

3.2.1 *Synthesis and characterization*

DCDADQ was synthesized following the strategy developed in the previous chapter. (*S*,*S*), (*R*,*R*) and racemic *N*,*N*′-dimethylcyclohexane-1,2-diamine prepared from the respective cyclohexane-1,2-diamines,[3] were reacted with PTCNQ to yield DCDADQ (Scheme 3.1); the new compounds were recrystallized from acetonitrile. All the compounds were characterized using NMR, IR and high resolution mass spectroscopies, as well as single crystal structure analysis.

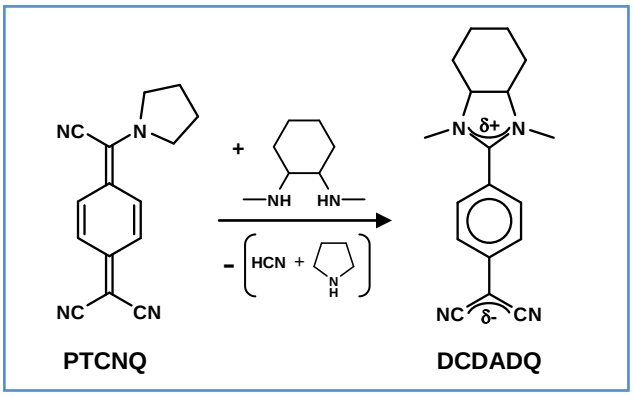

Scheme 3.1. *General scheme for the synthesis of 7,7-(N,N′-dimethylcyclohexane-1,2-diamino)-8,8-dicyanoquinodimethane (DCDADQ).*

7,7-(*N*,*N*′-dimethyl-(*S*,*S*)-cyclohexane-1,2-diamino)-8,8-dicyanoquinodimethane (DCDADQ-SS):

(*S*,*S*)-(+)-*N*,*N*′-dimethylcyclohexane-1,2-diamine (1.21 mmol) was added to a warm solution of 7-pyrrolidino-7,8,8-tricyanoquinodimethane, PTCNQ (0.81 mmol) in 25 ml acetonitrile (synthesis of PTCNQ is described in Sec. 2.2.1). The solution turned dark green immediately and then to yellow within 60 min (caution: small amount of HCN gas is formed as the byproduct of the reaction). It was stirred for 4 h at 65°C, cooled to room temperature and then at 4°C. The microcrystalline solid precipitated over three days was filtered, washed with acetonitrile and dried to give a greenish yellow compound (0.16 g, 71% yield). The compound was purified by multiple crystallizations from acetonitrile. Similar procedure was followed for (*R*,*R*) and racemic derivatives as well.

DCDADQ-**SS**: mp: 345°C (dec.); FTIR (KBr) - $\bar{\upsilon}$/cm^{-1}: 3466.0 (broad, O−H stretch), 2946.2 (methyl C−H stretch), 2174.2 and 2138.9 (asymmetric C≡N stretch), 1595.4 and 1555.0 (aromatic C=C stretch); NMR (500 MHz, DMSO-d_6) - δ/ppm ^{1}H: 7.25-7.23 (d, 2H), 6.90-6.88 (d, 2H), 3.39-3.37 (m, 2H), 2.98 (s, 6H), 2.29-2.27 (d, 2H), 1.90-1.88 (d, 2H), 1.49-1.46 (m, 2H), 1.37-1.33 (t, 2H) ^{13}C: 170.14, 148.66, 130.06, 123.84, 117.93, 108.19, 67.83, 33.66, 33.47, 27.59, 24.06; HRMS (ESI) - *m/z*: 293.1762 (calculated for $C_{18}H_{20}N_4$ [M^++H]: 293.1766), Specific rotation $[a]_D^{25} = +115°$ (c = 0.063 g/100 ml, CH_3CN). The optical rotation ($[a]_D^{25}$) establishes the chiral nature of the compound; the circular dichroism spectra of the two enantiomers is shown in Fig. 3.1.

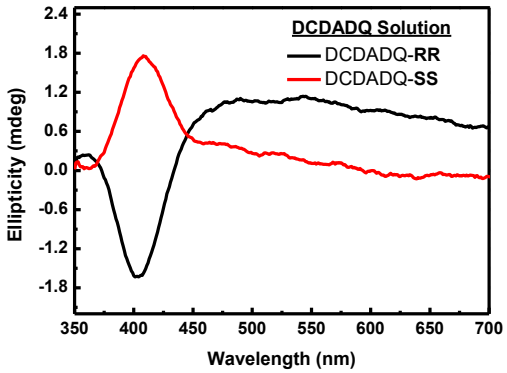

Figure 3.1. *Circular dichroism spectrum of **S,S** and **R,R** enantiomers of DCDADQ (acetonitrile solution).*

7,7-(*N*,*N*′-dimethyl-(±)-cyclohexane-1,2-diamino)-8,8-dicyanoquinodimethane (DCDADQ-**Rac**): mp: 345°C (dec.); FTIR (KBr) - $\bar{\upsilon}$/cm^{-1}: 2944.5 (methyl C−H stretch), 2169.5 and 2133.2 (asymmetric C≡N stretch), 1600.7 and 1492.6 (aromatic C=C stretch); NMR (500 MHz, DMSO-d_6) - δ/ppm ^{1}H: 7.25-7.23 (d, 2H), 6.90-6.88 (d, 2H), 3.39-3.38 (m, 2H), 2.98 (s, 6H), 2.29-2.27 (d, 2H), 1.90-1.88 (d, 2H), 1.49-1.45 (m, 2H), 1.37-1.33 (t, 2H) ^{13}C: 170.14, 148.66, 130.06, 123.84, 117.93, 108.18, 67.83, 33.66, 33.47, 27.59, 24.06; HRMS (ESI)-*m/z*: 293.1767 (calculated for $C_{18}H_{20}N_4$ [M^++H]: 293.1766). Optical rotation was verified to be zero.

3.2.2 *Crystallographic investigations*

Crystals of DCDADQ were grown from acetonitrile solution by cooling or evaporation. Concentrated solution of DCDADQ-**SS** in acetonitrile was kept for slow evaporation at 30°C. Rhombus-shaped crystals started forming within few hours and were filtered out immediately; they are designated as DCDADQ-**SS2**. The filtrate, on standing for two days showed the formation of needle-shaped crystals; these are designated as DCDADQ-**SS1**. Exploration of different solvents for crystallization did not yield any additional crystal structures or co-crystals. The (*R*,*R*) crystals showed identical structures and fluorescence responses as the (*S*,*S*) and are not discussed further. Solution of the racemate compound produced only a single crystal form, DCDADQ-**Rac**.

The molecular structures and the crystal packing in the three crystals are shown

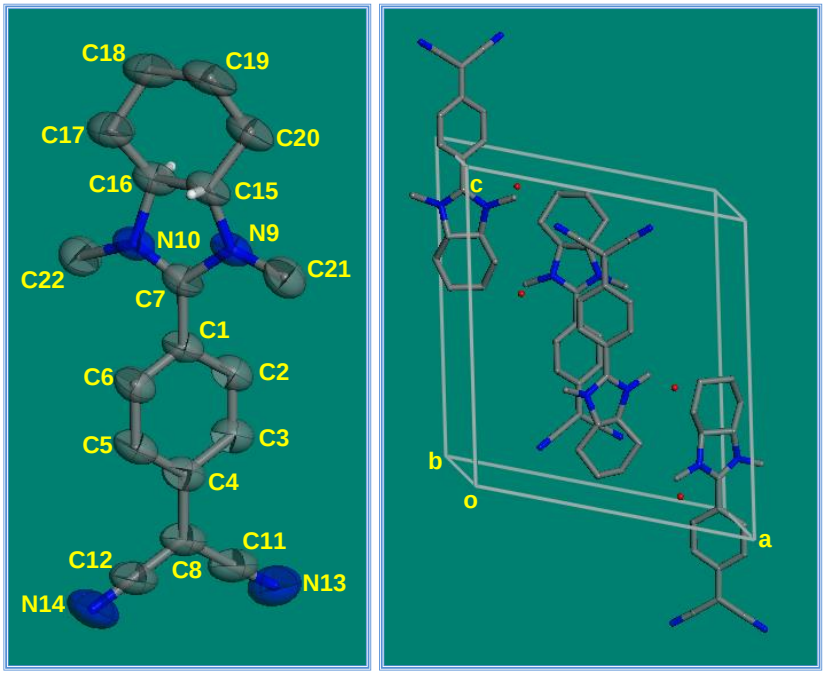

Figure 3.2. *Molecular structure showing 99% thermal ellipsoids and the unit cell of DCDADQ-**SS1**; all H atoms are omitted for clarity.*

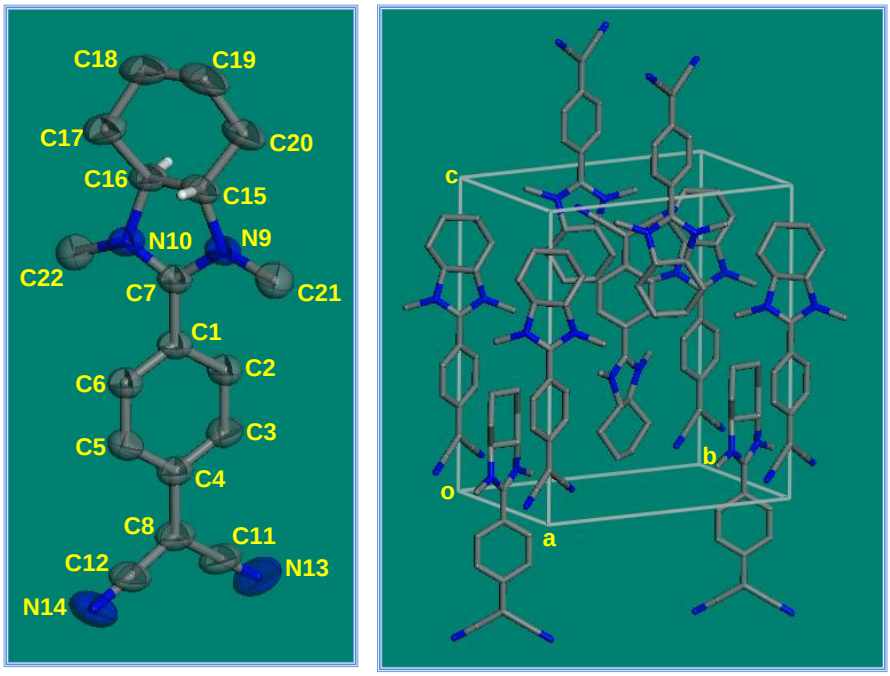

Figure 3.3. *Molecular structure showing 99% thermal ellipsoids and the unit cell of DCDADQ-**SS2**; all H atoms are omitted for clarity.*

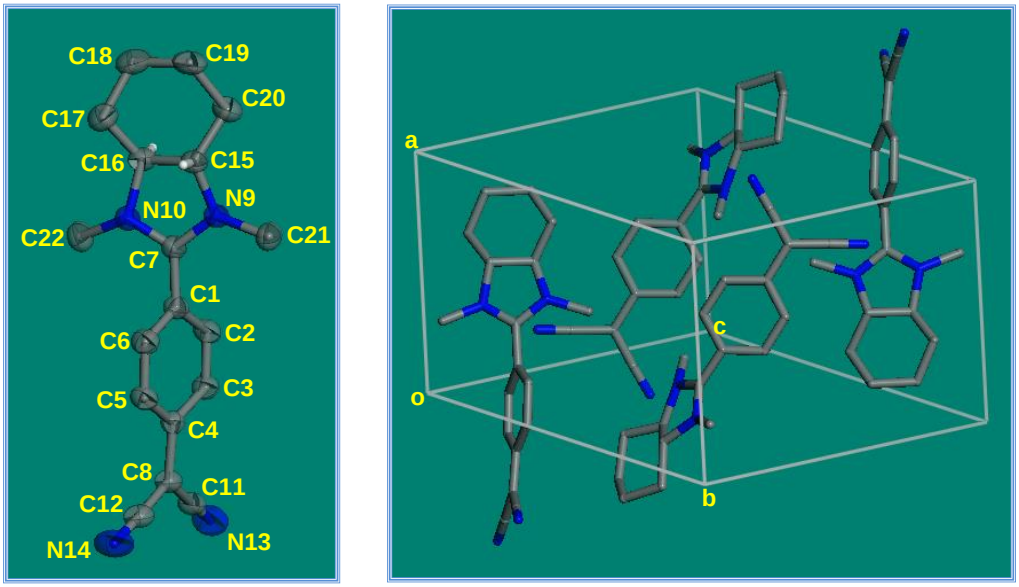

Figure 3.4. *Molecular structure showing 99% thermal ellipsoids and the unit cell of DCDADQ-**Rac**; all H atoms are omitted for clarity.*

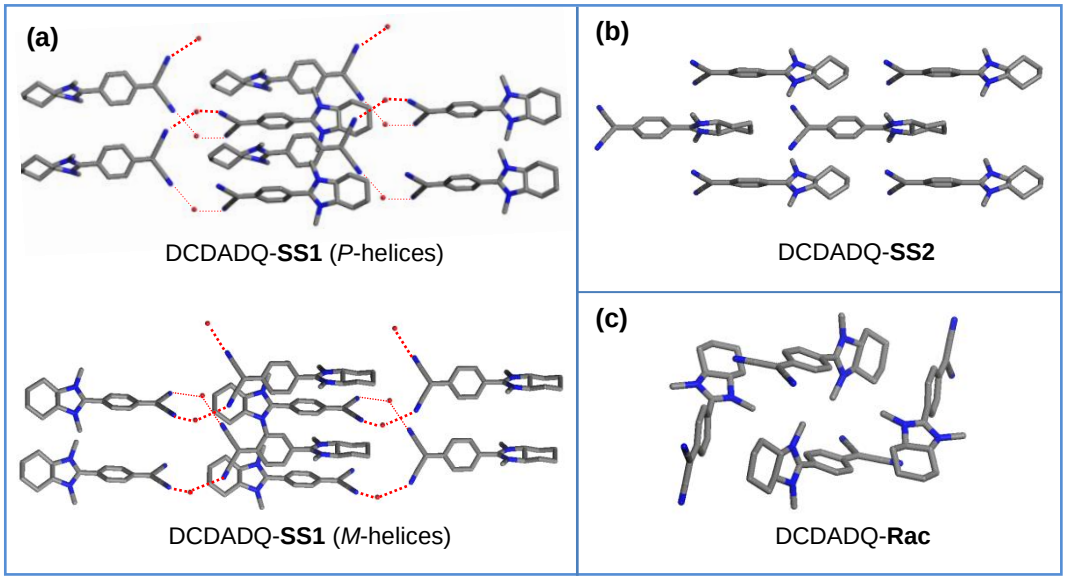

Figure 3.5. *Molecular assembly of DCDADQ in the crystals of **(a)** DCDADQ-**SS1**, **(b)** DCDADQ-**SS2** and **(c)** DCDADQ-**Rac**. In DCDADQ-**SS1**, the interdigitated H-bonded supramolecular helices (P and M-helices) are shown; H-bonds are indicated by red dotted lines and all H atoms are omitted for clarity.*

Table 3.1. *Crystallographic details of DCDADQ-**SS1**, DCDADQ-**SS2** and DCDADQ-**Rac**.*

Molecule	DCDADQ-**SS1**	DCDADQ-**SS2**	DCDADQ-**Rac**
Empirical formula	$C_{18}H_{20}N_4O_{0.42}$	$C_{18}H_{20}N_4$	$C_{18}H_{20}N_4$
Crystal system	Monoclinic	Orthorhombic	Monoclinic
Space group	$P2_1$	$P2_12_12$	$P2_1/n$
a / Å	13.3410(4)	8.48550(10)	9.0191(4)
b / Å	8.5991(2)	12.70650(10)	12.0864(4)
c / Å	14.9580(4)	14.7264(2)	14.9871(6)
α / deg.	90	90	90
β / deg.	104.063(2)	90	104.040(2)
γ /deg.	90	90	90
V / Å^3	1664.56(8)	1587.81(3)	1584.92(11)
Z	4	4	4
$\rho_{calc.}$ / g cm^{-3}	1.193	1.223	1.225
μ / cm^{-1}	0.588	0.585	0.075
Temperature / K	293(2)	293(2)	293(2)
λ / Å	1.54184	1.54184	0.71073
No. of reflections	5680	3142	2788
No. of parameters	434	212	210
Max., Min. transmission	0.902, 1.000	0.674, 1.000	0.646, 0.745
GOF	1.142	1.121	1.185
R [for $I \geq 2\sigma_I$]	0.0505	0.0478	0.0555
wR^2	0.145	0.153	0.1812
Largest difference peak and hole / eÅ^{-3}	0.170, 0.207	0.215, 0.291	0.285, 0.223
CCDC deposition number	1576145	1576144	1576146

in Figs. 3.2-3.4, and the significant crystallographic information are collected in Table 3.1. DCDADQ molecule has very similar structure in all the crystals; differences in the average dihedral twist angle θ, between the diaminomethylene and the aromatic ring planes are small, and the dicyanomethylene group is nearly coplanar with the aromatic ring, with the dihedral angles φ ~ 1-12° (Table 3.2). DCDADQ-**SS1** crystal contains ~ 0.4 water molecule per DCDADQ; the water possibly arises from the trace moisture in acetonitrile that is difficult to remove. The water molecule forms H-bonds with the cyano N atoms to form supramolecular helical motifs along the *b*-axis (Fig. 3.5a). While one of the molecules in the asymmetric unit forms the *P*-helices, the other forms *M*-helices; interdigitation of adjacent helices brings the π-conjugated fluorophore

moieties very close. DCDADQ-**SS2** has no water molecule in the crystal lattice and no intermolecular H-bonds; the DADQ fluorophores are farther apart, as the non-conjugated cyclohexane moiety comes in close proximity to the π-conjugated part of the neighboring molecule (Fig. 3.5b). Fig. 3.5c shows the assembly of two sets of enantiomer pair in DCDADQ-**Rac**; the fluorophore moieties are either in nearly orthogonal orientation or far apart and slipped significantly with respect to each other. It is seen clearly that the relative orientation of the fluorophores evolves across the series.

3.3. Spectroscopic Studies

The electronic absorption spectra of acetonitrile solution of DCDADQ and the microcrystalline solids of DCDADQ-**SS1,** DCDADQ-**SS2** and DCDADQ-**Rac** are collected in Fig. 3.6a. The absorption with λ_{max} ~ 380 nm is due to the intramolecular charge transfer, characteristic of the zwitterionic DADQs;[4] the small blue shift in the case of DCDADQ-**Rac** could be attributed to the slightly higher torsion angle in the molecular geometry.[2] The fluorescence emission spectra are collected in Fig. 3.6b. Emission from the solution is very weak with a λ_{max} ~ 500 nm, whereas the solids show enormous enhancement and a small blue shift with respect to the solution (Table 3.2); the shift results from the local field due to the neighboring dipolar molecules in the crystal lattice.[5] Fluorescence excitation spectra of the solids show peaks consistent with

Table 3.2. *Basic molecular structural data (θ and φ, the average intramolecular torsion angles of diaminomethylene and dicyanomethylene moiety respectively; in the cases where two similar molecules are present in the asymmetric unit, only one is considered), and the solid state absorption, fluorescence data [wavelength maxima (λ_{max})], absolute quantum yield (Φ) and fluorescence efficiency enhancement (FEE) based on Φ as well as the emission spectral intensity (I) of the three DCDADQ crystals (Φ_{soln} = 0.03%).*

DCDADQ	Torsion angle		Optical data				
	θ (°)	φ (°)	λ_{max}^{abs} (nm)	λ_{max}^{em} (nm)	Φ (%)	FEE based on I	FEE based on Φ
SS1	51.8	0.8	383	476	29	933	967
SS2	48.3	11.6	383	474	58	1723	1933
Rac	63.7	6.4	367	465	70	1925	2333

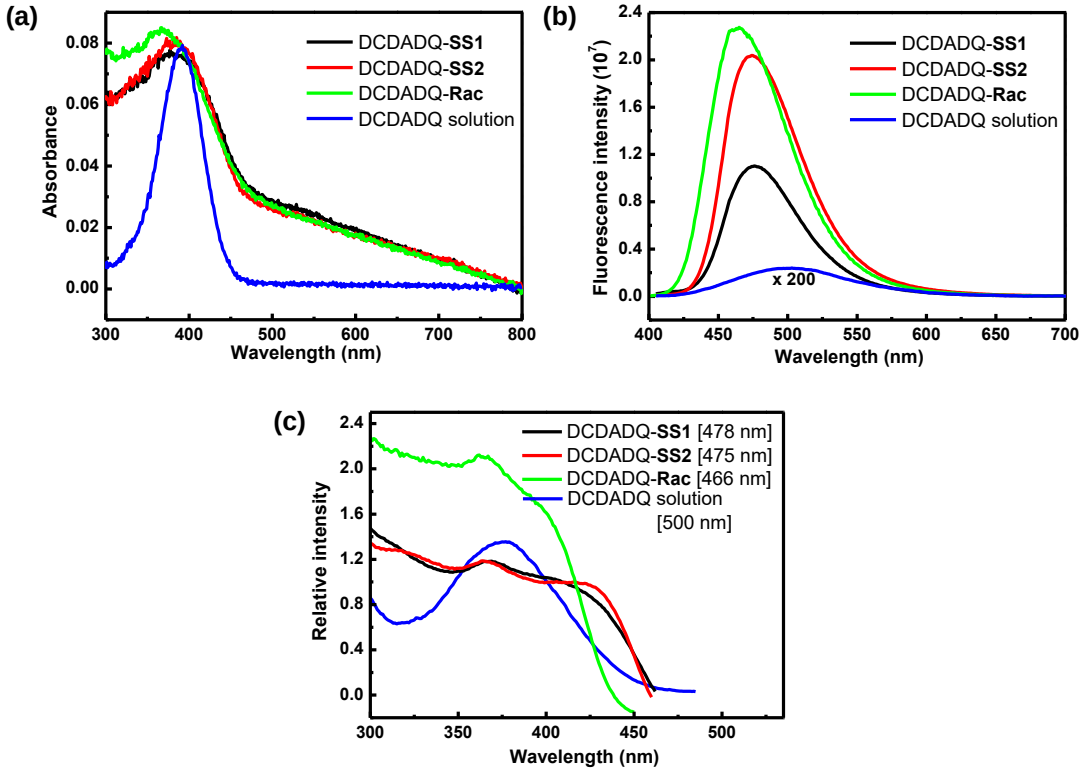

Figure 3.6. ***(a)*** *Electronic absorption,* ***(b)*** *fluorescence emission (λ_{exc} = 390 nm) and* ***(c)*** *fluorescence excitation spectra of DCDADQ (acetonitrile solution) and the microcrystalline solids DCDADQ-**SS1**, DCDADQ-**SS2** and DCDADQ-**Rac**. The spectra in (b) are recorded on samples with similar optical density at the excitation wavelength, and the solution spectrum is magnified by a factor of 200. In (c) the emission wavelength at which each excitation spectrum is recorded is indicated.*

solution (Fig. 3.6c) suggesting that the emitting state is the same as the one in solution. Emission intensities of the solid samples with matched optical density (adjusted to be equal to that of the solution) show large enhancements of ~ 900-1900, with a clear variation across the crystals DCDADQ-**SS1**, DCDADQ-**SS2** and DCDADQ-**Rac** (Table 3.2); since the solution reference is the same, these numbers reflect the relative solid state fluorescence intensities. FEE estimated based on the emission quantum yields of solids (~ 30-70 %) with respect to that of the solution (~ 0.03 %), follows the same trend. The distinct variation allows a systematic analysis of the relevance of molecular orientation in the different crystalline manifestations of the molecule.

3.4. Analysis of the Intramolecular Effects

The analysis follows closely, the methodologies adopted in Sec. 2.4. Earlier computational and spectroscopic studies have shown that DADQ molecules undergo significant structural changes in the excited state,[2,6] the most prominent being the opening of the dihedral angle θ and/or φ to ~ 90°; this was demonstrated in the case of the molecules discussed in Chapter 2 as well. We have carried out full geometry optimization of the DCDADQ molecule to model the electronic ground state geometry in acetonitrile solution; the optimized geometry was confirmed to be the energy minima by vibrational frequency calculation (Appendix C). θ and φ are found to be 49.4° and 0.1° respectively in the optimized structure obtained with a B3LYP/6-31G* computation (Fig. 3.7a).[7] This not only provides a model for the molecular structure in solution, but also of the molecule-in-the-crystal (Table 3.2); as pointed out in Sec. 2.4.1 the acetonitrile medium imposed in the computation mimics the dielectric environment in the crystal.[8]

Electronic excitation with the highest oscillator strength (*f*) computed using the TD-DFT method at 409.3 nm [f = 0.874 ($S_0 \rightarrow S_1$)] is in good agreement with the experiment on the acetonitrile solution; the corresponding values computed using the

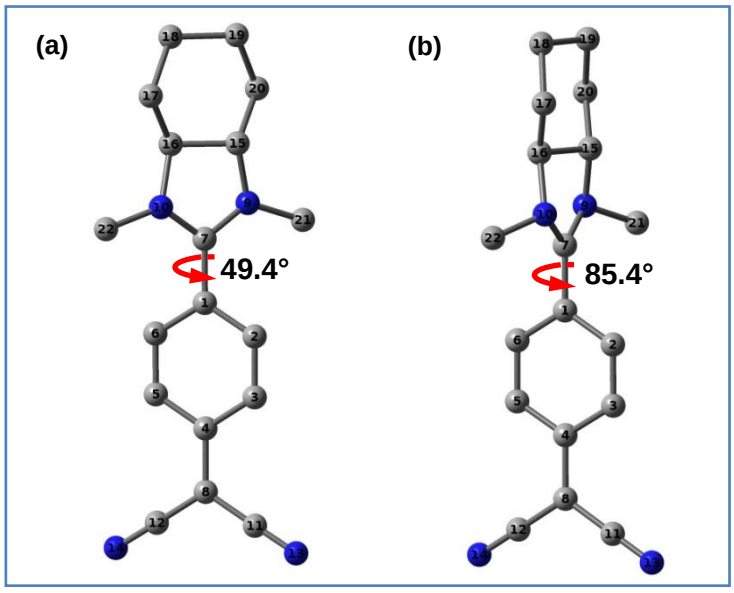

Figure 3.7. *Fully optimized [B3LYP/6-31G*; SCRF (acetonitrile); TD-DFT for excited state optimization]* ***(a)*** *ground state and* ***(b)*** *excited state geometry of the DCDADQ molecule; H atoms are omitted for clarity.*

molecular geometry from the three crystal structures, DCDADQ-**SS1**, DCDADQ-**SS2**,and DCDADQ-**Rac** are 383.2, 381.8 and 387.1 nm respectively, close to the observed λ_{max}^{abs} values (Table 3.2). Full optimization of the molecular geometry in the excited state showed θ increasing to 85.4° while the φ remains nearly zero (Fig. 3.7b). Interestingly, this structure shows no transition with any appreciable oscillator strength indicating that the relaxed excited state has no visible emission [the computed lowest energy state is at 746.8 nm, f = 0.002 ($S_1 \rightarrow S_0$)]; this is consistent with the very weak fluorescence of the solution. In the crystalline solid, such a large dihedral twist of the bulky diaminomethylene moiety is highly unlikely. In order to explore the effect of θ twist, lattice energy profiles were calculated for each of the three crystals using a cluster of ~ 60 molecules excised from their lattice, varying only the θ of the central molecule in steps, from its initial value. In each case, the energy increases forbiddingly (Fig. 3.8), implying clearly that such molecular structural relaxations are impossible in the crystalline lattice. This conclusion is supported by the emission spectra of the

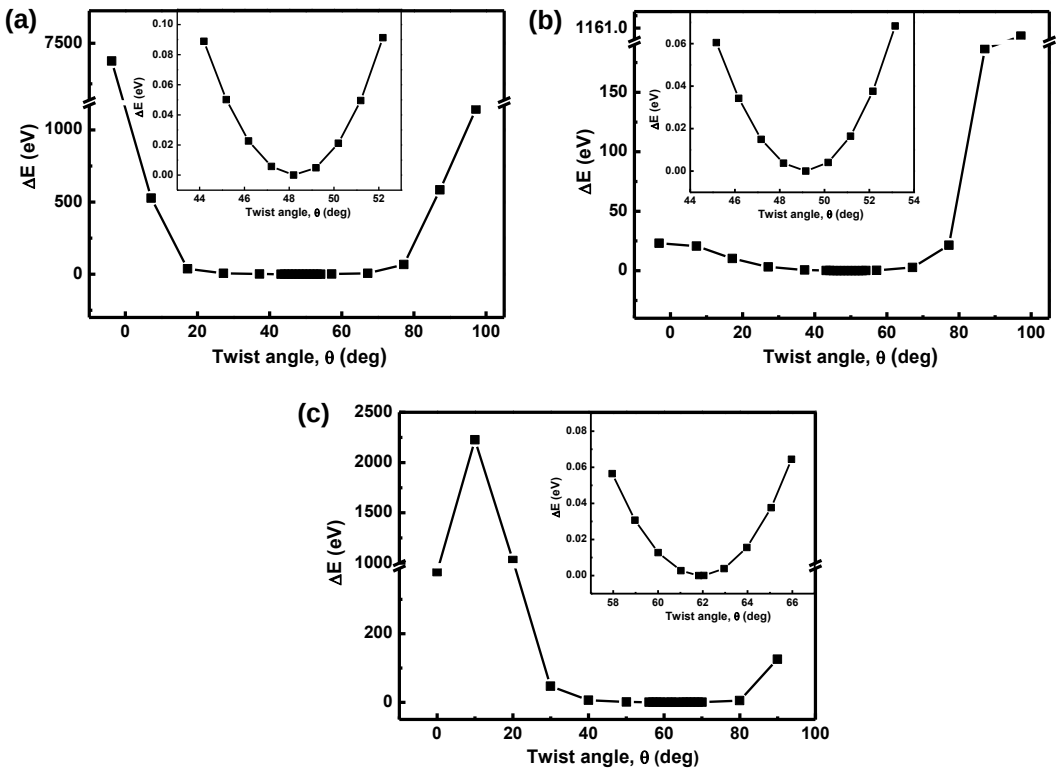

Figure 3.8. *Variation of the lattice energy as a function of the twist angle θ of the chosen central molecule in the cluster of* ***(a)*** *DCDADQ-**SS1**,* ***(b)*** *DCDADQ-**SS2** and* ***(c)*** *DCDADQ-**Rac**; magnified view of the plot close to the minimum is also shown.*

microcrystalline solids; the λ_{max}^{em} is very similar in all the crystals (except for a small blue shift in DCDADQ-**Rac** similar to that observed in the absorption spectra), and the Stokes shifts of 90-100 nm, typical of vibrational relaxation effects, point to the absence of any significant structural changes in the excited state. As the molecular structure is conserved in a similar manner during electronic excitation in all the three crystals, a consequence of the crystals being made up of the same molecule or its enantiomer, any intramolecular contribution to the fluorescence response must be similar too. It follows logically that, the distinctly different fluorescence enhancements observed in the three crystals must result primarily from intermolecular effects.

3.5. Analysis of the Intermolecular Effects

We have analyzed the effects of intermolecular energy transfer following the general methodology developed in Sec. 2.4.2. As noted, energy transfer can be dipole-induced (Förster mode) or exchange-induced (Dexter mode); both are sensitively

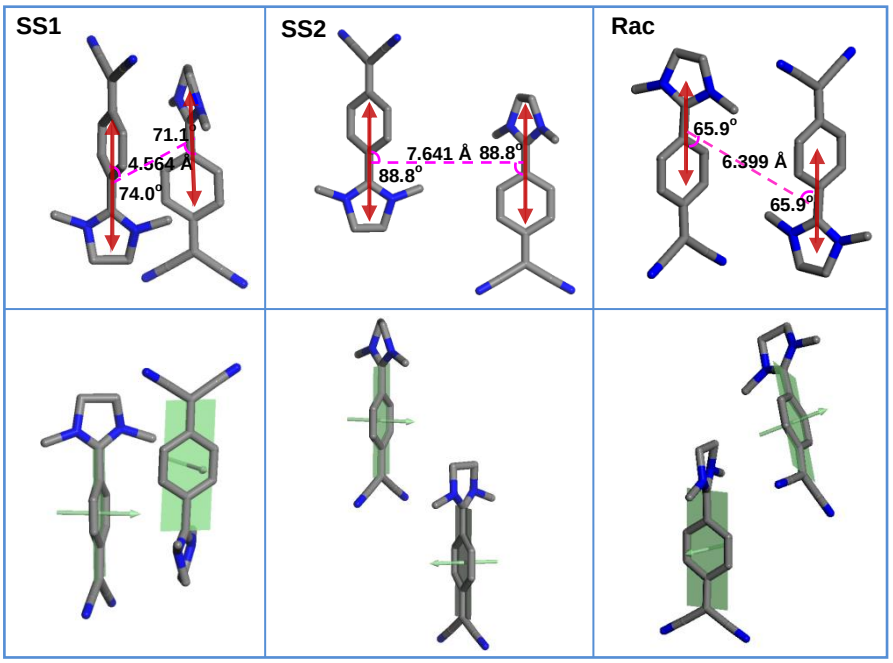

Figure 3.9. *Orientation of selected neighboring molecules in the crystals of DCDADQ-**SS1** (**SS1**), DCDADQ-**SS2** (**SS2**) and DCDADQ-**Rac** (**Rac**) with the dominant transition dipoles (double-headed arrow) and some of the relevant geometric parameters (top row) and the mean planes of the fluorophore moieties and their normals (bottom row) indicated schematically. The cyclohexane ring and H atoms are omitted for clarity.*

dependent on the molecular organization, the orientation of transition dipoles and the molecular planes. As the spectral overlaps are similar in the three crystals (Fig. 3.6), the rates are primarily controlled by the molecular assembly patterns.

Relative orientation of the transition dipoles and mean planes (of the fluorophore moiety defined as in Sec. 2.4.2) of selected pair of neighboring molecules in the three crystals are shown in Fig. 3.9. The nearly parallel and close transition dipoles in DCDADQ-**SS1** (Fig. 3.9, top row) favors efficient Förster energy transfer. The enhanced separation in DCDADQ-**SS2** and DCDADQ-**Rac** leads to the decrease in the energy transfer rate (Table 3.3); the reduced slip in the former leads to the observed overall trend. The increasing separation between the molecular planes across the series and the significantly higher interplanar angle in DCDADQ-**Rac** can be seen in Fig. 3.9 (bottom row); these structural factors lead to decreasing Dexter energy transfer rates across the series (Table 3.3). The relative energy transfer rates by both modes, estimated by considering all neighbors within reasonable cut-off distances are listed in Tables 3.4 and 3.5; the total values plotted in Fig. 3.10 reveal clearly the trend among the three crystals and the inverse correlation with the FEE observed. The direct implication is that the fluorescence quenching through intermolecular effects decreases

Table 3.3. *Geometric parameters related to selected neighboring molecules that control the Förster [distance (R) and angles ($\alpha_{12}, \alpha_1, \alpha_2$) between transition dipoles] and Dexter [distance (r') and angles (α, δ) between the molecular planes] modes of energy transfer in DCDADQ-**SS1**, DCDADQ-**SS2** and DCDADQ-**Rac** crystals; the net contribution to the energy transfer rate, k_{ET} is also shown. (Detailed description of the models and relevant equations for estimating the relative energy transfer rate are provided in Box 2.1).*

DCDADQ	**Förster mode**				
	R (Å)	**α_{12} (^{o})**	**α_1 (^{o})**	**α_2 (^{o})**	**$\frac{\kappa^2}{R^6}[\propto k_{ET}]$ (10^{-6})**
SS1	4.564	2.9	74.0	71.1	59.11
SS2	7.641	0.0	88.8	88.8	5.01
Rac	6.399	0.8	65.9	65.9	3.64
DCDADQ	**Dexter mode**				
	r' (Å)	**α (^{o})**	**δ (^{o})**	**$S.e^{-r'}[\propto k_{ET}]$**	
SS1	3.540	44.7	51.2	0.0129	
SS2	3.936	62.3	41.2	0.0069	
Rac	5.071	49.2	73.4	0.0012	

Table 3.4. *The relevant geometric parameters [for molecules within a distance (R) of 10 Å from a reference molecule] and the relative rates of Förster energy transfer in crystals of DCDADQ-**SS1**, DCDADQ-**SS2** and DCDADQ-**Rac**. (Detailed description of the models and relevant equations for estimating the relative energy transfer rate are provided in Box 2.1).*

Crystal	R (Å)	α_{12} (°)	α_1 (°)	α_2 (°)	|κ|	$\frac{\kappa^2}{R^6}$ (10^{-6})	Relative rate
SS1	4.564	2.9	74.0	71.1	0.7309	59.11	1.00
	4.564	2.9	71.1	74.0	0.7309	59.11	
	8.599	0.3	88.6	88.6	0.9981	2.46	
	8.599	0.0	88.6	88.6	0.9981	2.46	
	8.705	4.1	47.3	46.7	0.3973	0.36	
	8.758	4.1	47.8	47.0	0.3762	0.31	
	9.406	1.4	62.0	62.0	0.3381	0.17	
	9.602	1.4	61.2	59.9	0.2749	0.10	
					Total	**124.08**	
SS2	7.641	0.0	88.8	88.8	0.9987	5.01	0.359
	7.641	0.0	88.8	88.8	0.9987	5.01	
	7.641	0.0	88.8	88.8	0.9987	5.01	
	7.641	0.0	88.8	88.8	0.9987	5.01	
	8.477	0.0	30.0	30.0	1.2484	4.20	
	8.477	0.0	30.0	30.0	1.2484	4.20	
	8.486	0.0	90.0	90.0	1.0000	2.68	
	8.486	0.0	90.0	90.0	1.0000	2.68	
	8.520	0.0	29.9	29.9	1.2560	4.12	
	8.520	0.0	29.9	29.9	1.2560	4.12	
	9.589	0.0	41.5	41.5	0.6830	0.60	
	9.589	0.0	41.5	41.5	0.6830	0.60	
	9.863	0.0	40.1	40.1	0.7553	0.62	
	9.863	0.0	40.1	40.1	0.7553	0.62	
					Total	**44.48**	
Rac	6.399	0.8	65.9	65.9	0.5002	3.64	0.188
	6.851	38.4	87.7	57.6	0.7204	5.02	
	6.851	38.4	57.6	87.7	0.7203	5.02	
	7.952	38.4	37.8	49.8	0.7455	2.20	
	7.952	38.4	49.8	37.8	0.7456	2.20	
	8.766	0.8	57.5	57.5	0.1350	0.04	
	9.019	0.8	35.8	35.8	0.9755	1.77	
	9.019	0.8	35.8	35.8	0.9755	1.77	
	9.156	0.8	44.3	44.3	0.5393	0.49	
	9.800	38.4	84.0	77.1	0.7133	0.57	
	9.800	38.4	77.1	84.0	0.7134	0.58	
					Total	**23.30**	

Table 3.5. *The relevant geometric parameters (for molecules around a reference molecule, satisfying the conditions, r' > 2.5 Å and r.sinα < 10 Å, and the relative rates of Dexter energy transfer in crystals of DCDADQ-**SS1,** DCDADQ-**SS2** and DCDADQ-**Rac**. (Detailed description of the models and relevant equations for estimating the relative energy transfer rate are provided in Box 2.1).*

Crystal	r (Å)	r' (Å)	α (°)	δ (°)	r.sin α (Å)	S	$S.e^{-r'}$	Relative rate
SS1	4.98	3.540	44.7	51.2	3.503	0.4458	0.0129	1.000
	4.98	4.217	32.1	51.2	2.649	0.5311	0.0078	
	8.15	6.758	34.0	1.0	4.556	0.8290	0.0010	
	8.599	7.756	25.6	0.0	3.712	0.9020	0.0004	
	8.599	7.756	25.6	0.0	3.712	0.9020	0.0004	
	8.677	2.574	72.7	50.4	8.286	0.1892	0.0144	
	8.795	3.296	68.0	50.4	8.154	0.2391	0.0089	
	10.591	6.496	52.2	1.0	8.365	0.6132	0.0009	
						Total	**0.0467**	
SS2	8.453	3.936	62.3	41.2	7.481	0.3505	0.0069	0.730
	8.453	3.936	62.3	41.2	7.481	0.3505	0.0069	
	8.486	7.871	22.0	0.0	3.172	0.9275	0.0004	
	8.544	3.936	62.6	41.2	7.584	0.3468	0.0068	
	8.544	3.936	62.6	41.2	7.584	0.3468	0.0068	
	8.582	6.312	42.7	43.9	5.816	0.5298	0.0010	
	8.582	6.312	42.7	43.9	5.816	0.5298	0.0010	
	11.133	5.496	60.4	2.7	9.682	0.4931	0.0020	
	11.133	10.246	23.0	2.7	4.356	0.9192	0.0000	
	11.133	10.246	23.0	2.7	4.356	0.9192	0.0003	
	11.133	5.496	60.4	2.7	9.682	0.4931	0.0020	
						Total	**0.0341**	
Rac	6.271	5.404	30.5	2.6	3.182	0.8608	0.0039	0.148
	7.757	5.071	49.2	73.4	5.870	0.1872	0.0012	
	7.757	5.387	46.0	73.4	5.582	0.1988	0.0010	
	8.402	6.882	35.0	73.4	4.820	0.2345	0.0002	
	9.641	6.948	43.9	73.4	6.684	0.2063	0.0002	
	9.641	6.632	46.5	73.4	6.998	0.1970	0.0003	
	9.713	8.445	29.6	73.4	4.799	0.2489	0.0001	
						Total	**0.0069**	

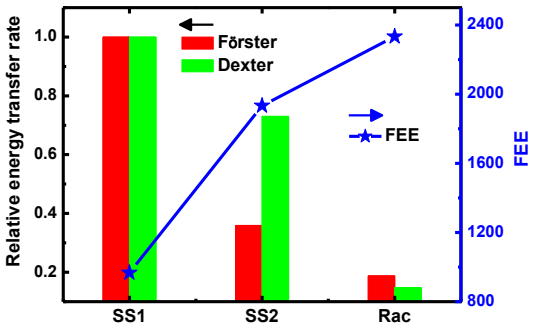

Figure 3.10. *Relative Förster and Dexter mode energy transfer rates in DCDADQ-**SS1**, DCDADQ-**SS2** and DCDADQ-**Rac** assessed based on the geometric parameters; plot of the FEE values for the three crystals based on the quantum yield values is also shown.*

along the series from DCDADQ-**SS1** to DCDADQ-**SS2** to DCDADQ-**Rac**, providing an unambiguous rationale for the increasing FEE. These observations with crystals of the same molecule or derivative closely parallel the case of the crystals of three closely related derivatives presented in Chapter 2.

3.6. Fluorescence Lifetime Studies

Fluorescence lifetime imaging microscopy (FLIM) of the three microcrystalline solids, DCDADQ-**SS1**, DCDADQ-**SS2** and DCDADQ-**Rac** were carried out using a time-resolved confocal fluorescence microscope (MicroTime 200, PicoQuant) coupled to an Olympus IX71 microscope (PicoQuant). Excitation was carried out using a 405 nm pulsed-laser diode and the fluorescence observed through a 430 nm long-pass filter; the corresponding full-width half maximum of pulse response function was 176 ps. Data acquisition was performed with a PicoHarp 300 TCSPC module using PicoHarp300 version 2.3 in a time-tagged time-resolved mode. Samples were prepared in the form of KBr pellet. The decay profiles and the representative images are shown in Fig. 3.11; homogeneity in the optical response can be seen from the images. Excited state lifetimes of the three materials are close to each other; average lifetime for each, determined from measurements on five different images of area 80 × 80 μm^2 are found to be 2.32 (standard deviation, $\sigma = 0.12$), 2.44 ($\sigma = 0.21$) and 2.24 ($\sigma = 0.05$) ns for DCDADQ-**SS1**, DCDADQ-**SS2** and DCDADQ-**Rac** respectively. The fluorescence decay of DCDADQ solution is too fast to measure within the resolution of the setup.

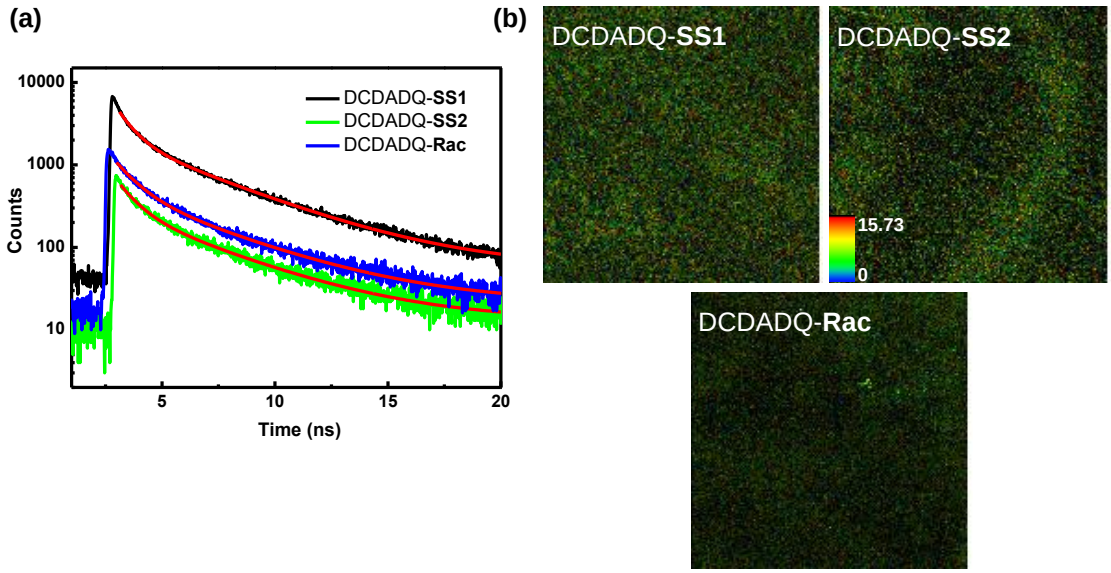

Figure 3.11. ***(a)*** *Fluorescence decay profiles, and* ***(b)*** *FLIM images of the three crystalline solids (the common scale bar is shown in the second image).*

Using the respective emission quantum yield values (Table 3.2) and the average lifetimes, the radiative and non-radiative decay rate constants were estimated (Fig. 3.12); the increasing and decreasing rates of the radiative and non-radiative decay resectively are consistent with the trend discussed and the conclusions drawn based on structural considerations. The non-radiative decay occurs through multiple channels including the Förster and Dexter intermolecular energy transfer. If we assume that the difference between the three crystalline solids arise only through the latter modes, the

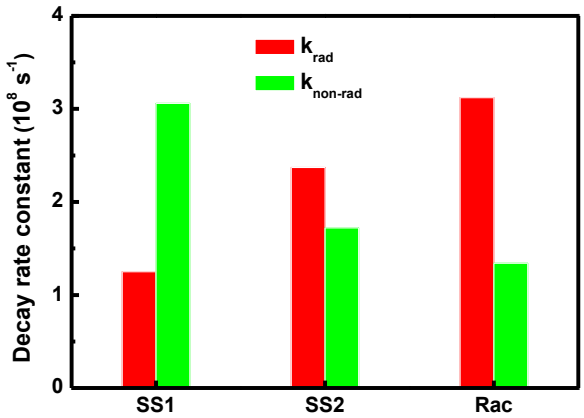

Figure 3.12. *Radiative and non-radiative decay rate constants estimated for DCDADQ-****SS1****, DCDADQ-****SS2****, DCDADQ-****Rac****.*

Table 3.6. *Values of $k_{non\text{-}rad}$, k', k_F and k_D of the microcrystalline solids DCDADQ-**SS1**, DCDADQ-**SS2** and DCDADQ-**Rac**.*

Sample	$k_{non\text{-}rad}$ (10^8 s^{-1})	k' (10^8 s^{-1})	k_F (10^8 s^{-1})	k_D (10^8 s^{-1})
DCDADQ-**SS1**	3.06	0.94	2.08	0.04
DCDADQ-**SS2**	1.72	0.94	0.75	0.03
DCDADQ-**Rac**	1.34	0.94	0.39	0.01

contributions of each pathway can be estimated as,

$$k_{non-rad} = k_F + k_D + k'$$

where k_F and k_D represent the Förster and Dexter contributions, and k', all the remaining intramolecular and any other unspecified pathways. Assuming k' remains the same among the three crystalline solids (as the molecule is same in all, intramolecular effects will be similar) and using their individual $k_{non\text{-}rad}$ values and the relative Förster and Dexter energy transfer rates (Fig. 3.10), the values of k', k_F and k_D are determined by solving the three equations; the values (Table 3.6) show a clear decrease in energy transfer rate through both the modes.

We have considered the relevance of the water of crystallization in DCDADQ-**SS1**. As the content is low, and the H-bonding is to the cyano groups that are not involved in any excited state structural relaxations, it is likely to have little impact on the fluorescence; however, the crystal structure resulting from its presence is crucial in the intermolecular energy transfer effects. Another point to be stressed is that there is no simple correlation between the FEE and the molecular structural parameter like the angle θ; only a detailed analysis of the impact of relative molecular orientations as carried out in the current study unravels the basis for the trends in the solid state fluorescence enhancements.

3.7. Summary

Different crystalline forms of the same molecular entity exhibiting vastly different solid state fluorescence responses that are significantly enhanced over the molecular response in solution state is not common. Discovery of such a system in the

present study allowed a systematic exploration and unequivocal confirmation of the critical role of the mode of assembly, and hence intermolecular excited state energy transfer pathways in this phenomenon. An inverse correlation between FEE and the relative energy transfer rates observed in the series once again corroborates the role of intermolecular energy transfer pathways. It is established that specifically oriented aggregation is crucial, and not the rigidification of the environment alone, to obtain large fluorescence efficiency enhancements.

References

1. J. Mei, N. L. C. Leung, R. T. K. Kwok, J. W. Y. Lam and B. Z. Tang, *Chem. Rev*., 2015, **115**, 11718-11940.
2. P. Srujana, T. Gera and T. P. Radhakrishnan, *J. Mater. Chem. C*, 2016, **4**, 6510-6515.
3. Y. L. Bennani and S. Hanessian, *Tetrahedron*, 1996, **52**, 13837-13866.
4. S. Jayanty and T. P. Radhakrishnan, *Chem. Eur. J*., 2004, **10**, 791-797.
5. P. Srujana and T. P. Radhakrishnan, *Angew. Chem. Int. Ed*., 2015, **54**, 7270-7274.
6. M. Szablewski, M. A. Fox, F. B. Dias, H. Namih, E. W. Snedden, S. M. King, D. Dai and L. Pålsson, *J. Phys. Chem. B*, 2014, **118**, 6815-6828.
7. M. J. Frisch, *et al*. Gaussian 09 (Revision C.01) (Gaussian Inc., Wallingford CT, 2010).
8. S. Jayanty and T. P. Radhakrishnan, *Chem. Mater*., 2001, **13**, 2460-2462.

CHAPTER 4

Impact of Molecular Assembly on Fluorescence Emission Enhancement in Aggregates/Solids

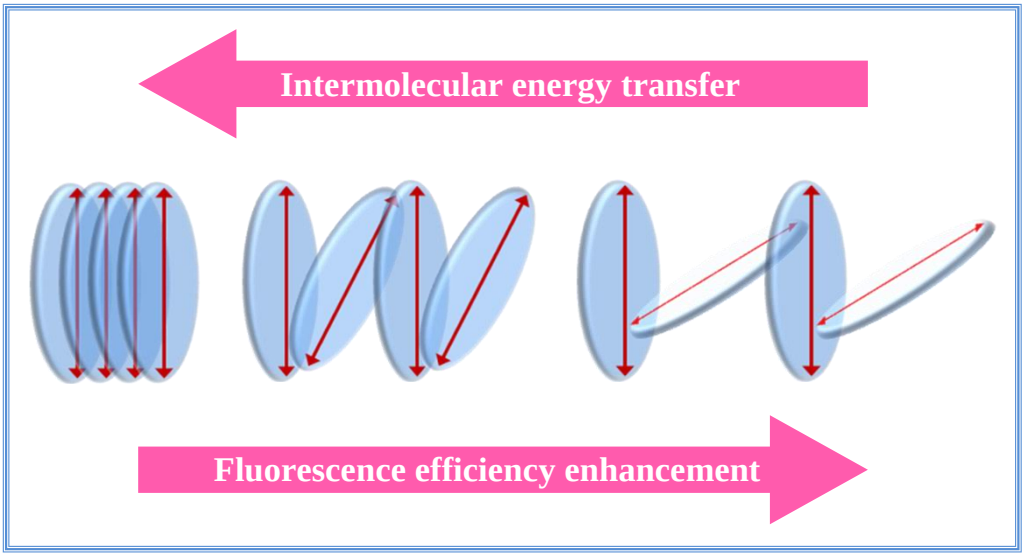

Molecular orientations impeding the intermolecular energy loss pathways play a crucial role in enhancing fluorescence emission from the solution to the solid state and modulating the emission enhancement in the aggregate/solid state.

Scope

Enhanced fluorescence emission in molecular aggregates and solids has received wide attention in view of its extensive application potential. As discussed in earlier chapters, the uncommon effect of enhancement over quenching has largely been attributed to the rigidification of the molecule and its environment, and the restriction of intramolecular non-radiative excited state decay channels. The critical role of molecular orientations in hindering intermolecular energy transfer and the associated non-radiative excited state energy loss has been demonstrated in previous chapters based on examples from the DADQ family of molecules. Further examples based on other families of molecules from earlier reports are analyzed to argue for a closer look at the concomitant role of intra and intermolecular effects in realizing enhanced fluorescence in molecular aggregates.

4.1. Introduction

Fluorophores exhibiting bright emission in the aggregated/solid state, their application in diverse fields and the classes of molecules exhibiting this phenomenon were highlighted in Sec. 1.2. The most widely discussed mechanism for enhanced emission in the solid state is based on the restriction of intramolecular motions (RIM) like rotations and vibrations resulting from the rigidification of the molecule and its environment.[1] Computational studies have illustrated the role of low frequency modes in the non-radiative energy dissipation of the excited state of AIE molecules in the isolated state compared to that in the solid.[2] Other mechanisms proposed for enhanced emission include the accessibility or not of a conical intersection between the ground and excited electronic states, leading to quenching or enhancement of emission in the isolated and aggregate molecules respectively[3] and non-Kasha processes.[4] Effect of the crystalline environment[5] as well as steric/electronic factors on the excited state[6] have also been discussed in the context of enhanced emission in the solid state. Detailed discussions of these mechanisms were provided in Sec. 1.2.2.

Most of the earlier mechanistic studies have focused on specific molecules (Sec. 1.2.2); it is important to analyze trends in solution-to-solid fluorescence efficiency enhancement (FEE) across a series of similar molecules to unravel the underlying factors. Excited state energy loss *via* intermolecular energy transfer is a critical factor that contributes to fluorescence quenching in molecular aggregates. Even though the

need to circumvent the detrimental effect of π-stacking to realize enhanced emission is often noted,[7] there has been relatively very few systematic and quantitative explorations of the correlation between molecular assembly and FEE. We have discussed in Chapters 2 and 3, two new classes of DADQs exhibiting systematic variation in FEE across the series of molecules in each. A detailed analysis of intramolecular energy loss and relative intermolecular energy transfer rates provided insight into the critical role of molecular assembly in tuning the FEE. In this Chapter, we present our explorations of two other families of fluorophores exhibiting varying FEE. These studies attempt to broader the generality of the correlation between molecular assembly and FEE established in the previous two chapters.

4.2. Analysis of Two Classes of Anthracene based Fluorophores

In order to explore the general applicability of our model, we focussed attention on families of crystals that satisfy the following basic criteria: (i) a common fluorophore with a well-defined molecular plane and only peripheral differences is present; (ii) the crystal structures and fluorescence quantum yields in solution and solid state are known; (iii) the crystals within a family show a systematic and significant variation of the fluorescence. We have identified two such families reported in the literature, based on 1,4,5,8-tetra(alkyl)anthracenes (TAA)[8] and bis(piperidyl)anthracenes (BPA)[9] (Fig. 4.1); in the TAA family, we have considered only those crystals which show substantial variation in the fluorescence quantum yield. Table 4.1 lists the fluorescence quantum yield reported for the various crystals and the FEE value estimated based on the

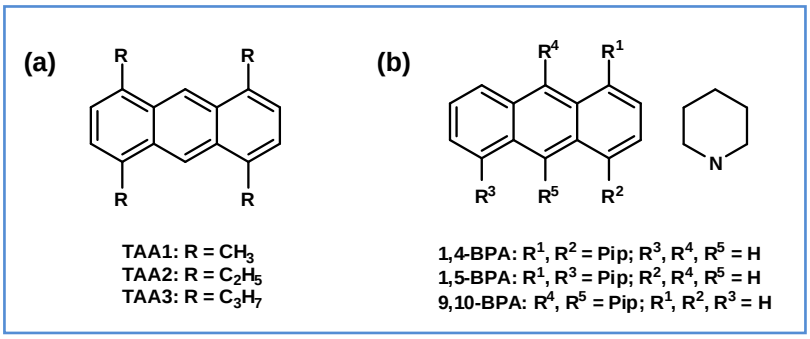

Figure 4.1. *Molecular structure of the fluorophores **(a)** tetra(alkyl)anthracenes (TAA) and **(b)** bis(piperidyl)anthracenes (BPA).*

***Table 4.1**. Emission quantum yield (Φ) in the solution and solid state, fluorescence efficiency enhancement (FEE) based on Φ and the relative energy transfer rates in the TAA and BPA crystals.*

Crystal	Φ (%)		FEE	Relative energy transfer rate	
	Solution	Solid		Förster	Dexter
TAA1	0.32	0.39	1.20	1.000	1.000
TAA2	0.25	0.68	2.72	0.079	0.361
TAA3	0.31	0.85	2.74	0.154	0.028
1,5-BPA	0.77	0.34	0.44	1.000	1.000
1,4-BPA	0.25	0.49	1.96	0.955	0.043
9,10-BPA	0.02	0.86	43.00	0.750	0.000

respective solution quantum yields. As the fluorophore unit is the anthracene moiety (common in the series) and the major differences are only in the peripheral substituents and their positions, intramolecular effects will be minimal.

Trends in the relative energy transfer rates in the crystals within a series are estimated by considering the relative orientation of the transition dipoles (Förster mode) and the π-conjugated fluorophore moieties (Dexter mode) of the molecules within reasonable cut-off distances from a reference molecule; the relevant equations and discussions have been presented in Sec. 2.4.2 and Box 2.1. Transition dipole moments were calculated using TD-DFT (B3LYP/6-31G*) computations[10] and their relative orientations determined from the reported crystal structures. A mean molecular plane was defined using all the atoms in the π-conjugated aromatic fluorophore and their relative orientations inferred from the crystal structure. The fluorophore in both the families is anthracene; its approximate length (9 Å) and width (5 Å) were taken as the cut-off distances for the molecular overlap, and all the near neighbours of a reference molecule considered for the transition dipole interactions.

Unlike in the cases of DADQ based fluorophores discussed in Chapters 2 and 3, the members in the present families of molecules show dissimilar spectral (absorption-emission) overlaps. Hence this factor was taken into account while estimating the relative energy transfer rates. The spectral overlap integral (J_F and J_D) required for the

energy transfer rate estimation through Förster and Dexter modes were calculated using the equations,[11]

$$J_F = \frac{\int \frac{F(\bar{\nu})\varepsilon(\bar{\nu})}{\bar{\nu}^4} d\bar{\nu}}{\int F(\bar{\nu})\, d\bar{\nu}} \qquad J_D = \frac{\int F(\bar{\nu})\varepsilon(\bar{\nu})\, d\bar{\nu}}{\int F(\bar{\nu})\, d\bar{\nu} \int \varepsilon(\bar{\nu})\, d\bar{\nu}}$$

Normalized absorption and emission spectra reported for the solids were used for spectral overlap calculation. The relative energy transfer rates through Förster and Dexter modes are estimated using the slightly modified form of the equations provided in Box 2.1; spectral overlap integral (J_F and J_D) is taken into consideration and the equations used are,

$$k_{ET}(Förster) \propto \frac{\kappa^2}{R^6} J_F \qquad k_{ET}(Dexter) \propto J_D S e^{-r\prime}$$

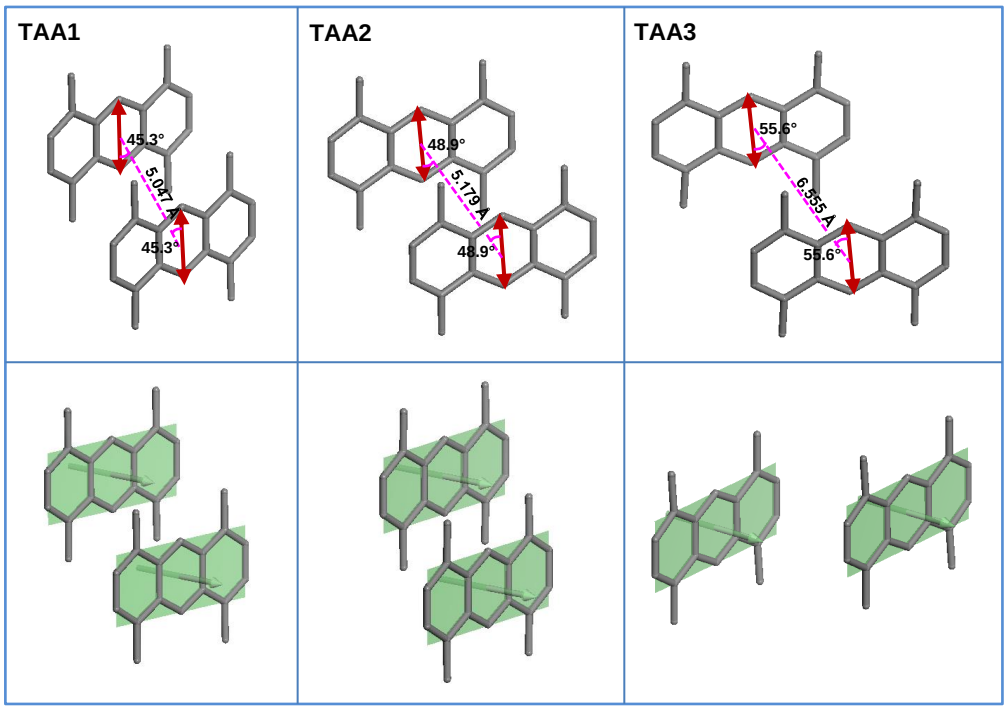

Figure 4.2. *Orientation of nearest neighbour molecules in the crystals of TAA1, TAA2 and TAA3 with the dominant transition dipoles (double-headed arrow) and some of the relevant geometric parameters (top row) and the mean planes of the fluorophore moieties and their normals (bottom row) indicated schematically. H atoms on the anthracene moiety and all atoms in the alkyl chains except the C connected to the anthracene ring are omitted for clarity.*

Relative orientation of the transition dipoles and mean planes of the closest neighbouring molecular pair (satisfying the cut-off criteria) that determine the orientation factor (κ and S for Förster and Dexter mode respectively) for the crystals of the two families TAA and BPA, are shown in Figs. 4.2 and 4.3 respectively. Increasing separation between the transition dipoles and the molecular planes, and their disposition across the series of TAA family is seen clearly in Fig. 4.2. Fig. 4.3 showing the trends in the BPA family reveals the unfavourable orientation of transition dipoles in 1,4-BPA and the increased separation in 9,10-BPA leading to decrease in the overall energy transfer through the Förster mode. Increase in the separation between the molecular planes from 1,5-BPA to 1,4-BPA and the interdigitation of neighbouring molecule in

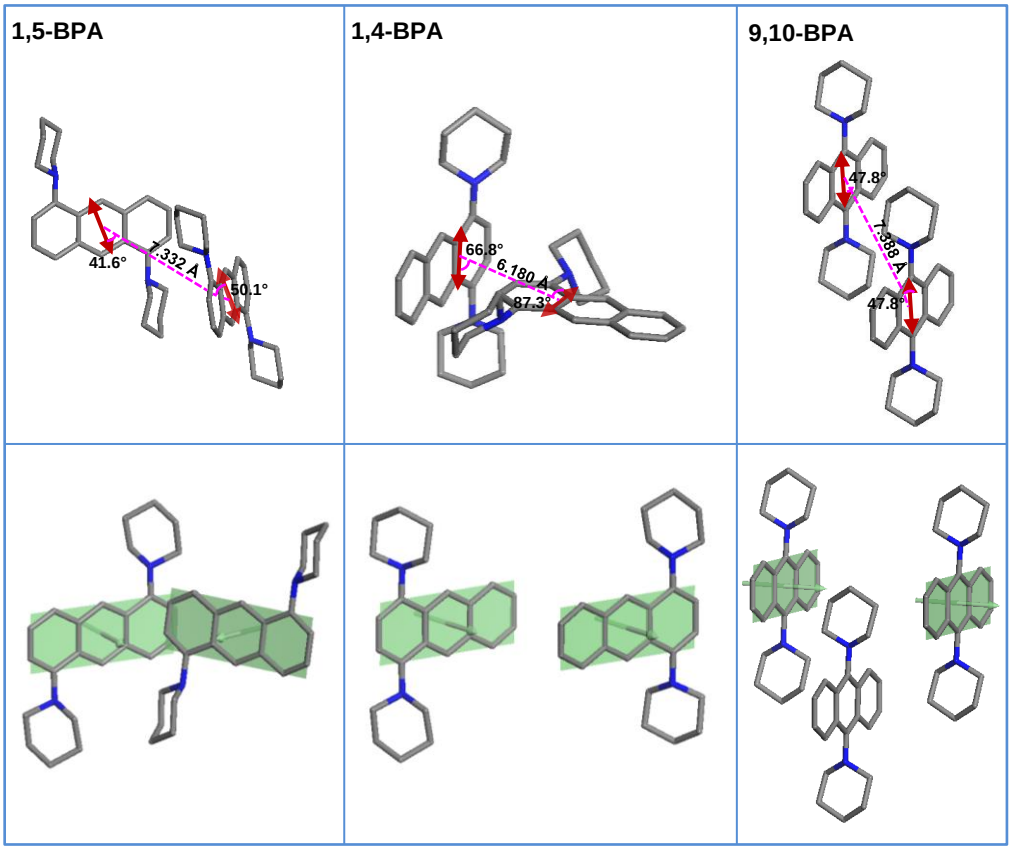

Figure 4.3. *Orientation of nearest neighbour molecules in the crystals of 1,5-BPA, 1,4-BPA and 9,10-BPA with the dominant transition dipoles (double arrow) and some of the relevant geometric parameters (top row) and the mean planes of the fluorophore moieties and their normals (bottom row) indicated schematically. All the H atoms are omitted for clarity.*

9,10-BPA lead to decreasing orbital overlap across this series and hence the Dexter mode of energy transfer. The relative energy transfer rates estimated in the two modes for the members of each family of crystals are collected in Table 4.1. Full list of all the neighbours within the cut-off distances, the relevant geometric parameters and the respective contributions to the energy transfer through Förster mode are collected in Tables 4.2-4.6. The relevant data for the Dexter mode are summarized in Table 4.7. It may be noted that the relative rates under each mode listed in Table 4.1 are derived from the data presented in Tables 4.2-4.7, taking into account the spectral overlaps as well.

Table 4.2. *The relevant geometric parameters for all the near neighbor molecules within the cut-off distances, and the sum of κ^2/R^6 contributing to the Förster energy transfer in TAA1 crystal.*

Crystal	R (Å)	α_{12} (^{0})	α_1 (^{0})	α_2 (^{0})	$\|\kappa\|$	$\frac{\kappa^2}{R^6}$ (10^{-6})
	5.047	0.0	45.3	45.3	0.4851	14.20
	5.047	0.0	45.3	45.3	0.4851	14.20
	7.084	89.4	27.0	67.1	1.0304	8.40
	7.084	89.4	67.1	27.0	1.0304	8.40
	7.084	89.4	27.0	67.1	1.0304	8.40
	7.084	89.4	27.0	67.1	1.0304	8.40
	9.880	0	71.2	71.2	0.6892	0.51
	9.880	0	71.2	71.2	0.6892	0.51
	10.056	89.4	85.5	11.3	0.2216	0.05
	10.056	89.4	11.3	85.5	0.2216	0.05
	10.056	89.4	11.3	85.5	0.2216	0.05
	10.056	89.4	85.5	11.3	0.2216	0.05
TAA1	11.033	89.4	87.8	73.5	0.0223	0.0
	11.033	89.4	73.5	87.8	0.0223	0.0
	11.033	89.4	73.5	87.8	0.0223	0.0
	11.033	89.4	87.8	73.5	0.0223	0.0
	11.094	0	52.7	52.7	0.1042	0.01
	11.094	0	52.7	52.7	0.1042	0.01
	11.094	0	88.1	88.1	0.9967	0.53
	11.094	0	88.1	88.1	0.9967	0.53
	12.308	88.9	32.4	89.2	0.0161	0.0
	12.308	88.9	32.4	89.2	0.0158	0.0
	12.308	88.9	89.2	32.4	0.0158	0.0
	12.308	88.9	89.2	32.4	0.0161	0.0
					Total	**64.3**

Table 4.3. *The relevant geometric parameters for all the near neighbor molecules within the cut-off distances, and the sum of κ^2/R^6 contributing to the Förster energy transfer in TAA2 crystal.*

Crystal	R (Å)	α_{12} (^{o})	α_1 (^{o})	α_2 (^{o})	$\lvert\kappa\rvert$	$\frac{\kappa^2}{R^6}$ (10^{-6})
TAA2	5.179	0	48.9	48.9	0.2984	4.61
	5.179	0	48.9	48.9	0.2984	4.61
	9.519	82.3	60.9	32.4	1.0979	1.62
	9.519	82.3	32.4	60.9	1.0976	1.62
	9.519	82.3	32.4	60.9	1.0976	1.62
	9.519	82.3	60.9	32.4	1.0976	1.62
	9.892	82.3	68.8	45.1	0.6316	0.43
	9.892	82.3	45.1	68.8	0.6316	0.43
	9.892	82.3	45.1	68.8	0.6318	0.43
	9.892	82.3	68.8	45.1	0.6318	0.43
	10.208	0	84.1	84.1	0.9681	0.83
	10.208	0.03	84.1	84.1	0.9681	0.83
	11.447	0.03	67.1	67.1	0.5444	0.13
	11.447	0	67.1	67.1	0.5444	0.13
	11.447	0	78.1	78.1	0.8731	0.34
	11.447	0.03	78.1	78.1	0.8731	0.34
	12.011	82.3	84.2	17.7	0.1566	0.01
	12.011	82.3	84.2	17.7	0.1564	0.01
	12.011	82.3	17.7	84.2	0.1564	0.01
	12.011	82.3	17.7	84.2	0.1566	0.01
					Total	**20.06**

Table 4.4. *The relevant geometric parameters for all the near neighbor molecules within the cut-off distances, and the sum of κ^2/R^6 contributing to the Förster energy transfer in TAA3 crystal.*

Crystal	R (Å)	α_{12} (°)	α_1 (°)	α_2 (°)	|κ|	$\frac{\kappa^2}{R^6}$ (10^{-6})
TAA3	6.555	0.1	55.6	55.6	0.0418	0.02
	6.555	0	55.6	55.6	0.0418	0.02
	7.915	0.1	78.5	78.5	0.8804	3.15
	7.915	0	78.5	78.5	0.8804	3.15
	9.163	0.1	54.8	54.8	0.0018	0.0
	9.163	0.1	54.8	54.8	0.0018	0.0
	10.940	0	18.7	18.7	1.6915	1.67
	10.940	0.1	18.7	18.7	1.6915	1.67
	10.977	0	52.7	52.7	0.1035	0.01
	10.977	0	52.7	52.7	0.1035	0.01
	11.282	0	79.1	79.1	0.8937	0.39
	11.282	0	79.1	79.1	0.8937	0.39
	11.376	0	63.5	63.5	0.4026	0.08
	11.376	0.1	63.5	63.5	0.4026	0.08
	12.258	0	44.2	44.2	0.5395	0.09
	12.258	0.1	44.2	44.2	0.5395	0.09
	14.642	0.1	35.3	35.3	0.9958	0.10
	14.642	0.1	35.3	35.3	0.9958	0.10
	15.39	0.1	57.6	57.6	0.1405	0.0
	15.39	0	57.6	57.6	0.1405	0.0
	16.237	0.1	77.6	77.6	0.8609	0.04
	16.237	0.1	77.6	77.6	0.8609	0.04
	17.497	0	65.7	65.7	0.4919	0.01
	17.497	0.1	65.7	65.7	0.4919	0.01
					Total	**11.12**

Table 4.5. *The relevant geometric parameters for all the near neighbor molecules within the cut-off distances, and the sum of κ^2/R^6 contributing to the Förster energy transfer in the crystals of 1,5-BPA and 1,4-BPA.*

Crystal	R (Å)	α_{12} (°)	α_1 (°)	α_2 (°)	|κ|	$\frac{\kappa^2}{R^6}$ (10^{-6})
1,5-BPA	7.332	16.9	41.6	50.1	0.4824	1.50
	7.332	16.9	41.6	50.1	0.4824	1.50
	7.588	16.9	73.3	56.8	0.4860	1.24
	7.588	16.9	73.3	56.8	0.4860	1.24
	9.315	16.9	62.4	56.2	0.1855	0.05
	9.315	16.9	62.4	56.2	0.1855	0.05
	9.768	0	77.4	77.4	0.8570	0.84
	9.768	0	77.4	77.4	0.8570	0.84
	10.058	0	70.8	70.8	0.6755	0.44
	10.058	0	70.8	70.8	0.6755	0.44
	10.297	16.9	42.3	56.2	0.2775	0.06
	10.297	16.9	42.3	56.2	0.2776	0.06
	10.371	0.08	19.2	19.2	1.6752	2.26
	10.371	0.03	19.2	19.2	1.6752	2.26
					Total	**12.79**
1,4-BPA	6.180	87.4	66.8	87.3	0.0100	0.0
	6.238	89.8	88.1	69.8	0.0303	0.02
	8.822	89.8	56.9	39.4	1.2625	3.38
	9.020	53.2	37.9	75.5	0.0065	0.0
	9.020	53.2	75.5	37.9	0.0065	0.0
	9.043	89.1	59.0	35.3	1.2432	2.83
	9.558	48.6	51.8	88.5	0.6119	0.49
	10.198	89.8	38.5	54.4	1.3624	1.65
	10.280	88.2	58.8	36.6	1.2181	1.26
	10.854	0	63.4	63.4	0.3990	0.10
	10.854	0	63.4	63.4	0.3990	0.10
	10.991	48.6	11.5	40.9	1.5622	1.38
	11.249	87.9	49.6	38.1	1.4952	1.10
	11.898	0	49.2	49.2	0.2799	0.03
	12.463	87.4	35.1	88.6	0.0163	0.0
	12.718	0	6.76	6.76	1.9584	0.91
					Total	**13.25**

Table 4.6. *The relevant geometric parameters for all the near neighbor molecules within the cut-off distances, and the sum of κ^2/R^6 contributing to the Förster energy transfer in 9,10-BPA crystal.*

Crystal	R (Å)	α_{12} (^{o})	α_1 (^{o})	α_2 (^{o})	|κ|	$\frac{\kappa^2}{R^6}$ (10^{-6})
9,10-BPA	7.388	0	47.8	47.8	0.3553	0.78
	7.388	0	47.8	47.8	0.3553	0.78
	7.625	0	49.3	49.3	0.2751	0.39
	7.625	0	49.3	49.3	0.2751	0.39
	9.047	0	60.6	60.6	0.2779	0.14
	9.047	0	60.6	60.6	0.2779	0.14
	9.686	0	90.0	90.0	1.0	1.21
	9.686	0	90.0	90.0	1.0	1.21
	10.301	0	87.1	87.1	0.9921	0.82
	10.308	0	87.1	87.1	0.9921	0.82
	10.845	0	65.8	65.8	0.4963	0.15
	10.845	0	65.8	65.8	0.4963	0.15
	12.951	0	87.6	87.6	0.9949	0.21
					Total	**7.19**

Table 4.7. *The relevant geometric parameters (for molecules around a reference molecule, satisfying the conditions, r' > 2.5 Å and r.sinα < 9 and 5 Å respectively along the length and width of the reference molecule, and the sum of $S.e^{-r'}$ contributing to the Dexter energy transfer in the crystals of TAA and BPA families.*

Crystal	r (Å)	r' (Å)	α (^{o})	δ (^{o})	r.sinα (Å)	S	$S.e^{-r'}$
TAA1	5.047	3.6266	44.1	0	3.5123	0.7186	0.0191
	5.047	3.6266	44.1	0	3.5123	0.7186	0.0191
						Total	**0.0382**
TAA2	5.179	3.512	47.3	0	3.8063	0.6781	0.0202
	5.179	3.512	47.3	0	3.8063	0.6781	0.0202
						Total	**0.0404**
TAA3	7.915	7.4064	20.7	0	2.7916	0.9357	0.0006
	7.915	7.4063	20.7	0	2.7917	0.4222	0.0006
						Total	**0.0012**
1,5-BPA	7.588	6.5841	0.5	1	3.7719	0.4875	6.74×10^{-4}
	7.588	6.5841	0.5	1	3.7719	0.4875	6.74×10^{-4}
						Total	**13.48×10^{-4}**
1,4-BPA	9.527	3.9064	20.6	0	3.356	0.9359	1.26×10^{-4}
						Total	**1.26×10^{-4}**
9,10-BPA	-	-	-	-	-	-	-

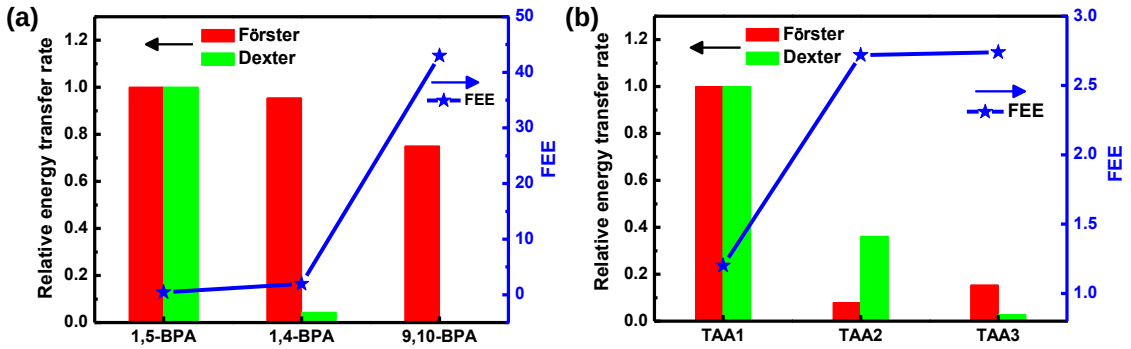

Figure 4.4. *The plot of relative energy transfer rates (Förster and Dexter modes) and the FEE values in the crystals of **(a)** TAA and **(b)** BPA families.*

Fig. 4.4 shows graphically, the relative energy transfer rates of the members of each family of crystals juxtaposed with the trends in the FEE values. The negative correlation between the two is clearly manifested; the FEE appears to be particularly sensitive to the Förster mode of energy transfer in these systems. The overall conclusion from this study shows that the model we have proposed in Chapter 2 for analysing the impact of molecular assembly on fluorescence enhancement in DADQ based molecular aggregates holds true for other families of molecules as well.

4.3. Summary

Restriction of intramolecular structural relaxation and consequently non-radiative excited state decay is important for inducing enhanced fluorescence in molecular aggregates and crystals. The studies presented in this chapter, as a logical extension of the studies presented in the previous two chapters establish unequivocally that the relative molecular orientations and the curtailment of intermolecular energy transfer are also critical in this context. A holistic evaluation of both intra and intermolecular factors is crucial for the effective design and development of molecular assemblies that can exhibit strong light emission useful in wide-ranging applications.

References

1. J. Mei, Y. Hong, J. W. Y. Lam, A. Qin, Y. Tang and B. Z. Tang, *Adv. Mater.*, 2014, **26**, 5429-5479.

2. T. Zhang, Y. Jiang, Y. Niu, D. Wang, Q. Peng and Z. Shuai, *J. Phys. Chem. A*, 2014, **118**, 9094-9104.

3. Q. Li and L. Blancafort, *Chem. Commun.*, 2013, **49**, 5966-5968.

4. H. Qian, M. E. Cousins, E. H. Horak, A. Wakefield, M. D. Liptak and I. Aprahamian, *Nat. Chem.*, 2017, **9**, 83-87.

5. D. Presti, L. Wilbraham, C. Targa, F. Labat, A. Pedone, M. C. Menziani, I. Ciofini and C. Adamo, *J. Phys. Chem. C*, 2017, **121**, 5747-5752.

6. J. Shi, L. E. A. Suarez, S. Yoon, S. Varghese, C. Serpa, S. Y. Park, L. Lüer, D. Roca-Sanjuán, B. Milián-Medina and J. Gierschner, *J. Phys. Chem. C*, 2017, **121**, 23166-23183.

7. Q. Li and Z. Li, *Adv. Sci.*, 2017, **4**, 1600484-(1-15).

8. C. Kitamura, Y. Abe, N. Kawatsuki, A. Yoneda, K. Asada, T. Kobayashi and H. Naito, *Mol. Cryst. Liq. Cryst*., 2007, **474**, 119-135.

9. S. Sasaki, K. Igawa and G. Konishi, *J. Mater. Chem. C*, 2015, **3**, 5940-5950.

10. Frisch, M. J. *et al*. Gaussian 09 (Revision C.01) (Gaussian Inc., Wallingford CT, 2010).

11. P. Ceroni, *The Exploration of Supramolecular Systems and Nanostructures by Photochemical Techniques*, Volume 78, Lecture Notes in Chemistry, Chapter 2 (Springer Science & Business Media, 2011).

CHAPTER 5

Reversible Thermal Transformations of Bistable, Fluorescence Switchable Solids Based on DADQs: Entry into Functional Molecular Phase Change Materials

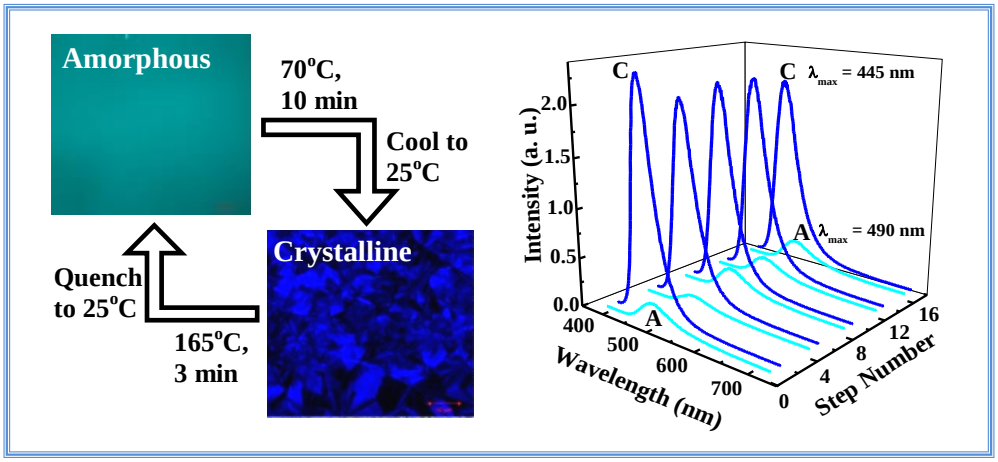

A subtle balance between robust supramolecular assembly and conformational flexibility is exploited in the development of functional molecular phase change materials based on DADQs showing reversible, thermally induced amorphous-crystalline transformation together with a prominent change in the fluorescence emission color and intensity. Dye-polymer composite films coated on a suitable substrate show reversible amorphous-crystalline transformation by laser irradiation.

Scope

*Most of the material attributes known in traditional inorganic materials have been translated into the realm of functional molecule based materials over the last several decades; a conspicuous absence is 'functional molecular phase change materials'. Phase change materials (PCMs) based on organic molecules are primarily limited to those that utilize the melting enthalpy change in thermal energy storage applications. On the other hand, the facile amorphous-crystalline transformation of inorganic materials like Ge-Sb-Te alloys find use in advanced applications like information storage; however sensitive responses such as fluorescence emission have not been harnessed in these PCMs as well. The versatility of molecular materials, with their unique optical, electrical and magnetic characteristics that can be tailored through facile synthesis, has not been exploited in PCM applications. This chapter describes the successful demonstration of thermally induced, reversible amorphous-crystalline (**A**↔**C**) transformation in diaminodicyanoquinodimethane based molecular solids, and the associated prominent switching of the fluorescence emission in terms of both energy and intensity. A family of new molecules that serve as prototypes are synthesized and characterized. Conditions for obtaining thin films of these materials in the bistable (crystalline and amorphous) forms are optimized. Molecular as well as bulk level details of the structural transformations and fluorescence emission changes are investigated through X-ray diffraction, calorimetry, spectroscopy and microscopy studies, combined with ab initio computational modeling that provides insight into the crucial optical characteristics. Stabilization of the amorphous form in dye-polymer composite thin films and reversible transformation by laser irradiation are also demonstrated. The present finding of a genuine molecule-based PCM not only marks the beginning of a novel domain of molecular materials, but also sets a new direction for the development of functional molecular PCMs.*

5.1. Introduction

Materials that can exist in reversibly inter-convertible phases, with a substantial transition enthalpy or switching of a property between the phases, are known as phase change materials (PCMs).[1] Different kinds of PCMs (organic/inorganic) and their applications in energy and information storage have been discussed in Sec. 1.3. Inorganic PCMs like $Ge_2Sb_2Te_5$ (GST) have found unique applications in information storage owing to the efficient switching between the crystalline and amorphous phases possessing significantly different optical reflectivity and electrical conductivity (Sec. 1.3).[2-4] The amorphous-crystalline PCMs are of special interest due to the all solid-state

nature and the small volume/strain changes across the phase boundary; the bistability is critical for device applications. Compared to inorganic materials, small molecule-based organic solids are advantageous due to their tailorable fabrication *via* soft chemistry and lower operating temperatures. The unique optical, magnetic or electronic responses of functional molecular materials can expand the scope of PCMs significantly.

Most of the properties observed in inorganic materials have been realized in functional molecular materials over the last several decades,[5] and the relevance of the amorphous state in molecule-based materials (Sec. 1.1.1)[6] and pharmaceuticals[7] has been established; however, no PCM has been developed based on this class of soft materials. Bistable amorphous-crystalline PCMs of any kind, organic or inorganic, capable of thermally induced, repeated, reversible switching of sensitive optical attributes such as fluorescence emission are unknown. The closest cases are the hybrid systems in which the luminescence of a semiconductor quantum dot or a conjugated polymer is switched indirectly through phase changes of an over-layer of GST or *in situ* deposited paraffin wax respectively.[8,9] Fluorescence switching in molecular systems have been achieved via photo-activated reactions[10] and thermochromism.[11] Fluorescence change upon crystal-to-crystal transformation[12] and formation of partially amorphous states upon grinding[13] with limited cycling have been reported. In none of the cases was either a well-characterized amorphous phase and bistability established, or extensive amorphous-crystalline cycling exclusively by thermal processing demonstrated. Even though reversible thermal transformations of an anthraquinone derivative accompanied by an ~ 20% variation in the reflectivity was reported, the phases (amorphous/crystalline) were not fully characterized, and more significantly, there is no switching of functional attributes like fluorescence emission.[14]

Molecular materials based on the DADQ system[15] that produce strong optical second harmonic generation[5,16] as well as enhanced fluorescence in the solid state[17] have been discussed in Sec. 1.2.1. Earlier in our laboratory, amorphous nanoparticles of a DADQ derivative were fabricated and transformed to the crystalline state with different fluorescence emission, by solvent vapor fuming.[18] However, reversible transformation, preferably thermally induced, is required to realize a viable PCM. Most of the DADQs possess melting temperatures near or above 250°C and decompose during melting, preempting the possibility of realizing an amorphous state or reversible

transformations; decomposition during melting is indeed, a problem with many functional organic molecule-based materials. We explored a variety of substituent groups, finally realizing the synthesis of novel derivatives of DADQ that melt at lower temperatures (T_m ~ 150°C) with no decomposition. These are alkoxypropylamine substituted molecules, BMADQ, BEADQ and BPADQ (Scheme 5.1). Quenching the melts produces amorphous materials at ambient temperatures, which can then be transformed back to the crystalline state by heating to temperatures (T_c) ~ 70°C and cooling slowly; this reversible transformation can be repeated several times. Most significantly, the bistable amorphous/crystalline forms exhibit strikingly different fluorescence emission responses, in terms of intensity (weak/strong) as well as color (cyan/blue). We describe in detail the investigations with BEADQ in Secs. 5.2-5.7; the observations with BMADQ and BPADQ are described briefly in Sec. 5.8.

The amorphous form of BEADQ could be stabilized by fabricating dye-polymer composite thin films, and localized reversible amorphous-crystalline transformation by laser irradiation is demonstrated. Preliminary explorations in this direction are presented in Sec. 5.9.

5.2. Synthesis and Characterization of BEADQ

The new DADQs that exhibit clear melting were synthesized by the direct single step reaction of 3-alkoxypropylamine with TCNQ in acetonitrile. The general synthesis scheme is shown in Scheme 5.1. Detailed procedure followed for the synthesis of one of the derivatives, 7,7-bis(ethoxypropylamino)-8,8-dicyanoquinodimethane, BEADQ, is described below.

***Synthesis*:** 3-Ethoxypropylamine (7.84 mmol) was added to a warm solution of TCNQ (1.96 mmol) in 40 ml acetonitrile; the solution turned dark green immediately and then changed to orange-brown (caution: small amount of HCN gas is formed as the byproduct of the reaction). The reaction mixture was stirred for 4 h at 65°C and then cooled to 4°C. The microcrystalline solid which precipitated over 2 days was filtered, washed with acetonitrile and dried to give BEADQ (0.51 g, 77% yield). Crystallization from acetonitrile solution yielded plate-like crystals and was recrystallized thrice to obtain the pure compound.

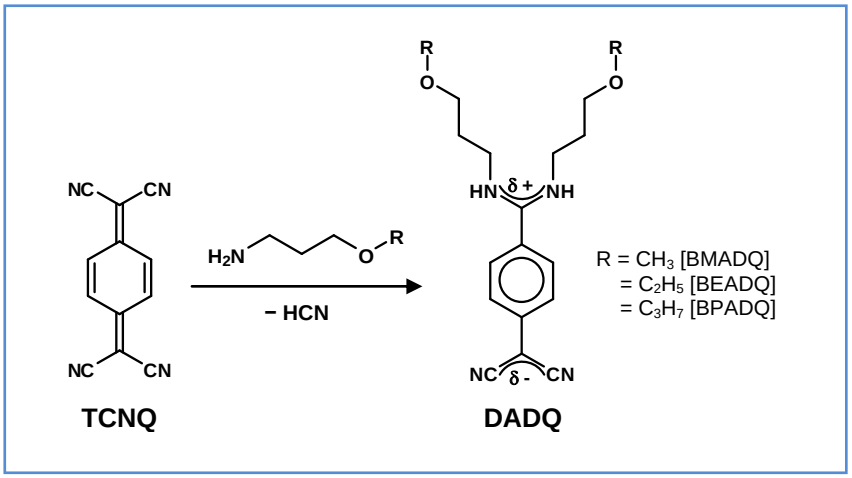

Scheme 5.1. *General scheme for the synthesis of alkoxypropylamine substituted DADQs.*

***Characterization*:** M. P. (°C) = 157-159; FTIR (KBr): wavenumber/cm^{-1} = 3201.9 (N−H stretch), 3071.3 (aromatic C−H stretch), 2973.0 (aliphatic C−H stretch), 2178.5 and 2132.3 (asymmetric C≡N stretch), 1598.2 (aromatic C=C stretch), 1103.7 (C−O stretch); ^{1}H-NMR ($CDCl_3$): δ/ppm = 8.65 (s,1H), 7.66 (s, 1H), 7.28-7.21 (d, 2H), 6.94-6.92 (d, 2H), 3.62-3.47 (m, 12H), 2.02 (s, 2H), 1.86 (s, 2H), 1.22-1.21 (t, 6H); ^{13}C-NMR ($CDCl_3$): δ/ppm = 164.5, 148.9, 129.1, 125.5, 118.9, 113.3, 70.2, 67.5, 67.1, 66.6, 46.4, 40.5, 34.0, 29.6, 27.9, 15.2.

The molecular structure and unit cell in crystals of BEADQ are shown in Fig. 5.1a and b. Basic crystallographic details are collected in Table 5.1. The molecule has the zwitterionic structure typical of DADQs,[16,19] with a dihedral twist angle (θ) of ~ 46.7° between the diaminomethylene moiety and the benzenoid ring. The conformationally flexible alkoxyalkyl chains are the crucial structural elements that can induce disorder in the lattice and disturb the packing of the DADQ framework under suitable conditions. Molecular assembly in the crystal involves intertwining, linked helical superstructures of H-bonded molecules (Fig. 5.1c); the extended supramolecular interactions are likely to help in regaining the integrity of ordered assemblies from the amorphous state.

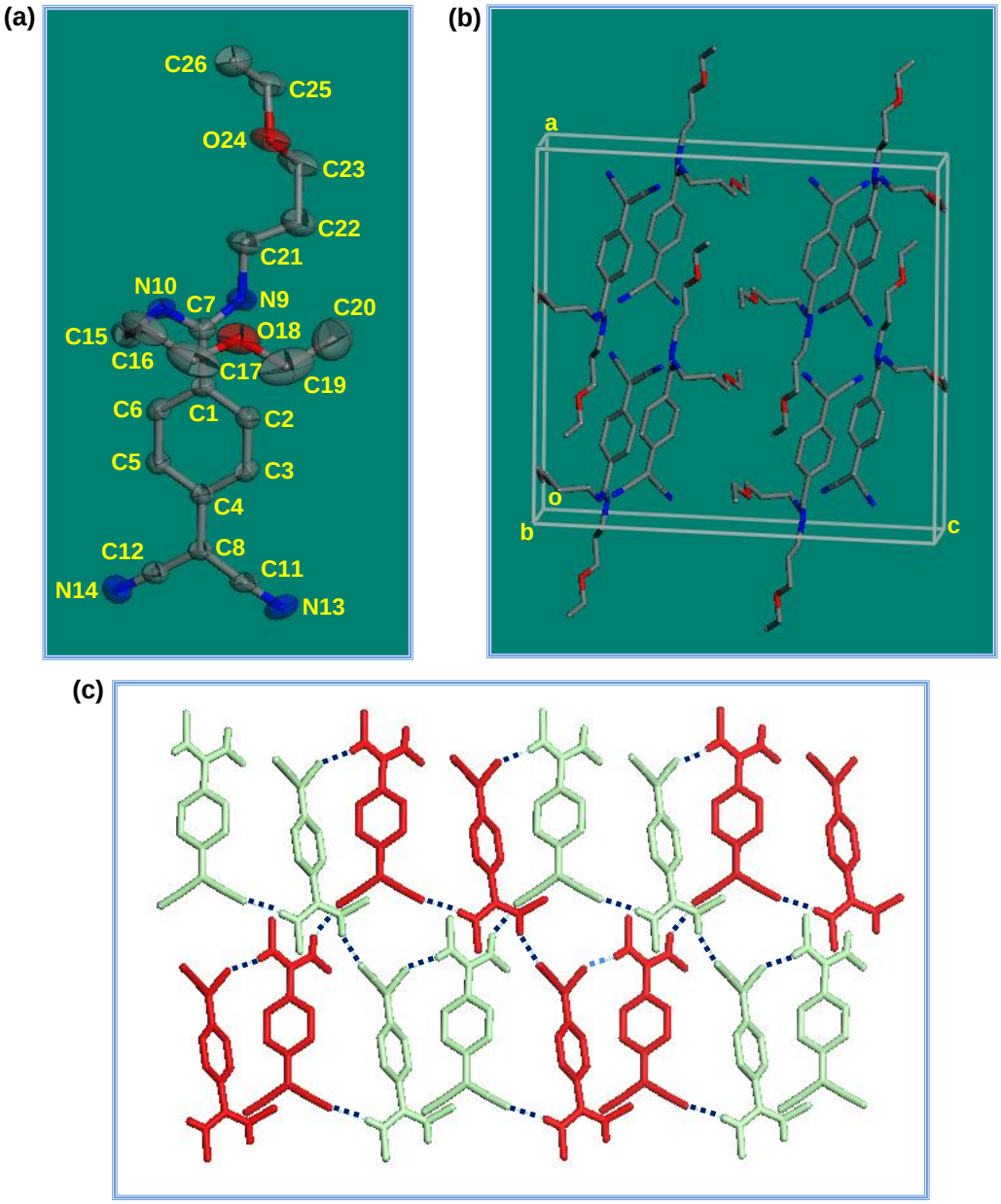

Figure 5.1. ***(a)*** *Molecular structure showing 99% thermal ellipsoids and* ***(b)*** *the unit cell of BEADQ; all H atoms are omitted for clarity.* ***(c)*** *The intertwined and linked helical assemblies of molecules in the crystal lattice formed through intermolecular H-bonds (broken lines); molecules in the two chains are shown in green and red and H atoms on the benzenoid ring and all atoms in the ethoxypropyl chains except the C connected to the amino group are omitted for easier viewing.*

Table 5.1. *Basic crystallographic details of BEADQ.*

Molecule	BEADQ
Empirical formula	$C_{20}H_{28}N_4O_2$
Crystal system	Monoclinic
Space group	*C2/c*
a / Å	19.999(9)
b / Å	9.687(4)
c / Å	21.343(9)
α / deg.	90.00
β / deg.	92.069(8)
γ /deg.	90.00
V / $Å^3$	4132(3)
Z	8
$\rho_{calc.}$ / g cm^{-3}	1.146
μ / cm^{-1}	0.076
Temperature / K	100(2)
λ / Å	0.71073
No. of reflections	3705
No. of parameters	347
Max., Min. transmission	0.989, 0.986
GOF	1.036
R [for $I \geq 2\sigma_I$]	0.0594
wR^2	0.1638
Largest difference peak and hole / e$Å^{-3}$	0.587, 0.047
CCDC deposition number	1046619

5.3. Characterization of the Phases

Amorphous (**A**) and crystalline (**C**) phases of BEADQ were charaterized by calorimetry, diffraction and spectroscopy techniques. Differential scanning calorimetry (DSC) thermograms are collected in Fig. 5.2a. In the first heating run carried out at a slow rate of 2°/min, the microcrystalline sample melts at 158°C (T_m); a fast cooling reveals no crystallization event. Heating in the second cycle shows an exothermic peak at 65°C; this corresponds to the crystallization temperature (T_c), since the endothermic peak due to the melting reappears clearly at 156-157°C. The melt-quench-recrystallize cycle can be repeated several times with high reproducibility confirming the reversibility of the transformations. The slight depression in the T_m with respect to that

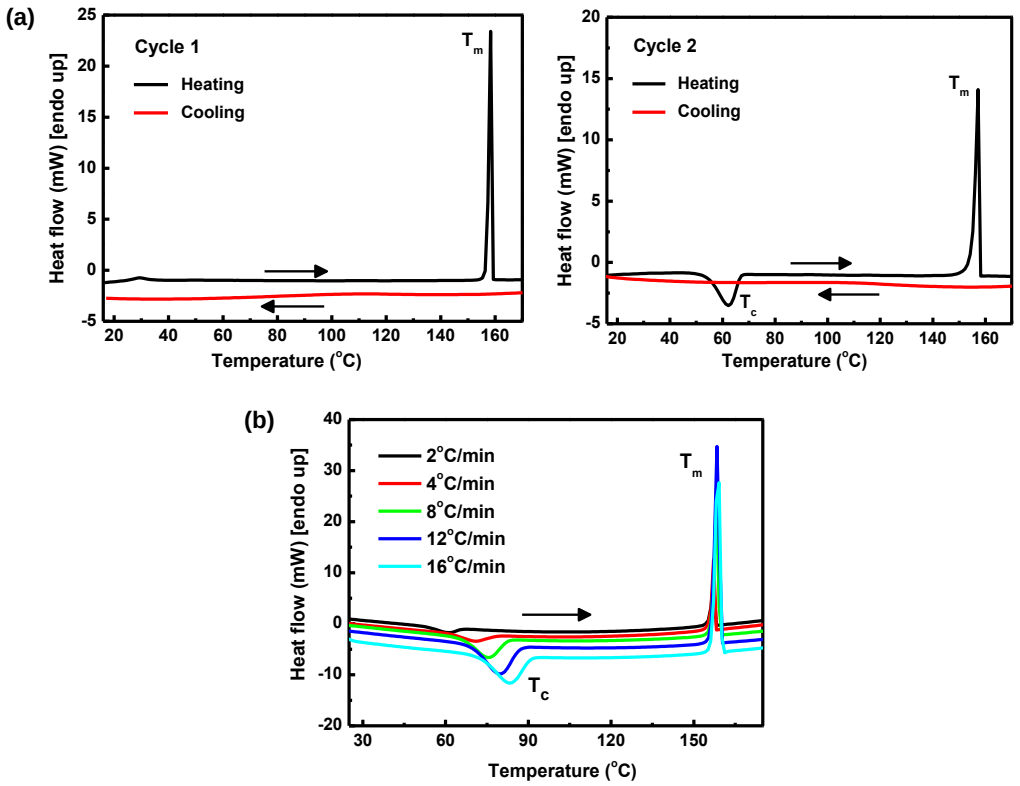

Figure 5.2. ***(a)*** *Differential scanning calorimetry thermograms of solid BEADQ through two heating (2°C/min) – cooling (20°C/min) cycles; the melting (T_m) and crystallization (T_c) temperatures are indicated.* ***(b)*** *Thermograms (second heating scan) recorded at different heating rates with the melt-quench sample; the crystallization temperature (T_c) is found to increase with increasing heating rate.*

in the first cycle occurs consistently in the repeat cycles. The enthalpy change associated with the melting and crystallization transitions (Table 5.2) are smaller than that of the melting of organic PCMs used in energy storage (~ 100-300 J/g).[20] The T_c was found to increase from 65°C to 83°C when the heating rate was varied from 2°/min to 16°/min (Fig. 5.2b) indicating the relevance of kinetic effects in the recrystallization.

The powder X-ray diffraction patterns (Fig. 5.3) confirm the amorphous and crystalline state of the melt-quench (**A** form) and recrystallized (**C** form, the melt-quench heated at 70°C for 10 min and cooled) samples respectively; the former shows no clear diffraction peaks whereas the latter agrees with the pattern of the original microcrystalline sample, which in turn can be simulated using the crystal structure.

Table 5.2. *Enthalpy changes (ΔH) associated with the melting (T_m) and crystallization (T_c) transitions of BEADQ in multiple cycles (heating rate = 20°C/min).*

Step No.	T_m (°C)	ΔH (J/g)	T_c (°C)	ΔH (J/g)
1	161.4	84.5	-	-
2	-	-	85.2	75.5
3	160.1	83.3	-	-
4	-	-	87.3	74.8
5	160.0	82.4	-	-
6	-	-	88.2	74.9
7	159.7	82.4	-	-
8	-	-	88.2	74.7
9	159.6	81.9	-	-
10	-	-	89.5	74.6
11	159.5	81.5	-	-
12	-	-	89.4	74.2
13	159.2	81.0	-	-
14	-	-	90.1	73.1
15	159.2	80.7	-	-
16	-	-	91.5	73.0
17	158.9	79.8	-	-
18	-	-	93.5	73.3
19	158.9	79.6	-	-
20	-	-	93.8	73.0

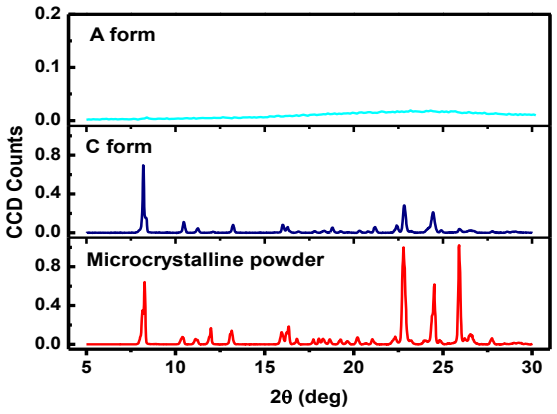

Figure 5.3. *X-ray diffraction pattern of the microcrystalline powder and the **C** and **A** forms of BEADQ.*

Raman spectroscopy is often used to characterize the various polymorphs of pharmaceutically active compounds, as it provides information about both intramolecular (high frequency) and intermolecular (low frequency) vibrational modes.[21] Lattice vibrations (phonons) characteristic of the ordered/crystalline solids appear in the low-frequency region and are generally absent in amorphous solids. Raman spectra of the microcrystalline powder and the **C** and **A** forms of BEADQ recorded in a confocal Raman microscope are collected in Fig. 5.4. Fabrication of melt-quench (**A** form) and crystalline (**C** form) thin film samples of BEADQ are describe in the following section. Spectrum of the **C** form clearly matches that of the microcrystalline material; as often found,[22] the spectrum of the **A** form has relatively broader peaks and background. Even though the **C** and **A** forms show many common bands, some are conspicuously absent and a few split bands merge in the **A** form. This effect could be due to the soft phonon (intermolecular) or librational modes, or split-degeneracies which arise only in the crystalline structure. Possibility of some of the modes that are sensitive to the conformation of the alkoxyalkyl chains changing between the two phases cannot be ruled out. Even though the origin of the spectral differences requires further investigation, the spectra provide a sensitive molecular level signature of the phase change.[22,23]

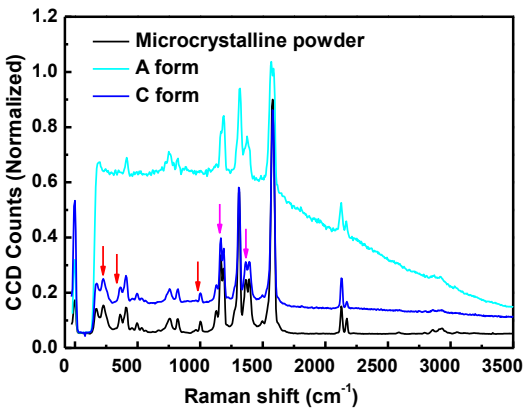

Figure 5.4. *Raman spectra of microcrystalline powder and the **C** and **A** forms of BEADQ; peaks present in the microcrystalline powder and **C** form, but missing (red arrow) or merging (magenta arrow) in the **A** form, are indicated on the spectrum of the **C** form.*

5.4. Fabrication of the A and C forms

Several protocols were explored to prepare BEADQ in the **A** and **C** forms, in order to carry out spectroscopy/microscopy investigations and realize multiple inter-conversions. **A** was found to convert to **C** fairly quickly in bulk powder samples. On the other hand, thin films prepared on different substrates by drop-casting the solution as well as by covering a drop-cast film with a thin polymer over-layer, tended to stabilize **A**, making the conversion to **C** difficult. Finally it was found that microcrystalline powder of BEADQ sandwiched between 0.15 mm thick glass cover slips when melted and quenched produced stable **A** form. ~ 5 mg of BEADQ was placed between glass cover slips and kept on the hot stage (Labindia model MR-VIS$^+$ visual melting range apparatus) maintained at 165°C. After the compound melted completely in ~ 3 min, it was removed and kept in contact with a cold surface to obtain a film of the **A** form. The fluorescence emission signature (discussed in Sec. 5.5) of the **A** form was fully reproducible for several hours when maintained at laboratory temperature of 25°C, during which the spectroscopy and microscopy studies were carried out. The **C** form was fabricated by placing the **A** form in the melting range apparatus maintained at 70-72°C for 10 min. Fig. 5.5 shows the photographs of the **A** and **C** forms under visible light and 365 nm light irradiation.

5.5. Spectroscopic and Computational Studies

Electronic absorption spectra of BEADQ in solution, microcrystalline solid and the **A** and **C** forms are collected in Fig. 5.6a. Broadening of the absorption spectra of

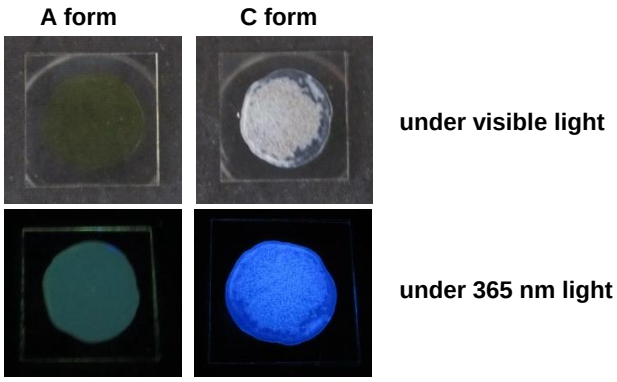

Figure 5.5. *Photographs of the **A** and **C** forms of BEADQ under visible light and the corresponding emission observed under 365 nm light irradiation.*

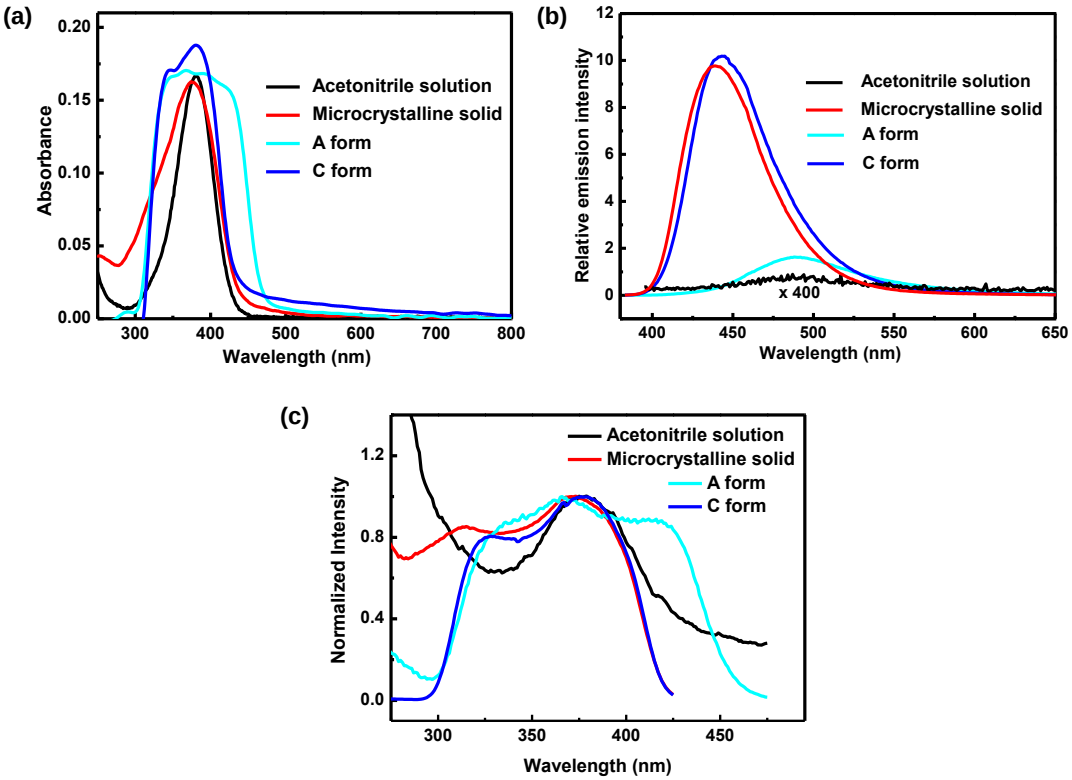

Figure 5.6. ***(a)*** *Electronic absorption,* ***(b)*** *fluorescence emission [λ_{exc} = 380 nm (solution) and 368 nm (others); relative intensities of the samples with similar optical density are shown; the solution spectrum is magnified by a factor of 400] and* ***(c)*** *fluorescence excitation [λ_{em} = 490 nm for solution and* ***A*** *form, and 441 nm for microcrystalline solid and* ***C*** *form] spectra of acetonitrile solution, microcrystalline solid, melt-quench (****A****) and recrystallized (****C****) forms of BEADQ.*

the solids arises due to the intermolecular interactions; the relatively higher broadening in **A** points to the disordered environment of the chromophores. In order to understand the influence of molecular interactions on the optical spectra of the crystals and thin films[18,24] we have computed the electronic excitation energies of BEADQ molecule in different environments, using *ab initio* TD-DFT calculations at the B3LYP/6-31G* level. Table 5.3 shows the good agreement between the λ_{max} computed for the lowest energy excitation having appreciable oscillator strength, and the relevant experimental observations; in the case of the solids, the experimental value corresponds to the approximate midpoint of the broad peak. Polar solvents shift the absorption to higher energy with respect to that of the molecule in vacuum, due to the stabilization of the

Table 5.3. *The lowest energy electronic absorption peak maxima (λ_{max}) for BEADQ in different experimental conditions and the values computed by TD-DFT method at B3LYP/6-31G* level, using different environments – in vacuum, with solvation using the SCRF model, and with a field of 5 nearest neighbor dipoles kept at distances as in the crystal lattice as well as moved away from their positions by 12% (Fig. 5.7).*

Experiment		**Computation**		
State of BEADQ	**λ_{max} (nm)**	**λ_{max} (nm)**	**Molecular geometry**	**Molecular environment**
-	-	460.3	From crystal[$]	Vacuum
Acetonitrile solution	384	385.6	Optimized*	Acetonitrile
Microcrystalline solid	377	376.2	From crystal[$]	Field of dipoles (as in crystal)
C form	374			
A form	390	391.7	From crystal[$]	Field of dipoles (moved away)
[$]Average dihedral angle, $\theta = 46.7^o$ *Fully optimized with acetonitrile solvation; average $\theta = 37.2^o$				

strongly zwitterionic ground electronic state; this solvatochromic effect is adequately modeled by inclusion of the solvent in the computation. The simplest approach to model the impact of the local field due to the neighboring molecules in the solid state of the DADQ molecule is to introduce positive and negative point charges at the positions of the diaminomethylene and dicyanomethylene carbons respectively, of the closest neighbors in the crystal lattice, representing the major dipole due to the zwitterionic structure (Fig. 5.7a). Magnitude of the charge, 0.83*e* was estimated from the computed dipole moment of a BEADQ molecule and the distance between these carbons. λ_{max} estimated with the imposition of such a local field around BEADQ agrees very well with the experimental observation on the microcrystalline solid and the **C** form. The physical basis for the blue shift of the absorption with respect to that of the isolated molecule is the enhancement of the intramolecular charge transfer energy due to the

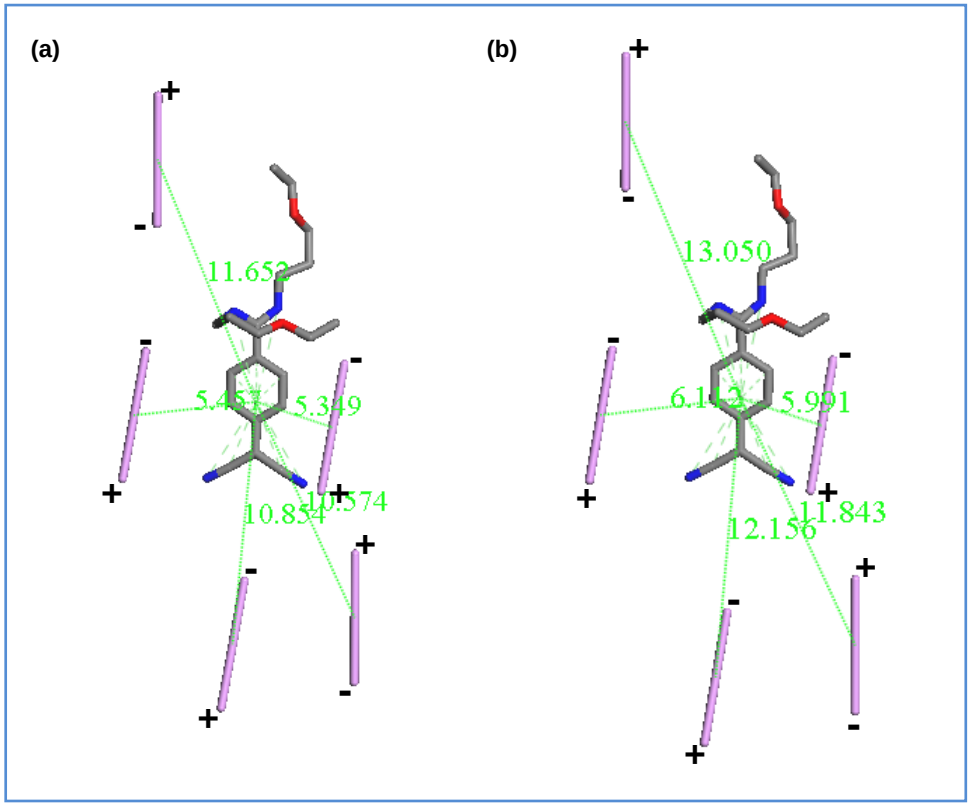

Figure 5.7. *BEADQ molecule with neighboring dipoles **(a)** present in the crystal and **(b)** the neighboring dipoles moved away. The dipoles around the central BEADQ molecule are indicated by pink lines and point charges at the ends; centroid-centroid distances in Å. In **b**, the distance between the centroid of the BEADQ chromophore and the centroid of each of the dipoles was increased by 12%.*

opposing field of near neighbor dipoles. Moving the dipoles away from the BEADQ molecule (Fig. 5.7b) increases the λ_{max}, explaining the red shift of the absorption in the **A** form.

The fluorescence emission spectra of BEADQ in solution, microcrystalline solid and the **A** and **C** forms are collected in Fig. 5.6b. Molecule in the **A** form with a disordered structure resembles the solvated individual molecule in solution as seen from the similarity with the solution spectrum. The spectra show a distinct shift in the emission peak from 444 nm in **C** to 489 nm in **A**, reflecting the shift in the absorption. The emission intensity of **A** is approximately an order of magnitude lower than that of

C; the quantum yields measured are 3.5% and 40% respectively (quantum yield of the solution and microcrystalline solid are 0.1% and 48% respectively). Steady enhancement in the fluorescence emission from the solution, to the **A** form, and then to the **C** and microcrystalline forms can be attributed to the increasing rigidification of the molecular environment and the consequent reduction in the torsional relaxation of the electronic excited state which otherwise provides a non-radiative pathway for the excited state energy loss (Sec. 2.4.1).[17] Fluorescence excitation spectra of the solution, microcrystalline powder, **A** and **C** forms, recorded at the respective emission wavelengths are provided in Fig. 5.6c. Similarity of the spectra in solution and solid state suggests that the emitting state is the same. Fluorescence emission of **A** and **C** forms recorded at different wavelengths (as observed from excitation spectrum) resulted in similar emission spectra.

5.6. Reversible Amorphous-Crystalline (A↔C) Phase Transformation

Thermally induced **A↔C** transformation was realized with the thin films of BEADQ. Plots of the peak wavelength and intensity of the fluorescence emission accompanying the thermal transformation of the **A** to the **C** form (Fig. 5.8) demonstrates clearly, the bistability of the system; the reverse transformation is shown schematically. Fig. 5.9a shows the switching of the fluorescence emission wavelength as well as intensity of samples at ambient temperature, through repeated **A↔C** conversions. The regularity and uniformity of the switching demonstrates the new,

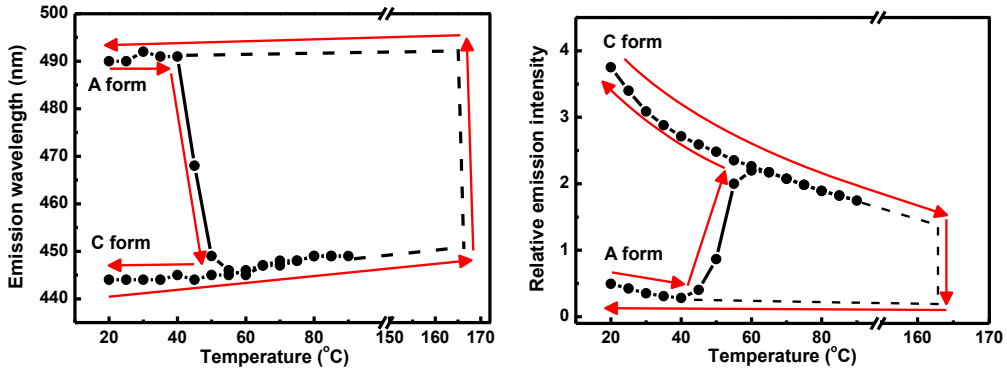

Figure 5.8. *Plots of the fluorescence emission peak wavelength and intensity during the transformation of the **A** to the **C** form; the broken line shows the reverse transformation schematically.*

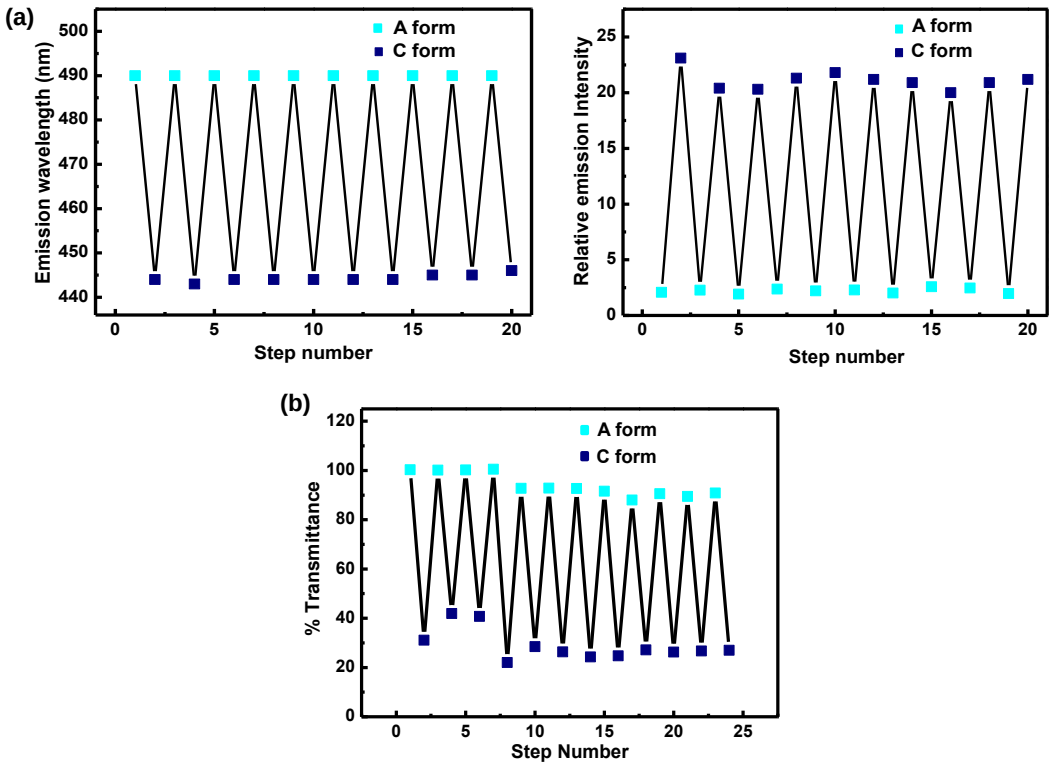

Figure 5.9. *Repeated switching of the* ***(a)*** *fluorescence emission wavelength and peak intensity and* ***(b)*** *transmittance associated with the reversible* ***A↔C*** *transformations of BEADQ. [transmittance monitored at λ = 790 nm, where there is no absorption for either form]*

extensively reversible functional PCM based on a molecular material; it is important to note that the cycling is induced by easily accessible thermal conditions. As the transmittance also changes between the **A** and **C** forms, its switching (~ 30 – 100%) can also be monitored through repeated cycles (Fig. 5.9b). The fluorescence variation in terms of energy and intensity is indeed, more sensitive than the changes in polarized light transmittance observed between crystalline and amorphous forms.[14]

5.7. Microscopy Studies

Laser scanning confocal fluorescence microscope images of the **A** and **C** forms (Fig. 5.10a) show that, while the former is a smooth film, the latter has a polycrystalline morphology. Overlap of the spectral responses recorded in the microscope (Fig. 5.10b) shows that in the narrow window, 400-430 nm, only the **C** form emission is observable.

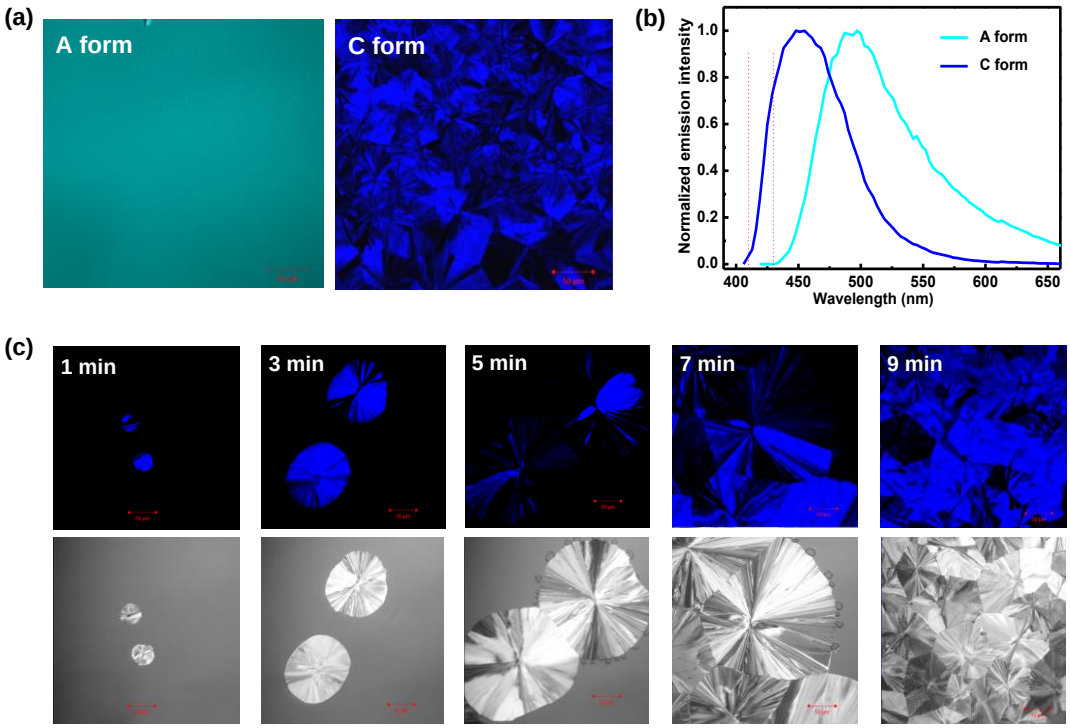

Figure 5.10. ***(a)*** *Laser scanning confocal microscope images and* ***(b)*** *the corresponding emission spectra of the* ***A*** *and* ***C*** *forms of BEADQ (the images are false-colored based on the chromaticity coordinates determined by the emission spectral response in the 400-720 nm range; scale bar = 50 μm).* ***(c)*** *Images recorded using the fluorescence emission in the 400-430 nm window (upper) and optical transmittance (lower), of the* ***A*** *form heated at 70°C for 1-9 min (scale bar = 50 μm).*

Images of **A** samples heated at 70°C for 1-9 min, recorded using the emission in this narrow range (Fig. 5.10c) reveals graphically, the formation and growth of the crystalline domains in the thin film. Similar observations can be made also with **A** samples heated for 1 min at temperatures ranging from 60-100°C, the spectral response shifting smoothly from that of the **A** form to the **C** form (Fig. 5.11).

5.8. PCM Behavior of BMADQ and BPADQ

In order to explore the generality of the phase change characteristics in this class of DADQs, we have investigated the thermally induced reversible phase

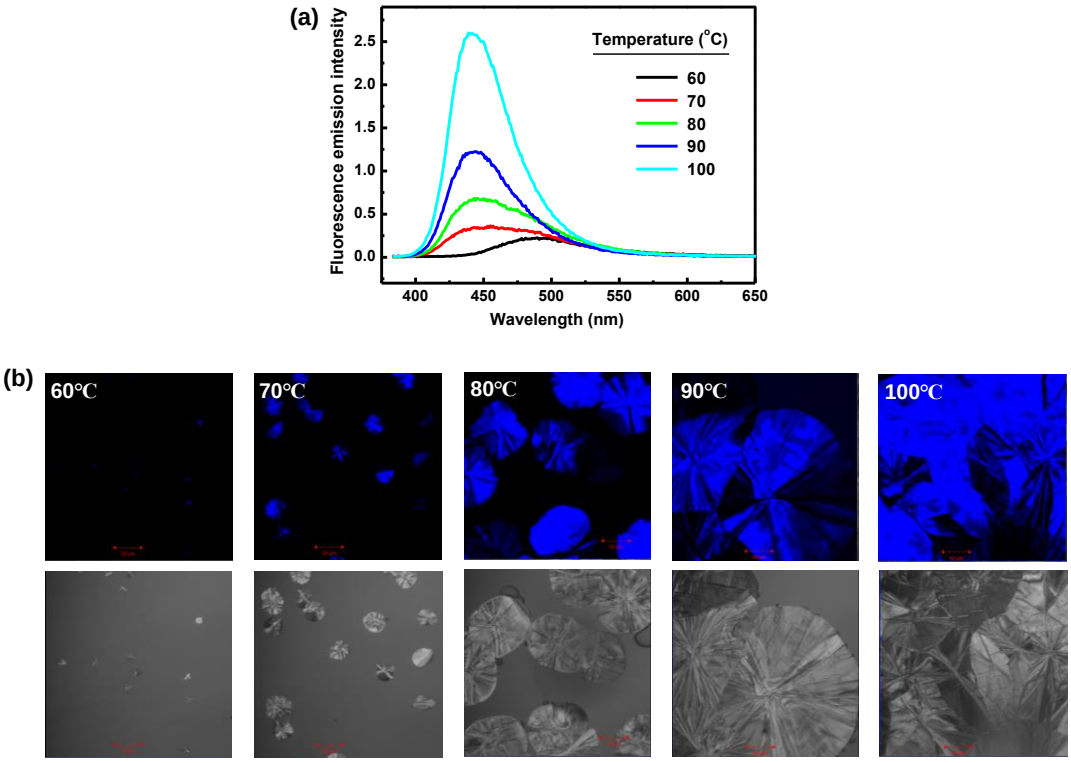

Figure 5.11. ***(a)*** *Fluorescence emission spectra (λ_{exc} = 368 nm) and* ***(b)*** *Laser scanning confocal fluorescence microscope images [fluorescence emission (upper) and optical transmittance (lower) modes] of the* ***A*** *form of BEADQ heated for 1 min at different temperatures ranging from 60-100°C (scale bar = 50 μm). [The images are false-colored based on the chromaticity coordinates determined by the emission spectral response in the 400-720 nm range].*

transformation with the other two alkoxypropylamine substituted DADQs, BMADQ and BPADQ listed in Scheme 5.1. The molecular structure, unit cell and the molecular assembly in the lattice of BMADQ and BPADQ are shown in Figs. 5.12 and 5.13 respectively; BMADQ crystallizes with one molecule of water. The basic crystallographic details are collected in Table 5.4. Similar to BEADQ, the molecular assembly in the crystals of BMADQ and BPADQ involves intertwined supramolecular helical structures formed by intermolecular H-bonds.

DSC thermograms recorded for microcrystalline powders revealed clear melting and crystallization behavior in the successive heating cycles (Fig. 5.14). Origin of the minor spikes observed at lower temperatures in the first heating cycle is not clear;

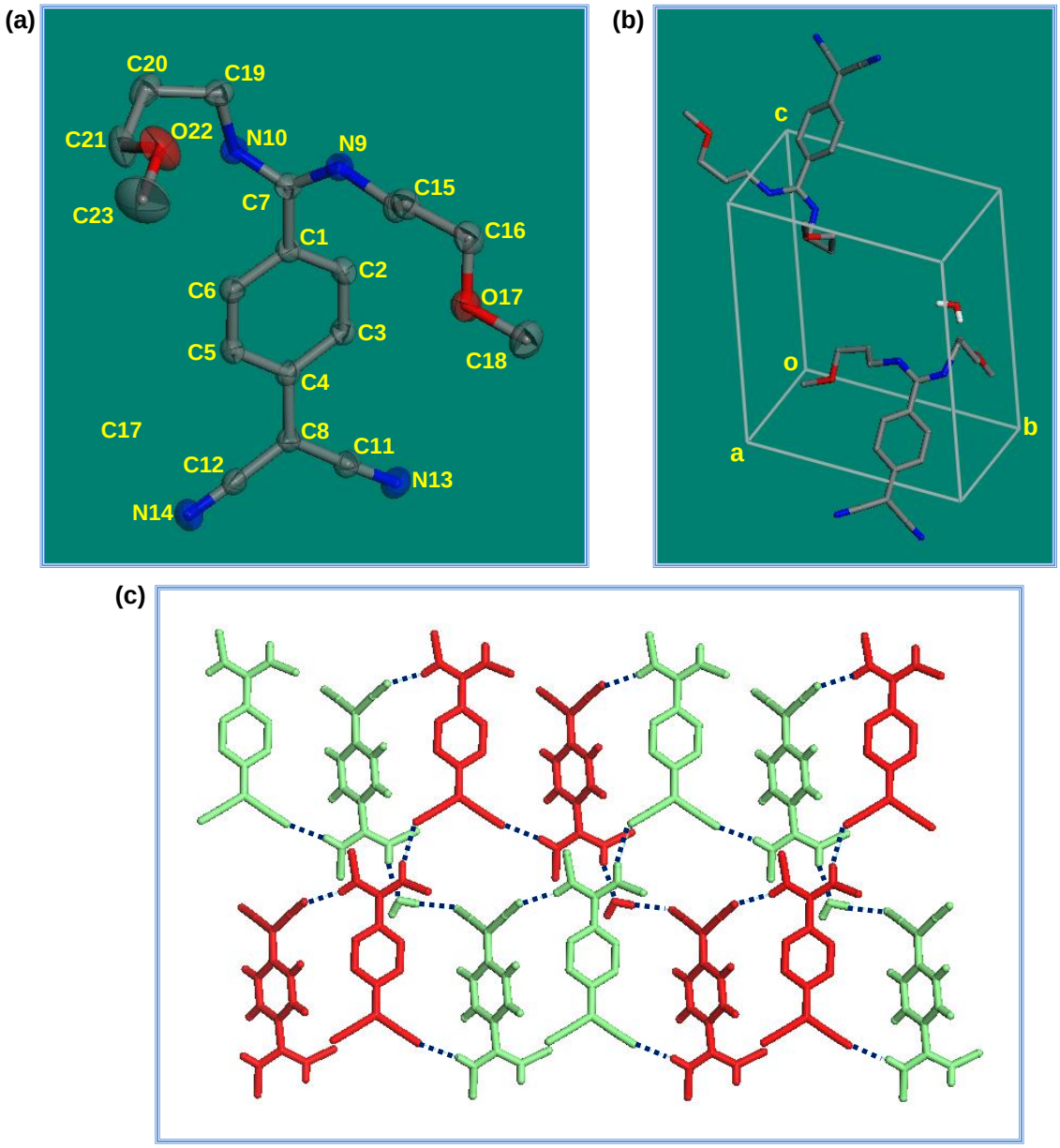

Figure 5.12. ***(a)*** *Molecular structure showing 99% thermal ellipsoids and* ***(b)*** *the unit cell of BMADQ; all H atoms and water molecule are omitted for clarity.* ***(c)*** *The intertwined and linked helical assemblies of molecules in the crystal lattice formed through intermolecular H-bonds (broken lines); molecules in the two chains are shown in green and red, and H atoms on the benzenoid ring and all atoms in the methoxypropyl chains except the C connected to the amino group are omitted.*

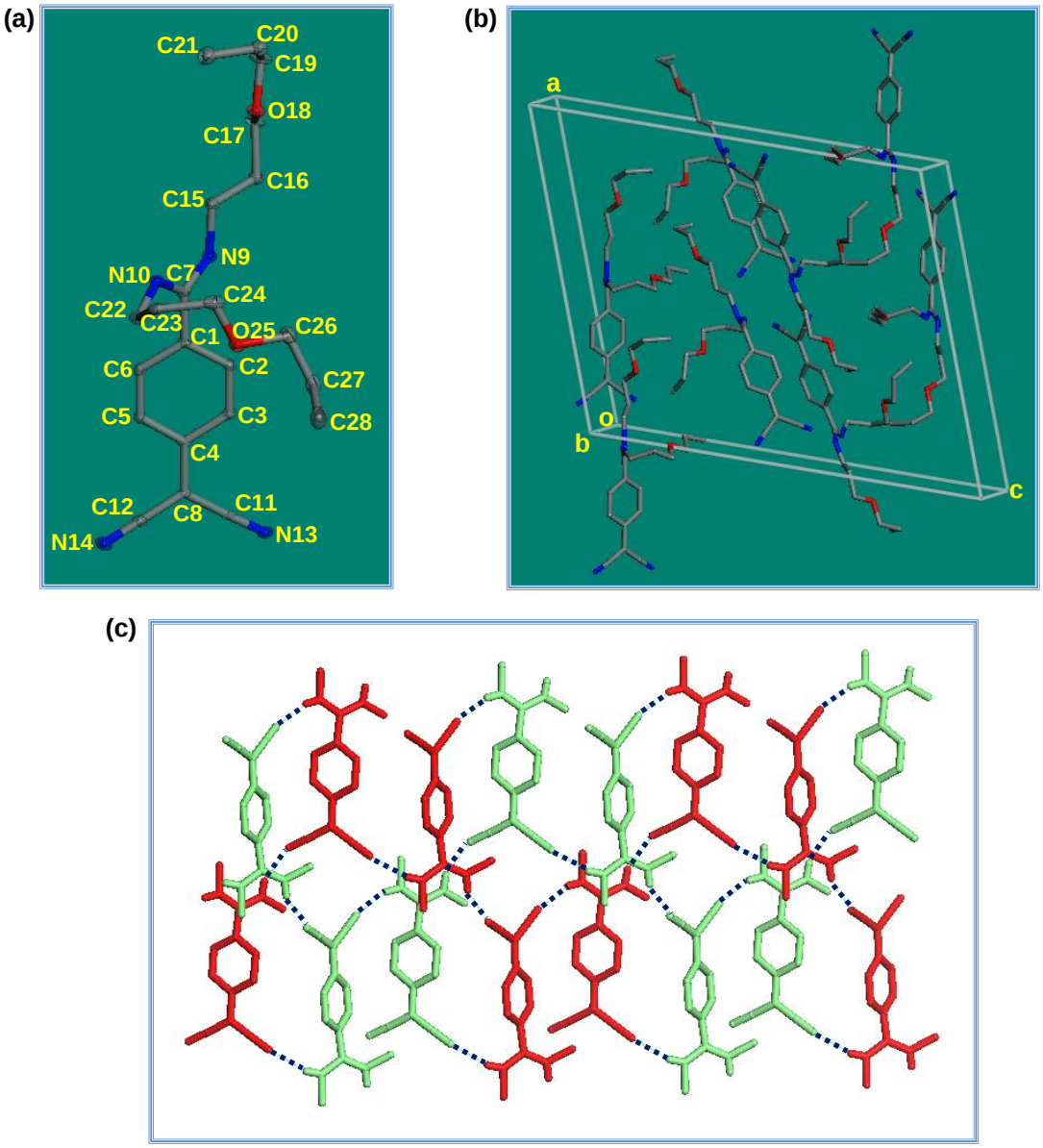

Figure 5.13. ***(a)*** *Molecular structure showing 99% thermal ellipsoids and* ***(b)*** *the unit cell of BPADQ; all H atoms are omitted for clarity.* ***(c)*** *The intertwined and linked helical assemblies of molecules in the crystal lattice formed through intermolecular H-bonds (broken lines); molecules in the two chains are shown in green and red, and H atoms on the benzenoid ring and all atoms in the propoxypropyl chains except the C connected to the amino group are omitted.*

Table 5.4. *Basic crystallographic details of BMADQ and BPADQ.*

Molecule	BMADQ. H_2O	BPADQ
Empirical formula	$C_{18}H_{24}N_4O_{2.5}$	$C_{22}H_{32}N_4O_2$
Crystal system	Triclinic	Monoclinic
Space group	*P1*	*C2*
a / Å	9.2596(12)	20.201(3)
b / Å	10.4998(13)	9.6344(14)
c / Å	11.2446(14)	24.199(4)
α / deg.	109.178(2)	90.00
β / deg.	106.922(2)	109.632(2)
γ /deg.	92.675(2)	90.00
V / $Å^3$	975.5(2)	4435.9(11)
Z	2	8
$\rho_{calc.}$ / g cm^{-3}	1.145	1.152
μ / cm^{-1}	0.078	0.075
Temperature / K	298(2)	100(2)
λ / Å	0.71073	0.71073
No. of reflections	6633	7761
No. of parameters	470	629
Max., Min. transmission	0.995, 0.989	0.973, 0.985
GOF	0.968	1.191
R [for $I \geq 2\sigma_I$]	0.0413	0.0676
wR^2	0.0979	0.1914
Largest difference peak and hole / e$Å^{-3}$	0.120, 0.027	0.384, -0.305

however, the associated enthalpies are negligeable. Electronic absorption, fluorescence emission and excitation spectra of acetonitrile solution, microcrystalline powder, **A** and **C** forms for the two derivatives are collected in Figs. 5.15 and 5.16. As with BEADQ, BMADQ and BPADQ also showed similar variation in the fluorescence response between solution and solid, and the **A** and **C** forms. The difference in the alkoxypropyl group among the three derivatives is clearly reflected in the stability of the amorphous form and its conversion to the crystalline form. Stability of the **A** form decreases in the order BMADQ > BEADQ > BPADQ. BMADQ takes significantly long time for

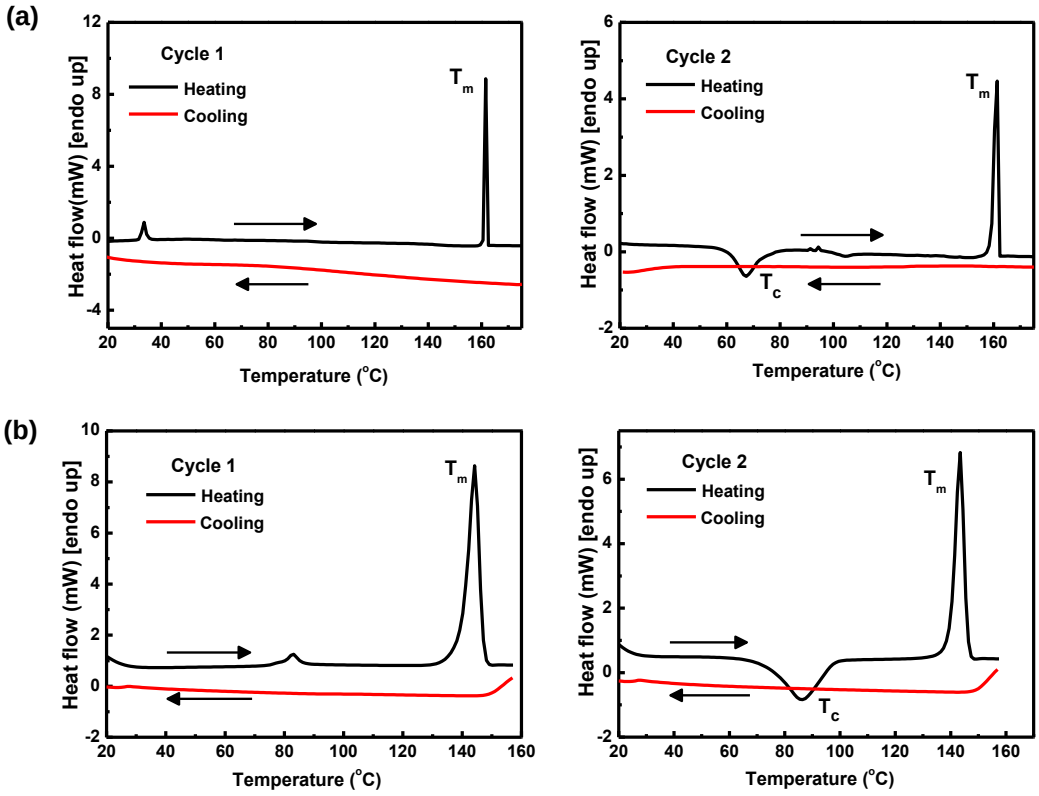

Figure 5.14. *DSC thermograms of **(a)** BMADQ and **(b)** BPADQ showing two heating-cooling cycles; scan rate: 2°C/min (heating) and 20°C/min (cooling) for BMADQ and 10°C/min (heating) and 40°C/min (cooling) for BPADQ.*

crystallization, whereas BPADQ is easily converted into the **C** form. Fluorescence emission response of the thin films of BMADQ and BPADQ during multiple A↔C transformations are shown in Figs. 5.17a, b. The plots also shows the stability of the phases during multiple thermally induced reversible transformation.

5.9. Spatially Controlled A↔C Transformation

All the studies discussed above were carried out by heating the entire thin film at T_m and T_c for amorphization and crystallization respectively. However, potential applications in information storage require spatially localized transformation in the phase change material.

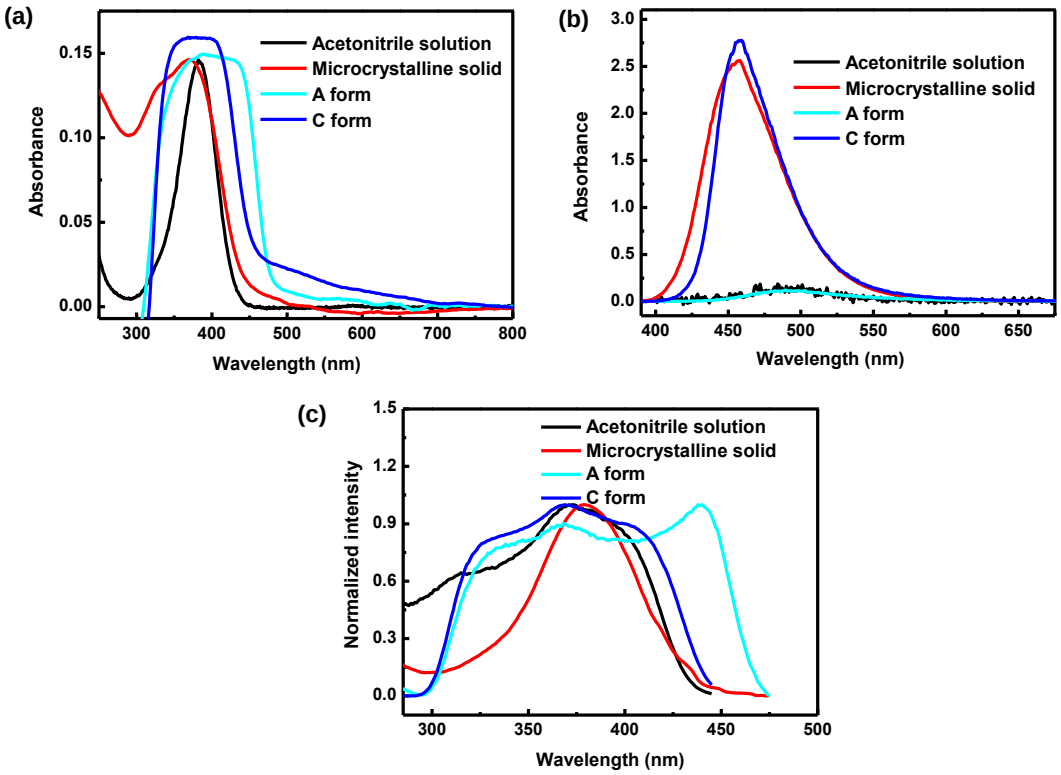

Figure 5.15. ***(a)*** *Electronic absorption,* ***(b)*** *fluorescence emission [λ_{exc} = 383 nm (solution) and 369 nm (others); relative intensities of the samples with similar optical density are shown; the solution spectrum is magnified by a factor of 400] and* ***(c)*** *fluorescence excitation [λ_{em} = 493 nm (solution and* ***A*** *form) and 457 nm (microcrystalline solid and the* ***C*** *form)] spectra of acetonitrile solution, microcrystalline solid, melt-quench (****A****) and recrystallized (****C****) forms of BMADQ. The* ***A*** *form was prepared by heating the thin film sample at 158^{o}C for 1 min and cooling rapidly to 25^{o}C; the* ***C*** *form was prepared by heating the* ***A*** *form at 70^{o}C for 12 min.*

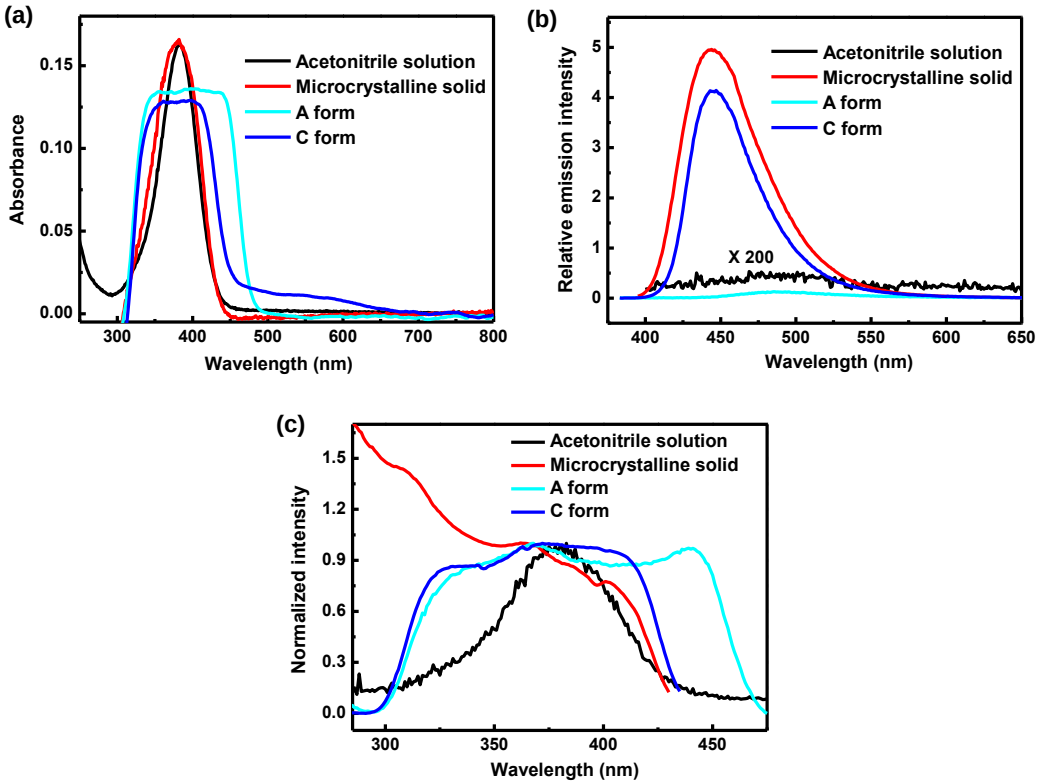

Figure 5.16. ***(a)*** *Electronic absorption,* ***(b)*** *fluorescence emission [λ_{exc} = 383 nm (solution) and 368 nm (others); the solution spectrum is magnified by a factor of 200] and* ***(c)*** *fluorescence excitation [λ_{em} = 490 nm (solution and* ***A*** *form) and 445 nm (microcrystalline solid and the* ***C*** *form)] spectra of acetonitrile solution, microcrystalline solid, melt-quench (****A****) and recrystallized (****C****) forms of BPADQ. The* ***A*** *form was prepared by heating the thin film sample at 145^{o}C for 1 min and cooling rapidly to 25^{o}C; the* ***C*** *form was prepared by heating the* ***A*** *form at 90^{o}C for 3 min.*

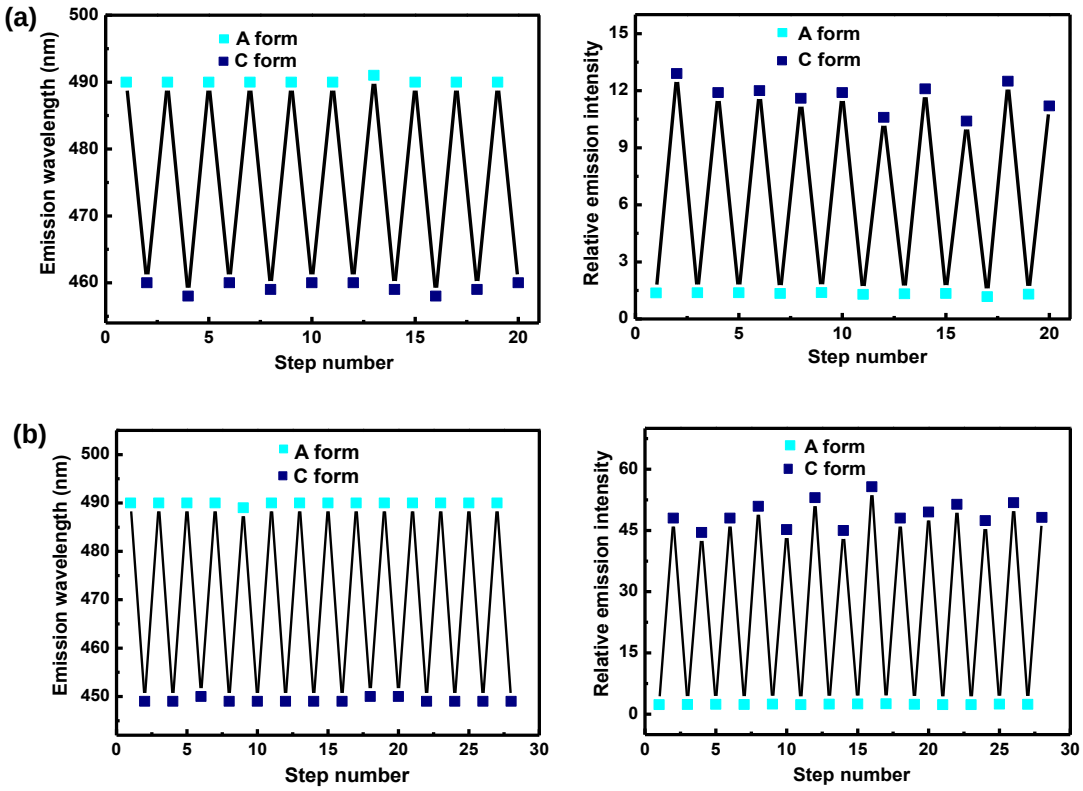

Figure 5.17. *Repeated switching of the fluorescence emission wavelength and peak intensity associated with the reversible* ***A*↔*C*** *transformations of* ***(a)*** *BMADQ and* ***(b)*** *BPADQ.*

5.9.1. Fluorescent pattern writing and erasure

As a preliminary experiment, we have attempted to carry out repeated writing and erasing of strongly fluorescent patterns by spatially localized heating and subsequent melt-quench operations. Microcrystalline powder of BEADQ sandwiched between 0.15 mm thick glass cover slips was melted and quenched to prepare a thin film of the **A** form as discussed earlier. A 1 mm wide nichrome strip (R ~ 20 Ω) was placed on a teflon film and the sample was placed above the strip in close contact with it; the strip was heated by applying 20 V across it for ~ 2 min; the heated region of the thin film showed strong bluish fluorescence under 365 nm irradiation indicating the formation of the **C** form (Fig. 5.18). Subsequent heating of the film at 165^{o}C for 2 min followed by quenching to 25^{o}C erased the design and brought the thin film back to the **A** form. The writing and erasing could be repeated as shown in the figure.

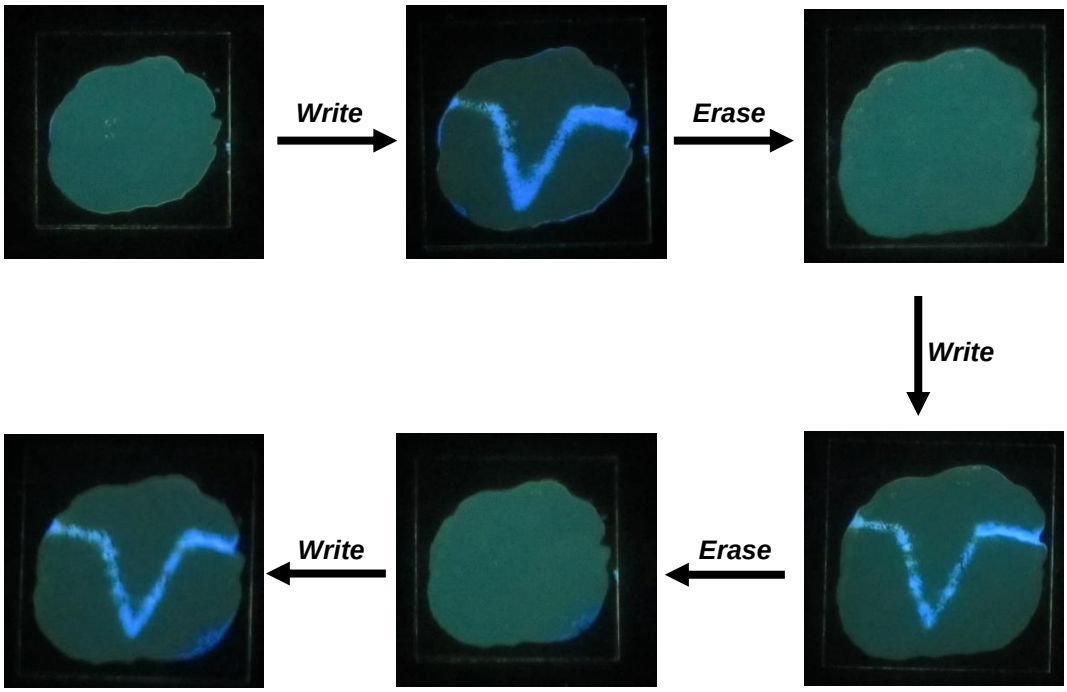

Figure 5.18. *Writing of fluorescent pattern on a BEADQ thin film in the **A** form, followed by erasure and a repeat cycle.*

5.9.2. BEADQ-polymer composite films

As mentioned in Sec. 5.4, the **A** form of BEADQ produced by melt-quench is stable only for a limited period, and tends to transform back to **C** form slowly. We have experimented with a number of techniques to stabilize the **A** form for extended periods, and subsequently induce localized **A**↔**C** transformation. Doping BEADQ in polymer films appeared to be the most promising approach. Based on extensive trials, it was found that dye-polymer composite films made of BEADQ with poly(vinyl acetate) (PVAc) as well as polymer blend of PVAc and poly(methyl methacrylate) (PMMA), stabilize the amorphous form for extended time, while allowing efficient conversion to the **C** form by heating at 70°C. We refer to the initial film also as in the **A** form, to be consistent with earlier discussion.

The dye-polymer composite films were fabricated as follows. BEADQ and the polymer [PVAc in acetonitrile solution or PVAc-PMMA (1:1 weight ratio) in

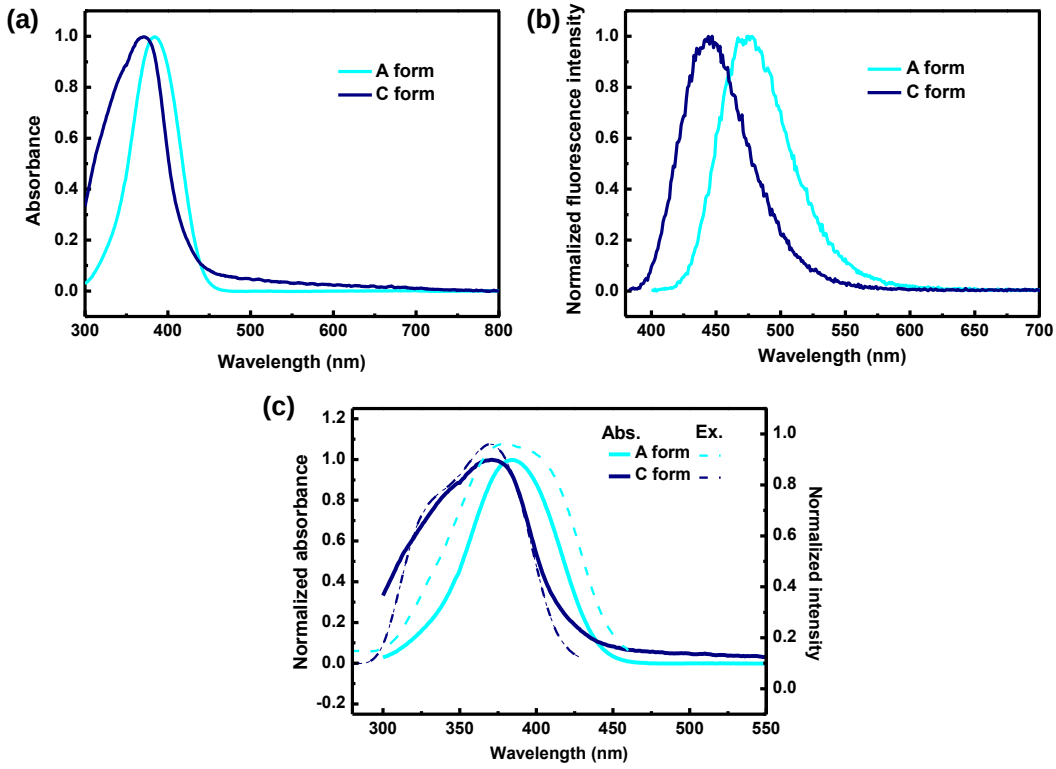

Figure 5.19. Normalized ***(a)*** *electronic absorption and* ***(b)*** *fluorescence emission [λ_{exc} = 384 nm (**A** form) and 368 nm (**C** form)] spectra of the **A** and **C** forms of BEADQ-PVAc films (x = 0.019).* ***(c)*** *Plot of the normalized absorption and fluorescence excitation [λ_{em} = 475 nm (**A** form) and 445 nm (**C** form)] spectra.*

chloroform solution] were mixed in the required dye-polymer weight ratio (*x*). Thin films were fabricated by spin-coating the dye-polymer solution on glass cover slips at 1000 rpm for 10 s and drying under vacuum for 15 min.

Normalized electronic absorption, fluorescence emission and excitation spectra of the **A** and **C** forms of the BEADQ-PVAc films (*x* = 0.019) are collected in Fig. 5.19. The absorption/emission of the **A** and **C** films are observed with λ_{max} at 384/475 nm, and 371/445 nm respectively; the absorption peaks closely coincide with that of the solution and solid (Table 5.3). The small blue shifted emission of the **A** form of the film compared to the melt-quench film is possibly due to the specific environment of the molecules in the polymer matrix, stabilizing the ground state. Fig. 5.20a demonstrates the stability of the **A** form of the film over ~ 10 days, based on the unchanged emission

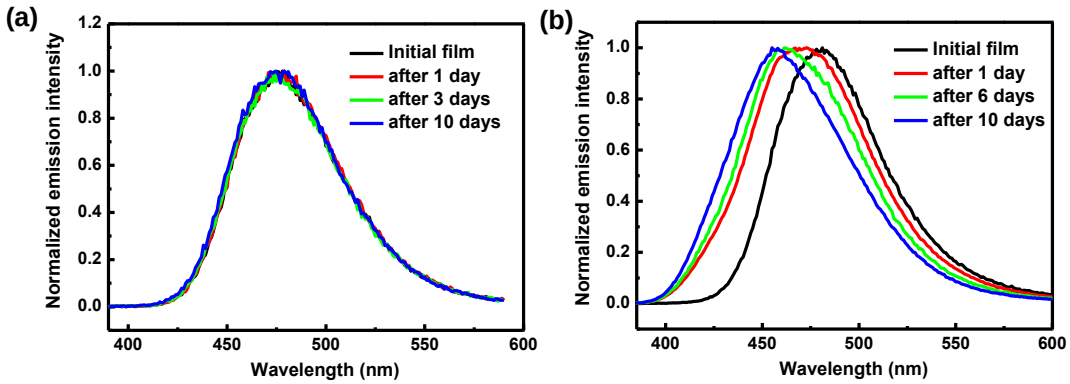

Figure 5.20. *Stability of the **A** form of BEADQ-PVAc films **(a)** x = 0.019 and **(b)** x = 0.125, monitored through fluorescence emission spectra.*

response at low dye loading (x = 0.019). It is seen that the stability is significantly compromised when the dye content is increased to x = 0.125. The amorphous and crystalline nature of BEADQ in the PVAc matrix is confirmed by the powder X-ray diffraction patterns recorded with the films (Fig. 5.21). Film in the **A** form exhibits no diffraction whereas the diffraction from the **C** form matches with that of the bulk microcrystalline powder; the relatively weak diffraction and absence of many peaks in the **C** form possibly arises due to the polymer matrix present and the exposure of only selected planes of the crystallites present near the surface of the film.

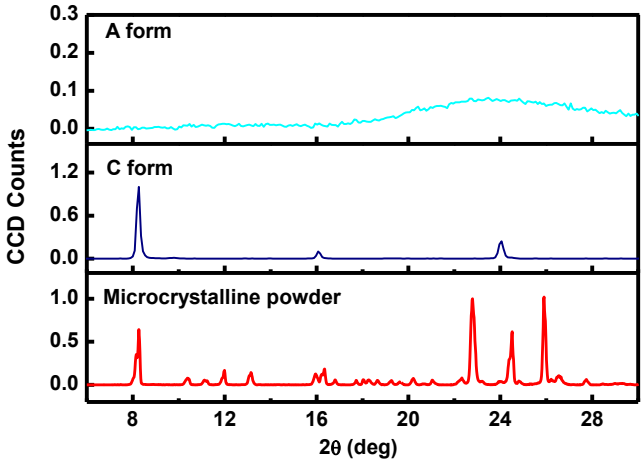

Figure 5.21. *X-ray diffraction pattern of the microcrystalline powder of BEADQ and the **C** and **A** forms of BEADQ-PVAc film.*

In Sec. 5.9.1, we demonstrated the writing and erasure of a fluorescent pattern on the melt-quench sample. Optical data storage in phase change materials involve localized heating of the material, by laser pulses, to induce the **A**↔**C** transformations. We have explored the possibility of inducing localized phase transformation of the dye-polymer composite films using a modified protocol; heat generated by irradiation of the substrate is used to bring about the phase transformation in the dye-polymer film. BEADQ-PVAc films coated on indium tin oxide (ITO) coated glass substrate were irradiated with 1030 nm laser. BEADQ-PVAc films with low dye content showed no A→C transformation; films with higher dye content suffer from the loss of the stability of **A** form as discussed earlier (Fig. 5.20b).

In view of these observations, we have explored further by modifying the polymer matrix. It was found that films fabricated with a blend of PVAc and PMMA tend to stabilize the **A** form of the films even with high values of *x*, for several days (Fig. 5.22). No change in the electronic absorption and emission response is observed by the addition of PMMA. Presence of PMMA does not affect the electronic absorption/emission spectra.

Laser scanning confocal fluorescence microscope images and fluorescence spectra reveal the amorphous and crystalline nature of the untransformed and transformed (by laser irradiation) regions respectively of the BEADQ-PVAC/PMMA composite film (x = 0.5) (Fig. 5.23a, b); emission response recorded from the imaged area matches with that of the **A** and **C** forms formed by melt-quench and

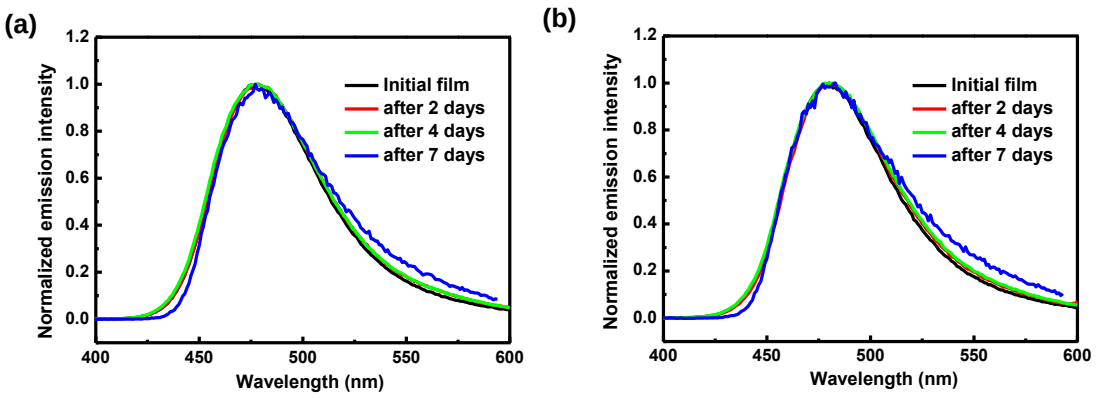

Figure 5.22. *Stability of the* ***A*** *form of BEADQ-PVAc/PMMA films* ***(a)*** *x = 0.25 and* ***(b)*** *x = 0.50, monitored through fluorescence emission spectra.*

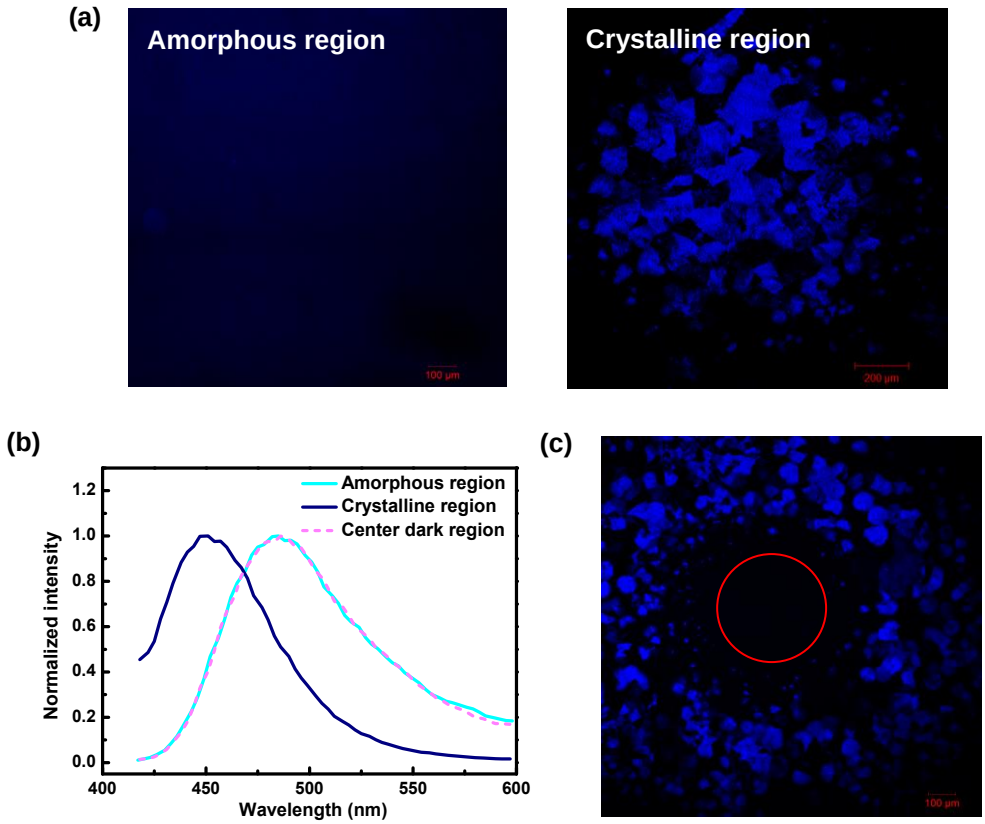

Figure 5.23. ***(a)*** *Laser scanning confocal microscope images and* ***(b)*** *the fluorescence emission response showing the amorphous and crystalline nature of untransformed and transformed region of BEADQ-PVAc/PMMA film respectively.* ***(c)*** *Image of the film irradiated with high power laser beam showing the amorphous and crystalline forms in the central and outer region of the irradiation spot; emission spectrum of the center region (red circle) is shown in* ***b****.*

recrystallization of pure BEADQ (Fig. 5.10b). Irradiation of the BEADQ-PVAc/PMMA film using a laser beam of high power (0.78 W) resulted in a pattern at the irradiation spot involving a central **A** form and peripheral **C** form (Fig. 5.23c); amorphous nature of the central dark region is confirmed by the emission response (Fig. 5.23b). It appears that the Gaussian profile of the laser beam is responsible for the formation of the observed pattern. Thus peak power in the center of the laser beam induces the formation of the **A** form whereas the region affected by lower laser intensity leads to the formation of the crystalline region.

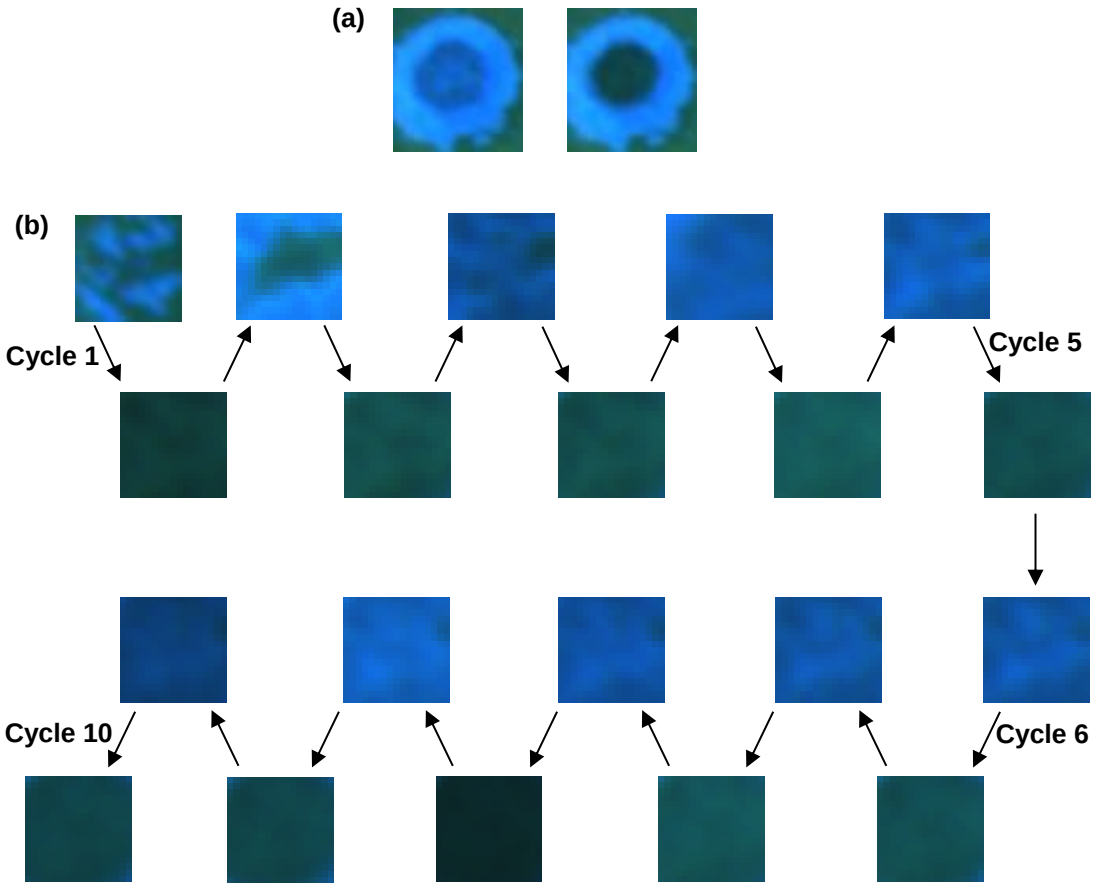

Figure. 5.24. ***(a)*** *Images of the laser irradiated region of BEADQ-PVAc/PMMA film (x = 0.5) under UV light illumination and* ***(b)*** *successive cycles of amorphization and crystallization events. [Central region of the images as shown in (a) is enlarged for clear visualization of the amorphous and crystalline forms in (b)].*

Several cycles of **A↔C** transformation on the BEADQ-PVAc/PMMA films (*x* = 0.5) was explored using laser beams with different power. Crystallization happened within 2 min by irradiating the film with a laser of power ~ 0.9 W and amorphization by ~ 3.0 W for 20 s. Images of the irradiated region were captured by a camera (Model ARTCAM-150P III) under UV light illumination. Fig. 5.24 shows the variation in the fluorescence of the laser irradiated region of the film through successive cycles of **A↔C** transformation while the outer ring of crystalline form was unavoidable throughout the present experimental conditions. The central region showed reversible transformation.

5.10. Summary

The alkoxyalkyl chain substituted DADQs we have synthesized show similar PCM behavior and fluorescence switching responses. The relative stability and rates of inter-conversion are found to vary with the alkoxy group, suggesting that tailoring the molecular structure can lead to optimal materials for unique PCM applications; this highlights the inherent versatility of molecular materials. The significant changes in the fluorescence emission as well as the transmittance of BEADQ between the **C** and **A** forms can be exploited in potential applications in information storage; preliminary experiments demonstrate the feasibility of repeated writing and erasing of strongly fluorescent patterns by spatially controlled heating and subsequent melt-quench operations as well as crystallization and amorphization by laser irradiation. Aspects like the long term stability of the phases, writing by irradiation to achieve higher resolution and enhancement of switching speeds remain to be addressed. The new family of molecules developed in this study, capable of facile and cyclic phase changes between crystalline and amorphous forms exhibiting prominent fluorescence emission color and intensity switching, represents the birth of a novel class of functional organic molecular materials. The switching optical responses mark a new direction in the evolution of PCMs.

References

1. D. C. Hyun, N. S. Levinson, U. Jeong and Y. Xia, *Angew. Chem. Int. Ed.*, 2014, **53**, 3780-3795.
2. S. Raoux, *Annu. Rev. Mater. Res.*, 2009, **39**, 25-48.
3. C. E. Giusca, V. Stolojan, J. Sloan, F. Börrnert, H. Shiozawa, K. Sader, M. H. Rümmeli, B. Büchner and S. R. P. Silva, *Nano Lett.*, 2013, **13**, 4020-4027.
4. C. Rios, P. Hosseini, C. D. Wright, H. Bhaskaran and W. H. P. Pernice, *Adv. Mater.*, 2014, **26**, 1372-1377.
5. T. P. Radhakrishnan, *Acc. Chem. Res.*, 2008, **41**, 367-376.
6. Y. Shirota, *J. Mater. Chem.*, 2000, **10**, 1-25.
7. B. C. Hancock and G. Zografi, *J. Pharm. Sci.*, 1997, **86**, 1-12.

8. M. Takahashi, N. S. Humam, N. Tsumori, T. Saiki, P. Regreny and M. Gendry, *App. Phys. Lett.*, 2013, **102**, 093120-1-3.

9. Y.-J. Jin, B. S.-I. Kim, W.-E. Lee, C.-L. Lee, H. Kim, K.-H. Song, S.-Y. Jang and G. Kwak, *NPG Asia Mater.*, 2014, **6**, e137-1-8.

10. F. Li, J. Zhuang, G. Jiang, H. Tang, A. Xia, L. Jiang, Y. Song, Y. Li and D. Zhu, *Chem. Mater.*, 2008, **20**, 1194-1196.

11. D. Yan, J. Lu, J. Ma, M. Wei, D. G. Evans and X. Duan, *Angew. Chem. Int. Ed*., 2011, **50**, 720-723.

12. T. Mutai, H. Satou and K. Araki, *Nat. Mater.*, 2005, **4**, 685-687.

13. X. Luo, J. Li, C. Li, L. Heng, Y. Q. Dong , Z. Liu, Z. Bo and B. Z. Tang, *Adv. Mater.*, 2011, **23**, 3261-3265.

14. A. H. Sporer, *App. Opt.*, 1987, **26**, 1240-1245.

15. W. R. Hertler, H. D. Hartzler, D. S. Acker and R. E. Benson, *J. Am. Chem. Soc.*, 1962, **84**, 3387-3393.

16. P. Gangopadhyay, S. Sharma, A. J. Rao, D. N. Rao, S. Cohen, I. Agranat and T. P. Radhakrishnan, C*hem. Mater.*, 1999, **11**, 466-472.

17. S. Jayanty and T. P. Radhakrishnan, *Chem. Eur. J.*, 2004, **10**, 791-797.

18. C. G. Chandaluri and T. P. Radhakrishnan, *Angew. Chem. Int. Ed.*, 2012, **51**, 11849-11852.

19. S. Jayanty and T. P. Radhakrishnan, *Chem. Mater.*, 2001, **13**, 2460-2462.

20. B. Zalba, J. M. Marín, L. F. Cabeza and H. Mehling, *App. Therm. Eng.*, 2003, **23**, 251-283.

21. P. J. Larkin, M. Dabros, B. Sarsfield, E. Chan, J. T. Carriere and B. C. Smith, *Appl. Spectrosc*., 2014, **68**, 758-776.

22. A. Alkhalil, J. B. Nanubolu and J. C. Burley, *RSC Adv.*, 2012, **2**, 209-216.

23. F. Zhang, O. Kambara, K. Tominaga, J.-i. Nishizawa, T. Sasaki, H.-W. Wang and M. Hayashi, *RSC Adv.*, 2014, **4**, 269-278

24. K. Rajesh and T. P. Radhakrishnan, *Chem. Eur. J.*, 2009, **15**, 2801-2809.

CHAPTER 6

Overview and Future Prospects

6.1. Overview of the Present Work

Enhanced emission in the aggregate/solid state of molecular materials has attracted extensive research initiatives in view of the fundamental photophysical aspects involved, as well as wide-ranging application potential. The phenomenon confined to select classes of molecules has mainly been attributed to the restriction of intramolecular motions like rotations and vibrations, as a consequence of the rigidification of the molecule in the aggregates/solids. This relatively uncommon enhanced emission response of aggregates/solids of such select systems and their contrast with most fluorophores and dye molecules which are generally prone to concentration quenching or aggregation caused quenching; clearly points to the role of factors other than just intramolecular effects that could affect the fluorescence emission efficiency in aggregates/solids. The broad theme developed in this thesis, addresses the relevance of intra and intermolecular effects acting concomitantly to effect fluorescence enhancement in aggregates/solids. Another general aspect we studied relates to reversible amorphous-crystalline phase transformation in molecular materials with a relevant fluorescence signature. Materials exhibiting reversible phase transformation accompanied by a significant change in some property, have found applications in energy and information storage. While the former has been realized in both organic and inorganic materials, the latter has been observed primarily in inorganic materials like alloy materials. Even though a few organic systems capable of undergoing thermally induced reversible amorphous-crystalline phase transformation have been reported, there have been no systematic demonstration of molecular phase change materials that exhibit switching of a functional property like fluorescence during the reversible transformation. Stabilizing the amorphous form of small organic molecule based materials that generally tend to crystallize with time, is itself an interesting problem.

We summarize below, our investigations into the two broad fields of explorations noted above, using the versatile class of fluorophore molecules based on the diaminodicyanoquinodimethane (DADQ) framework. Specifically we have developed new families of DADQs and explored their structural and electronic aspects to address the following aspects: (i) the critical role of molecular assembly in tuning fluorescence enhancement in molecular solids and (ii) phase change behavior and the associated fluorescence emission switching in a family of molecular materials.

DADQs with linked diaminomethylene group (formally an imidazolidine moiety) were synthesized systematically for the first time, using a new protocol (Scheme 2.1) that we have developed. The gradual variation in the fluorescence efficiency enhancement (FEE) from the molecules to the crystals in a series allowed the systematic investigation of the role of intra and intermolecular energy loss pathways on the phenomenon (Chapter 2). *Ab initio* computations centered around the molecular structures obtained from single crystal X-ray diffraction analysis revealed the possibility of the excited state energy decay through intramolecular motions like diaminomethylene or dicyanomethylene twist; this explains the weak fluorescence of solutions. Lattice energy studies indicated that such molecular twists are not feasible in some of the derivatives with substituent groups; the unsubstituted molecule is an exception as the diaminomethylene twist had low barrier, explaining its very small FEE value. To further understand the observed variation in the FEE of the whole series, we developed a simple model taking into account the relative orientation of fluorophore moieties and their transition dipoles to quantitatively estimate the relative rates of intermolecular energy transfer through the Dexter and Förster modes. We observed an inverse correlation between FEE and the relative energy transfer rates emphasizing the role of molecular assembly on the emission enhancement in molecular solids. The model was consolidated further by a detailed analysis of a series of crystals assembled from the same molecule and its enantiomer (Chapter 3). The general applicability of our model and analysis approach was tested using two families of fluorophores other than DADQs (Chapter 4); the inverse correlation between the FEE and relative energy transfer rates could be observed in these systems as well. Thus the studies presented in these three chapters project a simple approach to explore the role of intermolecular interactions

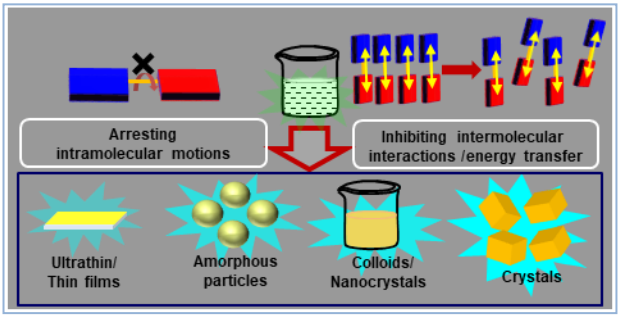

Figure 6.1. *Schematic diagram showing the fluorescence emission enhancement in various materials state, upon hindering of the intramolecular geometry relaxations and intermolecular energy transfer.*

together with intramolecular effects that lead to useful insight into the critical role of oriented aggregation of molecules resulting in enhanced fluorescence emission in aggregates/solids (Fig. 6.1).

Exploratory experiments with a wide range of substituent groups led us to the discovery that alkoxypropylamine substituted DADQs are useful candidates to demonstrate thermally induced reversible amorphous-crystalline transformation accompanied by remarkable changes in the fluorescence emission response (Chapter 5). While the flexible chain substituents possibly promote the amorphization process, the supramolecular assembly in the lattice formed through intermolecular hydrogen bonding is likely to help in regaining the ordered assemblies during recrystallization. Detailed calorimetry, diffraction, microscopy and spectroscopy investigations shed light on the important characteristics of bistability and extensive reversibility and cycling of the novel phase change material. The issue of the extended stability of the amorphous state was addressed by the fabrication of dye-polymer composite thin films. These thin films facilitated the demonstration spatially localized, reversible amorphous-crystalline transformation by laser irradiation, with potential for developing into patterning applications.

6.2. Future Prospects

Our investigations towards understanding the effect of intramolecular relaxation and intermolecular energy transfer on fluorescence enhancement in molecular solids demonstrated the crucial role of molecular assembly in the aggregate/solid state. Most of the earlier studies as well as those that we have presented relate to excited state intramolecular relaxations involving a torsional motion; however, many systems involve complex geometry changes during the excited state relaxation. In order to develop generalized models for a wide range of molecular systems, detailed analysis of the structural and electronic features of molecules in the solution and in the solids are required. Extensive and sophisticated computational modeling and ultrafast spectroscopy are required to address these issues. All the families of solids we have explored, consisted of three members with a well-defined molecular/crystal structure trends and FEE variation. It would be highly rewarding to study series with several more structures (polymorphs) exhibiting well-defined trends in the fluorescence enhancement. Rigorous evaluation of the energy transfer rates and logical evaluation of

the relevance of different modes of transfer are further open questions to explore. The proposed methodology of analyzing intramolecular and intermolecular effects could be applied to the understanding of structure-property relationship of newly emerging systems for the synthesis and development of novel solid state fluorescent materials.

The functional molecular phase change materials that we have studied are limited by the stability of amorphous form, and the reversible transformation by laser irradiation required a substrate that absorb the photons and produce local heating. New derivatives that can produce stable amorphous form for extended periods need to be explored. If the laser can directly heat the phase change material either by exciting the vibrational modes or by the fraction of molecules undergoing non-radiative decay during electronic de-excitation, the spatially localized transformation could be more effectively realized. Other important issues to be addressed are the time scales involved in phase switching, and long term photochemical stability of the molecules under laser irradiation.

In the broader context of developing novel optical materials, it is notable that the facile synthesis of DADQs has enabled the development of a large number of solid state fluorescent derivatives that emit in the blue, green and red regions. Deep red/near infrared emitting materials have found applications in light emitting devices and bioimaging. Red being one of the primary colors is useful for producing white light in combination with the other two, near infrared light has large penetration depths and is less harmful compared to the visible light. It would be interesting to look for deep red/near infrared emitting DADQs; extending the conjugation of the fluorophore framework could possibly shift the emission to higher wavelengths. The series of new DADQs studied in Chapters 2 and 3, prompted us to explore the reactions of 7,7,8,8-tetracyanoquinodimethane (TCNQ) or 7-pyrrolidino-7,8,8-tricyanoquinodimethane (PTCNQ) with aromatic diamines and polyamines (diethylenetriamine and triethylenetetraamine). Preliminary experiments in this direction were carried out by the reactions of *o*-phenylenediamine and 1,1′-binaphthyl-2,2′-diamine (Fig. 6.2) with PTCNQ. Product in the latter case could be characterized using ^{1}H NMR, and indicated the formation of the cyclic structures. Thus the reaction of PTCNQ with aromatic diamines is feasible and indicates the possibility of extending the synthesis protocol developed in this thesis to aromatic diamines like 2,3-diaminonaphthalene and 9,10-diaminophenanthrene (Fig. 6.2) with increased extent of conjugation. In another

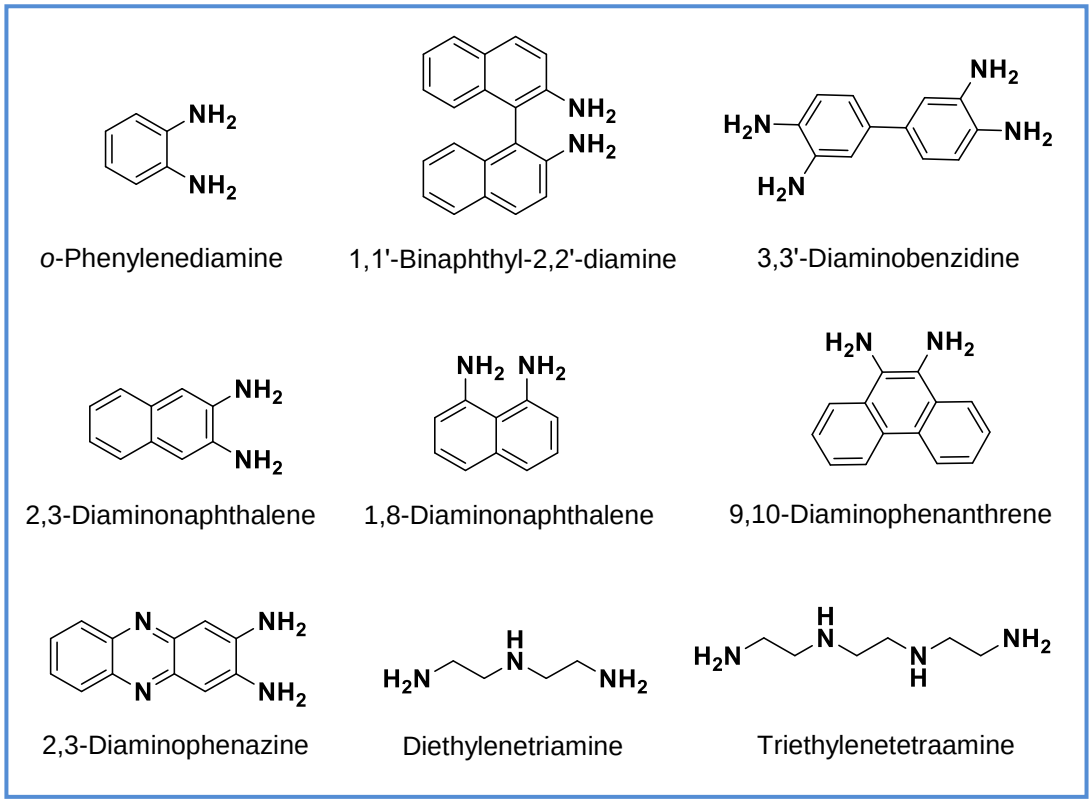

Figure 6.2. *Molecular structures of some of the amines discussed in the text.*

direction, effect of the ring size at the diaminomethylene end on the molecular structure parameters like the dihedral twist and further on the assembly in crystals and optical properties can be studied; some of the amines that could be tested are listed in Fig. 6.2. The resulting DADQs containing the conjugated diamine could form a class of deep red/near infrared emitting materials and their applications in bio-imaging and light emitting devices could be explored. The possible products of the reaction of TCNQ/PTCNQ with polyamines (Fig. 6.2) are either DADQ based polymers or simple DADQ chromophores with free amine groups; the latter, in particular can be used for the fabrication of metal-organic hybrid materials with wide a range of applications.[1]

Most of the DADQs explored till now are based on the chemical modification of the molecular structure (which further affect the electronic structure and hence their properties), primarily by varying the amine (1°/2°, aliphatic, alicyclic, aromatic etc.). The substituents present on the amino nitrogen determine the dihedral twist in the final

DADQ structure. Recently Lou et al. have reported a new synthesis method for these zwitterionic molecules which involved a methyl substitution on the *ortho* position of the benzenoid ring and also alkyl substitution on the amino nitrogen as well.[2] This new strategy allows the synthesis of N-alkylated derivatives which helps in improved solubility of the DADQs synthesized using aromatic diamines and can potentially increase the intermolecular separations in the crystal which helps in reducing the intermolecular energy transfer issues. Incorporating long alky chains could lead to amphiphilic derivatives which allow the fabrication of ultrathin films by the Langmuir-Blodgett technique; it could be interesting to explore in detail the role of controlled molecular assembly on the fluorescence enhancement phenomenon, extending the preliminary investigations reported from our lab earlier.[3]

Phenazine and its derivatives have been used as acceptors in some of the thermally activated delayed fluorescence emitters.[4] Introducing such moieties in the DADQ frameworks will be of interest to explore the properties of DADQs in this new direction. One possibility is to use commercially available 2,3-diaminophenazine. Reaction of PTCNQ with 3,3′-diaminobenzidine (Fig. 6.2) could yield acceptor-donor-acceptor kind of structures. These structures can exhibit combination of new optical characteristics with the enhanced emission of DADQs. The versatility of DADQs combined with the new modes of understanding the impact of molecular assembly in tuning and switching solid state fluorescence emission response opens up innumerable new avenues for further research in this field.

References:

1. (a) M. D. Allendorf, A. Bauer, R. K. Bhakta and R. J. T. Houk, *Chem. Soc. Rev*., 2009, **38**, 1330-1352. (b) Y. Zhao, *Chem. Mater*., 2016, **28**, 8079-8081.
2. A. J. T. Lou, S. Righetto, C. Barger, C. Zuccaccia, E. Cariati, A. Macchioni and T. J. Marks, *J. Am. Chem. Soc*., 2018, **140**, 8746-8755.
3. B. Balaswamy, L. Maganti, S. Sharma and T. P. Radhakrishnan, *Langmuir*, 2012, **28**, 17313-17321.
4. Z. Yang, Z. Mao, Z. Xie, Y. Zhang, S. Liu, J. Zhao, J. Xu, Z. Chi and M. P. Aldred, *Chem. Soc. Rev*., 2017, **46**, 915-1016. (b) Y. Im, M. Kim, Y. J. Cho, J. A Seo, K. S. Yook and J. Y. Lee, *Chem. Mater*., 2017, **29**, 1946-1963.

Appendix

APPENDIX A

Materials and Methods

7,7,8,8-tetracyanoquinodimethane	TCI Chemicals
3-alkoxypropylamine	TCI Chemicals
Ethylenediamine	Aldrich
N-Ethylehtylenediamine	Aldrich
N,*N*′-Dimethylethylenediamine	Aldrich
Pyrrolidine	Aldrich
trans-(±)-1,2-diaminocyclohexane	Aldrich
Poly(vinyl acetate)	Aldrich, M_w = 100 kDa
Poly(methylmethacrylate)	Aldrich, M_w = 120 kDa

7,7,8,8-tetracyanoquinodimethane (TCNQ) was recrystallized from acetonitrile prior to use, remaining chemicals were used as supplied. Pure enantiomers of *trans*-1,2-diaminocyclohexane were obtained by resolving 1,2-diaminocyclohexane (mixture of isomers) following the procedure from: J. F. Larrow, E. N. Jacobsen, Y. Gao, Y. Hong, X. Nie, C. M. Zepp, *J. Org. Chem.* 1994, **59**, 1939.

APPENDIX B

Instrumentation

Melting Point

Melting temperatures of solids were determined using Labindia model MR-VIS^{+} visual melting range apparatus.

Differential Scanning Calorimetry

Thermal properties of the crystals/polymers were examined using Perkin Elmer PYRIS Diamond DSC instrument following ramp method with exo-up mode. Data was analyzed using version 8.0 Pyris software.

Nuclear Magnetic Resonance Spectroscopy

^{1}H and ^{13}C NMR spectra were recorded on a Bruker 400 and 500 MHz NMR spectrometer.

Infrared Spectroscopy

FT-IR spectra were recorded on a Jasco5300 FTIR spectrometer. Spectra for all the solid samples were recorded as KBr pellets.

Mass Spectroscopy

High resolution mass spectrometer equipped with ESI-TOF analyzer was used to record the mass spectra of the compounds.

Absorption Spectroscopy

Absorption spectra were recorded on a Varian model Cary 100 UV-Vis spectrometer. Absorption spectra of solution samples were recorded in transmission mode and solid samples in diffuse reflectance mode.

Fluorescence Spectroscopy

Steady state fluorescence emission and excitation spectra were recorded on a Horiba Jobin Yvon model FL3-22 Fluorolog spectrofluorimeter, in right angle geometry. Quantum yield of solid samples were determined using an integrating sphere and the PLQY Calculator v.3 software (Jobin Yvon). Fluorescence emission of samples

at different temperatures were recorded on a Jobin-Yvon Spex Fluoromax-4 spectrometer coupled with a Peltier device.

Spin-coating

Laurell Technologies Corporation Model WS-650HZ-23NPP/LITE photoresist spinner was used for the fabrication of dye-polymer thin films.

Single Crystal X-ray Diffraction

Single crystal X-ray diffraction studies were carried out on a Bruker SMART APEX CCD area detector system equipped with a graphite monochromator and a MoK_{α} fine-focus sealed tube (λ = 0.71073 Å) operated at 1200 W (40 kV, 30 mA) or Rigaku Oxford XtaLAB Pro-Pilatus3 R 200K-A detector system equipped with a CuKα (λ = 1.54184 Å) MicroMax-003 microfocus sealed tube operated at 50 kV and 0.6 mA or a Bruker D8 Quest-Photon II detector system equipped with a MoKα (λ = 0.71073 Å) microfocus sealed tube operated at 50 kV and 1 mA. Data was collected at 100 K (as well as 298 K), and the reduction was performed using Bruker SAINT or CrysAlisPro software; the structure was solved and refined using the Bruker SHELXTL software.

Confocal Raman Microscope

WITec model Alpha300 R equipped with an AFM was used for recording the Raman spectra.

Laser Scanning Confocal Microscope

Carl Zeiss model LSM 710 NLO ConfoCor 3 microscope was used for confocal fluorescence microscopy studies. Second harmonic frequency of 780 nm laser was used for excitation.

Fluorescence Lifetime Imaging Microscopy

Time-resolved confocal fluorescence microscope (MicroTime 200, PicoQuant) coupled to an Olympus IX71 microscope (PicoQuant) was used for fluorescence lifetime imaging studies. Excitation was carried out using a 405 nm pulsed-laser diode and the fluorescence observed through a 430 nm long-pass filter; the corresponding fwhm of pulse response function was 176 ps. Data acquisition was performed with a PicoHarp 300 TCSPC module using PicoHarp300 version 2.3 in a time-tagged time-resolved mode.

Computations

Computations reported in the various chapters were carried out on SGI Altix 8200/4700 machines with 2.5/9.2 GHz processors, IBM p755 with 3.3 GHz power 7 processor and Sataseersha with 4 AMD processors. Gaussian 09 software package was used for DFT/TD-DFT calculations and Materials Studio (v 6.0.0, Accelrys Software Inc.) for lattice energy calculations.

APPENDIX C

Computed Frequencies for the Fully Optimized Strucutres

Frequencies calculated for the fully optimized structure of **1a-c** (Chapter 2) and DCDADQ (Chapter 3) are all positive, indicating that these are the minimum energy structures.

Table C.1. Computed frequencies of the fully optimized structure of **1a** in vacuum (Vac.) and acetonitrile (ACN) environments.

No.	Frequency (cm^{-1})		No.	Frequency (cm^{-1})		No.	Frequency (cm^{-1})	
	ACN	Vac.		ACN	Vac.		ACN	Vac.
1	47.9	45.4	26	733.8	724.0	51	1405.0	1427.0
2	57.2	61.7	27	750.1	745.7	52	1411.3	1437.6
3	85.9	86.7	28	829.6	809.8	53	1498.4	1495.0
4	91.7	109.9	29	851.1	850.1	54	1528.7	1533.8
5	127.3	127.5	30	897.7	908.8	55	1538.9	1542.7
6	131.6	130.2	31	921.7	915.2	56	1550.2	1555.9
7	155.6	157.5	32	959.3	958.4	57	1558.8	1556.2
8	169.0	201.4	33	969.8	970.4	58	1597.2	1565.0
9	211.2	208.2	34	977.9	981.6	59	1622.3	1652.0
10	284.7	288.9	35	1012.8	1002.2	60	1658.9	1676.3
11	302.0	289.1	36	1026.0	1005.4	61	2253.1	2297.3
12	340.6	336.8	37	1031.5	1049.3	62	2288.7	2318.9
13	420.6	425.6	38	1059.1	1051.6	63	3079.2	3037.6
14	440.6	444.7	39	1135.2	1131.9	64	3082.7	3045.4
15	499.0	475.6	40	1156.6	1142.2	65	3147.5	3125.6
16	507.6	487.1	41	1162.6	1157.1	66	3156.5	3132.1
17	512.4	519.8	42	1227.0	1223.7	67	3196.9	3179.1
18	524.2	521.2	43	1228.1	1236.2	68	3197.5	3179.5
19	544.6	538.8	44	1249.7	1236.6	69	3213.6	3217.7
20	556.5	586.8	45	1254.3	1247.9	70	3215.5	3218.7
21	617.3	617.4	46	1327.6	1312.6	71	3637.7	3626.8
22	635.7	623.6	47	1329.7	1347.6	72	3640. 6	3627.1
23	645.2	638.6	48	1355.5	1349.4			
24	689.7	667.9	49	1361.0	1363.5			
25	729.1	723.2	50	1373.7	1406.5			

Table C.2. Computed frequencies of the fully optimized structure of **1b** in propanonitrile (PCN) and acetonitrile (ACN) environments.

No.	Frequency (cm^{-1})		No.	Frequency (cm^{-1})		No.	Frequency (cm^{-1})	
	ACN	PCN		ACN	PCN		ACN	PCN
1	33.4	33.8	31	746.6	746.5	61	1401.3	1401.3
2	48.6	48.6	32	792.5	792.5	62	1409.3	1409.4
3	66.7	67.0	33	805.1	805.1	63	1439.7	1439.9
4	78.0	78.3	34	841.7	841.6	64	1492.6	1493.1
5	100.5	100.6	35	856.0	856.1	65	1508.7	1508.9
6	103.0	103.2	36	886.6	886.3	66	1513.0	1513.1
7	126.8	126.9	37	951.4	951.4	67	1526.8	1526.8
8	130.2	130.2	38	970.6	970.5	68	1529.7	1529.7
9	150.4	150.5	39	978.5	978.4	69	1533.5	1533.5
10	164.5	164.7	40	984.8	984.8	70	1549.6	1549.6
11	216.7	216.8	41	999.6	999.5	71	1560.1	1559.8
12	226.8	226.8	42	1013.7	1013.6	72	1594.1	1593.9
13	271.0	271.1	43	1028.4	1028.3	73	1609.2	1609.0
14	282.8	282.8	44	1055.5	1055.6	74	1652.7	1652.8
15	346.7	346.6	45	1107.2	1107.3	75	2248.7	2249.1
16	367.8	367.8	46	1124.6	1124.6	76	2285.9	2286.1
17	378.8	378.8	47	1144.4	1144.5	77	3062.2	3062.2
18	428.7	428.8	48	1159.6	1159.7	78	3065.1	3065.0
19	479.5	479.5	49	1212.5	1212.5	79	3071.9	3071.7
20	510.1	510.0	50	1222.3	1222.1	80	3085.0	3084.7
21	513.1	513.2	51	1231.4	1231.4	81	3129.1	3129.1
22	520.5	520.6	52	1240.1	1240.2	82	3137.0	3136.7
23	539.5	539.7	53	1252.2	1252.1	83	3138.1	3138.2
24	560.6	561.4	54	1279.3	1279.2	84	3148.6	3148.5
25	617.8	617.9	55	1323.2	1323.2	85	3159.3	3159.3
26	634.8	634.8	56	1333.1	1333.1	86	3197.7	3197.7
27	636.7	636.5	57	1558.8	1352.6	87	3204.6	3204.7
28	646.0	646.0	58	1597.2	1359.4	88	3213.1	3213.2
29	695.8	695.7	59	1622.3	1368.3	89	3222.4	3222.5
30	736.2	736.1	60	1658.9	1376.8	90	3629.8	3629.8

Table C.3. Computed frequencies of the fully optimized structure of **1c** in acetonitrile (ACN) environment.

No.	Frequency (cm^{-1})	No.	Frequency (cm^{-1})	No.	Frequency (cm^{-1})
	ACN		ACN		ACN
1	35.8	31	742.2	61	1463.5
2	43.8	32	745.5	62	1473.8
3	66.7	33	844.3	63	1485.4
4	69.7	34	853.9	64	1503.6
5	102.2	35	866.7	65	1506.0
6	105.2	36	950.6	66	1511.2
7	124.2	37	970.5	67	1520.8
8	127.9	38	977.4	68	1530.8
9	132.8	39	985.6	69	1539.0
10	140.9	40	1010.8	70	1551.8
11	192.1	41	1015.6	71	1568.8
12	192.4	42	1029.4	72	1604.3
13	229.4	43	1102.7	73	1626.7
14	251.6	44	1104. 3	74	1649.1
15	285.1	45	1118.5	75	2244.2
16	347.1	46	1155.0	76	2283.3
17	352.8	47	1164.1	77	3064.6
18	371.1	48	1173.1	78	3065.5
19	428.3	49	1214.6	79	3077.8
20	475.2	50	1240.9	80	3081.5
21	508.1	51	1253.2	81	3120.0
22	511.0	52	1253.6	82	3124.0
23	525.5	53	1257.3	83	3125.0
24	542.5	54	1278.5	84	3135.7
25	608.9	55	1319.2	85	3192.2
26	618.0	56	1341.8	86	3192.4
27	637.2	57	1351.4	87	3198.3
28	641.9	58	1357.0	88	3199.2
29	663.8	59	1362.9	89	3212.5
30	698.2	60	1408.8	90	3214.4

Table C.4. Computed frequencies of the fully optimized structure of **DCDADQ** in acetonitrile (ACN) environment.

No.	Frequency (cm^{-1})	No.	Frequency (cm^{-1})	No.	Frequency (cm^{-1})	No.	Frequency (cm^{-1})
	ACN		ACN		ACN		ACN
1	26.5779	31	546.516	61	1162.835	91	1520.051
2	34.046	32	616.4104	62	1169.763	92	1520.819
3	40.124	33	636.821	63	1170.753	93	1529.351
4	80.0045	34	642.0765	64	1216.196	94	1541.991
5	98.4616	35	647.2932	65	1226.064	95	1562.364
6	103.0994	36	656.3651	66	1252.01	96	1583.233
7	114.3026	37	710.7981	67	1253.953	97	1588.305
8	121.95	38	747.1403	68	1270.075	98	1647.854
9	132.7837	39	754.7739	69	1277.071	99	2244.28
10	171.6288	40	811.1475	70	1277.506	100	2283.208
11	193.9233	41	836.23	71	1304.05	101	2983.197
12	197.4601	42	842.869	72	1344.986	102	2994.08
13	217.5367	43	846.0223	73	1347.128	103	3041.803
14	218.9199	44	857.7015	74	1354.415	104	3046.254
15	233.375	45	887.9135	75	1357.678	105	3058.125
16	256.8137	46	932.7392	76	1362.616	106	3058.354
17	269.1908	47	944.6141	77	1370.116	107	3059.915
18	303.873	48	976.0378	78	1384.056	108	3061.193
19	326.2568	49	983.2155	79	1394.367	109	3097.257
20	339.7924	50	987.3955	80	1408.718	110	3098.873
21	374.3988	51	1015.172	81	1422.749	111	3106.924
22	397.1616	52	1025.319	82	1433.139	112	3108.213
23	422.8753	53	1028.086	83	1459.181	113	3136.996
24	433.6014	54	1068.579	84	1470.57	114	3137.012
25	471.6515	55	1074.45	85	1485.003	115	3187.283
26	496.2523	56	1092.297	86	1505.809	116	3187.304
27	498.8034	57	1094.692	87	1506.222	117	3199.227
28	511.752	58	1117.944	88	1506.656	118	3200.146
29	526.3392	59	1151.597	89	1511.451	119	3213.965
30	541.7156	60	1155.668	90	1513.331	120	3215.837

Publications and Presentations

PUBLICATIONS

1. P. Srujana and T. P. Radhakrishnan, Extensively Reversible Thermal Transformations of a Bistable, Fluorescence-Switchable Molecular Solid: Entry into Functional Molecular Phase-Change Materials, *Angew. Chem. Int. Ed.*, 2015, **54**, 7270-7274.
2. P. Srujana, T. Gera and T. P. Radhakrishnan, Fluorescence Enhancement in Crystals Tuned by a Molecular Torsion Angle: A Model to Analyze Structural Impact, *J. Mater. Chem. C*, 2016, **4**, 6510-6515.
3. P. Srujana and T. P. Radhakrishnan, Establishing the Critical Role of Oriented Aggregation in Molecular Solid State Fluorescence Enhancement, *Chem. Eur. J.*, 2018, **24**, 1784-1788.
4. P. Srujana and T. P. Radhakrishnan, Impact of Molecular Orientation on Fluorescence Emission Enhancement in Aggregates, *Mater. Chem. Front*., 2018, **2**, 632-634.
5. P. Srujana, P. Sudhakar and T. P. Radhakrishnan, Enhancement of Fluorescence Efficiency from Molecules to Materials and the Critical Role of Molecular Assembly, *J. Mater. Chem. C*, 2018, **6**, 9314-9329.

PRESENTATIONS

1. Poster presentation: Chemfest-2015, School of Chemistry, University of Hyderabad, Hyderabad, India, February 20-21, **2015**.
   Tuning the Fluorescence Emission by Structural Modification and Phase Transition of Molecular Optical Materials. (Received Best Poster Presentation Award)
2. Poster presentation: International Conference on Materials for the Millennium (MATCON 2016), Cochin University of Science and Technology, Kochi, India, January 14-16, **2016**.

Structural Control of Fluorescence Emission Enhancement in DADQ based Molecular Crystal.

3. Poster presentation: CRSI National Symposium in Chemistry, Punjab University, Chandigarh, India, February 5-7, **2016**.
   Tuning the Fluorescence Emission in DADQ Based Molecules by Modifying Structure and Assembly.

4. Oral presentation: Chemfest-2017, School of Chemistry, University of Hyderabad, Hyderabad, India, March 3-4, **2017**.
   Fluorescence Emission Enhancement and Switching in DADQs Tuned by Molecular Structure and Assembly. (Received Best Oral Presentation Award)

5. Poster presentation: National Meeting of Synthetic and Theoretical Chemists (NMSTC), School of Chemistry, University of Hyderabad, Hyderabad, India, October 13-14, **2017**.
   Fluorescence Emission Enhancement in DADQs Tuned by Molecular Structure and Assembly.

6. Poster presentation: International Collaborative and Cooperative Chemistry Symposium (ICCCS-8), School of Chemistry, University of Hyderabad, Hyderabad, India, December 18-19, **2017**.
   Fluorescence Emission Enhancement Tuned by Molecular Structure and Importance of Oriented Aggregation.

7. Oral presentation: Dr. K. V. Rao Annual Research Award Program 2017-2018, Hyderabad, India, March 31, **2018**.
   Synthesis of Novel Fluorescent Molecular Materials: Functional Phase Change Materials and Effect of Oriented Assembly on Solid State Emission Enhancement. (Received "*2nd Runner-up trophy*")

8. Oral presentation: Young Scientist's Colloquium (YSC-2018), conducted by Materials Research Society of India (MRSI), Kolkata Chapter, Indian Association for the Cultivation of Science, Jadavpur, Kolkata, India, September 20, **2018**.
   Fluorescence Efficiency Enhancement from Molecular to Material State: Critical Role of Oriented Aggregation.

Fluorescence Emission Enhancement in Molecular Solids: Insight into the Critical role of Oriented Assembly and Entry into Functional Molecular Phase Change Materials

by P Srujana

Submission date: 02-Nov-2018 09:55AM (UTC+0530)
Submission ID: 1031462225
File name: 12CHPH14_Srujana_Ph.D_Thesis.pdf (8.5M)
Word count: 38183
Character count: 197782

Fluorescence Emission Enhancement in Molecular Solids: Insight into the Critical role of Oriented Assembly and Entry into Functional Molecular Phase Change Materials

ORIGINALITY REPORT

27%	3%	27%	1%
SIMILARITY INDEX	INTERNET SOURCES	PUBLICATIONS	STUDENT PAPERS

PRIMARY SOURCES

1	P. Srujana, Tarun Gera, T. P. Radhakrishnan. "Fluorescence enhancement in crystals tuned by a molecular torsion angle: a model to analyze structural impact", J. Mater. Chem. C, 2016 Publication	7%
2	Srujana, P., and T. P. Radhakrishnan. "Extensively Reversible Thermal Transformations of a Bistable, Fluorescence-Switchable Molecular Solid: Entry into Functional Molecular Phase-Change Materials", Angewandte Chemie International Edition, 2015. Publication	7%
3	P. Srujana, T. P. Radhakrishnan. "Establishing the Critical Role of Oriented Aggregation in Molecular Solid State Fluorescence Enhancement", Chemistry - A European Journal, 2018	6%

Publication

4	P. Srujana, T. P. Radhakrishnan. "Impact of molecular orientation on fluorescence emission enhancement in aggregates", Materials Chemistry Frontiers, 2018 Publication	3%
5	Ju Mei, Nelson L. C. Leung, Ryan T. K. Kwok, Jacky W. Y. Lam, Ben Zhong Tang. "Aggregation-Induced Emission: Together We Shine, United We Soar!", Chemical Reviews, 2015 Publication	<1%
6	Chandaluri, Ch. G., and T. P. Radhakrishnan. "Hierarchical assembly of a molecular material through the amorphous phase and the evolution of its fluorescence emission", Journal of Materials Chemistry C, 2013. Publication	<1%
7	B. Balaswamy, Lasya Maganti, Sonika Sharma, T. P. Radhakrishnan. "Mechanical Control of Molecular Aggregation and Fluorescence Switching/Enhancement in an Ultrathin Film", Langmuir, 2012 Publication	<1%
8	Ch.G. Chandaluri, T.P. Radhakrishnan. "Zwitterionic diaminodicyanoquinodimethanes with enhanced blue–green emission in the solid	<1%

state", Optical Materials, 2011
Publication

9	A. Patra. "Molecular Materials with Contrasting Optical Responses from a Single-Pot Reaction and Fluorescence Switching in a Carbon Acid", Chemistry - A European Journal, 03/09/2009 Publication	<1%
10	www.freepatentsonline.com Internet Source	<1%
11	Submitted to University of Newcastle upon Tyne Student Paper	<1%
12	A. Patra. "Tris(4-cyanophenyl)amine: Simple Synthesis via Self-assembly; Strong Fluorescence in Solution, Nano/microcrystals, and Solid", Advanced Functional Materials, 09/03/2007 Publication	<1%
13	archivia.unict.it Internet Source	<1%
14	tel.archives-ouvertes.fr Internet Source	<1%
15	Lecture Notes in Chemistry, 2015. Publication	<1%
16	Rosemary A. Croft, James J. Mousseau, Chulho Choi, James A. Bull. "Oxetane ethers	<1%

are formed reversibly in the lithium-catalyzed Friedel–Crafts alkylation of phenols with oxetanols: Synthesis of dihydrobenzofurans, diaryloxetanes, and oxetane ethers", Tetrahedron, 2018
Publication

---

17 Simone Raoux, Wojciech Wełnic, Daniele Ielmini. "Phase Change Materials and Their Application to Nonvolatile Memories", Chemical Reviews, 2009 — <1%
Publication

---

18 "Anion Recognition in Supramolecular Chemistry", Springer Nature America, Inc, 2010 — <1%
Publication

---

19 ubm.opus.hbz-nrw.de — <1%
Internet Source

---

20 core.ac.uk — <1%
Internet Source

---

21 dyuthi.cusat.ac.in — <1%
Internet Source

---

22 Liu, Qiang, Xiaoming Qiang, Yan Li, Zhipei Sang, Yuxing Li, Zhenghuai Tan, and Yong Deng. "Design, synthesis and evaluation of chromone-2-carboxamido-alkylbenzylamines as multifunctional agents for the treatment of Alzheimer’s disease", Bioorganic & Medicinal — <1%